Structure-Property Relationships of Solids in Pharmaceutical Processing

A DISSERTATION
SUBMITTED TO THE FACULTY OF THE GRADUATE SCHOOL
OF THE UNIVERSITY OF MINNESOTA
BY

Sayantan Chattoraj

IN PARTIAL FULFILLMENT OF THE REQUIREMENTS
FOR THE DEGREE OF
DOCTOR OF PHILOSOPHY

Changquan Calvin Sun, Ph.D. (Adviser)

November 2012

Acknowledgements

"Success is not to be pursued; it is to be attracted by the person we become." - Jim Rohn. This adequately summarizes the guiding motivation with which I have operated within both my professional and personal space over the past few years. While the end result matters, it is the process and the associated paths I traverse leading to the result that I find more intriguing and therefore, particularly gratifying. With this mental framework in place, I approached my doctoral research with the objective of continuous advancement in both my scientific acumen, as well as holistic personality development. In this endeavor, several great individuals came together to share my journey. I want to thank each and every one of those individuals who has made a lasting impression on my research, as well as helped me develop into the person who I am today.

This research would not be possible without the continuous support, encouragement and guidance of my adviser, Dr. Changquan Calvin Sun. His passion for science is contagious, and has helped me pursue my research in a timely and systematic manner. I thank him for giving me the opportunity to interact with him on a nearly day-to-day basis for the past four years. I have always enjoyed these interactions, whether they involved science or not. I am also especially grateful to him for providing me with the opportunity to simultaneously work on preformulation, formulation and materials science aspects of drug development, a rare combination that has already served me well as I transition into my next career.

It is also very gratifying to have Prof. Raj Suryanarayanan, Prof. Tim Wiedmann, and Prof. Bill Gerberich as my other mentors in the doctoral dissertation committee. It has just been a pleasure interacting with them over the years, and I thank them for all their guidance, suggestions and friendship. I want to thank Dr. Sury and Dr. Wiedmann, in particular, for introducing me to the field of solid-state pharmaceuticals, and ascribe a significant portion of my understanding of this topic to them. I am also grateful to Dr. Sury and his laboratory members for instrumental support to our research.

I have had the good fortune of associating with exceptional industrial collaborators at Boehringer-Ingelheim Pharmaceuticals, Inc at Connecticut, USA, who funded my doctoral project for the past three years. I thank Dr. Chandan Bhugra, Dr. Jane Zheng Li, Dr. Chitra Telang, Dr. Zeren Wang and Dr. Keith Horspool for their continued interest in my research, support and encouragement. I especially am indebted to Chandan for his helpful suggestions in experimental design, and providing the industrial perspective to my research. This effective collaboration has, in essence, shaped my future career.

My research productivity has largely depended on the support and insight of my fellow researchers in the laboratory. I thank Dr. Limin Shi, Dr. Reddy Perumalla, Dr. Kou Xiang, Dr. Qun Zhou, Dr Miles Chen, and Frederick Osei-Yeboah for all their assistance. I especially thank Limin with whom I collaborated on several projects, and have learnt significantly from his work ethics and ability to multi-task. Research discussions with him have, in part, guided my thought process at various stages of my work.

This journey would not be possible without the unconditional love, support and guidance of Mom and Dad. I am forever grateful for having them in my life and being such exemplary role models to emulate. I owe my soft skills, such as poise, objectivity and humility, to these two very special individuals. I am excited to look forward to the next phases in our lives, and if the past is an indicator, then we are on a delightful ride.

Through my experiences over the years, it has become exceedingly apparent that finding like-minded peers is integral in maintaining a productive work-life balance. My time here at the University has been well spent in identifying, knowing and nurturing a few of such acquaintances with whom I would be delighted to maintain a sustained interaction going forward in life. It has been a pleasure knowing Dr. Paroma Chakravarty, Ramola Sane, Khushboo Kothari, Dr. Jing Wang and Dr. Bakul Bhatnagar. A special thanks to Paroma for providing me with invaluable guidance throughout the duration of my Ph.D.

I will conclude by thanking everyone in Pharmaceutics and the College of Pharmacy for creating a congenial work environment. I have enjoyed a frank and friendly relationship with all the faculty members, in particular, Prof. Bill Elmquist, Prof. Cheryl Zimmerman, Prof. Ron Siegel and Prof. Esam El-Fakahany, in addition to my doctoral committee members. Finally, I cannot thank enough Candice McDermott and Erica Stapic, who contributed in countless ways to ensure the smooth running of my doctoral career by taking care of all the administrative issues.

Abstract

Pharmaceutical development and manufacturing of solid dosage forms is witnessing a seismic shift in the recent years. In contrast to the earlier days when drug development was empirical, now there is a significant emphasis on a more scientific and structured development process, primarily driven by the Quality-by-Design (QbD) initiatives of US Food and Drug Administration (US-FDA). Central to such an approach is the enhanced understanding of solid materials using the concept of Materials Science Tetrahedron (MST) that probes the interplay between four elements, *viz.,* the structure, properties, processing, and performance of materials. In this thesis work, we have investigated the relationships between the structure and those properties of pharmaceutical solids that influence their processing behavior. In all cases, we have used material-sparing approaches to facilitate property assessment using very small sample size of materials, which is a pre-requisite in the early stages of drug development when the availability of materials, drugs in particular, is limited. The influence of solid structure, either at the molecular or bulk powder levels, on crystal plasticity and powder compaction, powder flow, and solid-state amorphization during milling, has been investigated in this study. Through such a systematic evaluation, we have captured the involvement of structure-property correlations within a wide spectrum of relevant processing behaviors of pharmaceutical solids. Such a holistic analysis will be beneficial for addressing both regulatory and scientific issues in drug development.

Table of Contents

List of Tables

Chapter 2.

Chapter 3.

Chapter 5.

Chapter 6.

Chapter 7.

Chapter 8.

List of Figures

Chapter 1.

Chapter 2.

Chapter 3.

Chapter 5.

Chapter 7.

Chapter 1.

Structure-property relationships of solids in pharmaceutical processing: Introduction

1.1 Introduction

The state of formulation development and manufacturing of solid dosage forms is witnessing a strategic shift in the recent years. There is a conscious effort to transform the traditional, mostly empirical pharmaceutical development to a more scientific and structured process. Some of the goals of such an effort include streamlined and more efficient development steps, minimized risk of batch failure during scale-up, and ensured quality built into a drug product at every stage of its manufacture rather than depending on quality determination at the end point. Such a reformed attitude in drug processing has, in part, been driven by the Quality-by-Design (QbD) initiatives of US Food and Drug Administration (US-FDA).[1, 2] These efforts are timely and necessitated, especially as the drug pipeline is drying up in the recent years, resulting in fewer successful newer drug molecule launches, and causing an ever increasing dependence to re-process existing molecules into innovative formulations.

Such an approach to drug development involves several key steps, starting with a judicious solid form selection[3-5] with the goal to overcome specific deficiencies in a drug, such as poor solubility,[6] poor physical-chemical stability,[7] or poor mechanical properties.[8] Once a solid form has been selected, the particulate properties of the drug substance may be modified through steps, such as milling to reduce size,[9, 10] and crystallization to modify morphology.[11] Finally, the drug is formulated with additional inert additives and processed through blending, granulation, and powder compaction, to manufacture drug products. At each step, it is essential to correlate the structure and properties of the solid materials with their processing performance. This falls within the

scope of an emerging field of research, Pharmaceutical Materials Science.[12] The ultimate goal of such research is to replace product development, enabled through a trial and error approach, with that by proper design.

The overall objective of this thesis research work is to correlate the structure of molecular organic solids, either in the pure forms or as bulk composites, with the properties relevant to their pharmaceutical processing behaviors. Specifically, the focus of this work is on the following aspects of structure-property correlations of solids:

(a) Relationship between the crystal structure and single crystal mechanical properties, with subsequent impact on bulk powder compaction

(b) Relationship of the surface structure of cohesive powders with their flow properties

(c) Relationships between the structure of crystals and various aspects of amorphous stability with solid-state amorphization of crystals by milling

Through this work, we have captured the involvement of structure-property correlations within a wide spectrum of relevant processing behaviors of pharmaceutical solids. Such a holistic analysis will be beneficial for addressing both regulatory and scientific issues in drug development.

1.2 Small molecular organic solids

A significant proportion of pharmaceutical solids, both biologically active drugs and inert additives, are small molecular organic materials with molar weights below 1000 g/mol. Molecular organic solids can either be crystalline or amorphous, which have distinct structures, leading to very different physical-chemical[13, 14] and mechanical properties.[15] Both crystalline and amorphous solids have important applications in drug development. Crystalline solids are characterized by the presence of three-dimensional long range molecular order or periodicity.[16] Traditionally, crystalline solids have been extensively used as drugs due to the advantages in their superior thermodynamic stability, normally better chemical stability, and chemical purity.[16] Crystalline solid forms of a drug can either be single component (e.g., polymorphs),[3, 5, 17-19] or multi component systems (e.g., solvates,[20] hydrates,[21] salts and cocrystals[22]).

An amorphous solid has higher free energy compared to its crystalline counterparts.[13, 14, 23] Contrary to crystals, amorphous lacks the three-dimensional long range molecular order, even though, long range order in single dimensions within amorphous glass is possible.[24] The elevated free energy makes the amorphous phase very promising for improving the apparent solubility and enhancing the dissolution kinetics of poorly soluble drug molecules,[25-28] which constitute a large fraction of newer drugs due to the greater emphasis on biological target-specific lipophilic drug molecules in the recent years.[29, 30] Additionally, the random molecular packing in amorphous solids is sometimes also advantageous for improving the chemical stability of molecules,[31] when reactive

functional moieties are proximally packed in the crystalline state lowering the chemical stability of crystals.[32, 33]

Given the diversity of solid forms of individual drugs, the selection of an optimum solid form for drug product development can be daunting, especially if an empirical approach is adopted. On the other hand, it is more efficient if the selection is based on well characterized structure-property relationships. A substantial amount of work has already been done to correlate the structure of materials with their physical properties, such as solubility and stability, both thermodynamic and chemical.[16] Factors like the strength of lattice packing interactions, enthalpy of fusion, among others, have shown promising correlations with the solubility of crystals.[34] As for physical stability, the location of a solid form in the free energy landscape of a material seems to be the major determinant. For instance, the physical stability of different polymorphs of a drug has been correlated with their free energy.[17] Chemical stability is correlated with the packing arrangement of reactive functional moieties in a solid.[35]

Such instructive observations support the notion that the material structure directly influences its properties. However, the relationships between the structure of pharmaceutical solids and properties relevant to their processing, such as the mechanical properties, are still not clearly understood. Our current work is aimed at addressing this specific knowledge deficit in the current state of pharmaceutical drug development for a wide range of relevant processes, such as powder compaction, powder flow, and solid-state crystal → glass transformations by milling.

1.3 Materials Science Tetrahedron

The concept of Materials Science Tetrahedron (MST) is well established in the field of materials science,[36] and routinely applied to metals and ceramics. According to MST, there is significant interplay between four elements of materials, *viz.,* the structure, properties, processing, and performance (Figure 1.1). The application of this concept to pharmaceutical materials, however, is relatively new. The key aspect of MST, relevant to this research work, is the structure-property relationship of materials. A clear understanding of this fundamental relationship allows us to adopt optimized processing steps to alter the material properties to address performance related problems in pharmaceutical manufacture.

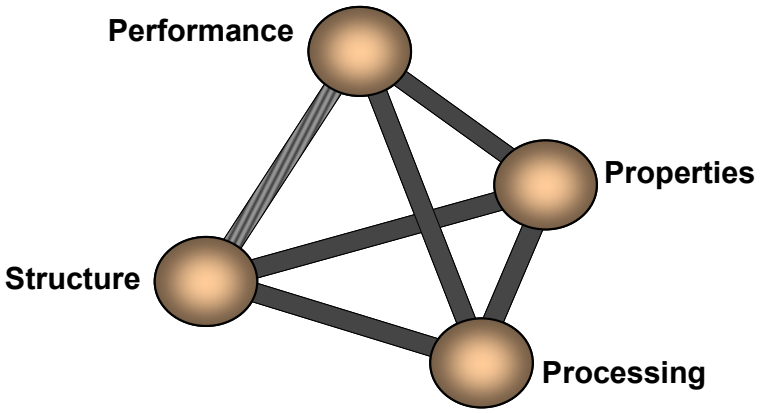

Figure 1.1. The interplay between structure, properties, processing and performance of materials forms the basis of Materials Science Tetrahedron (MST)

The structure-property correlation in the MST framework can be applied at different levels, starting from the molecular, to solid particles (crystalline or amorphous), granular and bulk powders. The various structures and properties of interest in pharmaceutical solid processing are described below:

Structure: Crystal structure and bonding strength, bonding patterns, amorphous structure (e.g., the surface versus bulk structure of glasses), surface structure of powders, granule structure, tablet structure (e.g., porosity), and chemical composition of molecules.

Properties from a processing viewpoint: Mechanical properties (elasticity, plasticity, fragmentation), particulate properties, surface properties, powder tabletability, powder flow and cohesion, and amorphization potential

Even though the terminology of MST is relatively new to pharmaceutical scientists, the application of this concept is not. For instance, a clear correlation was found between the chain length of a benzoic acid ester homologous series and the mechanical properties of corresponding powders in 1990s.[37, 38] Around a similar timeframe, investigators started to probe the relationship between the mechanical properties with other intrinsic properties of drugs, such as their cohesive energy density.[39-42] Additionally, correlations were observed between properties, such as the particle size and surface roughness,[43] moisture content,[44] and crystal brittleness,[45, 46] with compaction behavior of powders (a processing parameter). However, most of these earlier attempts have had limited industrial applicability in actual drug development. A primary reason for this was the requirement of a large amount of material to establish such correlations. In addition, often the experimental design for such structure-property correlation studies lacked practicality. For instance, the Hiestand indices, a common set of descriptors to describe powder compaction, required specialized equipment to prepare unique shaped donut tablets to assess mechanical properties.[46] In light of these drawbacks, the way forward

for pharmaceutical MST is to identify material-sparing approaches that can assess the structure-property correlations of pharmaceutical solids with very limited amount of sample and using relatively simple experimental design. The knowledge gained through such an assessment can be used to design novel functional materials with tailored properties and superior processing behavior.

1.4 Incorporating material-sparing approaches within MST framework

Earlier efforts of building MST correlations have often been limited by the elaborate sample size requirements. To make the MST application more appealing to drug development, the requirement of large sample size, or complex sample preparation steps must be eliminated. This is particularly true during the early formulation development stages of a new drug, when the average amount of available drug is often less than 5g. Therefore, formulations must be developed on a small scale under the constraint of small sample size, which will subsequently be tested for their robustness during scale-up when more material is available. The importance of developing the best possible small scale formulations cannot be over-emphasized, as any scale-up failure leads to financial losses for the industry, in addition to unmet deadlines both in terms of patient administration during clinical trials, or delays in filing for regulatory approval.

Therefore, suitable material characterization tools must be identified that can test and predict the large-scale processing performance of pharmaceutical solids, using very small sample size and preferentially in a non-destructive manner. Thus, the use of material-sparing characterization tools is at the heart of the effective implementation of the MST

principles in the pharmaceutical industry (Figure 1.2). Such tools are also necessary to address the high attrition rates of new pharmaceutical molecules. In this thesis work, several material-sparing tools have been utilized, tailored to test specific processing-related properties. For mechanical properties, we rely on nanoindentation for determining single crystal mechanical properties, and powder compaction simulation for bulk powder mechanical properties. Our goal is to correlate single crystal mechanics with bulk powder compaction performance, using less than ~2g of material in total. For characterizing powder flow, we utilize shear cell analysis, which is non-destructive to the sample, with typical sample weight requirement of less than ~300mg. For solid-state amorphization studies, we use a combination of calorimetry and diffractometry techniques as the material-sparing tools to predict amorphization potential of crystals. In this case, the sample requirement is less than ~50 mg. Therefore, all our studies have been consistent with the material-sparing approach that we think is critical in this age of drug development.

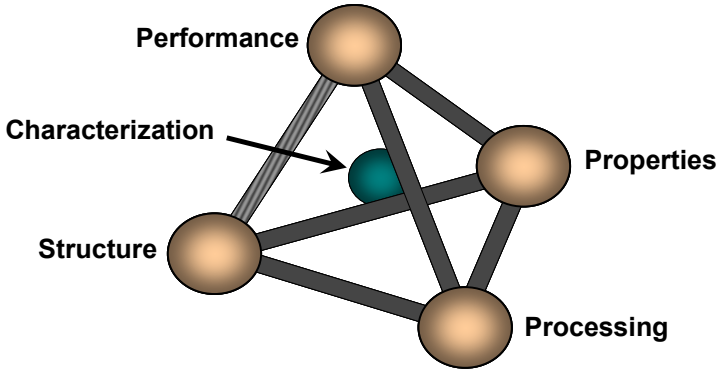

Figure 1.2. Role of material-sparing characterization tools within the Materials Science Tetrahedron framework.

1.5 Structure-property relationships

As mentioned earlier, in this work, we will evaluate the influence of structure-property relationships on three key processing behaviors of materials.

(a) Powder compaction

(b) Powder flow

(c) Mechanical amorphization of crystals during milling

All three factors are intricately involved in the development of solid dosage forms.

1.5.1. Relationship of structure, plasticity and compaction

Understanding the relationship between crystal packing and the mechanical properties of organic crystalline solids is a topic of considerable interest in the fields of solid–state chemistry and crystal engineering.[47-52] The net mechanical strength of tablets depends largely on the contact bonding area between particles that is created by powder compaction. During powder compaction, inter–particulate bonding area develops as a result of particle rearrangement and their mechanical deformations under stress.[53] However, compacts can retain full integrity only if an adequate amount of the inter–particulate bonding area, thus created, is preserved once the compaction pressure is withdrawn during the decompression cycle.

Powder compaction depends on the mechanical deformations of solids. Mechanical deformations have been extensively investigated for inorganic materials, such as metallic crystals and glasses.[54-56] However, such investigations on organic molecular materials are relatively few. The key deformation mechanisms include elastic, plastic, viscoelastic

deformation, and fragmentation. Most pharmaceutical solids are viscoelastic, with both elastic and plastic behaviors depending on the strain levels. The mechanical performance of their bulk powders are determined by the relative predominance of elastic and plastic deformation components.[54, 57] Elasticity of a material is its ability to undergo reversible deformation under an externally applied stress, such that once the external stress is removed, the particles undergo complete recovery and the deformation does not persist. Typically, elastic deformations take place in the regime of small displacements under low stresses. For perfect elastically deforming materials (e.g., rubber particles), the contact area between particles retained after stress removal during decompression is negligible, and these materials, therefore, cannot be made into intact tablets. For this reason, materials with high elasticity, e.g., acetaminophen,[58] have poor powder compaction properties. Strategies for addressing poor compaction properties of these elastic crystals include surface coating with a plastic material to intentionally reduce the elastic response of the resultant composite,[59] and modification of solid–state chemistry to confer adequate plasticity for bonding area retention.[50, 60]

The permanent plastic deformation is necessary for sufficient contact area retention during decompression phase of powder compaction. It is a prerequisite for forming intact tablets by powder compaction.[53] Using polymorphs, which are different crystalline phases of the same molecule, it has been shown that plasticity depends on crystal packing and higher plasticity generally leads to superior compaction properties.[47, 61, 62] Recognized mechanisms that promote crystal plasticity include slip of lattice planes,[63, 64] dislocation motion,[54, 65] lattice twinning,[54, 66] kinking[67] and perturbation of lattice

stability.[54] Of these mechanisms, the presence of slip planes and twinning are perhaps the leading contributors of crystal plasticity of organic materials.

In the slip mechanism, plasticity arises from the motion of dislocations (linear crystal defects) through preferential planes in crystals known as slip planes. The principal slip planes are crystallographic planes that have the weakest inter-planar interactions in a given crystal. They generally are associated with the highest molecular density and the largest separation between adjacent planes.[68] The presence of flat, un-corrugated slip planes in crystals has been used to successfully guide plasticity enhancement, which then results in better tabletability of materials. This has been illustrated with materials, such as sulfamerazine and acetaminophen, where the polymorphs with flat slip layers (polymorph I in case of sulfamerazine and polymorph II in case of acetaminophen) favor compaction.[12] In the twinning mechanism, successive slip planes are displaced about a mirror plane (the twin plane). This causes the lattice portions above and below the twin plane to be mirror images of each other.[69] Twinning has been shown to cause plasticity enhancement of organic materials, such as L-lysine monohydrochloride dihydrate.[69]

In addition to plasticity, fragmentation is another irreversible deformation mechanism, where the material structure fails under stress because of the inability to accommodate further strains. The particles formed as a result of brittle fragmentation can show two types of behaviors. The fragmented particles can either deform elastically or plastically under stress. Fragments undergoing plastic deformation will lead to improved powder compaction.

For viscoelastic materials, the mechanical properties that show promising correlations with bulk powder tabletability are crystal hardness and elastic modulus. Crystal hardness is a measure of plasticity, a lower value indicating higher plasticity. Elastic modulus is a measure of elastic deformation in materials, a lower modulus indicating higher elasticity and stronger bonding. Higher elasticity, tends to deteriorate tabletability and increase lamination tendency on decompression of tablets due to higher elastic recovery. The impact of material hardness on compaction can, however, be complicated.[70] At very high hardness, compaction properties are very poor due to very low plastic deformation in materials, leading to little generation of bonding area by compaction. Similarly, materials with very low hardness, also do not necessarily favor compaction, as the materials do not impart adequate strength to the tablet matrix. The best compaction profiles are observed in materials with intermediate hardness values (Figure 1.3).[70]

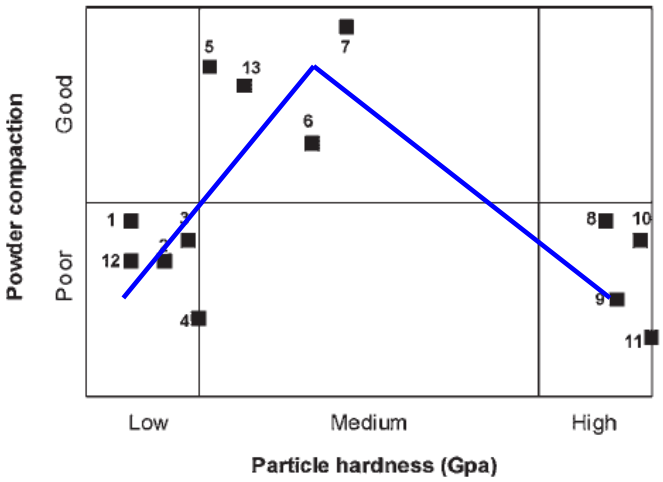

Figure 1.3. Correlating powder compaction behavior with particle hardness measured by Atomic Force Microscopy [70]

An example to illustrate the importance of flat slip layers to promote material plasticity, and hence powder tabletability, is that of acetaminophen. Polymorph I of this

molecule has corrugated crystal packing with poor powder compaction properties. When the same molecules are packed into flat layers in polymorph II, the compaction properties are significantly enhanced. This introduction of flat slip layers into a crystal can be achieved by forming different polymorph,[12] cocrystals[71] and salts.[72] Figure 1.4 compares the compaction properties of Form I acetaminophen with its ionized salt, acetaminophen hydrochloride monohydrate.[72] The ionized form, due to layered packing, shows significantly improved tabletability originating from better plasticity of this form.

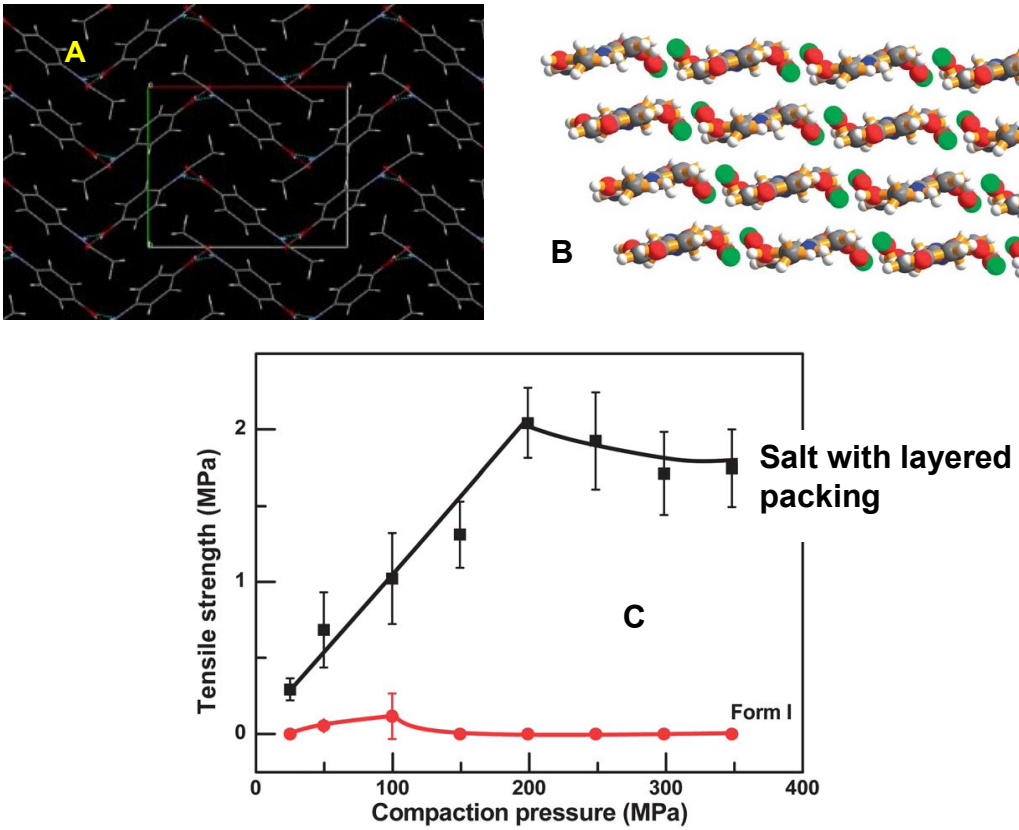

Figure 1.4. **(A)** Crystal packing in acetaminophen polymorph I is corrugated, herringbone; **(B)** Crystal packing in ionized salt of acetaminophen is flat layered; and **(C)** comparison of compaction properties of the two forms. The layered structure shows much better tabletability[72]

Figure 1.5 summarizes the three-level interaction between material structure, fundamental mechanical properties (hardness and modulus), and bulk powder compaction of materials. We have probed such correlations in Chapters 2 and 3 of this thesis.

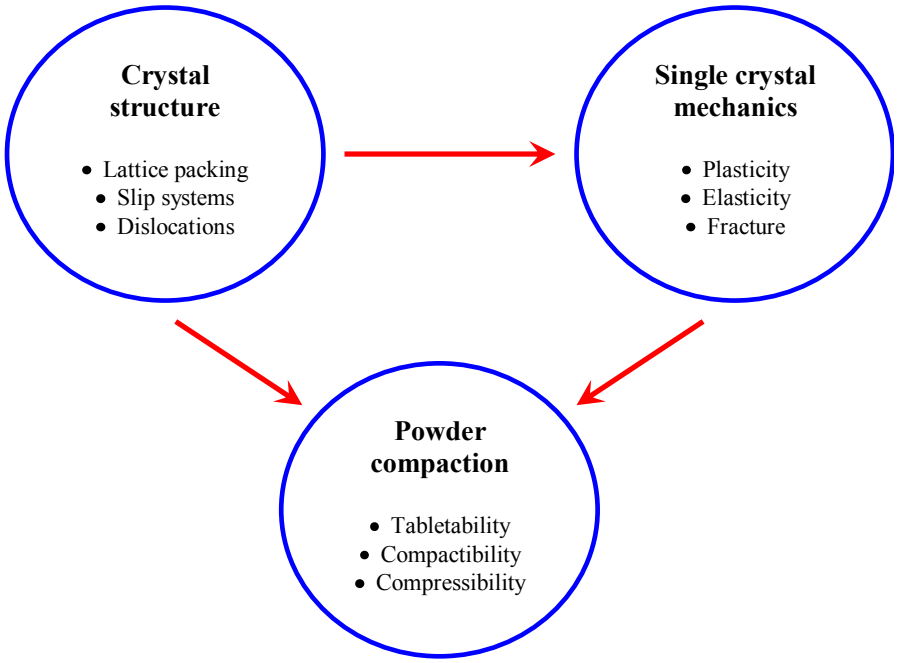

Figure 1.5. The three-levels of association between crystal structure, crystal mechanics, and powder compaction behavior. Three types of powder compaction plots, *viz.,* tabletability, compressibility, and compactibility, describe different aspects of powder compaction. Tabletability describes the dependence of tablet tensile strength (a property) on compaction pressure (a process parameter). Compressibility describes the dependence of tablet porosity (tablet structure) on compaction pressure (a process parameter). Compactibility describes the dependence of tensile strength (a tablet property) on porosity (tablet structure).

1.5.2 Role of surface structure in powder flow

The next aspect of processing, we are interested in, is powder flow. Powder flow impacts several pharmaceutical unit operations, such as powder compaction, capsule

filling, granulation, and blending. The physics of powder flow involves the interplay between two universal forces, inter-particle cohesion (which is mainly *van der* Waals bond) and gravitational force (Figure 1.6).[73-75] While gravity favors powder flow, cohesive force hinders flow by creating inter-particle attraction. As long as gravity can dominate over cohesion, powder flow is spontaneous and generally non-problematic. Gravity typically can dominate over cohesion till approximately a critical average particle size of ~30 μ. Powder flow becomes a major issue when cohesion starts dominating over gravity. For this reason, powders constituted of particles < 30 μm are very cohesive and generally problematic during processing. The main concerns with poor powder flow properties in pharmaceutical manufacturing include highly variable tablet weight, powder segregation, and problematic capsule filling.

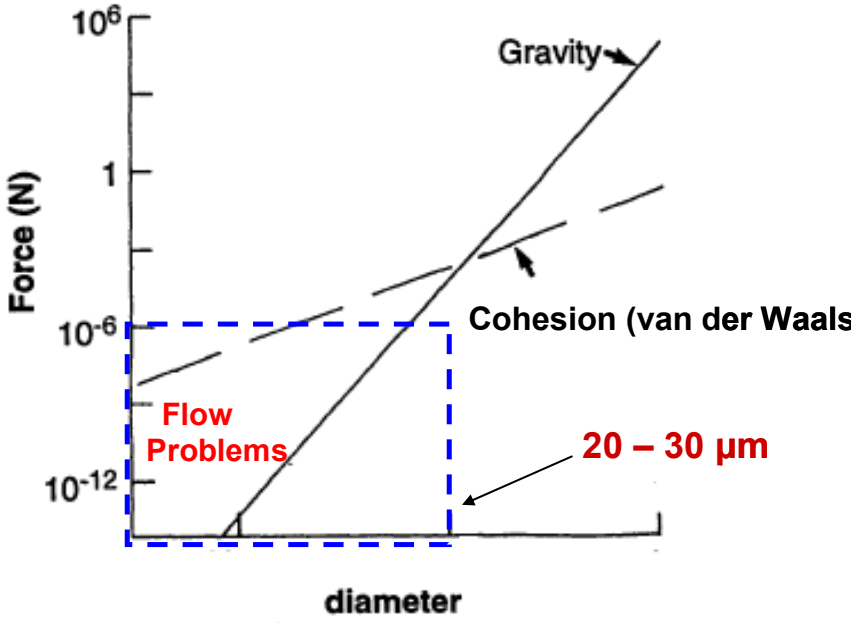

Figure 1.6. Relative predominance of gravity and cohesion at different particle size levels. The flow problem regime is indicated by dotted box. The graph is not to scale.

The conventional way to address the flow problem in the pharmaceutical industry is to granulate the powders to increase particle size. However, the size enlargement by granulation can often be extremely detrimental to the compaction properties of materials, as shown in Figure 1.7 for Avicel PH 101, a phenomenon known as over-granulation that is caused by a significant increase in median particle diameter.[76]

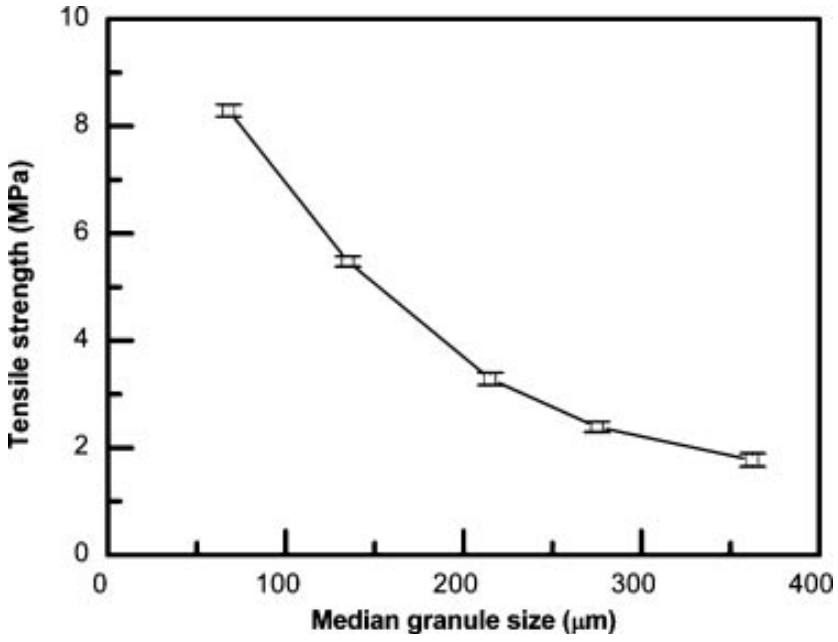

Figure 1.7. Negative impact of size enlargement through granulation on powder tabletability[76]

Several literature reports have instead suggested using an alternate route to enhance powder flow by surface modification of cohesive powders without increasing the particle size. This surface modification concept is based on manipulating the level of cohesive interactions, using an understanding of the structural factors affecting powder flow. According to Hamaker's theory,[77] the cohesive interaction (F) between adjacent particles

(*van der* Waals interactions), which will limit flow, is inversely proportional to the square of their distance of separation, as shown in equation 1.

$$F = \frac{- A D_1 D_2}{12 d^2 (D_1 + D_2)} \quad (1)$$

Where, A is Hamaker's constant, D_1 and D_2 are particle diameters, and d is the distance of separation between particle surfaces. If we assume that the two host particles have equal diameters, then the cohesion between adjacent host particles is given by the simplified equation 2.[74]

$$F = \frac{- A D}{24 d^2} \quad (2)$$

The inverse dependence of cohesion on interparticlulate separation distance suggests that, if this separation at the surface can be increased by some physical means, it is possible to reduce cohesion and improve powder flow. The involvement of surface structure in powder flow is implicated, for example, in the work of Yang et al,[78] who have shown that the flow properties of cornstarch can be improved significantly by coating with silica particles using mechanical coating processes such as magnetic-assisted impaction coating (MAIC) and hybridizer process.[79, 80] Similarly, by dry coating using a plasma downstream reactor, the flow of cohesive lactose particles (d ~ 30.9 μm) is increased by a factor of 3.1.[73] Likewise, the flow characteristics of cohesive lactose monohydrate powder are modified by intensive dry-coating with magnesium stearate and fumed silica through mechanofusion.[81, 82]

All these cases depend on increasing the inter-particle separation in equation 2 to overcome flow related problems. The coating particles act as spacers to increase inter-substrate separation, thereby reducing cohesion. These illustrate an application of the MST principles at the level of powder composite, distinct from the level of single crystals in the earlier discussion with powder compaction. We have probed such structure-property correlation, related to flow, in Chapter 3 of this thesis by exploring the utility of shearing stress to enhance the flow properties of a cohesive cellulose powder.

1.5.3 Solid-state amorphization of crystals

The final aspects of this thesis (Chapters 5-8) are related to another critical processing behavior of crystals, their propensity to undergo processing-induced phase amorphization during milling. Solid-state amorphization of crystals under mechanical stress is a transformation from a crystal directly into the higher energy amorphous form, when materials are subjected to operations such as milling.[83-86] Milling-induced amorphization has been extensively probed for non-pharmaceutical crystals, such as metal alloys, intermetallics, semi-conductors and minerals.[83] Amorphization in pharmaceutical organic crystals has also been observed in several materials, such as indomethacin,[87] griseofulvin,[85, 88, 89] trehalose,[90] and felodipine.[85] Any solid-state phase transformation in pharmaceutical materials during processing can have serious consequences on drug product performance, such as their physicochemical stability, solubility, dissolution kinetics, and product appearance,[21, 91] which are of concern both from product quality and regulatory viewpoint.[91, 92] Preserving the selected solid form of a material during various

stages of development and manufacture is critical for ensuring consistent product performance and quality.

The amorphous phase of a material can either be generated intentionally or unintentionally. Often, a drug may be intentionally formulated as amorphous due to its higher apparent solubility and faster dissolution kinetics compared to corresponding crystalline form, with the goal of improving the drug bioavailability[93, 94] However, since the higher solubility is a result of higher free energy of the amorphous solid,[95] stabilization strategies must be employed to minimize recrystallization of the amorphous phase with time, for instance by using crystallization inhibitors.[93] When amorphous generation is unintentional (e.g., under processing stress), then faster crystallization back to the stable form will be the preferred option before the subsequent processing step.

In this work, we have termed the ability of preparing an amorphous phase from a crystalline solid as the *amorphization potential* of the material. The true mechanism of milling-induced amorphization has been under speculation for a long time.[86, 96-98] Early literature suggested localized melt-quenching at the vicinity of the milling, due to temperature rise by impact stress, as a possible mechanism for amorphization during milling. However, this mechanism of localized melt-quenching was potentially invalidated by the observation of amorphization occurring even under cryogenic milling conditions ($T<<T_g$), where the localized temperature rise is minimum, and insufficient to melt the materials due to the liquid nitrogen environment. Additional results from milling experiments on α–lactose anhydrate were very insightful in abolishing the

localized melt-quenching hypothesis during milling.[99] By using ^{13}C-NMR, it was shown that pure α-anomeric form of lactose existed in the amorphous phase, when created by ball milling under a dry nitrogen environment However, glass generated by any route involving a liquid intermediate (such as, melt-quenching, lyophilization or spray drying) led to lactose mutarotation, and an equimolar amorphous mixture of α/β lactose was generated. This shows that milling-induced amorphization purely occurs in the solid-state that does not involve any liquid intermediate, and is a direct crystal to glass transformation.

While making form selection of a drug, a fundamental difficulty in the pharmaceutical industry has been the inability to predict *a priori* whether the drug would be a good candidate to develop the amorphous form, by performing a simple assessment of its material properties. Drugs displaying higher amorphization potential during early assessment might be superior candidates to develop amorphous drug products. On the contrary, these candidates will also likely create greater challenges if the crystalline form is selected for drug development, due to the propensity to undergo processing-induced solid-state amorphization during operations such as milling and powder compaction.[100-102]

In both scenarios, the question at hand is which crystalline materials will undergo easy conversion to the amorphous phase. Unlike some other processing properties that we already discussed here, e.g., powder compaction, there is dearth of experimental data on the relationship between the structure and the amorphization tendency for molecular

organic crystals. The involvement of crystal lattice structure in amorphization is indicated in mathematical theories on the physical mechanism of solid-state amorphization, such as the violation of the stability criterion of crystal lattice due to anharmonicity of lattice vibrations under mechanical stress,[103, 104] and the progressive generation of crystal dislocations leading to the loss of crystalline order.[86, 102, 105] However, very few experimental studies have clearly established that the strength of crystal lattice of the starting material influences the amorphization potential. Crowley and Zografi[87] evaluated the amorphous generation on milling of three indomethacin polymorphs and solvates, and showed significant differences in amorphization of the various phases. But no correlation of amorphization with lattice strength of various crystalline forms was attempted in that study. Patterson et al[106] ball milled carbamazepine polymorphs (forms I and III) and found that form I is susceptible to solid-state transformations during milling, while form III is not. In polymorph I, molecules exist in planar arrangement through the formation of intermolecular hydrogen bonds with neighbors. However, in form III, both inter- and intra-molecular hydrogen bonds are formed and dimerization of molecules occurs. This qualitatively suggests that stronger lattice packing can lead to higher resistance to solid-state phase transformations.

In addition to crystal lattice strength, there is one additional aspect in solid-state amorphization, *i.e.,* the recrystallization tendency of the amorphous generated by milling. Recrystallization will limit the extent of amorphization under processing stress. The impact of amorphous stability, hence recrystallization, on solid-state amorphization has been indicated, for instance, by showing that glass transition temperature (T_g) can

influence amorphization,[107] especially in relation to the milling temperature.[100] For the same crystal, milling at temperatures above T_g reduces the amorphization potential, compared to when milled below T_g, perhaps due to different amorphous crystallization kinetics above and below T_g. However, as T_g does not necessarily correlate with the crystallization tendency of a material, it is hard to imagine that T_g will play a consistent role in amorphization when a large number of model compounds are studied. These theoretical and experimental studies indicate that solid-state amorphization of crystals, which involves a direct crystal to glass conversion,[108] is concurrently influenced by two sets of factors (Figure 1.8):

1) Conversion from crystal to amorphous (c→a phase transformation), and
2) Recrystallization from amorphous to crystal (a→c recrystallization)

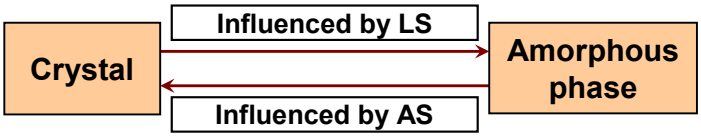

Figure 1.8. Schematic illustrating the concurrent effects of crystal lattice strength (*LS*) and amorphous stability (*AS*) on amorphous generation and elimination, respectively

While c→a conversion is expected to depend on crystal structure and crystal lattice strength, the a→c conversion depends on recrystallization kinetics and amorphous stability of the materials. Therefore, to properly characterize milling-induced amorphization, it is necessary to study both factors, which is the focus of chapters 5 and 6 in this thesis. In this work, we will systematically investigate the involvement of both

crystal structure and amorphous stability of materials in an attempt to better understand the structure-property relationships for solid-state amorphization of crystals.

1.6 Crystal and particle engineering

The application of MST principles should not end simply at the stage of understanding the relationships between structure and properties of materials. The next step is to use such knowledge to design and innovate functional materials, with tailored properties, by modifying the material structure, once the correlation between structure and property is clearly established.[109] There are broadly two approaches to do this, depending on the level at which MST principles are being applied. If we are interested in pure solid form, for instance, a crystalline form, then rational modification of crystal packing, either by preserving the chemical composition (*e.g.*, polymorphs) or through introduction of additional components in the lattice (*e.g.*, salts, cocrystals, solvates and hydrates) is a well tested method to alter material properties. These approaches fall within the scope of crystal engineering. However, when the MST principles are being applied at the bulk powder level, then particulate properties, *e.g.* morphology, size or surface structure, can be manipulated to alter manufacturing performance of materials. This latter approach is referred to as particle engineering. We have already provided an example of particle engineering in this discussion, where powder flow is shown to improve by coating particle surfaces with dry silica nanoparticles.

Crystal engineering approaches to modify processing behavior of solids is now receiving much attention. The effects of different crystalline solid forms of a material,

such as, polymorphs, solvates, salts and cocrystals, on their processing behavior are of practical interest both from the development and regulatory viewpoint. The effect of cocrystallization, for instance, on crystal mechanical properties has been studied by multiple research groups.[71, 110] In one of the earlier studies on this topic, the mechanical properties of caffeine, a drug with poor compaction properties, were significantly enhanced by cocrystallization with coformer methyl gallate.[110] This cocrystallization step introduced flat slip planes in the crystal lattice that promoted the plasticity of the material. Similarly, other solid forms of materials, such as salts, can also lead to improved processing of pharmaceutical powders.[72]

Engineering new solid structures to modify their processing performance is an attractive option because it allows drug manufacturers an opportunity to tackle the issue of patent expiry of blockbuster drug molecules. A different solid form of the same drug, which shows acceptable efficacy and toxicological profiles, can be patented and new drug formulations prepared. With this consideration, in this thesis work, wherever appropriate, we have designed new crystal forms of materials to address a processing-related issue (Chapters 2, 3 and 7). These attempts also serve to test the structure-property relationships for various processing behaviors of pharmaceutical solids.

1.7 Thesis organization and hypotheses

Chapter 2

The objective of the study in chapter 2 is to provide a mechanistic understanding of the relationship between the crystal packing, crystal plasticity, and bulk powder compaction

of theophylline, methyl gallate, and their 1:1 cocrystal. This is the first instance where we demonstrated that cocrystallization can, in fact, deteriorate the compaction properties of a drug. We have shown that theophylline anhydrate displays exceptional tabletability that is compromised on cocrystal formation due to reduced plasticity corresponding to changes in crystal packing.

Hypothesis 1: Bulk powder tabletability is directly proportional to the plasticity of corresponding single crystals

Hypothesis 2: Cocrystallization either improves or deteriorates the compaction properties of materials, depending on the extent of plastic deformation afforded by the crystal packing.

Chapter 3

In chapter 3, the molecular origin of deteriorated plasticity on cocrystallization of molecular organic materials is investigated using nanoindentation. Using this technique, a thorough analysis of the mechanical property landscape of the model system of β-piroxicam, methyl gallate, and their 1:1 cocrystal has been performed. Nanoindentation is an ideally suited material-sparing tool for probing the correlations between crystal mechanical properties with bulk powder performance. The hypotheses of this chapter are the same as in chapter 2.

Chapter 4

In chapter 4, we apply the structure-property relationships at the level of bulk powder composites to improve the flow properties of poorly flowing, cohesive solids. By using a comilling technique of dry surface nanocoating with silica particles (loading <1.0 wt%), we are able to reduce the cohesion of cohesive substrate particles and improve the flow factor by almost 5 fold. Such an approach is attractive because it holds the potential to transform poorly flowing materials into direct compression enabled formulations, thereby reducing the operating steps and minimizing the number of additional excipients in a formulation.

Hypothesis: Flow properties of cohesive fine particle solids are enhanced when their surfaces are dry coated with nanoparticles, which allow increased physical separation among adjacent substrates reducing the inter-particulate cohesion.

Chapter 5

From chapter 5 onwards, the thesis focuses on solid-state amorphization of crystals under milling-induced stresses. The extent of solid-state amorphization of crystals, contrary to other amorphization routes involving fluid intermediates, is dependent on both the lattice strength of the starting crystal and the stability of the generated amorphous phase. In chapter 5, we have investigated the concurrent influence of crystal lattice strength and amorphous stability on the rate and extent of amorphization of crystals using a large number of model compounds. Based on such information, an amorphization classification map has been developed with drugs categorized into four

classes. Class I materials, with the strongest crystal lattice and very unstable amorphous phase, are the best suited for developing the crystalline solid form. Class IV crystals, with the ability to easily convert into kinetically stable amorphous phase within timescales of pharmaceutical interest, will be the best suited to develop amorphous drug products.

Hypothesis: The ability of a crystal to amorphize under mechanical stress is inversely proportional to its crystal lattice strength, and directly proportional to the stability of the corresponding amorphous glass

Chapter 6

In chapter 6, we have probed the influence of molecular weight of materials on their amorphization potential, where low molecular weight materials have lower amorphization tendency. Using calorimetry-based thermodynamic calculations on molecular configurations and mobility, we have further correlated the molecular weight of compounds with their configurational entropy (*i.e.,* flexibility in the disordered phase), which is then correlated to molecular mobility and recrystallization tendency. Further, by fixing the molecular weight using polymorphs of same molecules, we have shown that for the same molecular weight, crystal packing difference leads to different amorphization propensity, especially when molecular weight is in the intermediate range.

Hypothesis 1: Higher molecular weight materials are easier to amorphize due to slower recrystallization, attributed to a larger number of molecular configurations in the disordered phase that kinetically slow down the crystallization process

Hypothesis 2: For the same molecule, different crystal packing of polymorphs leads to different amorphization potential.

Chapter 7

In chapter 7, based on the structure-amorphization correlations established in chapters 5 and 6, we have employed crystal engineering via cocrystallization to modify the amorphization potential of a model drug, sulfamethazine. Here, we observe that both crystal lattice strength as well as the amorphous stability of the cocrystals must be considered while attempting to interpret the influence of changing crystal packing on the amorphization tendency of a crystal.

Hypothesis: Forming cocrystals of drugs can either improve or deteriorate the amorphization potential of crystals, depending on the relative contributions of crystal lattice strength and amorphous stability in the cocrystals

Chapter 8.

In chapter 8, we focus on how the surface structure of the amorphous glass can influence its crystallization behaviors under non-isothermal conditions. Amorphous glass generated by milling can show two modes of crystallization: unimodal and bimodal. In

this work, we probe the factors, such as faster surface mobility and the presence of seed nuclei on the manifestation of different modes of non-isothermal crystallization.

Hypothesis 1: Faster surface crystallization of glass below T_g leads to the appearance of bimodal crystallization events under non-isothermal conditions.

Hypothesis 2: It is possible to flip the crystallization modes of glasses by altering crystallization kinetic factors, such as heating rate, surface area, and seed concentration.

1.8 Conclusions

With the advent of more stringent guidelines governing pharmaceutical drug development and manufacture, the principles of Materials Science Tetrahedron are invaluable to pharmaceutical development scientists. Our focus is primarily on the structure-property relationships of pharmaceutical materials, both crystalline and amorphous solids, to modulate their processing behaviors. Such an understanding is the stepping stone towards designing functional materials with tailored processing behaviors. We have focused in this dissertation on three aspects of processing of crystals, *viz.,* powder compaction, powder flow, and amorphization during milling. For each of these key parameters, we have probed the relationships between material structure and properties, such as, plasticity, elasticity, flow, lattice strength, and amorphous stability. A holistic and systematic study of these parameters is expected to benefit the drug development process well into the future.

Chapter 2.

Cocrystallization-induced decline in plasticity and powder compaction: Part 1. Crystal structure contributions

This chapter is based on the following published research article: Chattoraj *et al.*, *Crystal Engineering Communications*, 12, 2466–2472, 2010.

The purpose of this study was to probe the effect of changing crystal structure of drugs by co-crystallization, on their plasticity and powder compaction. For the model system of 1:1 cocrystal formed between theophylline and methyl gallate, significant deterioration in powder compaction is observed relative to the parent drug, theophylline, even though compaction is improved compared to the other co-former, methyl gallate. We demonstrate that these differences in the bulk powder compaction originate from different crystal plasticity of the materials, probed with single crystal nanoindentation. The rank orders of bulk powder compaction and single crystal plasticity are identical in this case: theophylline > cocrystal >> methyl gallate. Unique molecular packing features in the respective crystal lattices drive the plasticity differences. The presence of an extremely dense three-dimensional hydrogen bonded network structure lowers the plastic deformation in methyl gallate crystal, leading to its poor compaction. In contrast, the cocrystal exhibits a two-dimensional hydrogen bonded layered structure, which improves its plasticity and compaction properties relative to methyl gallate by facilitating slip. Theophylline undergoes the highest plastic deformation (indicated by the lowest crystal hardness), due to multiple slip layers conferred by hydrogen bonded columns. The extremely high plasticity of theophylline is essentially insensitive to significant alteration in particle morphology or size distribution. This work clearly demonstrates the relationship between structure, plasticity and powder compaction for organic molecular solids, consistent with the principles of Materials Science Tetrahedron.

2.1 INTRODUCTION

Organic crystals can be readily modified through crystal engineering to address key challenges in the formulation and manufacture of drugs, such as low solubility and dissolution rate,[1, 2] physicochemical instability,[3] and poor tablet compaction.[4, 5] In addition to the more traditional crystal engineering approaches, such as salts, polymorphs and solvates,[6] cocrystallization has shown considerable promise in overcoming many processing deficiencies in drug molecules.[3, 4, 7-9] Cocrystals are solid phases where two or more non-volatile components crystallize in stoichiometric ratios within the same crystal lattice, and may be distinguished from salts in having at least one of the components neutral, irrespective of the temperature. Using a wide range of structurally diverse co-former molecules, cocrystallization can significantly improve the probability of successful solid form selection of drugs with desired solid-state properties.[3, 10, 11]

Understanding the relationship between crystal structure and material properties is important for the effective application of crystal engineering to attain the desired product performance.[3, 8] In this work, we have examined the relationship between crystal structure, crystal plasticity, and powder compaction behavior. Plasticity is the ability of a material to undergo permanent, irreversible deformation upon the application of stress, and is one of the most critical material properties that directly influences powder tabletability.[12, 13] Plasticity is affected by several features of crystal packing, such as slip,[4, 14] dislocation motion,[15, 16] twinning,[16, 17] kinking,[18] and perturbation of lattice stability.[16] Motion of dislocations along specific slip planes leads to crystal plasticity. Slip planes are crystallographic planes that have the weakest inter-planar interactions in a

given crystal, and are associated with the highest molecular density and the largest separation between adjacent planes.[19] Thus, introducing more slip planes in a crystal is a valid strategy for plasticity enhancement, which facilitates the compaction of powders with poor tabletability.[4, 5]

However, in the current work, we have found that forming cocrystals between theophylline anhydrate (Figure 2.1a) and methyl gallate (Figure 2.1b) can not only improve the plasticity and tabletability of methyl gallate, but also significantly compromise that of theophylline. To our knowledge, this is the first report where cocrystallization has resulted in deterioration of the tableting behavior of a material. Thus, this model system provides an opportunity to holistically examine the effects of cocrystallization on crystal mechanical properties. Further, using this system, we can get a more clear insight into how a crystal's mechanical properties such as plasticity and tabletability get influenced by changes in crystal packing features.

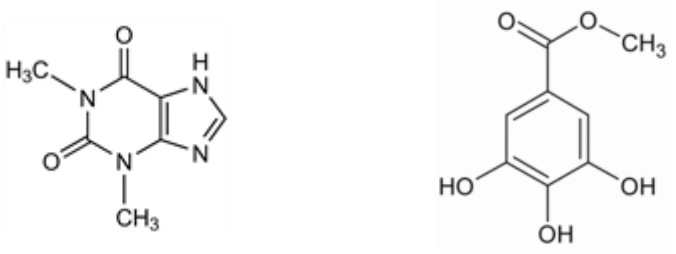

(a) **(b)**

Figure 2.1. Molecular structures of (a) theophylline anhydrate and (b) methyl gallate

2.2 MATERIALS AND METHODS

2.2.1 Preparation of bulk cocrystal powder

Bulk powder of the 1:1 cocrystal between theophylline (purity > 99%, Acros Organics, NJ) and methyl gallate (purity > 98%, Fluka Chemicals Corp., Milwaukee, WI) was prepared by solvent mediated transformation in ethanol, using controlled slurry agitation. Theophylline (5.04 g) and methyl gallate (5.16 g), 0.028 moles each, were suspended in 500 ml of ethanol in a conical flask. The slurry was continuously stirred magnetically to maintain a stable vortex. The conversion to the cocrystal was verified by powder X-ray diffractometry (PXRD, Bruker AXS D5005, Madison, WI). The suspension was subsequently filtered and vacuum dried. For powder XRD studies, a Cu X-ray source (45 kV, 40 mA) providing $CuK\alpha_1$ emission of 1.5414 Å was used. Data were collected at 5 - 40^o 2θ at a step size of 0.01^o with a dwell time of 1s at each step.

2.2.2 Physical characterization of powders

Melting points of bulk cocrystal and starting materials were measured using differential scanning calorimetry (model 2920, TA Instruments, New Castle, DE) operated in standard mode. Samples were placed in hermetically sealed aluminum pans having pinholes, and heated at 10 ^{o}C/min to 20 ^{o}C beyond the melting point, under a nitrogen purge of 50 ml/min. Temperature and cell constant were calibrated using indium standard after performing baseline calibration. The room temperature true densities of the powders were measured using a helium pycnometer (Ultrapycnometer 1000e, Version 4.00, Quantachrome, Boynton Beach, FL). The true density can also be calculated from the crystal structure. However the crystal structure solutions at room temperature are not

available for methyl gallate and the cocrystal, necessitating the true density measurements. Particle size distributions were obtained using a light scattering particle size analyzer (Helos H1588, Sympatec, Germany, dry powder dispersion, 2.0 bar dispersion air pressure).

2.2.3 Compaction behavior of powders

The tabletability of the bulk powders (theophylline, methyl gallate, and cocrystal) was determined using Zwick Materials Testing Instrument (Zwick-Roell MaterialPrufung 1485, Germany) over a compaction pressure range of 50 to 400 MPa at increments of 50 MPa using 8 mm round, flat-faced punches. The in-die elastic recovery of the compacts was calculated using the tablet thickness values at peak compaction pressure, and at the end of the decompression cycle, as previously described.[4] Tablets were stored for 48 hours in an ambient atmosphere to allow for the relaxation of residual stress. Radial breaking strength of each tablet was obtained using a Texture Analyzer (TA-XT2i, Texture Technologies Corp., NY, 30 Kg load cell, test speed of 0.01 mm/s with a trigger force of 5 gm). The tablet tensile strength was calculated based on the tablet dimensions and the breaking force.[20]

2.2.4 Crystal growth and structure solution

The single crystals of theophylline, methyl gallate and their 1:1 cocrystal were prepared by slow evaporation of the respective ethanolic saturated solutions at room temperature. The crystal structures of methyl gallate and the cocrystal were solved using single crystal X-ray diffractometry (Siemens SMART platform CCD diffractometer, NY)

at 173 K. The crystal structure of methyl gallate at 100 K has already been published,[21] and we report a new determination at 173K. The crystal structure of theophylline has been obtained from the literature through CCDC.[22]

2.2.5 Mechanical properties of single crystals

The elastic modulus and indentation hardness values of the predominant faces of single crystals of theophylline, methyl gallate, and the cocrystal were obtained using nanoindentation (NanoXP, MTS-Nano Instruments, Oak Ridge, TN) with a Berkovich diamond tip.[23] During the indentation experiment, the indenter tip was pressed into the crystal surface at a constant rate of 5 nm/s. Once the maximum penetration depth of 1000 nm was reached, the indenter was held for 10s before being withdrawn to allow time for stress relaxation of plastic materials. For all of the three crystals, the Poisson ratios were assigned a value of 0.3.[24] Indentation data between the penetration depth of 600 and 900 nm were analyzed to derive the indentation hardness and elastic modulus values.[23]

2.2.6 Crystal slip planes and Burgers vector

The principal slip plane in each crystal was identified both by direct visualization of the crystal packing and attachment energy calculations, as described previously (Materials Studio, v5.0, Accelrys, San Diego, CA).[19] A Dreiding 2.21 force field was employed in the attachment energy calculations because it has been frequently applied to small organic molecules.[19] The direction of slip were computed from the Miller indices (h k l) of the identified slip plane.[16] Slip system is composed of slip plane (h k l) and slip

vector <u v w>, which is any vector parallel to the slip direction. The magnitude of the Burgers vector, *b*, was determined for each crystal based on the identified slip system and lattice spacing in slip direction.

2.3 RESULTS AND DISCUSSION

2.3.1 Characterization of powders

The PXRD profile of the bulk cocrystal powder was distinct from either that of theophylline or methyl gallate (Figure 2.2). Also, both the melting point and true density of the cocrystal were different from those of the starting materials (Table 2.1). These data confirmed that the cocrystal was structurally singular from the starting materials.

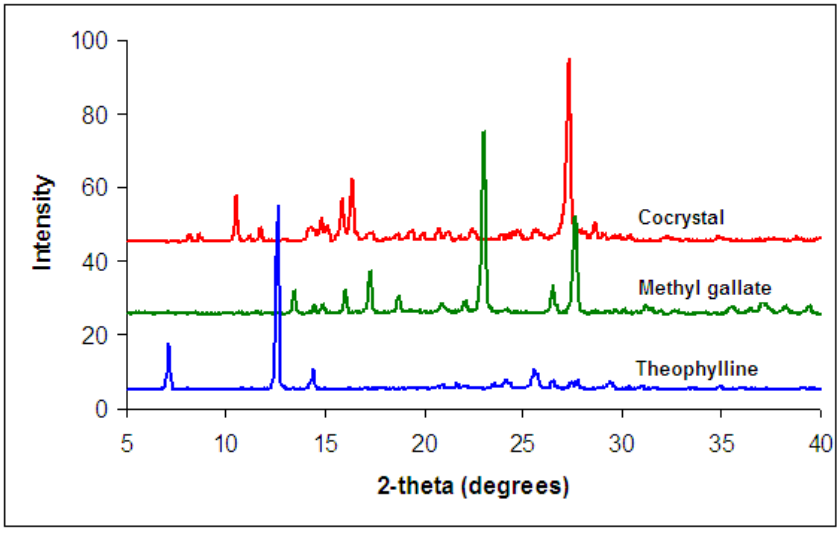

Figure 2.2. Powder X-ray diffraction profiles of theophylline, methyl gallate, and cocrystal

2.3.2 Compaction behavior of powders

On evaluating the powder compaction properties of different materials, theophylline was found to demonstrate the highest tabletability, while methyl gallate's

tabletability was extremely poor. Tabletability plots show the dependence of tablet tensile strength on the compaction pressure used to prepare the tablets. The bulk powder tabletability decreased in the order of theophylline > cocrystal >> methyl gallate (Figure 2.3).

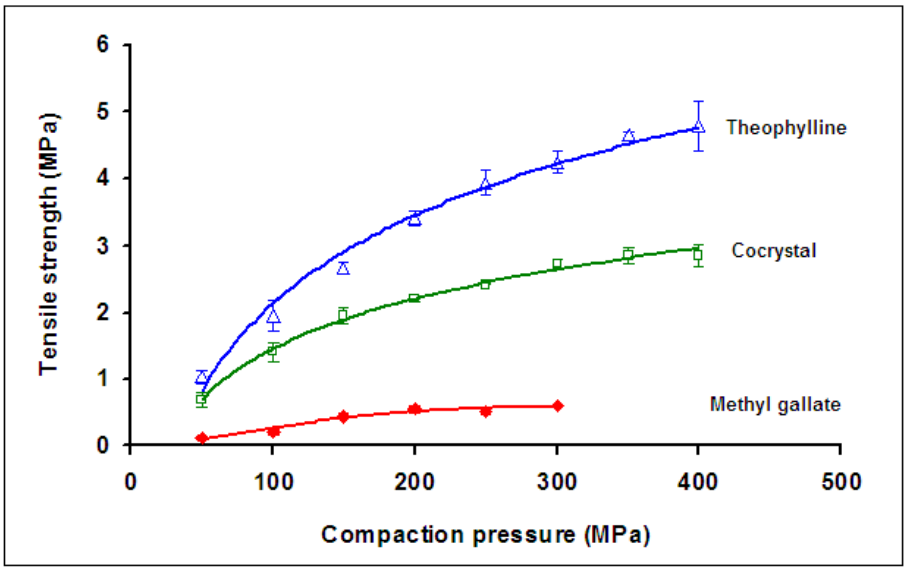

Figure 2.3. Bulk powder tabletability of theophylline, cocrystal, and methyl gallate over compaction pressure range of 50-400 MPa. No intact tablets could be formed for methyl gallate at pressures exceeding 300 MPa. Error bars represent one standard deviation of measurements (n = 3).

Because of the poor tabletability, methyl gallate did not form intact tablets easily and many tablets laminated after ejection from die. Those tablets were discarded because they could not be used for testing tablet tensile strength. In contrast, the cocrystal powder formed intact tablets over the entire range of compaction pressures, indicating significant improvement in the tabletability compared to that of methyl gallate. At any given compaction pressure, the tablet tensile strength of the cocrystal was always much higher than methyl gallate. This is similar to our earlier observations with the methyl

gallate-caffeine 1:1 cocrystal system.[4] However, the tabletability of theophylline was compromised on cocrystal formation.

Powder compaction can also be assessed using compactibility plots, which show the dependence of tablet tensile strength on tablet porosity (*i.e.,* the dependence on solid fraction). From the compactibility plots (Figure 2.4), the tablet tensile strength extrapolated to zero porosity (σ_0) was found to be the highest for theophylline (Table 2.1). σ_0 is routinely used to assess the powder compaction properties of materials, and is a property intrinsic to the material devoid of any contribution from porosity. The compactibility of theophylline is exceptionally high, because σ_0 values for most pharmaceutical powders generally range between 0.1-10 MPa.[26] Both tabletability and compactibility plots indicate that theophylline has exceptionally good powder compaction properties.

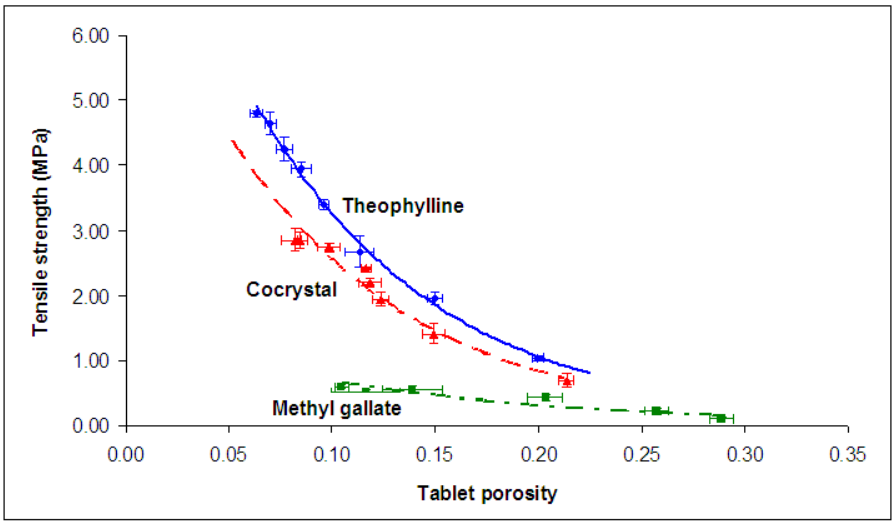

Figure 2.4. Compactibility (dependence of tablet tensile strength on compaction pressure) of theophylline, methyl gallate, and cocrystal. Error bars represent one standard deviation of measurements (n = 3).

Table 2.1. Properties of theophylline, methyl gallate, and cocrystal relevant for assessing plasticity and compaction. Data presented as mean ± one standard deviation of measurements (n = 3).

Materials	Bulk powder properties			Crystal properties			
	Melting point (^{o}C)	**True density (g/cc) [n=10]**	**D_{50} (µm)**	**Tensile strength at zero porosity (MPa)**	**Indentation Hardness (GPa) (n ≥ 10)**	**Elastic modulus (GPa) (n ≥ 10)**	**Dislocation density $\times 10^{16}$ (m^{-2})**
Theophylline	272.19	1.481 ± 0.0003	128.98	9.98 ± 0.36	0.28 ± 0.01	11.59 ± 0.27	27.3
Methyl gallate	194.48	1.481 ± 0.001	55.86	NA	0.78 ± 0.14	9.38 ± 0.67	3.5
Cocrystal	242.76	1.548 ± 0.0009	6.28	8.81 ± 0.24	0.48 ± 0.05	15.09 ± 0.92	4.0

2.3.3. Particle size and morphology effects on theophylline compactibility

For many plastic materials, smaller particles lead to higher compactibility due to the larger area available for bonding during compression.[27] However, it was found that in spite of having a much larger particle size compared to the other two materials (Table 2.1), theophylline displayed the best compaction behavior. To examine the effect of particle size and morphology on the compaction behavior of theophylline, we compared the compactibility of three batches of theophylline having very different particle size and morphology. Batch 1 was commercial theophylline anhydrate powder with prism-shaped crystals (Figure 2.5, Batch 1). Batch 2 was prepared from commercial theophylline by cryomilling the powder under liquid nitrogen at 77K (SPEX SamplePrep 6750 Freezer/Mill, Metuchen, NJ). We verified that the samples, immediately after cryomilling, did not show reduction in crystallinity, based on DSC and PXRD data. For Batch 2, the powdered material was not subjected to any further treatment, and the compactibility was measured directly. The prism-shaped crystals of commercial theophylline were converted to more iso-dimensional crystals in Batch 2. For Batch 3, after following a similar cryomilling protocol as in Batch 2, the sample was suspended in ethanol with continuous stirring, using magnetic stirrer in a sealed round bottom flask. This treatment produced crystals of prism morphology, similar to commercial theophylline, but with significantly reduced average particle size.

Even with such drastic changes in particle size or morphology, the compactibility of theophylline was not significantly altered (Figure 2.6). A 50-fold reduction in particle

size only slightly altered the compactibility of theophylline, as expected due to larger available bonding area for fine particles.

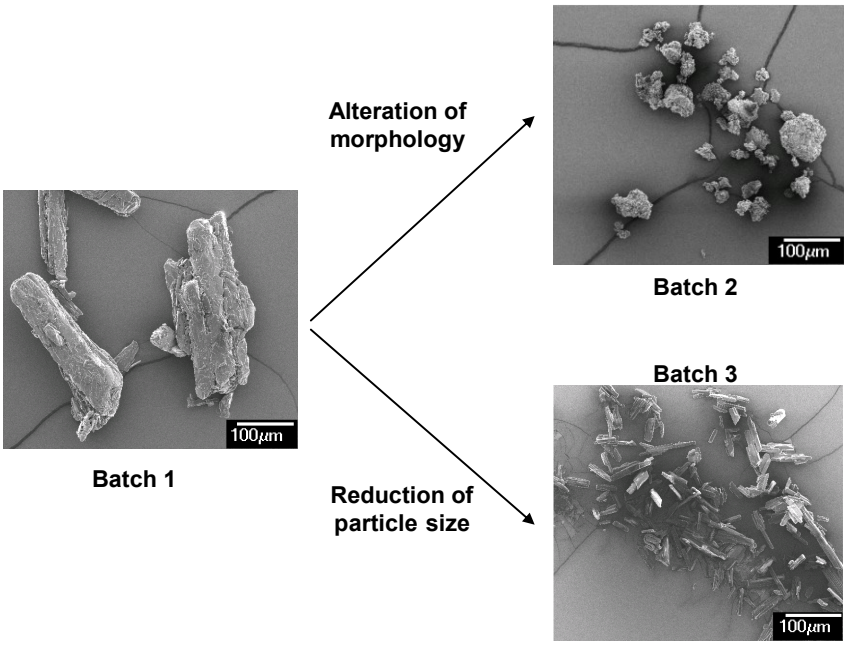

Figure 2.5. SEM images of the three batches of theophylline produced by particle engineering strategies, such as milling and recrystallization.

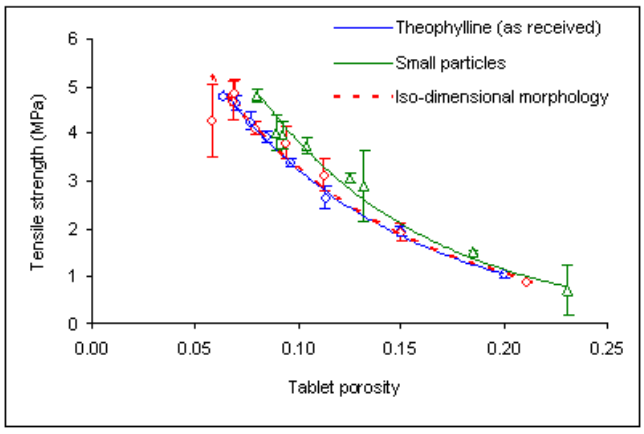

Figure 2.6. Compactibility of three batches of theophylline with engineered particle size and morphologies

The insensitivity of compaction to particle size/morphology can only occur if the intermolecular interaction strength at the bonding surface of a material is the same as that within the crystal. The fracture plane, then, can run through individual particles when a tablet breaks under an applied tensile stress.[21] Due to this factor, the tablet strength of theophylline is essentially unaffected by size and morphology of the initial theophylline particles. Thus, due to its higher plasticity, analogous to plastic metals, pressure-induced bonding between particles of theophylline can readily occur on application of stress. In addition, theophylline particles yield under stress during tablet breaking (tablet tensile strength determination), which further obscures the differences in pore distribution caused by different particle size and morphology. Due to the above reasons, the superior plasticity and hence, the tabletability of theophylline can be regarded as property intrinsic to this material, and not artifacts of extrinsic factors like particle shape and morphology.

2.3.4 Mechanical properties of crystals

The differences in tableting performance of the three materials can be interpreted based on the different mechanical properties of the corresponding crystals. During compaction, plastic materials can undergo permanent and irreversible deformation that is necessary to form inter-particulate bonding.[27] The indentation hardness is an indicator of material plasticity, a lower hardness corresponding to higher plasticity. Of the three crystals, the indentation hardness of theophylline was approximately half of that of the cocrystal and one third of methyl gallate (Table 2.1). The theophylline crystals are therefore the most plastic, while methyl gallate crystals are the least plastic. Overall, the rank orders of plasticity and powder tabletability are the same (theophylline > cocrystal >

methyl gallate), indicating a positive correlation between single crystal plasticity and powder tableting performance.

Crystal plasticity can also be qualitatively assessed from load-displacement curves during nanoindentation tests (Figure 2.7). For the same indenter that penetrates crystals to the same depth, a higher load corresponds to higher crystal hardness, and hence lower plasticity.[28]

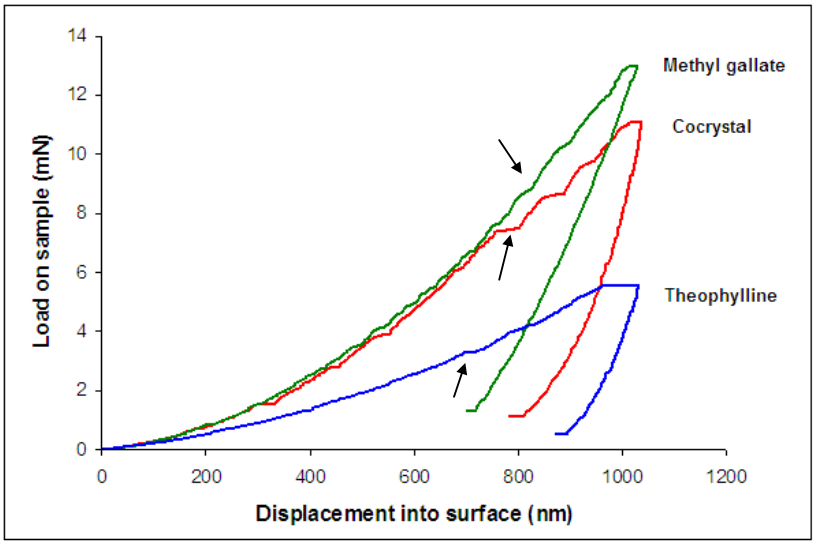

Figure 2.7. Load-displacement nanoindentation curves of theophylline, methyl gallate, and cocrystal. Arrows indicate some selected pop-in events.

From Figure 2.7, it can be observed that the maximum load follows the order of methyl gallate > cocrysal > theophylline, again confirming the lowest plasticity of methyl gallate. Moreover, breaks in the nanoindentation loading curves or "pop-in events" can be seen for both theophylline and cocrystal at low loads (Figure 2.7). These pop-in events are characteristic of slip between crystal slip planes under applied load.[29] Pop-in events

occurred at a lower frequency for theophylline than for the cocrystal. This observation is consistent with the presence of multiple slip mechanisms in theophylline crystal (discussed later), which facilitates easier stress dissipation in this lattice. The enhanced stress dissipation reduces the need of frequent "pop-in" events in theophylline, compared to the cocrystal, for which slip between flat layers is the only mode of plastic deformation. Methyl gallate also showed pop-in events. However, these events occurred at higher loads compared to the other two crystals, consistent with its lowest plasticity. Considering the rigid three-dimensional hydrogen bonded structure and lack of slip planes in methyl gallate crystal (discussed later), these events were probably caused by micro-cracking near the site of indentation.

Besides plasticity, important insights into tabletability may also be obtained from the crystal elasticity, which can be represented either as the elastic modulus of crystal or the elastic recovery of tablets during decompression.[30] The elastic modulus of crystals was found to decrease in the order of cocrystal > theophylline > methyl gallate (Table 2.1), a lower value of elastic modulus indicating higher elasticity. Based on this rank order, methyl gallate would exhibit the largest elastic strain under the same applied stress, and the highest elastic recovery after stress removal. This agrees well with the highest elastic recovery of methyl gallate tablets during decompression (Figure 2.8). A high elastic recovery during bulk powder compaction can break inter-particulate bonding sites and thus, leads to deterioration in the powder compaction properties. Thus, both low plasticity and high elasticity of methyl gallate contribute to its extremely poor tableting performance.

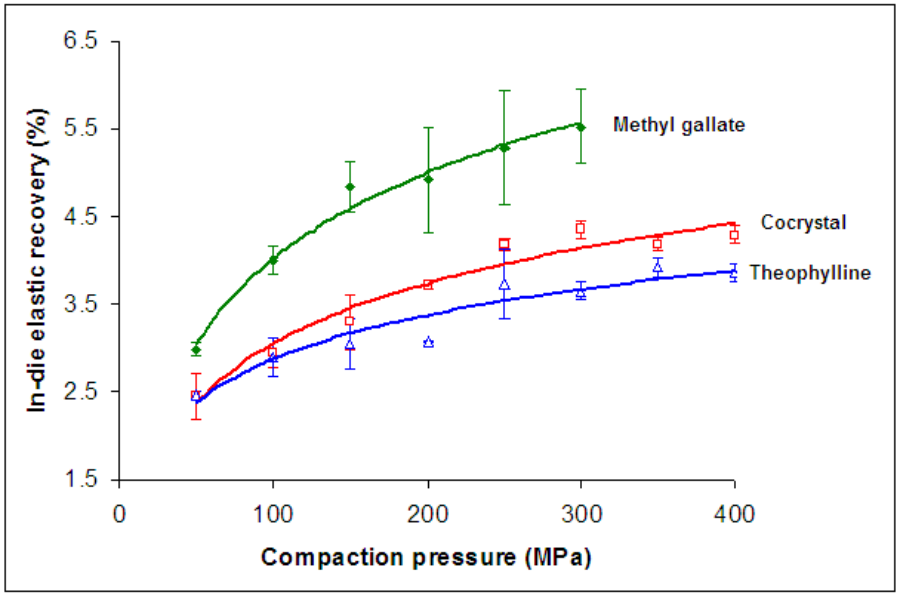

Figure 2.8. In-die elastic recovery during compaction of bulk powders of theophylline, cocrystal, and methyl gallate.

The in-die elastic recovery of theophylline bulk powder was lower than that of the cocrystal at moderate to high compaction pressures (Figure 2.8). This means that, despite the lower elastic modulus of theophylline crystal, the apparent elastic modulus of theophylline tablet is higher than that of the cocrystal, under the same compaction pressure. This may be explained by considering the difference in the crystal hardness of theophylline and cocrystal. Under the same applied pressure, the net area of a plane perpendicular to the loading axis during stress application is larger for softer theophylline. The larger area leads to a higher apparent modulus of theophylline tablet, even though the elastic modulus of the corresponding crystal is lower than that of the cocrystal. It is also possible that the rank order of elastic modulus measured on the predominant crystal face by nanoindentation may slightly differ from that of the bulk powder because of the anisotropy of mechanical properties of organic crystals.[16]

2.3.5 Identification of slip systems

To properly understand the plasticity differences, it is important to describe the slip systems and dislocations for each of the three crystals. Attachment energy (E_{att}) calculations have been extensively used in literature to assist the identification of slip planes.[19] Slip planes, among all planes in a crystal, possess the lowest absolute E_{att}, which is defined as the energy released on attaching a new layer (slice) of molecules to a growing crystal face.[19] The accuracy of E_{att} prediction is dependent on the choice of the force field. Although the Dreiding force field performs better than many other force fields for organic crystals, it does not always yield a correct prediction.[19, 31] In such cases, direct visualization of crystal packing using Materials Studio software results in a more accurate identification of predominant slip plane.

The predominant slip plane in the theophylline crystal was identified as (1 0 0) both by E_{att} calculations and direct visualization of crystal packing. The corresponding slip vector for theophylline was <0 1 0>. For the cocrystal, slip plane identified by E_{att} calculations was (1 0 0), while that by visualization was (3 0 -2). The (3 0 -2) plane was used as the slip plane, because slip along (1 0 0) required traversing hydrogen bonded layers of molecules, which is not energetically favorable.[22] It should be pointed out that in addition to the principal slip plane, potential secondary slip planes in a crystal may become activated under favorable external stress conditions.[16] However, the principal slip planes can be considered to be more influential to crystal plasticity.[16, 19] The slip plane in methyl gallate could not be easily identified by visualization of crystal packing due to the unique molecular arrangement in its lattice. E_{att} calculations identified (1 1 0) as the slip plane, with <0 0 1> as slip vector.

2.3.6 Qualitative assessment of crystal packing effects on mechanical properties

The differences in plasticity of the three crystals can be interpreted based on their different crystal structures. In the theophylline crystal, molecules form stacking layers (Figure 2.9a and b), within which, these molecules are arranged in hydrogen bonded V-shaped rigid columns (Figure 2.9c). These columns can undergo facile relative motion when stressed. In adjacent layers, these columns are oriented at obtuse angles of 111.61^{o}, each layer accommodating stress at a different orientation, increasing the resolved shear stress beyond the critical yield stress needed for plastic deformation. The columnar arrangement of theophylline molecules in the flat layers offers additional lattice flexibility over flat slip planes. Compared to the slipping of rigid sheets of molecules in the cocrystal (Figure 2.10), there is also a lower energy barrier for the columns to move with respect to each other when stressed. This results in easier dislocation motion in theophylline crystals, thereby enhancing its plasticity. In addition, these composite layers of columns can still slip relative to each other, similar to that between rigid slip planes. The dual mechanisms for slipping correlate well with the superior plasticity of theophylline crystals.

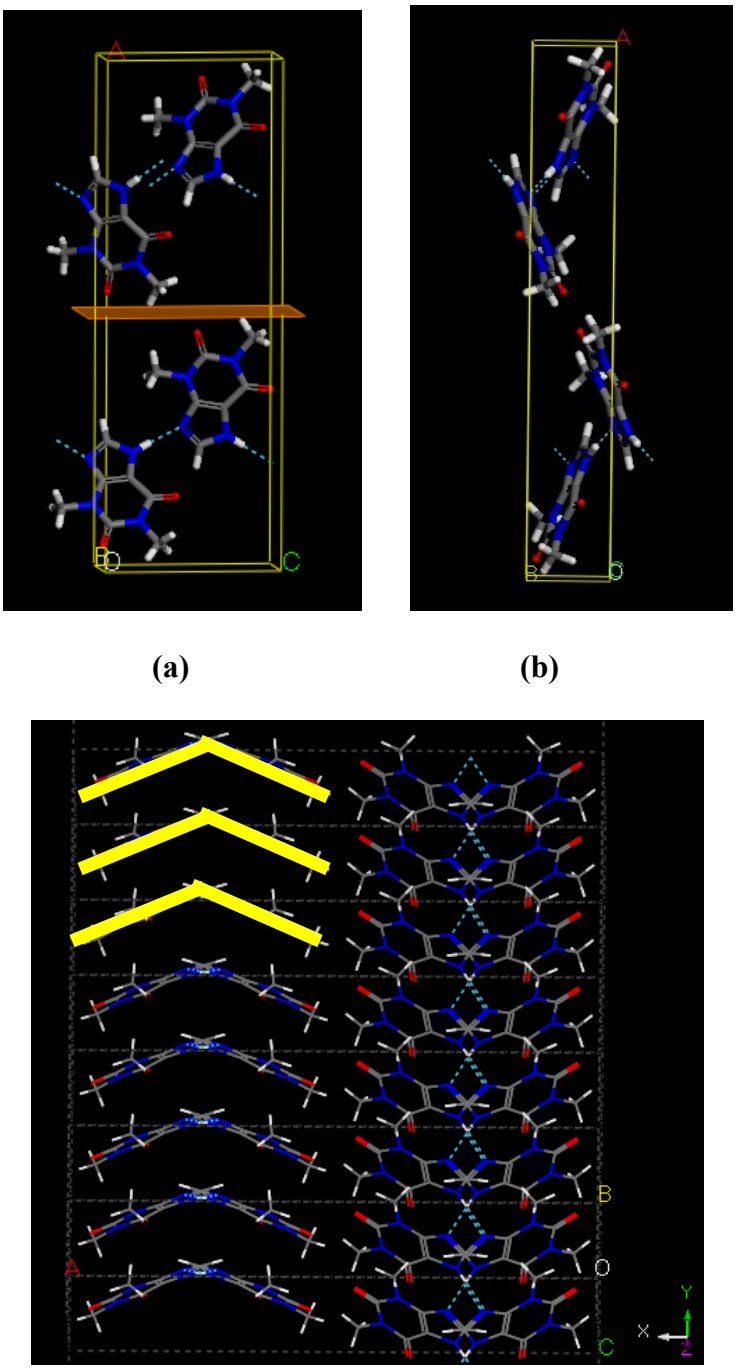

Figure 2.9. Theophylline crystal packing (a) unit cell viewed along *b*-axis, showing predicted slip plane, (b) unit cell viewed along *c*-axis, and (c) stacking V-shaped columns within a flat layer

The cocrystal, on the other hand, exhibits extensively hydrogen bonded flat-layers (Figure 2.10). This type of layered structure, analogous to the structure of graphite, is expected to enhance crystal plasticity by permitting easy slip between layers. However, the plasticity resulted from slip of flat-layers alone is less effective than that from structures similar to theophylline, which have multiple slip mechanisms.

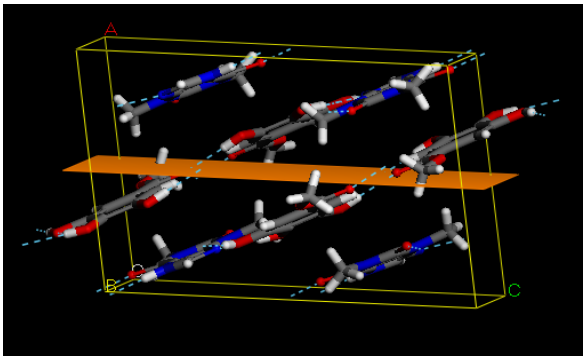

(a)

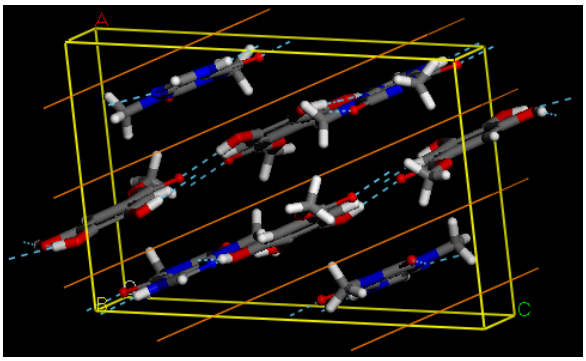

(b)

Figure 2.10. (a) Hydrogen bonded flat layers of cocrystal molecules showing slip plane along (1 0 0) predicted by attachment energy calculations, and **(b)** slip plane along (3 0 -2) predicted by direct visualization of lattice

Lastly, the crystal lattice of methyl gallate is characterized by an extensively hydrogen bonded three-dimensional network structure (Figure 2.11a and b). Such a

network makes this crystal extremely difficult to deform plastically, because of the absence of potential slip planes. In fact, the existence of such a hydrogen bonded network in methyl gallate crystal was predicted on the basis of its poor tabletability, even before its structure was solved.[4] This is consistent with the view that mechanical properties of crystalline materials are closely related to their crystal structures. Hence, a proper understanding of the molecular packing in crystals provides a clear interpretation of the mechanical behavior of materials.

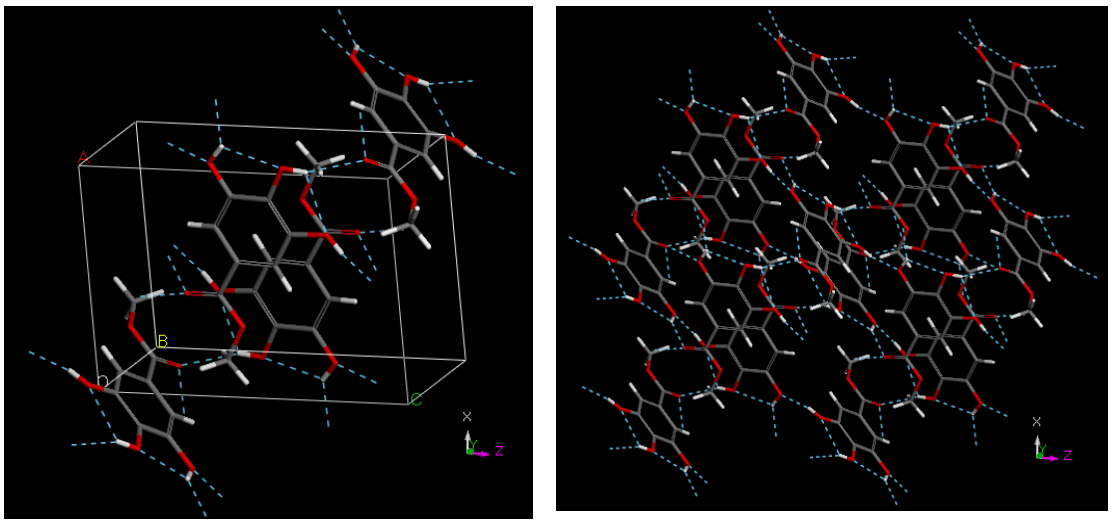

(a) **(b)**

Figure 2.11. (a) The unit cell of methyl gallate, and **(b)** three-dimensional hydrogen bonded network in methyl gallate lattice

2.3.6 Correlation between crystal dislocations and plasticity

An additional interpretation of plasticity difference between the crystals can be provided by calculating dislocation density.[14, 16, 32, 33] All crystals have a certain number of intrinsic dislocations arising from imperfect crystal growth, whose motions under

stress contribute to crystal plasticity.[16, 34] New dislocations may additionally be created during plastic deformation.[16, 33] Irrespective of the origin, crystal dislocations generally weaken lattice and facilitate plastic deformation, neglecting work hardening. In work hardening, plasticity is reduced due to entanglement of dislocations at very high dislocation concentrations. However, work hardening is not important in this study because the extent of plastic deformation, and thus, dislocation generation, is limited during powder compaction in a die.

Each crystal dislocation possesses an associated stress field, which has two primary components – an inner inelastic core, and an outer region where the theories of linear elasticity hold.[16] An appropriate measure of the inelastic core is 5*b*, which can be considered as a characteristic distance parameter (***d***) of dislocations.[16,35,35] Essentially, this is also the minimum distance of separation between two adjacent dislocations, with allowance for stress field overlap. Based on this distance, a limiting dislocation density (ρ_d) for each crystal, defined as the length of dislocation line (L) per unit volume of core (d^2L), can be calculated using the equation (1).[16]

$$\rho_{..} = \frac{1}{d^2} \qquad (1)$$

Here, we have defined ρ_d in a way that it quantifies the dislocation density at the minimum possible separation between two dislocations in a crystal. We note that ρ_d (with a unit of m^{-2}) is different from the total number of dislocations within a unit volume of lattice (i.e. the concentration of dislocations in lattice, with a unit of m^{-3}).

A higher ρ_d for a crystal indicates that the crystal lattice can accommodate adjacent dislocations to a smaller effective distance of separation (d). This should facilitate easier plastic deformation due to the increased potential of dislocation motion at the same strain rate and temperature,[14, 16, 33, 34] without considering work hardening.[34, 36] Theophylline has the smallest Burgers vector magnitude, b = 0.383 nm, so the smallest d compared to the other two crystals. ρ_d of theophylline is 6 to 7-fold higher than the other two crystals (Table 2.1). The highest ρ_d for theophylline explains its highest plasticity. The cocrystal, on the other hand, possesses a significantly longer d (Burgers vector magnitude, b = 1.012 nm) compared to theophylline. The resultant ρ_d of cocrystal is much lower than theophylline (Table 2.1). Corresponding to its lowest plasticity, methyl gallate shows the lowest ρ_d with the largest d (Burgers vector magnitude b = 1.060 nm). The rank order of crystal plasticity (theophylline > cocrystal > methyl gallate) correlates with that of the limiting ρ_d (theophylline > cocrystal > methyl gallate). Thus, the dislocation density model of plasticity provides an additional quantitative interpretation for the lower plasticity of the cocrystal compared to theophylline.

2.4 CONCLUSIONS

The different mechanical properties of theophylline, methyl gallate, and their 1:1 cocrystal originate from differences in crystal packing. Methyl gallate crystals, which contain three-dimensional hydrogen bonded networks, exhibit low plasticity and high resistance to deformation. The cocrystals, containing hydrogen-bonded two dimensional flat slip planes exhibit higher plasticity. The highest crystal plasticity of theophylline is due to flat slip planes composed of hydrogen bonded columns, which provides additional

flexibility for slip leading to a more effective mechanism for plastic deformation. Thus, it is not surprising that cocrystallization can reduce the crystal plasticity and deteriorate tableting performance of materials such as theophylline, while improving the mechanical properties of other materials such as methyl gallate. These results show that a holistic understanding of the relationship between crystal structure and mechanical properties is essential for effectively implementing crystal engineering to address pharmaceutical challenges.

Chapter 3.

Cocrystallization-induced decline in plasticity and powder compaction: Part 2. Quantitative assessment of plasticity of molecular organic crystals with nanoindentation

Following on the qualitative assessment of crystal structure contribution in material plasticity and compaction properties in Chapter 2, in this chapter, the objective is to quantitatively investigate using nanoindentation the origin of deteriorated plasticity of cocrystals based on an analysis of crystal mechanical deformations. The mechanical properties of the materials have been studied at two levels: bulk powders and single crystals. The bulk mechanical properties of the cocrystal and co–formers have been assessed by studying their compaction properties over 10–300 MPa compaction pressure. The compact tensile strength of the cocrystal was lower than both the co–formers, as well as to their 1:1 physical mixture. The inferior mechanical performance of the bulk cocrystal powder stems from a sharp increase in crystal hardness after cocrystallization, resulting in high resistance towards plastic deformation. The rank order of bulk powder compaction (saccharin > piroxicam > cocrystal) was identical to that of crystal plasticity (probed with nanoindentation). Using multiple load–displacement cycling at small strains, mechanical properties such as the yield strength (σ_{ys}) were quantified for each material, which proved that the cocrystal has the highest resistance to plastic deformation onset. This work clearly demonstrates that altering crystal packing of solids may lead to worsened mechanical properties, which in turn will affect their processability. Further, nanoindentation, a material–sparing technique, can successfully elucidate, and in principle predict, the bulk mechanical behavior of materials by quantifying their mechanical property landscape at a sub–micron level.

3.1 INTRODUCTION

The design of molecular packing in crystals for tailored physicochemical and mechanical properties is a topic of fundamental importance for organic materials with pharmaceutical,[1] food,[2] optical [3] and magnetic applications.[4] Crystal engineering,[5] the technique for intentionally modifying the solid–state chemistry of crystals, is receiving substantial interest in materials research. Some of the key forms of molecular organic crystals, relevant for product development, are polymorphs,[6] salts,[7] solvates,[8] and cocrystals.[9] Cocrystals, in particular, have been under immense scrutiny over the past decade, especially for innovative pharmaceutical applications.[10] Cocrystallization, a process by which two or more non-volatile molecules in unionized or zwitterionic forms [11] pack together within the same crystalline lattice through non–ionic interactions,[12, 13] offers several advantages for drug development, such as improved physical [14] and chemical stability,[15] enhanced thermodynamic solubility and faster dissolution kinetics,[16] chiral resolution,[17] and opportunity for intellectual property.[18] The focus of this work is on an aspect of cocrystal research that has, thus far, received only limited attention, *i.e.*, the impact of changing crystal composition and packing by cocrystallization on the mechanical properties of molecular crystals.

The mechanical properties and deformation mechanisms have been extensively investigated for inorganic materials, such as metallic crystals and glasses.[19-21] However, such investigations on organic molecular materials are few. The mechanical properties of organic crystals, as with any material, govern their deformation behaviors under mechanical stress. The key deformation mechanisms include elastic, plastic, viscoelastic

deformation, and fragmentation. Elasticity is the ability of a material to undergo reversible deformation under an externally applied stress, with no residual deformation once stress is removed.[22] At molecular level, elastic deformation is a consequence of reversible stretching of bonds, and therefore limited to deformations under small loads.[22] Plastic deformation, on the contrary, is a permanent deformation caused by gliding of molecular layers under stress and dislocation motion.[19] Viscoelastic deformation is controlled by the relative predominance of elastic and plastic deformations.[23] Fragmentation or fracture of a material results when the rearrangement of molecules under stress cannot accommodate the strain. In this study, we have confined our investigations to the viscoelastic deformation region of organic crystals by operating within small strains without causing fragmentation or cracking.

Depending on the crystal packing, plasticity of a cocrystal can either improve [24, 25] or deteriorate [26] relative to parent cocrystal formers (co–formers). The goal of this study is to investigate the origin of cocrystallization–induced deterioration of mechanical properties (especially plasticity), using the model system of a 1:1 cocrystal formed between piroxicam and saccharin [11] shown in Figure 3.1.

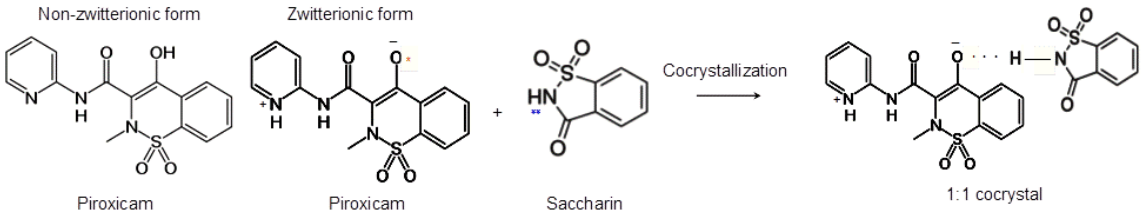

Figure 3.1. Molecular structures of piroxicam and saccharin. Piroxicam exists in zwitterionic form in the cocrystal. The cocrystal is stabilized through N-H···O⁻ hydrogen bonds.

Piroxicam is a drug molecule with anti–inflammatory properties and saccharin is an artificial sweetener used in foods and pharmaceuticals. We have probed the mechanical properties of the materials at two levels: bulk powders (by assessing powder compaction properties) and single crystals by nanoindentation. Nanoindentation can probe the mechanical deformation landscape of materials by initially inducing reversible elastic deformation at low loads and then irreversible plastic deformation by increasing the load to exceed the elastic–plastic limit. If strain is sufficiently large, crystal fragmentation or cracking may result. Because the mechanical properties of a molecular crystal is dependent on its chemistry and crystal packing,[26] nanoindentation is an indirect probe of crystal packing stability and strength of lattice interactions. Therefore, we have used this technique to investigate the origin of deteriorated material plasticity upon cocrystallization.

3.2 MATERIALS AND METHODS

3.2.1 Materials and crystallization strategies

Both piroxicam (β–polymorph) and saccharin were purchased from Sigma-Aldrich (St. Louis, Missouri, USA). The cocrystal is formed between saccharin and zwitterionic piroxicam (Figure 3.1), which is stabilized by N–H$^{\cdots}$O^{-} hydrogen bond interactions. Bulk cocrystal powder was prepared by suspending equi–molar quantities (~0.02 moles) of piroxicam (6.627g) and saccharin (3.664g) in ~30 ml of 1:1 (v:v) mixture of ethanol and ethyl acetate. The suspension was stirred for 48 hrs at room temperature prior to filtration under vacuum for one hour.

Single crystals for both the cocrystal and co–formers were obtained by slow solvent evaporation under ambient conditions. β–piroxicam crystals were grown from benzene, while saccharin crystals were grown from 1:1 mixture of ethanol and ethyl acetate. Single crystals of the cocrystal were generated by evaporating a 1:1 mixture of ethanol and ethyl acetate containing equi–molar quantities of piroxicam and saccharin.

3.2.2 Phase purity of bulk powders

The phase purity of bulk powders (API, coformer and cocrystal) was analyzed by obtaining their powder X-ray diffraction patterns (Siemens DIFFRAC plus 5000 powder diffractometer with Cu-Kα radiation, 1.54056 Å) at room temperature and overlaying them with calculated diffraction patterns obtained from CSD (Conquest ver 1.13, Cambridge Crystal Database Center, Cambridge, UK). The tube voltage and amperage were set at 40 kV and 40 mA, respectively. The sample stage was spun at 30 rpm. The divergence slit and antiscattering slit settings were variable for illumination on the 20 mm area on the sample. Each sample was scanned between 5 and 40 °2θ, with a step size of 0.05° at 1 step/sec. The instrument was pre-calibrated using silicon standard.

3.2.3 Mechanical properties of crystals

Crystal hardness, *H* (a measure of plasticity) and elastic modulus, *E* (a measure of elasticity) were quantified using a nanoindenter (TriboIndenter TI-900, Hysitron Inc., MN, USA) fitted with a standard pyramidal Berkovich diamond indenter tip (tip radius approximately 100nm, total included angle of 142.3°, and half angle of 65.3°) under ambient conditions (~21°C, ~38% relative humidity). The area function of the tip was

derived using a series of indentations on fused quartz standard (modulus of 69.6 GPa). Nanoindentation experiments were performed under displacement–controlled mode, which is more sensitive than load–controlled mode.[20] The loading and unloading rates were both 100 nm/s. Once the maximum penetration depth of 500 nm was reached, a 10s holding time was applied to allow for stress relaxation. During nanoindentation, force and displacement were recorded simultaneously with resolutions of ~1 nN and ~0.2 nm, respectively. A total of 12 - 15 indentations were performed on each sample. Based on the standard methods of analyzing indentation data,[27] the elastic modulus and hardness of each material was obtained from the unloading portion of the load-displacement nanoindentation curves. The reduced elastic modulus (E_r), *i.e.,* modulus of the sample taking into consideration the effects of elastic deformation of the indenter material, was then computed for each material. The yield strength of materials, defined as the limit of elastic deformation beyond which plastic deformation onsets, was determined by partial loading and unloading experiments [28] at low deformations (up to 50 nm displacement into crystal surface at rate of ~2nm/s).

To select crystals suitable for nanoindentation, crystals were first washed with silicone oil to remove fine crystallites and other extraneous adherents from the crystal surfaces. The washed and dried crystals were observed under an optical microscope (10X, Wild M32, Heerbrugg, Switzerland). Crystals with large flat surfaces were selected for indentation studies. The phase nature of single crystals was verified by unit cell parameters, determined with single crystal X-ray diffraction (SMART diffractometer, Bruker AXS, equipped with an APEX II CCD detector). The selected crystals were face indexed using single crystal X–ray diffraction. Under optical microscope, the crystals

were then carefully affixed on glass disks using epoxy (setting time ~5 min) ensuring that the selected crystal faces were parallel to the horizontal plane. The samples were stored under ambient conditions for ~24 hours before indentation to ensure that epoxy was firmly set to fix crystals in position during indentation. Finally, crystal surfaces were imaged by scanning tip (resolution ~1nm) to measure the surface roughness. Only surfaces with low roughness (<10 nm) were indented.

3.2.4 Mechanical properties of bulk powders

The mechanical properties of bulk powders were assessed by quantifying their tabletability, which describes the variation in compact tensile strength with changing compaction pressure.[29] A Materials Testing Machine (Zwick-Roell MaterialPrufung 1485, Germany) was used to compress powders into flat-faced round tablets (8 mm diameter) at a speed of 1 mm/min. Approximately 200–250 mg of each powder was compressed at pressures ranging between10 - 300 MPa (at ~23°C and ~34% relative humidity). Before compaction, the powders were mildly ground and sieved to obtain similar particle size fractions for all three powders. Particle size was estimated by digital microscopy (AD413T Dino-Lite Pro2, Hsinchu, Taiwan). Phase purity of the milled powders was verified with powder X-ray diffraction to eliminate the possibility of milling-induced loss in crystallinity of crystals.[30]

Compacts were stored for ~48 hr at ambient conditions to allow for relaxation of any residual stress after tablet ejection. Compact tensile strength (σ) was calculated using Eq. 1, by measuring the compact diametrical breaking force with a texture analyzer (TA-

XT2i, Texture Technology Corps, NY, 30 Kg load cell, test speed of 0.01 mm/s with a trigger force of 5 g).

$$\sigma = \frac{2F}{\pi D t} \qquad (1)$$

where F is tablet breaking force, D and t are tablet diameter and thickness, respectively. The elastic behavior of the bulk powders was assessed from the in–die elastic recovery (ER) calculated using Eq. 2.

$$ER = \left(\frac{h - h_0}{h_0} \right) \times 100 \qquad (2)$$

where h and h_0 are respectively the tablet thickness at peak compaction pressure and when the pressure reaches zero at the end of the decompression. ER is related to the elastic energy stored in the material during compaction, which is released during decompression.

3.2.5. Molecular properties of crystal lattice

The principal slip plane in each crystal was identified by attachment energy calculations using molecular modeling of crystal packing (Materials Studio, v5.0, Accelrys, San Diego, CA), the slip plane being the crystal plane having the lowest attachment energy. A Dreiding 2.21 force field was employed in the attachment energy calculations because it has been frequently applied to small organic molecules. The magnitude of the Burgers vector, b, was determined for each crystal based on the identified slip system and lattice spacing in the direction of slip.

3.3 RESULTS

3.3.1 Phase purity of bulk powders

Powder X-ray diffraction patterns, before and after grinding, are compared with calculated patterns from single crystal structures in Figure 3.2.

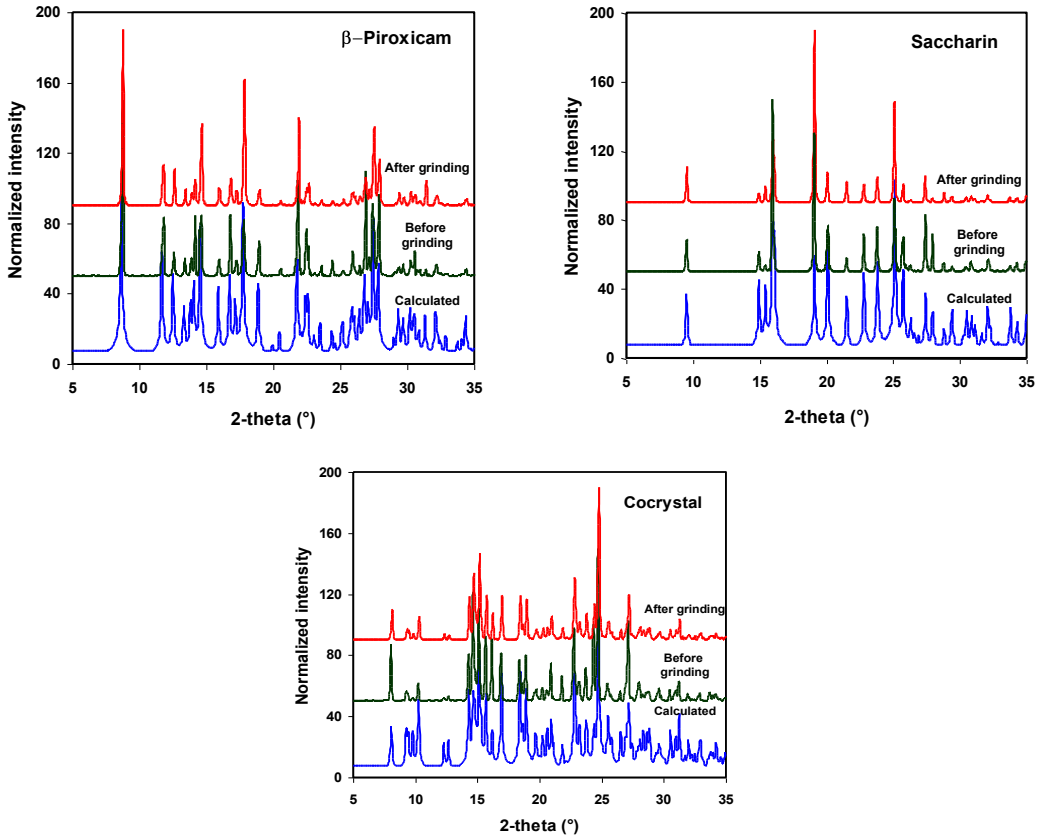

Figure 3.2. Powder X-ray diffraction profiles of unmilled and milled β-piroxicam, saccharin, and PiroSac cocrystal, compared with respective calculated diffraction patterns from single crystal structures, to confirm phase purity of milled powders

All milled powders retained crystallinity after grinding, due to the very mild grinding stress. Slight changes in intensity of some peaks are attributed to preferred orientation differences.

3.3.2 Mechanical properties of bulk powders

The tabletability of the three powders (piroxicam, saccharin and cocrystal), along with that of an equi-molar physical mixture of piroxicam and saccharin, is shown in Figure 3.3a. The average particle size of the powders used for compaction were in the comparable range (~17μm for piroxicam, ~24μm for saccharin, and ~27μm for the cocrystal). The tabletability for piroxicam and the cocrystal were extremely poor and no intact compacts were formed at compaction pressures exceeding 100 MPa. On the contrary, saccharin demonstrated the best tabletability among the three materials, and formed intact compacts over the entire compaction pressure range explored. Overall, the tabletability of the powders decreased in the order of saccharin > physical mixture > piroxicam > cocrystal. Figure 3.3b shows the in–die elastic recovery (*ER*), as a function of compaction pressure, which decreased in the order of cocrystal > saccharin > physical mixture > piroxicam.

The tensile strength of compacts (σ) displayed an exponential relationship with tablet porosity (Figure 3.3c), which can be described using Eq. 3, the compactibility of materials.[32]

$$\sigma = \sigma_0 \, e^{-b\varepsilon} \qquad (3)$$

where b is a fitting constant, σ_0 is tensile strength extrapolated to zero porosity, and ε is compact porosity calculated using Eq. 4.

$$\varepsilon = 1 - \frac{\rho_{compact}}{\rho_{true}} \qquad (4)$$

In Eq. 4, ρ_{tab} and ρ_{true} are the compact density and powder true density, respectively. True densities of different powders (Table 3.1) were measured using helium pycnometry under ambient conditions.

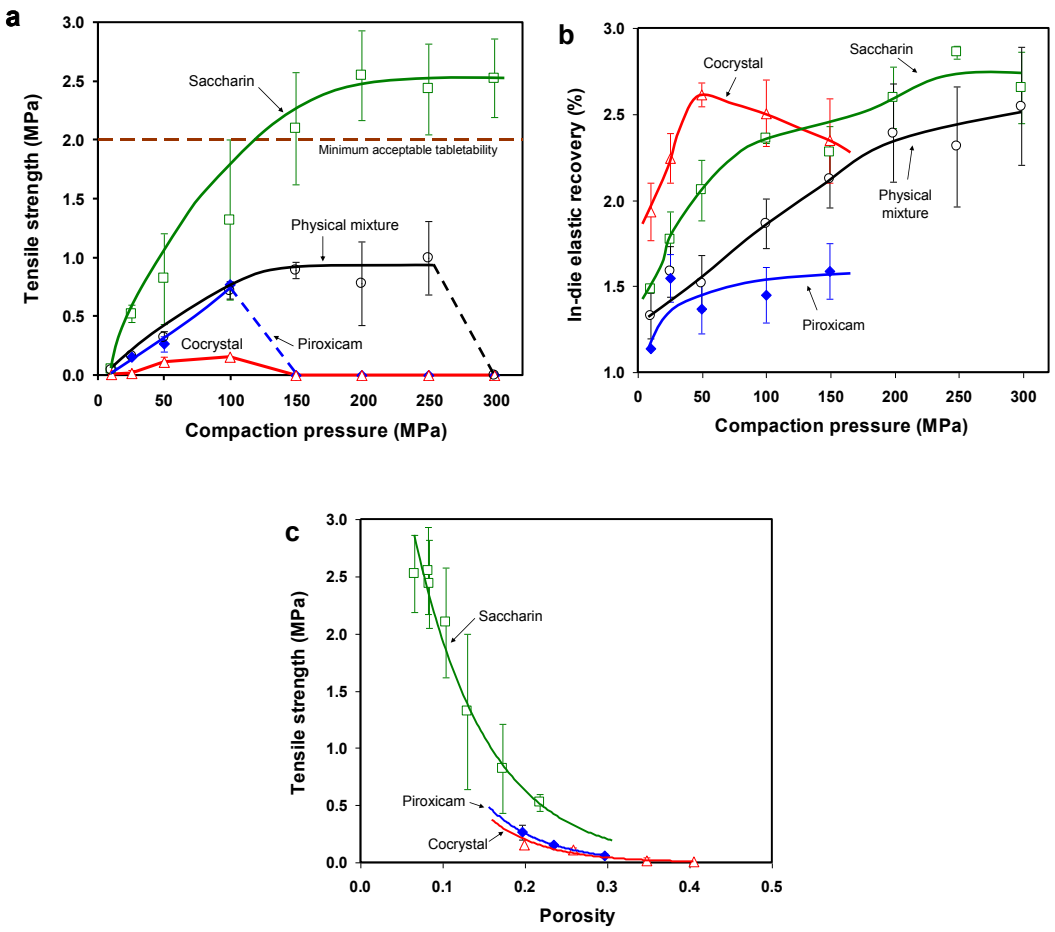

Figure 3.3. Powder compaction properties of saccharin, piroxicam, 1:1 cocrystal and 1:1 (molar ratio) physical mixture: **(a)** tabletability, **(b)** in-die elastic recovery and **(c)** compactibility. Error bars represent one standard deviation of measurements (n=3).

Although σ_0 may be obtained by extrapolating the compactibility plot (Figure 3.3c) to zero porosity, large errors may result in such extrapolations especially if the tensile strengths of only highly porous compacts are experimentally accessible.[33] For instance, piroxicam and cocrystal powders could not be compacted below ~20% porosity, and

extrapolated tensile strength at zero porosity would likely have large errors. To minimize such errors, the tensile strength at 20% porosity, σ_{20}, was used to rank order the mechanical performance of the three powders (Table 3.1).

Table 3.1. Relevant physico-mechanical properties of β–piroxicam, saccharin and cocrystal at room temperature.

Material	True density of powder, ρ_{true} (g/mL) †	Crystal density, ρ_{crys} (g/mL) ‡	Water content (%w/w) ↑	Tensile strength at 20% porosity, σ_{20} (MPa)
β-piroxicam	1.499±0.0003	1.481	0.167	0.254
Saccharin	1.585±0.0005	1.603	0.055	0.632
Cocrystal	1.525±0.0005	1.548	0.228	0.199

† Helium pycnometer (Ultrapycnometer 1000e, Version 4.00, Quantachrome, Boynton Beach, FL, n=10). ‡ Single crystal X-ray diffraction. ↑ Weight loss of powders when heated to 110°C uner dry nitrogen purge by thermogravimetry (Q500 TA Instruments, DE) at 10°C/min heating rate.

3.3.3 Mechanical properties of crystals

Crystal surface roughness and crystal orientation are two key factors affecting nanoindentation results.[34-36] Table 3.2 summarizes these and key mechanical properties of the three crystals. The average surface roughness (α) of the crystal surfaces indented in this study was less than 10nm.

Table 3.2. Summary of mechanical properties of crystals measured by nanoindentation.

Material	Crystal face indented	Surface Roughness α (nm)	Crystal hardness *H* (GPa)	Reduced elastic modulus E_r (GPa)	Yield Strength σ_y (MPa)	Zone of plastic deformation at L_{max}† ψ (nm)
β-piroxicam	[100]	0.54 - 4.2	0.47±0.03	6.50±0.2	749.57	1081.7
Saccharin	[100]	0.98 - 5.7	0.33±0.04	4.23±0.1	446.35	1175.9
Cocrystal	[001]	0.92 - 5.9	0.74±0.06	19.6±1.0	1864.23	929.71

† L_{max}= load at maximum displacement

Figure 3.4 shows the representative load–displacement curves for the three materials. At any fixed displacement on this plot, the load necessary to create the corresponding displacement into the crystal decreased in the order of cocrystal > piroxicam > saccharin. Also, the loading portions of the indentation curves showed distinct excursions or 'drop–in' at constant displacements. The same event is termed as 'pop–in' for load–controlled indentation, where it involves change in displacement at constant load.[26] Based on the load–displacement curves, various mechanical properties of the three materials can be estimated (Table 3.2). Hardness decreased in the order of cocrystal > piroxicam > saccharin, which is consistent with the hierarchy of the load–displacement curves shown in Figure 3.4. The reduced elastic modulus also followed the same order of cocrystal > piroxicam > saccharin.

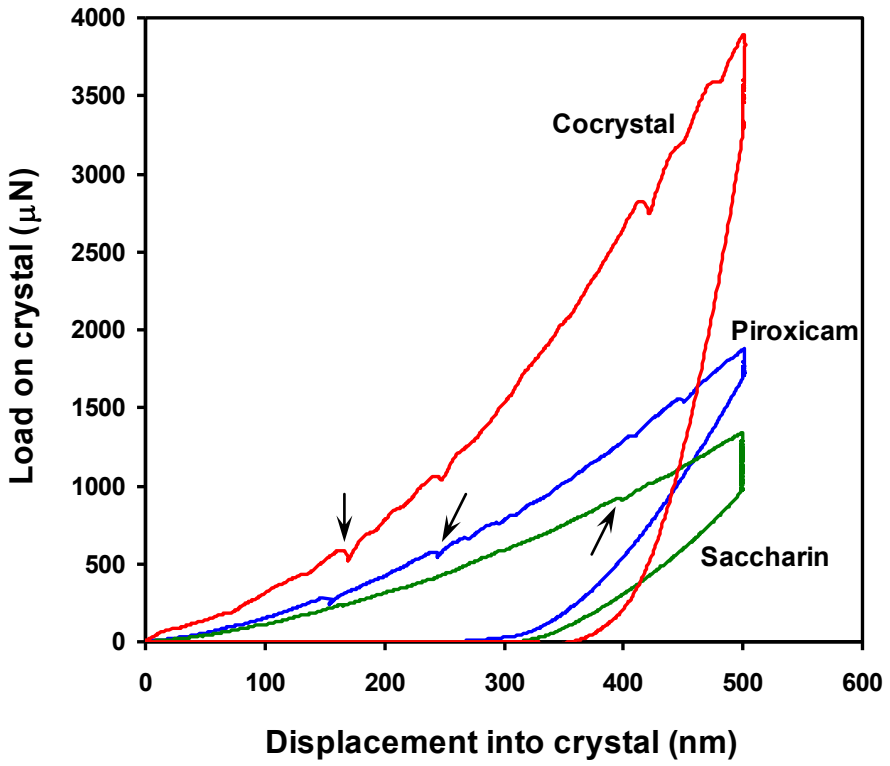

Figure 3.4. Load–displacement nanoindentation curves of β-piroxicam, saccharin and cocrystal. Arrows indicate some drop-in events.

Nanoindentation may provide a direct measurement of the yield strength by performing multiple loading and unloading cycles (Figure 3.5a) until the yield point is exceeded, which is typically at a small strain (<50nm). Below the yield point, the indenter loads produce purely elastic response and no hysteresis between the loading and unloading curves is observed (Figure 3.5b). Beyond the yield point, hysteresis between the loading and unloading curves is clearly visible due to the occurrence of irreversible deformation in the samples. The yield point corresponds to the maximum shear stress (τ_{max}) necessary to nucleate a single dislocation under indenter stress, which is given by Eq. 5.[37]

$$\sigma_{ys} = \tau_{max} = \frac{1}{\pi}\left(\frac{6 E_r^2}{\pi^3 R^2}\right)^{1/3} L^{1/3} \qquad (5)$$

where, L is the load on sample, E_r is the reduced elastic modulus, R is the indenter tip radius, and δ is the penetration depth into the sample.

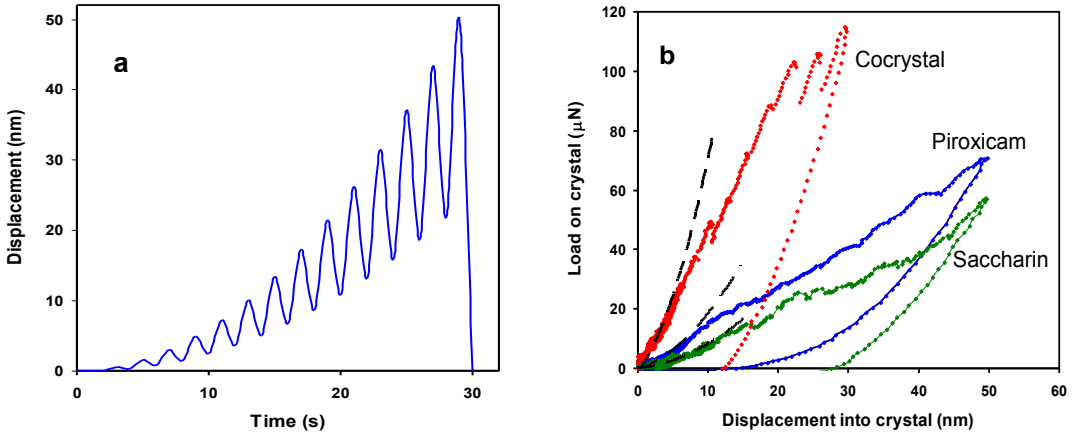

Figure 3.5. (a) Partial loading-unloading profiles used for yield strength estimation. **(b)** Overlays of the load-displacement profiles with a partial unload to assess elasticity-plasticity transition. The initial elastic loading segment has been fitted with Hertz equation.

The yield strength, calculated using equation 5, decreased in the order of cocrystal > piroxicam > saccharin (Table 3.2). The corresponding contact radii (a) at the yield point, calculated using equation 6 following the classical Hertzian model of elastic contact mechanics,[37] were ~57.0 nm (cocrystal), ~60.4 nm (piroxicam) and ~55.2 nm (saccharin).

$$a = \left(\frac{3 L}{4 E_r} R\right)^{1/3} \qquad (6)$$

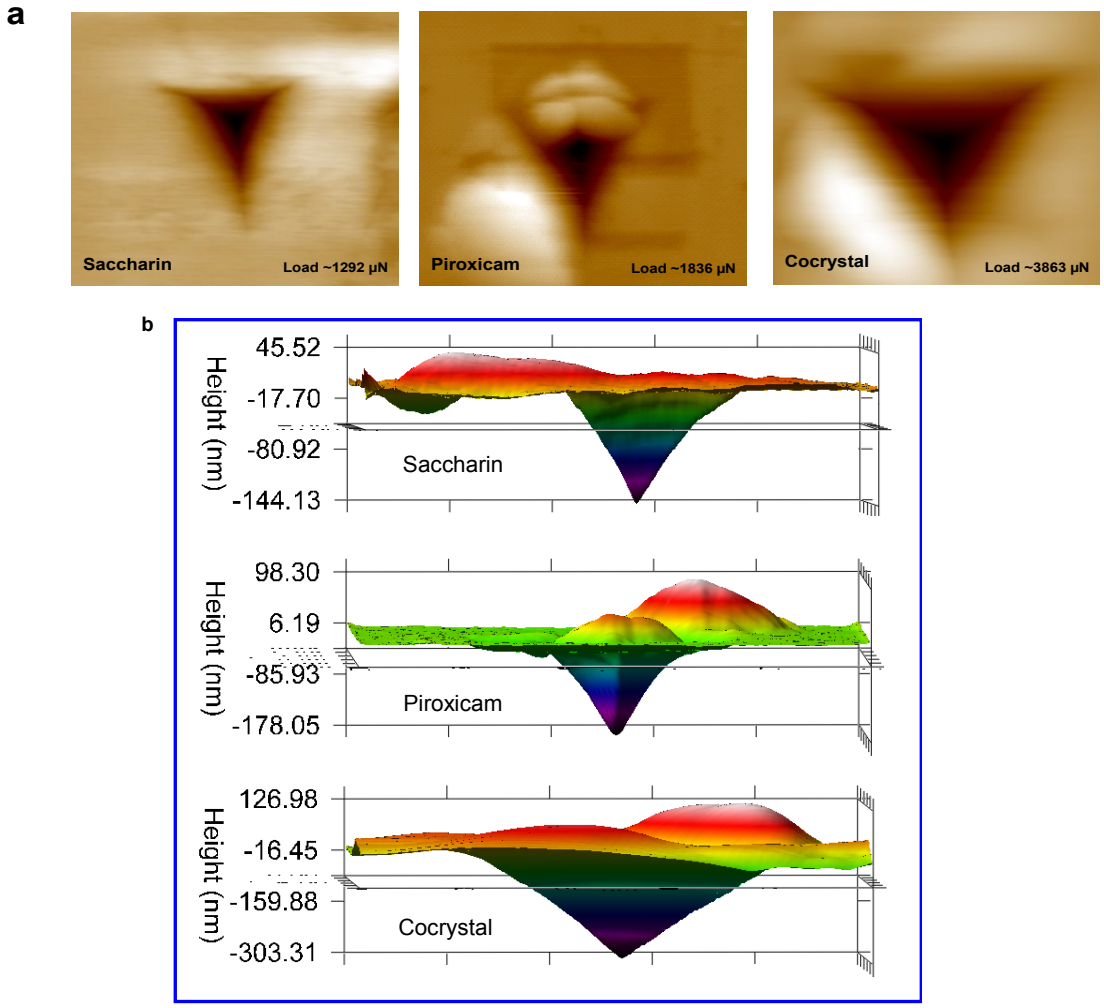

Figure 3.6. **(a)** 2D images of indents of saccharin, β-piroxicam and cocrystal. The loads at maximum displacement decrease in the order of cocrystal > piroxicam > saccharin. **(b)** Corresponding 3D plots showing pile up and residual indent after withdrawal of indenter tip.

Under indenter load, a zone of plastic deformation (ψ) is created surrounding the contact region between the indenter tip and the material being indented. Using Hill's theory of elastic–plastic contact mechanics,[38] ψ can be calculated using Eq. 7.

$$\psi = \sqrt{\frac{3L}{2\pi\sigma_{ys}}} \qquad (7)$$

Saccharin and the cocrystal have the largest and the smallest ψ, respectively (Table 3.2). Figure 3.6a shows the 2D images of the surfaces after indentation. The loads corresponding to the maximum displacements of ~500nm are noted for each material on the 2D plots. The corresponding 3D images of the indented surfaces (Figure 3.6b) show clear pile–up [27] and residual indent after withdrawal of the indenter tip.

3.3.4. Molecular properties of crystals

The molecular properties of crystals, determined by molecular modeling of crystal structures of the three materials, are summarized in Table 3.3. Crystal lattice enthalpy, which indicates the strength of lattice interactions, follow the order of saccharin < piroxicam < cocrystal, even though the values are comparable. A higher lattice enthalpy indicates stronger lattice. The slip planes are identified based on attachment energy (E_{att}) calculations. E_{att} is defined in equation 8, where E_L is lattice enthalpy and E_g is the enthalpy required to add a slice of molecules from a growing crystal face. Slip plane in a crystal has the lowest E_{att} value.

$$E_{att} = E_l - E_g \qquad (8)$$

Burgers vector, which quantifies the extent of lattice mismatch in a crystal caused by dislocation, is the largest for the cocrystal.

Table 3.3. Summary of molecular properties quantified by molecular modeling based on crystal structure data collected at room temperature

Material	Lattice enthalpy (kcal/mol)	Slip system [hkl] (uvw)	
		Based on attachment energy calculations	Burgers vector *b* (nm)
β-piroxicam	-208.45	[020] (100)	0.713
Saccharin	-199.62	[100] (010)	0.691
Cocrystal	-209.63	[001] (010)	1.046

3.4 DISCUSSION

Understanding the relationship between crystal packing and the mechanical properties of organic crystalline solids is a topic of considerable interest in the fields of solid–state chemistry and crystal engineering.[9, 26, 39-42]

3.4.1 Mechanical properties of crystals

Nanoindentation of crystalline samples has been widely used to characterize the mechanical properties of materials at sub–micron scale based on the principles of contact mechanics.[27, 43] The progression of indentation as a function of load[38] is schematically represented in Figure 3.7.

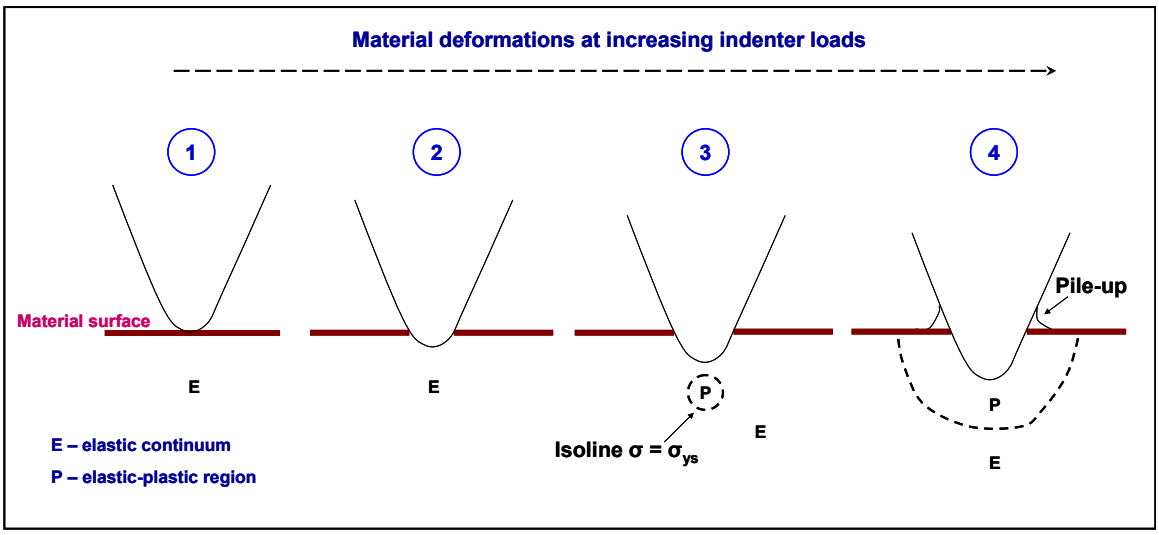

Figure 3.7. Stages of indentation: 1. Indenter tip touching the surface of the material; 2. at $\sigma < \sigma_{ys}$, purely elastic deformation; 3. at yield point ($\sigma = \sigma_{ys}$), elastic-plastic transition, plastic region completely surrounded by elastic medium; and 4. at $\sigma > \sigma_{ys}$, load-dependent regional distribution of elastic and plastic deformations under indenter tip.

At relatively small strains corresponding to a few nanometers in displacement, the deformation of a crystal is purely elastic, and the load–displacement plot approximately follows a Hertzian relationship. At the yield point, there is the onset of plastic deformation, with the plastic zone relatively small and fully contained within the surrounding elastically deforming continuum. Consistent with the previous results,[44] the yield point for all three crystals in this study is associated with a displacement excursion with approximately the magnitude of one Burgers vector (Table 3.3). Burgers vector is a measure of the lattice mismatch caused by the nucleated dislocation,[19] As the load on crystal is further increased, the plastic zone grows in dimension. The plastic zone diameter (ψ) is a measure of the ease of nucleation of crystal dislocations or linear defects, whose motion along slip planes is one of the primary mechanisms of plastic

deformation.[19] ψ represents the extent of plastic deformation occurring in the crystals as a result of the applied load. In the current system, ψ is the highest for saccharin and the lowest for the cocrystal when evaluated at the same maximum penetration depth of 500 nm under maximum indenter load.

At loads exceeding the yield strength of a material, the plastic zone has radial stress and strain symmetry,[38] which pushes a portion of the material up along the sides of the indenter tip by plastic flow, a phenomenon known as pile–up. Pile-up is observed for all three materials (Figure 3.6). The extent of pile–up at either the same load or depth of penetration has been used in the past as a measure of plasticity. However, the extent of pile–up depends on the indenter load applied. In this study where the maximum penetration depth of 500 nm was used, both the maximum load and the extent of pile–up are the highest for the cocrystal even though it is the least plastic (highest *H*). Once we normalize the extent of pile–up with the load applied, we obtain similar values of normalized pile–up for the three crystals. This indicates that even though pile–up is a consequence of plastic flow of materials, the extent of pile-up alone is not a reliable descriptor of material plasticity.

Beyond the yield strength, multiple 'drop–in' events are visible in the loading portions of the indentation curves (Figure 3.4). The dimensions of these excursions are the largest for the cocrystal and the smallest for saccharin. The appearance of multiple excursions corresponds to bursts of dislocations under applied load.[44] The size of these excursion events are typically in integral multiples of Burgers vector. Consistent with this idea,

excursions are the largest for the cocrystal, which has the largest Burgers vector (Table 3.3), and the smallest for saccharin. The importance of Burgers vector in the excursion events can be understood based on the stress field configuration of dislocations. A crystal dislocation has a stress field composed of two components—an inner inelastic core and an outer region where the theories of linear elasticity hold. No two adjacent dislocations can approach each other to a distance closer than the inelastic core, which has a size ~3 to 5 times the Burgers vector for a material.[19] Therefore, the dimensions of these 'drop–in' events, which are bursts of multiple dislocations, have to be integral multiples of 3 -5*b*. For crystals in this study, most of these excursions are ~2 – 8 times 5*b* depending on load.

Insights into material deformations can also be gained by analyzing indent images after indenter withdrawal (Figure 3.6). The residual indent depth after indenter withdrawal, for instance, is material specific, even though the same maximum indentation displacement was used for all three materials. This depth is the smallest for saccharin and the largest for cocrystal. The difference in depth is attributed to the differences in elastic recovery of the three materials. Saccharin crystal surface likely undergoes more elastic deformation to accommodate for the stress applied by the indenter tip, leaving a shallower residual impression upon withdrawal of the indenter tip. This is consistent with the lowest E_r of saccharin. A similar mechanism explains the differences in residual indent angles, which is the smallest for the most elastic saccharin and the largest for the least elastic cocrystal. The similar residual indent angles between saccharin and piroxicam also agree with their similar E_r. Finally, high lattice enthalpy of the cocrystal

(Table 3.3) seems to correlate with its low deformability, which is manifested as high *E* and *H*.

3.4.2 Correlation between powder compaction and crystal mechanical properties

Mechanical performance of bulk powders of viscoelastic materials are determined by the relative predominance of elastic and plastic deformation components.[10, 19] Inter–particulate bonding area develops as a result of rearrangement and deformations of particles under mechanical stress during powder compaction.[23] However, compacts retain integrity only if an adequate amount of the inter–particulate bonding area is preserved once the compaction pressure is withdrawn. Therefore, permanent plastic deformation is a prerequisite for forming intact tablets by powder compaction.[23] For this reason, materials with low plasticity, e.g., acetaminophen,[45] have poor powder compaction properties. Strategies for addressing poor compaction properties of these crystals include surface coating with a plastic material [46] and modification of solid–state chemistry to render adequate plasticity for bonding area retention.[25, 41] Using polymorphs, it has also been shown that plasticity is crystal packing dependent and higher plasticity generally leads to superior compaction properties.[39, 47, 48]

It has been proposed that the minimum tensile strength of ~2 MPa is required for the successful commercial tableting.[49] By this measure, both piroxicam and the cocrystal exhibit very poor tabletability (Figure 3.3a). This is also supported by the very low σ_{20} values for these materials (Table 3.1). In comparison, the compaction properties of saccharin are much superior, with tensile strength exceeding 2 MPa at pressures >150

MPa. Using 1:1 (mole ratio) physical mixture of piroxicam and saccharin as a control, we show that the mechanical properties of the cocrystal were far inferior to that of the physical mixture, indicating that the worsened mechanical properties of the cocrystal are a consequence of its unique crystal packing features.

The differences in powder mechanical properties may be well explained based on their different mechanical properties of the three crystals. The contribution of elasticity and plasticity on the compaction behavior is of special interest. Saccharin is the most plastic among the three crystals, indicated by its lowest hardness and lowest yield strength determined using nanoindentation (Table 3.2). A lower hardness indicates the greater ability of a material to undergo plastic deformation under mechanical stress. Based on our experience, organic materials with either very low (<0.2 GPa) or very high (>0.7 GPa) hardness are prone to suffer from poor tabletability. Within the intermediate hardness range, tabletability generally increases with decreasing hardness. The cocrystal has a much higher hardness compared to both the co–formers and therefore smaller bonding area retention and inferior tabletability.

In addition to plasticity, important insight into tabletability is also provided by elasticity, which can be characterized either by elastic modulus (E_r) of a crystal or the elastic recovery (*ER*) of compacts during the process of decompression (withdrawal of compaction pressure). A lower value of E_r (Table 3.2) or higher value of *ER* (Figure 3.3b) indicates higher elasticity. High degree of elastic recovery can break inter–particulate bonding sites and deteriorate tabletability. In this work, the cocrystal shows

the highest degree of elastic recovery of compacts (Figure 3.3b). Saccharin has high plasticity but also low E_r, (Table 3.2) which leads to large elastic recovery. This high elasticity of saccharin compacts may be one reason for the high degree of variability seen in the saccharin tabletability data.

The mismatch between the rank orders of E_r for the crystals and *ER* for their compacts may be explained by the porous nature of the compacts (ε>20%). *ER* of a compact is determined by the mechanical property of the crystal–air composite confined in a die, rather than the E_r of the crystal. It has been known that the elastic modulus of a compact generally decays exponentially with increasing porosity.[50] Although E_r of the cocrystal is the highest among the three crystals, its compact is also more porous at the same compaction pressure. Consequently, the apparent elastic modulus of its compact is low, which leads to high ER. Similar mismatch in rank orders of the two parameters have previously been reported for other materials.[26]

3.5 CONCLUSIONS

We have shown that cocrystallization between saccharin and piroxicam leads to reduced plasticity and compromised tableting behavior. The mechanism of the deteriorated mechanical performance of the cocrystal has been investigated by probing the mechanical properties of the cocrystal and the co–formers using nanoindentation, which is supported by an analysis of crystal packing. The multi-scale investigation reveals that much reduced cocrystal plasticity (or higher hardness) is responsible for the poor tableting behavior of its bulk powder. Moreover, high lattice enthalpy of the cocrystal seems to

correlate with its low deformability, which is manifested as high E and H. Our efforts of probing the mechanical properties and deformations of molecular organic materials cater to a long-lasting need of systematically studying such properties in these classes of molecular organic materials at sub-micron and bulk levels.

Chapter 4.

Modifying surface structure of microcrystalline cellulose by dry mechanical coating to improve powder flow

This chapter is based on the following published research article: Chattoraj *et al.*, *Journal of Pharmaceutical Sciences*, 100, 4943-4952, 2011. The article has been reproduced with permission from John Wiley and Sons.

The objective of this chapter is to apply the concept of Materials Science Tetrahedron at the level of bulk powder to modify the surface structure of powders to address the problem of poor powder flow. Poor flow properties hinder the easy handling of powders during industrial scale processing. In this work, we show that powder flow can be substantially improved by reducing the cohesion of powders through coating them with nano-sized guest particles, by the application of shear stress with comilling of guest and host particles. We have systematically investigated the effects of total number of comilling cycles (varied between 1 to 70 cycles) and silica loading (varied between 0 to 1.0 wt%) on the flow behavior of a highly cohesive and poorly flowing grade of microcrystalline cellulose powder (Avicel PH105). Optimum flow enhancement has been achieved with 1.0 wt% silica loading at 40 comilling cycles. The flow properties of nanocoated Avicel PH105 are comparable with those of Avicel PH102, which exhibits adequate flowability for processing on a high speed tablet press. Comilling is fast and suitable for continuous processing. It holds potential for addressing industrial powder handling problems caused by poor powder flow properties.

4.1 INTRODUCTION

Adequate powder flow is a necessary prerequisite for the successful pharmaceutical manufacturing using unit operations such as powder compaction and encapsulation.[1-3] Manufacturing problems, arising from poor powder flow properties, are regularly encountered during the industrial handling of bulk powders.[1, 2, 4, 5] Flow-related problems are expected for fine powders (d_{50} < 30 μm), which are generally highly cohesive and poorly flowing.[1, 4, 6, 7] A common approach adopted in the industry for improving powder flow is particle size enlargement through granulation. Despite recent technological advancements, granulation can often lead to processing problems, such as deteriorated powder tabletability and poor drug release behavior.[8-11] Tabletability suffers due to size enlargement of particles during granulation. Moreover, granulation invariably lengthens the manufacturing process, and results in higher production costs. Thus, it would be extremely useful to develop an alternate technique for flow improvement of cohesive powders without the requirement of granulation. Such a technique should also be economical, easy to set-up, and suitable for industrial scale powder processing.

An attractive alternate way to improve the flow properties of fine powders, without the need of granulating, is dry particle coating of the cohesive powder surfaces, which facilitates the physical separation of adjacent substrate particles, thereby reducing cohesion. For example, Yang et al [12] have shown that the flow properties of cornstarch can be improved significantly by coating with silica using mechanical coating processes, such as magnetic-assisted impaction coating (MAIC) and hybridizer process.[13, 14]

Coating using fine guest particles tends to produce better flow of cohesive powders. Similarly, by dry coating using a plasma downstream reactor, the flow of cohesive lactose particles (d ~ 30.9 μm) is increased by a factor of 3.1.[6] Likewise, the flow characteristics of cohesive lactose monohydrate powder are modified by intensive dry-coating with magnesium stearate and fumed silica through mechanofusion.[16, 17]

Even though these techniques can improve powder flow, they invariably require specialized instruments that are not commonly available in manufacturing plants. In addition, most of these processes involve intense mechanical impact that significantly alters particle properties, such as particle size and shape and can induce mechanical amorphization in crystals. Potential chemical degradation of the material due to impact during powder processing is another serious problem.[18] Finally, scaling up these processes is generally difficult and costly. Thus, there is a need of finding a cost-effective and scalable dry surface coating (nanocoating) technique for improving the flow of cohesive powders that will not suffer from these deficits. Herein, we show that comilling is a process that successfully meets these criteria. In this process, a powder is subjected to only shear stresses (no impact) when it is pushed through a screen by a rotating impeller, and thereby avoids most of the problems in the earlier processes arising from impact stress on materials. The comilling process is fast and suitable for continuous operation, which makes it ideal for industrial scale powder nanocoating.

4.2. MECHANISM OF NANOCOATING

The physics behind the beneficial role of nanocoating on powder flow has been well explained in the literature.[19] Briefly, flow improvement by nanocoating can be easily understood by considering the interplay between two universal forces affecting powder flow, *i.e.,* inter-particle cohesion (mainly *van der* Waals forces) and gravitational force.[6, 15, 19] Let us consider a container with a small opening at the bottom, assuming that 1) the particles at the air-powder interface on the bottom opening are influenced mainly by gravity and cohesion, and 2) the opening is sufficiently large so that particle jamming is avoided during flow. While gravity favors powder flow by pulling particles downward, cohesive force hinders flow by inter-particle attraction. As long as gravity dominates over cohesion, powder flow is spontaneous. Conversely, powder flow is problematic when cohesion dominates over gravity. According to Hamaker's theory,[20] the cohesive interaction (F) between adjacent particles (*van der* Waals interactions) is inversely proportional to the square of the distance of separation, as shown in equation 1.

$$F = \frac{-A D_1 D_2}{12 d^2 (D_1 + D_2)} \qquad (1)$$

Where, A is Hamaker's constant, D_1 and D_2 are particle diameters, and d is the distance of separation between particle surfaces. If we assume that the two host particles have equal diameters, then the cohesion between adjacent host particles is given by the simplified equation 2.[19]

$$F = \frac{-A D}{24 d^2} \qquad (2)$$

Nanocoating helps to increase the distance of separation (*d*) between adjacent host particles and hence reduces cohesion, sometimes by several orders of magnitude [6, 19]. The substantially reduced cohesion, in turn, leads to profoundly improved powder flow as gravity is allowed to outplay cohesion. As a secondary mechanism, the guest nanoparticles can act as ball bearings to further improve powder flow by reducing the friction between host particles. It should be noted that, for optimum flow improvement, nanoparticle coating must be discrete. A continuous layer of guest nanoparticles on the host particles slightly increases the diameter (*D*) of the host particles. When such particles are in contact, the *d* is very small while *D* is slightly larger than before coating. Thus, the cohesion remains high according to equation 2. Alternatively, this may be understood by considering the scenario where two host particles are initially separated by a single guest nanoparticle. In this situation, cohesion is significantly lower than if the two host particles are in contact because of the larger *d*. If the surfaces of both host particles are progressively covered with more guest particles, the attraction force between the host particles increases because of the increased mass. When a continuous coating layer is achieved, the attraction force is the highest.

4.3 MATERIALS AND METHODS

4.3.1 Materials

Microcrystalline cellulose (Avicel PH105, Batch: 50843C, FMC Biopolymer, Philadelphia, PA) was selected as the cohesive host (substrate). Avicel PH105 is well known for exhibiting exceptional tabletability, but very poor flow properties.[4] Colloidal silica (grade M-5P, ~14 nm, Cab-o-sil, Cabot Corp., Boston, MA) was selected as the

coating material (guest). Before comilling, both powders were first vacuum dried for 24 hrs at room temperature and then exposed to ambient conditions for approximately 1 hr before coating operations by comilling. The moisture contents of coated and uncoated powders were found to be similar by thermogravimetric analysis. Avicel PH102 (Batch: P208819629, FMC Biopolymer, Philadelphia, PA) was utilized as a reference powder to assess, by way of comparison, whether the coated powders exhibited adequate flowability for successful high speed tableting.[1]

4.3.2 Nanocoating procedure

Nanocoating was performed by comilling Avicel PH105 and silica (Comil®, Model U3, Quadro Engineering Corp., Waterloo, OT, Canada). Avicel PH105 and silica powders were mixed by geometric dilution and passed through a standard sieve with 150μm opening before the comilling operation. The pre-sieving step improved the nanocoating efficiency by breaking large silica agglomerates, which otherwise tended to 'float' on the top of the powder bed and did not easily pass through the comilling screen. The pre-sieved powder mixture was then placed within the comill powder-receiving chamber fitted with a stainless steel screen (round holes of 0.9905 mm, or 0.039", diameter, part number: 7B039R03125). The lowest speed (2200 rpm) of the impeller (150 Grit round impeller with square arms) was used to minimize mechanical stress on the powders. SEM data, particle size data, and powder XRD data showed no evidence that suggested any change in particulate properties or crystallinity of MCC particles after comilling. Factors such as the total number of comilling cycles, silica loading, type of screen used (mesh size), impeller speed, and impeller type can all potentially influence

the efficiency of the nanocoating process. However, in this study, we focused on evaluating the effects of the number of comilling cycles and silica loading, while fixing the other variables. The effect of comilling cycles (0 to 70 at increments of 10 cycles) on flow was evaluated at a constant silica loading of 1.0% (wt%). The effect of silica loading (0 – 1.0%) on flow was assessed by fixing the total number of comilling cycles at 40, which corresponds to optimum flow enhancement (discussed later). A constant batch size of 100 g was used throughout our study. Fewer cycles are expected to achieve the same degree of flow improvement if industrial scale comilling is used for nanocoating the powders. Due to the high efficiency of this process, it took only a few seconds to process 100 g of powder by comilling.

4.3.3 Particle size distribution

Particle size distributions (PSD) of uncoated and nanocoated MCC were measured in triplicates using a laser scattering particle sizer (Mastersizer 2000 with a Scirocco dry module, Malvern Instruments Ltd., UK) operated at an inlet air pressure of 1 bar and feed-rate of 30%.

4.3.4 Specific surface area

The specific surface areas (SSA) of powders were measured by Brunauer, Emmett, and Teller (BET) nitrogen gas adsorption method (Tristar, Micromeritics, Norcross, GA). Before each measurement, the sample was purged with a continuous stream of nitrogen gas at 30 °C for at least 1 h. Nitrogen adsorption was measured at multiple partial pressures (P/P_0) ranging from 0.05 to 0.2.

4.3.5 Ring shear cell measurement of powder flow

Powder flow properties were measured using a ring shear cell tester (RST-XS, Dietmar Schulze, Wolfenbuttel, Germany).[4, 21, 22] Before flow measurement, the performance of the instrument was verified using limestone standard. For shear cell measurements, powders were first over-filled into a ring-shaped cell (approximately 30 mL in volume). The excess powder was then gently scraped off to produce a flat surface, which was coplanar with the top edges of the cell. Care was taken while adding powder to the shear cell to avoid the formation of large air pockets within the powder bed. Four pre-shear normal stresses, 1, 3, 6, and 9 kPa were used in shear cell study. Under each pre-shear normal stress, shear tests were conducted at a total of five progressively increasing normal stresses equally spaced between zero and the corresponding pre-shear normal stress. The sixth shear test was carried out at the stress conditions identical to the first shear test (the lowest normal stress). Any change in properties of constituting particles was deemed negligible when the flow difference between the first and sixth measurement was less than 5%, which was approximately the relative standard deviation in our typical shear cell measurements. According to this criterion, none of the powders tested for this study showed any change in properties during shear cell testing.

A yield locus was constructed by connecting the neighboring points on the plot of maximum shear stress versus normal stress during each shear test.[22] The average shear stress from the two shear tests at the lowest normal stress was used for plotting. The lowest portion of the yield locus was obtained by extending to y-axis (shear axis) the

segment defined by the points at the two lowest normal shear stresses (straight section method of data analysis). From each yield locus, unconfined yield strength, f_c, and the corresponding major principal stress, σ_n, were obtained by drawing two Mohr's circles by the following criteria: 1) one circle passing through origin and tangent to the yield locus, and 2) the second circle passing through the pre-shear point and tangent to the yield locus. Flow function of a powder was obtained by plotting f_c against σ_n, derived from different yield loci. At a given σ_n, a lower f_c indicates easier initiation of powder flow. Another way to represent the shear cell data is to calculate flow factor, *ff*, which is defined as σ_n/f_c. [22] All shear cell experiments in this study were performed at 23.5 ± 1.5 °C and 30 ± 3% RH.

4.3.6 Compaction studies

Powder tabletability properties were tested using a compaction simulator (Presster, Metropolitan Computing Company, East Hanover, NJ) simulating a Korsch XL100 (10 station) tablet press (production speed of 61600 tablets/hr, corresponding to a press speed of 102.7 rpm, dwell time of 20 ms). Round (9.5 mm in diameter) flat-faced punches were used for tableting. Tablet breaking forces were measured using Texture Analyzer (TA-XT2i, Texture Technologies Corp., NY, 50 kg load cell, test speed of 0.01 mm/s with a trigger force of 5g). Tablet radial tensile strength was calculated using the tablet breaking force, thickness, and diameter which were measured using digital caliper (Electron Microscopy Sciences, Hatfield, PA).[23]

4.3.7 Scanning electron microscopy-energy dispersive spectroscopy (SEM-EDS)

A thermally activated field emission gun type scanning electron microscope (FEG-SEM, JEOL 6500F, Tokyo, Japan) was used to obtain information on particle size and surface topography of uncoated and nanocoated powders (1% silica, 40 comilling cycles). Before SEM analysis, a thin layer of platinum (thickness ~50 Å) was deposited on the particle surfaces. The SEM sample chamber was maintained with a high vacuum (10^{-4} to 10^{-5} Pa) during the imaging process. Point scanning energy dispersive spectra were collected for both the coated and uncoated samples. This showed the relative proportions of different elements in the scanned spectra generated using Noran System 6 software (Thermo Fischer Scientific, West Palm Beach, FL).

4.3.9 Statistical analysis

Statistical analysis on data was performed using software package Arc XLISP-PLUS version 3.04 (R. D. Cook & S. Weisberg, University of Minnesota). At 95% confidence level, $p<0.05$ was considered significant.

4.4 RESULTS AND DISCUSSION

4.4.1 Particle size distribution and specific surface area

The very small particle size of Avicel PH105 (d_{10} = 6.8 ± 0.1 μm and d_{50} = 20.9 ± 0.1 μm, and d_{90} = 45.7 ± 0.5 μm, n = 3) is consistent with its high cohesiveness and poor flow properties. The particle size increases very slightly for Avicel PH105 after being coated with 1% silica after 40 comilling cycles, which can be attributed to the deposition

of nanoparticles on the surfaces of Avicel PH105 (Figure 4.1). Silica nanoparticle coating also helps to increase the specific surface area (SSA) of powder significantly (p=1.5×10^{-6}) with SSA= 1.999 ± 0.004 m^2/g for Avicel PH105 as received, and 6.171 ± 0.009 m^2/g for Avicel PH105 coated with 1.0% silica at 40 comilling cycles.

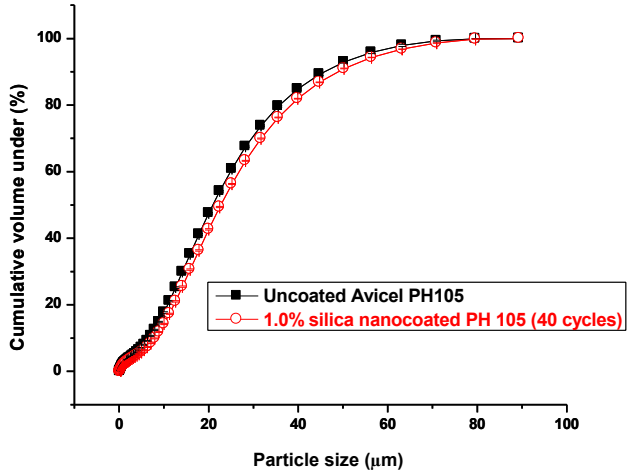

Figure 4.1. Cumulative particle size distribution (n = 3) of Avicel PH105, both uncoated and coated with 1% silica (40 comilling cycles).

4.4.2 Effect of comilling cycles on powder flow

At 1.0% silica loading, powder flow properties show considerable improvement with repeated comilling up to a total of 40 cycles, as shown by the lowering of the flow function line with increasing number of milling cycles (Figures 4.2). The reduction in slope of the flow function is statistically significant (p=4.4×10^{-5}), with the slope decreasing from 0.269 (for uncoated Avicel PH105) to 0.086 (for nanocoated with 1%

silica, 40 comilling cycles). However, repeated milling beyond 40 comilling cycles leads to no further flow improvement.

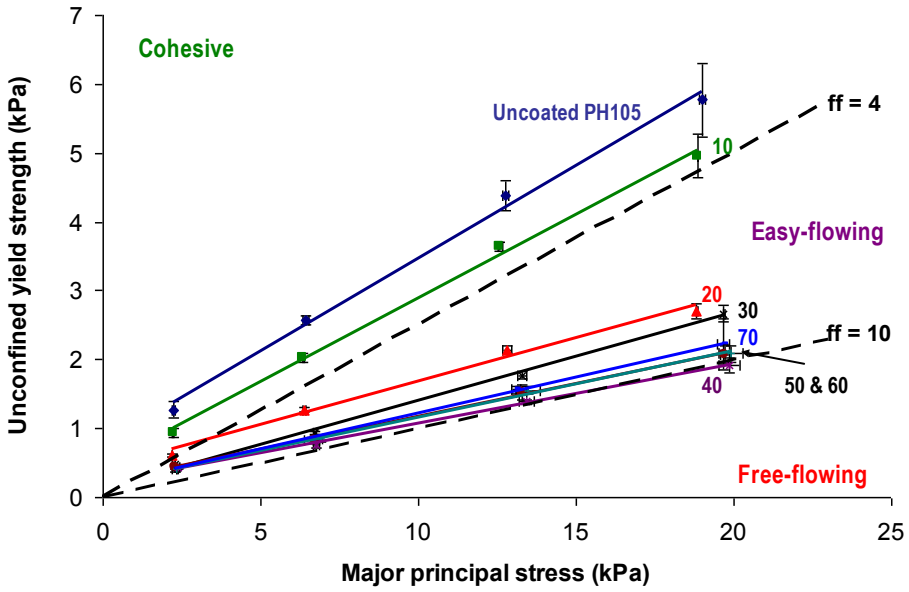

Figure 4.2. Effect of number of comilling cycles on flow functions of Avicel PH105 at silica loading of 1.0%. Numbers on the plots represent the corresponding comilling cycles employed. Error bars represent one standard deviation of the measurements (n = 3).

Jenike [24] has developed a scheme for classifying powder flow properties, based on flow factor (*ff*), defined above. A powder is considered unable to flow when $ff<1$, very cohesive when $1<ff<2$, cohesive when $2<ff<4$, easy-flowing when $4<ff<10$, and free-flowing when $ff>10$.[22, 24-26] It must be noted that Jenike's flow classification is based on flow characterization using a translation shear cell, and not the ring shear cell used in this study. It is possible that the exact numerical ranges of the classification may

not be valid for our studies. It is, nevertheless, a useful classification system to gain insight into the powder flow behavior. According to this classification, uncoated Avicel PH105 falls within the cohesive region (Figure 4.2). However, after nanocoating with 1.0% silica using only 20 comilling cycles, the flow function of the powder is moved into the easy-flowing zone ($4<ff<10$), at major principal stresses ≥ 3 kPa.

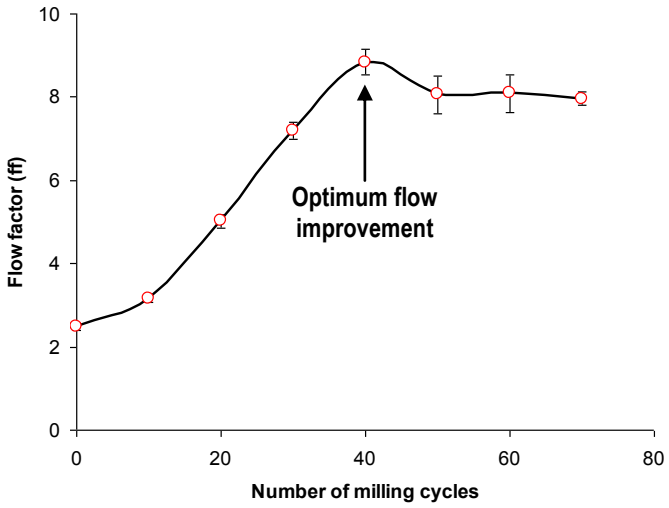

Figure 4.3. Variation of flow factor, *ff*, of Avicel PH105 with total number of comilling cycles with 1.0% silica loading at 3 kPa normal stress. Error bars represent one standard deviation of the measurements (n = 3).

The relationship between flow factor (*ff*) at a fixed normal stress of 3 kPa, and the number of comilling cycles is shown in Figure 4.3. 40 comilling cycles (at 2200 rpm comilling speed) correspond to optimum flow improvement for 1.0 wt% silica loading in this model system. For this batch, the flow is significantly improved (p=0.0007) compared to uncoated Avicel PH105. The lack of flow improvement after 40 cycles, shown by decreasing *ff*, suggests that at this stage, sufficient surface coverage of host

particles has been achieved so that two adjacent hosts, at random orientations, are always separated by nanoparticles.

4.4.3. Effect of silica loading on flow

The effect of silica loading on flow factor, *ff*, at 40 comilling cycles is shown in Figure 4.4. Silica loading has been varied from 0% (uncoated Avicel PH105) to 1.0% silica at increments of 0.2%. At normal stresses ≥ 3 kPa, the powders behave as non-cohesive (*ff*>4) at all silica loadings of ≥ 0.2%. Nanocoating with a silica loading of 1.0%, at 40 comilling cycles, produces a mean flow factor that is not statistically different (p=0.81) from flow factor of a free flowing product (*ff*=10). Thus, it appears that with this level of silica nanocoating, it is sufficient to transform the otherwise cohesive Avicel PH105 powder into a free-flowing product at preshear normal stresses ≥ 9 kPa.

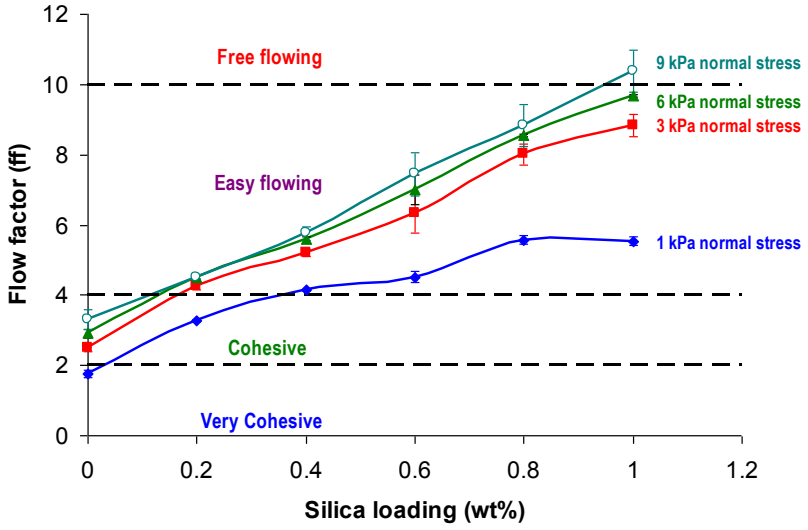

Figure 4.4. Effect of silica loading on flow factors of Avicel PH105 with 40 comilling cycles. Error bars represent one standard deviation of the measurements (n = 3).

In this context, it must be mentioned that colloidal silica has been commonly used in the pharmaceutical industry with the intention to enhance powder flow of formulated powders. Thus, to clarify that the flow enhancement of Avicel PH105 observed in this work can be attributed to comilling and not simply to the presence of silica, we have compared the flow properties of nanocoated Avicel PH105 (using a comill, 1% silica) and a blend prepared using a common V-shaped laboratory blender (Blend Master, Patterson-Kelley, PA, 10 min, 1.0% silica).

As shown in Figure 4.5, comilling leads to significantly improved flow properties (p=0.002) compared to standard blending at same silica loading. While the comilled sample flows easily, the powder after 10 min of simple blending and sieving remains cohesive and exhibits flow properties that are statistically similar to the starting Avicel PH105 (p=0.21). Clearly, ordinary blending process does not provide sufficient amount of shear stress necessary for effective de-agglomeration of silica particles and subsequent coating of host particles.

4.4.4. Flow comparisons with Avicel PH102

Avicel PH102 has recently been established as a reference material that lies near the boundary between zones of acceptable and unacceptable flow properties during high speed tableting.[1] By this measure, Avicel PH105 is clearly not suitable for high speed tableting because it exhibits much poorer flowability than Avicel PH102 (Figure 4.5). In contrast, Avicel PH105 comilled with 1.0% silica after 40 comilling cycles display flow

properties that are statistically similar (p= 0.65) to Avicel PH102 (Figure 4.5). Thus, due to its much improved flow properties, the nanocoated Avicel PH105 is expected to be acceptable for use on a high speed tablet press.

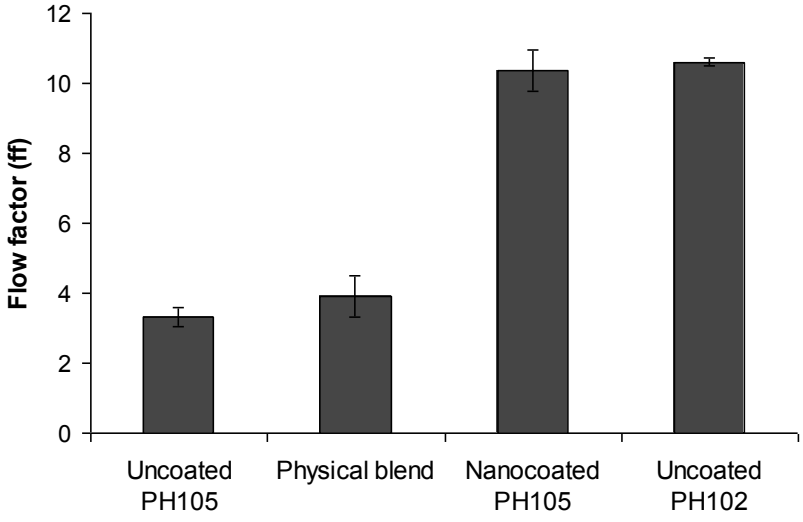

Figure 4.5. Flow factor difference of powders at 9 kPa normal stress. The nanocoated batch of Avicel PH105 was processed with 1% silica at 40 comilling cycles. Error bars represent one standard deviation of the measurements (n = 3).

4.4.5. Compaction studies

To examine the impact of nanocoating on the compaction properties of Avicel PH105, we have tested the tabletability (dependence of tablet tensile strength on compaction pressure) of uncoated and optimized nanocoated Avicel PH105 (1% silica, 40 comilling cycles) and Avicel PH102, which is commonly used in pharmaceutical tablet products (Figure 4.6).

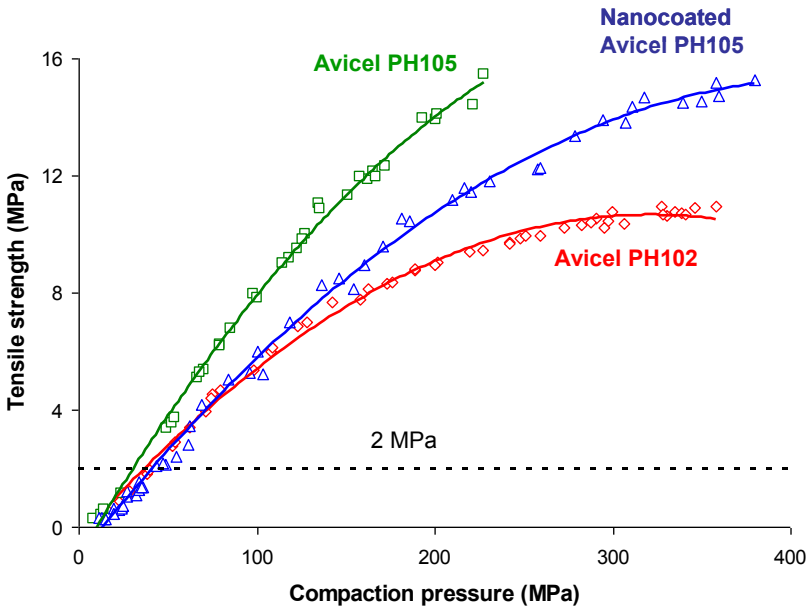

Figure 4.6. Tabletability of uncoated Avicel PH105, nanocoated Avicel PH105 and uncoated Avicel PH102. The broken line indicates the minimum tablet tensile strength, 2 MPa, for pharmaceutical tablets [3, 8].

Uncoated Avicel PH105 shows exceptionally high tabletability and forms hard tablets. Tablets compressed at compaction pressures higher than 220 MPa exceeded the limit of the load cell (50 kg) on the texture analyzer and could not be broken. However, as expected based on its poor flow, it was extremely difficult to reproducibly fill the die with Avicel PH105 from a hopper. The tabletability of nanocoated Avicel PH105 (1% silica, 40 comilling cycles) is inferior to the uncoated powder. We attribute this reduction in tabletability on nanocoating to the reduced bonding areas between microcrystalline cellulose (MCC) particles, since bonding strength between MCC and silica is expected to be much lower compared to MCC-MCC particles. The bonding between silica particles is negligible because they do not undergo appreciable amount of plastic deformation during compaction, so that tabletability of silica is essentially zero.[27] Despite the

reduction, the tabletability of nanocoated Avicel PH105 is still superior to that of Avicel PH102. Importantly, the nanocoated Avicel PH105 exhibits good flow behavior and is readily filled into the die from a hopper without any problem.

4.4.6. SEM studies on coated particles

After comilling, the discrete nanoparticle coating can be easily discerned on the surfaces of the Avicel PH105 particles using SEM (Figure 4.7). We have identified these nanoparticles as silica by analyzing the EDS spectra of the coated particles (Figure 4.8). When these nanoparticles are surveyed by SEM-EDS analysis, a peak corresponding to silicon (Si) is always present in the resulting spectra. When the nanoparticles are not included, the silicon peak is always absent. A few clusters of silica particles can be observed in the SEM pictures. The presence of some silica clusters is expected because of the cohesive nature of nanoparticles, which tend to agglomerate.

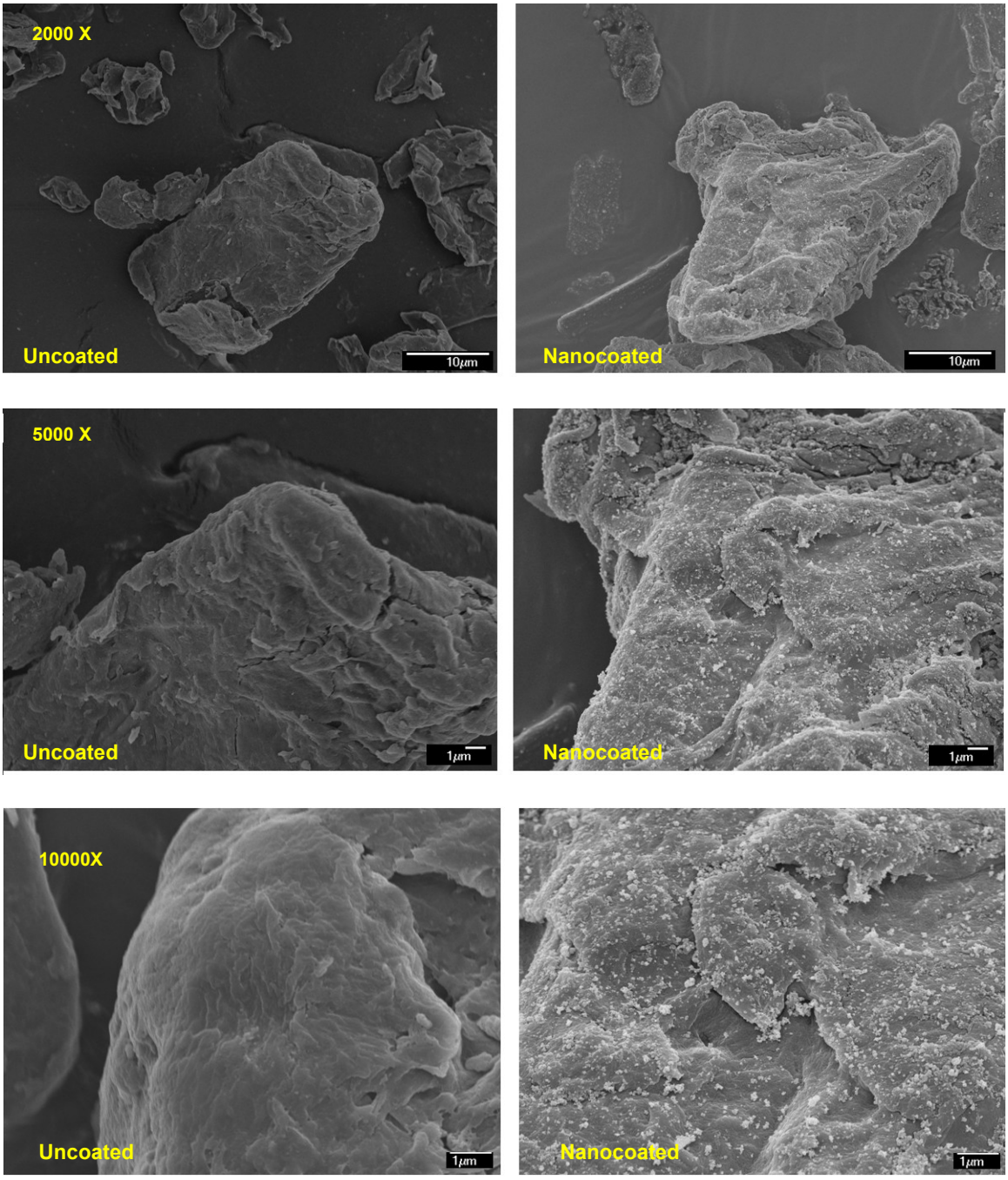

Figure 4.7. SEM images of Avicel PH105 uncoated (left) and coated (right) with 1.0% silica loading at 40 comilling cycles at different magnifications.

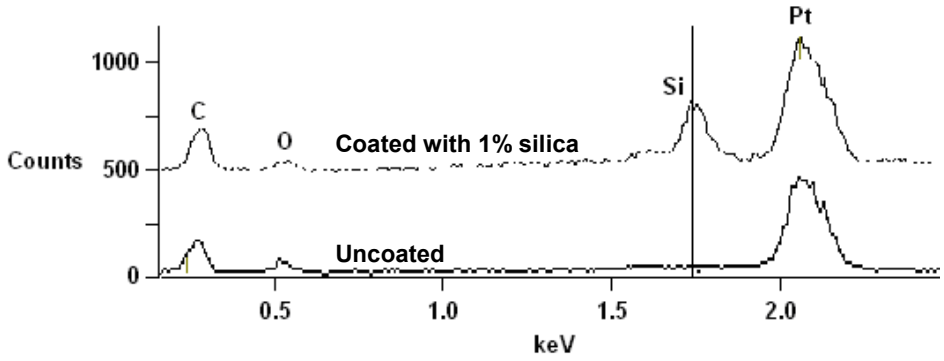

Figure 4.8. Energy dispersive spectra (EDS) of uncoated and 1.0% silica nanocoated Avicel PH105 (at 40 comilling cycles). The y-axis shows the counts of the number of photons received and processed by the EDS detector at different energy levels (x-axis).

4.4.7. Rationale for using comilling process and colloidal silica

Our results show that powder flow properties can be much improved through surface coating of cohesive cellulose with nanosized silica particles by comilling. There are several motivations for using the comilling process in this study: 1) no additional capital investment is necessary for adopting this flow improvement technique because comills are commonly available in pharmaceutical industries; 2) the comilling process provides mostly shear stress, which effectively de-agglomerates nano-sized guest particles and facilitate coating onto host particles. There is generally no significant temperature rise during comilling because of an absence of significant conversion of mechanical energy to heat through impact; 3) the comilling process is fast, continuous, and scalable. Hence, it can be readily adopted during both development and manufacturing of pharmaceutical products.

After showing that this simple, but elegant, process works, it is worth exploring why comilling has not been applied for improving powder flow before, when both the

problem of poor flow [1, 13, 14, 28, 29] and the comilling technique are prevalent in the recent decades. Traditionally, comilling has mainly been used to de-agglomerate powders for particle size reduction. Without a fundamental understanding of the physics of flow enhancement by nanocoating (described under the mechanism section), it is not intuitive to connect flow enhancement with the comilling process. Based on our understanding of materials science tetrahedron (MST),[30] performance related problems are tackled using the relationship between structure and property of a material. Thereafter, a suitable engineering process is developed to overcome the performance problems by modifying structure and, thus, the properties of the material. In essence, MST necessitates the seamless integration of materials science and engineering to tackle problems in material performance. In this work, the performance-related problem was poor powder flow properties. Based on the materials science portion of the problem in hand (*i.e.,* surface nanocoated particles lead to flow improvement of cohesive powders), we searched for an engineering strategy that would solve the performance problem of poor flow on an industrial scale without subjecting the powders to large impact stresses. Realizing the critical role of shear stress in nanocoating subsequently led us to identify the comilling process for achieving the desired goal.

4.5. CONCLUSIONS

We have shown that the simple, economical, and efficient comilling process can be successfully used to coat the surfaces of Avicel PH105 particles with nano-sized silica. Nanocoating results in profound improvement in the flow properties of the host powder without substantially compromising its tableting properties. Thus, it is expected to be an

excellent tool for enabling the direct compression process in tablet manufacturing. Comilling is fast and amenable to continuous operation, which makes this process attractive for ready implementation in manufacturing plants to address unmet challenges related to poor powder flow.

Chapter 5.

Assessing amorphization potential of crystals: Part 1. Concurrent influence of lattice strength and amorphous stability

From this chapter, we start our investigations on the involvement of structure-property relationships involved in solid-state amorphization of crystals under mechanical stress. The objective of this work is to develop a classification system for assessing the solid-state amorphization of crystalline pharmaceuticals based on their structural and thermodynamic properties. Amorphization of crystals is influenced both by crystal lattice strength (*LS*), which governs amorphous generation (crystal→amorphous), and amorphous stability (*AS*), which governs amorphous elimination (amorphous → crystalline). In this study, *LS* has been assessed by quantifying volume expansivity of single crystals by variable temperature single crystal-XRD, and lattice fusion enthalpy of bulk powders measured by DSC. *AS* is assessed using configurational entropy as a thermodynamic measure and activation energy of crystallization as a kinetic measure of stability. Four classes of materials have been distinguished based on *LS* and *AS*: I (high *LS*, low *AS*), II (low *LS*, low *AS*), III (high *LS*, high *AS*), and IV (low *LS*, high *AS*). Amorphous phase of classes I and II materials are highly unstable and tend to undergo fast recrystallization. Materials in these two classes, therefore, have low propensity to undergo processing-induced amorphization due to rapid amorphous elimination. On the contrary, materials in class IV are more suitable for amorphization, both due to weaker lattice favoring amorphous generation, and better amorphous stability than other classes. This knowledge of different amorphization classes of crystals is expected to facilitate the drug development process by an early identification of 1) the suitability of drugs for developing stable amorphous product, or 2) potential problems of unexpected processing-induced amorphization if the crystalline phase is used for development.

5.1 INTRODUCTION

Selection of an appropriate solid form of a drug is a critical step for developing a high quality drug product,[1, 2] which is characterized by optimum product properties, such as aqueous solubility and dissolution kinetics,[3] physical-chemical stability[4-6] and mechanical properties.[7, 8] Solids can either be crystalline or amorphous. Traditionally, crystalline phases have been preferred for drug development due to their superior thermodynamic stability, superior chemical stability, high chemical purity, and the ease of processability.[2, 5] Contrary to crystals, amorphous phase of a drug has higher free energy, which leads to the improved apparent solubility and dissolution kinetics of drugs.[9-12] This is an advantage in drug delivery because an increasing fraction of newer drugs are poorly soluble due to the recent emphasis on biological target-specific lipophilic drug molecules.[13, 14] Amorphous solids are characterized by the absence of three-dimensional long range molecular order and higher number of molecular configurations compared to crystals.[15-17] However, long range order along single dimensions is still possible in glasses.[18] Additionally, the more random molecular packing in amorphous solids can sometimes lead to improved chemical stability of drugs.[19] This happens when reactive functional moieties are proximally packed in the crystalline state, which lowers the chemical stability of crystals.[20, 21]

A key challenge with the selection of amorphous form for product development has been the tendency of amorphous to recrystallize during manufacturing or storage, which negates the solubility advantage conferred by the amorphous phase. Ideally, the suitability of the amorphous phase of a drug for development must be accurately

predicted *a priori* from its material properties that are readily accessible. If such an assessment is feasible, then an informed judgment can be made whether the crystalline or amorphous form of solid is preferred for further development. Drugs displaying higher amorphization potential will be superior candidates for developing amorphous products. Such drugs will, however, also be prone to processing-induced solid-state amorphization if the crystal form is selected for development,[22-24] which may lead to compromised product quality, such as variable dissolution, stability, and manufacturability.[25, 26]

Contrary to amorphous preparation routes that involve a liquid or vapor intermediate phase, solid-state amorphization of crystals, which involves a direct crystal to glass conversion,[27] is influenced both by (a) the ability of the starting crystal to resist the generation of disorder by mechanical stresses, and (b) the stability of the corresponding amorphous phase. Solid-state amorphization by mechanical activation [28] during milling has been observed for a large number of crystals, both pharmaceutical,[22, 24, 29, 30] and non-pharmaceutical.[31-33] Several theories have been proposed to explain the phenomenon of solid-state amorphization, including 1) the violation of the stability criterion of crystal lattice due to anharmonicity of lattice vibrations or phonons under mechanical stress,[34, 35] and 2) progressive generation of crystal dislocations leading to loss of crystalline order.[24, 36, 37] These theories, however, cannot be easily used to predict the amorphization potential of a candidate drug. From a more practical viewpoint for drug development, it is highly desirable to predict the amorphization propensity using easily accessible material properties. However, progress along this line has been limited, despite significant efforts in the recent years to correlate amorphization with properties of

crystals and glasses. For instance, T_g has shown some influence on amorphization,[29] especially in relation to milling temperature,[22] perhaps by affecting amorphous crystallization kinetics. However, this study will demonstrate that crystal amorphization can be more reliably predicted using more fundamental structural and thermodynamic properties of organic materials. Most of the earlier efforts have been limited to phenomenological approaches,[29] *i.e.,* they only considered whether or not amorphization had taken place after milling. A more quantitative approach to the phenomenon is clearly necessary to gain the insight needed for making reliable predictions.

According to the principles of Materials Science Tetrahedron (MST),[38] the performance of materials during processing is directly influenced by their structure and material properties. As such, it is a reasonable expectation that the phenomenon of crystal amorphization has its structural and molecular origins. The purpose of this work is to develop a classification system to readily assess the amorphization potential of crystals in the solid-state. This is achieved through a thorough understanding of the two factors that control crystal amorphization (Figure 5.1): a) crystal lattice strength (*LS*), which affects amorphization generation, and b) amorphous stability (*AS*), which affect elimination of any generated amorphous phase.

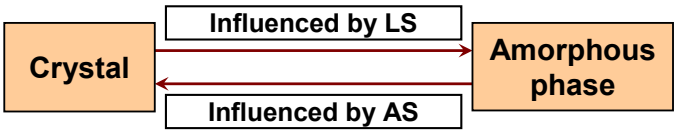

Figure 5.1. Schematic illustrating the concurrent effects of crystal lattice strength (*LS*) and amorphous stability (*AS*) on amorphous generation and elimination, respectively

A large set of structurally diverse model compounds have been used in this study to develop the classification. We have also adopted a material-sparing approach (<20mg) to predict amorphization, as the amounts of available materials are very limited during early stages of drug development. Such a generic classification of the amorphization potential of crystals is expected to facilitate the drug development process by an early identification of 1) potential problems of unexpected processing-induced amorphization, and 2) the suitability of drugs for developing stable amorphous forms.

5.2 MATERIALS AND METHODS

5.2.1 Materials

Amorphization propensity of a large number of structurally diverse model pharmaceutical crystals was investigated in this study. Acetaminophen, griseofulvin, hydrochlorothiazide, indomethacin, piroxicam, sulfacetamide, terfenadine, sulfamerazine, sulfisoxazole, sulfadiazine, sulfadoxin, sulfamethoxazole, aspirin, phenacetin, sulfanilamide, ibuprofen, and sucrose were commercially obtained from Sigma–Aldrich, Inc. (St. Louis, MO, USA). Felodipine, nifedipine and simvastatin were obtained from A.K. Scientific, Inc. (Union City, CA, USA). Danazol was purchased from Spectrum Pharmaceuticals, Inc. (Irvine, CA, USA). Ketoconazole was obtained from Hawkins, Inc. (Minneapolis, MN, USA). All crystalline materials were used for various studies without further purification. Table 5.1 summarizes some key molecular properties of different model compounds.

Table 5.1. Basic information on some relevant molecular properties of the model compounds. Data presented as mean ± one standard deviation of measurements (n = 3).

Compound	Molecular Weight M_w /g-mol^{-1}	Molar volume M_v/cc-mol^{-1} †	Melting point T_m /K	Melting enthalpy H_m/KJ-mol^{-1}	Glass transition T_g /K	ΔC_p at T_g J-g^{-1}K^{-1} ‡	Kinetic fragility T_g/T_m
Acetaminophen-I (ACM-I)	151.2	116.9	439.3±0.2	26.7±1.1	296.7±0.3	0.42±0.16	0.6754
Acetaminophen-II (ACM-II)	151.2	116.9	430.4±0.1	32.1±0.6	296.7±0.3	0.42±0.16	0.6895
Phenacetin (PHE)	179.2	146.3	405.9±0.2	19.7±1.1	-	-	-
Aspirin (ASP)	180.2	128.5	401.8±1.2	29.7±4.2	-	-	-
Sulfacetamide (SCT)	214.2	148.6	453.1±0.1	17.1±1.7	303.5±0.5	0.42±0.03	0.6698
Sulfadiazine (SDZ)	250.3	165.4	526.1±0.4	55.5±1.4	390.9±0.7	0.26±0.04	0.7430
Sulfamethoxazole (SMET)	253.3	171.4	439.5±0.3	38.8±2.1	302.8±0.9	0.38±0.08	0.6889
Sulfamerazine-I (SMZ-I)	264.3	196.2	505.4±0.2	40.4±1.1	334.1±2.4	0.43±0.04	0.6611
Sulfamerazine-II (SMZ-II)	264.3	184.8	483.7±0.8	27.9±2.8	334.1±2.4	0.43±0.04	0.6907
Sulfamethazine (SMT)	278.3	188.6	470.0±1.1	60.5±4.5	348.6±0.6	0.46±0.06	0.7417
Hydrochlorothiazide (HCT)	297.7	178.1	534.8±0.2	34.3±1.0	391.9±1.2	0.34±0.02	0.7362
Sulfadoxin (SDOX)	310.3	211.4	465.8±0.1	44.2±3.8	330.7±0.2	0.47±0.01	0.7097
β-piroxicam (PRX)	331.3	224.6	473.9±0.1	36.0±1.8	336.0±0.2	0.41±0.01	0.7091
Danazol (DNZ)	337.5	273.3	494.8±1.3	39.0±1.9	345.6±0.7	0.46±0.01	0.6984
Sucrose (SUC)	342.3	215.2	Decomp	-	347.2	0.54±0.02	-
Nifedipine (NFD)	346.3	251.3	443.1±0.5	40.6±4.1	318.9±0.2	0.36±0.02	0.7197
Griseofulvin (GRF)	352.8	240.7	493.4±0.1	39.2±0.7	363.9±0.8	0.37±0.04	0.7375
γ-Indomethacin (IMC)	357.8	260.8	433.2±0.6	39.1±3.5	318.9±1.0	0.37±0.05	0.7361
Felodipine (FLD)	384.3	264.9	411.5±0.2	30.6±0.7	319.7±0.2	0.30±0.03	0.7769
Terfenadine (TFD)	471.6	336.9	419.6±0.3	55.4±2.1	332.6±0.3	0.56±0.19	0.7927
Dipyridamole (DPD)	504.5	374.3	434.5±0.1	31.6±0.7	311.5±0.4	0.28±0.04	0.7169
Ketoconazole (KNZ)	531.4	379.6	419.4±0.3	57.4±1.7	317.6±0.4	0.46±0.06	0.7573

† Calculated based on single crystal X-ray density of crystals at room temperature (283-303K)

‡ Calculated using reversing C_p signal in DSC

5.2.2 Solid-state amorphization by cryomilling

Approximately 2g of crystalline powder for each material was cryomilled in a liquid nitrogen bath at ~77K (6750 Freezer Mill, SPEX CertiPrep, Metuchen, NJ) for up to 2 hours, with intermittent sample withdrawal at both short (10 min) and long (>30 min) milling times. Samples were milled under the impact of a magnetically-driven cylindrical stainless-steel milling bar on to two stainless-steel lids of a polycarbonate tube containing the samples. After the sample was loaded and prior to milling, the milling assembly was pre-cooled at liquid nitrogen temperature (~77K) for 2 minutes. Milling was conducted at a rate of 10 impacts per second. A 2 min cooling period was employed after each 2min of milling. Cryomilled samples were withdrawn inside a glove box purged with dry nitrogen and stored in desiccator containing anhydrous calcium sulfate (Dreirite®, W.A. Hammond Dreirite Co. Ltd., OH). Freshly milled samples were characterized typically within 5-10 minutes after sample withdrawal. Water content of milled samples was <0.5 wt% up to 100 ^{o}C by thermogravimetric analysis (TGA Q500, TA Instruments, New Castle, DE).

5.2.3 Characterization of milled samples

***Thermal* studies:** The milled samples were studied using Differential Scanning Calorimetry (DSC Q1000 and Q2000, TA Instruments, New Castle, DE) to assess their crystallinity after milling. Universal Analysis (Version 4.1D, TA Instruments) was used for DSC data analysis. The baseline of DSC was calibrated using empty cell, followed by sapphire discs. Temperature and enthalpy calibrations were done using high purity indium (standard mode, ramp rate of 10 K/min). The DSC cell was purged with nitrogen

at a rate of 50 mL/min. Hermetically sealed aluminum pans without pinholes were used for all studies. To enhance thermal contact with samples, aluminum pans were hermetically sealed by crimping the pan lids upside down to minimize headspace within the sealed pans. For standard DSC runs, a ramp rate of 10K/min was used. For temperature-modulated DSC (MDSC), a sinusoidal modulation of ±1K was employed every 100 seconds, with a ramp rate of 2K/min. For DSC runs, average sample weight was approximately 4 – 8 mg. Glass transition temperatures (T_g) are reported as the mid-points of the glass transition events determined from the reversing heat capacity (rev C_p) signal. Crystallization and melting temperatures are the extrapolated onset temperatures of the corresponding thermal events. Enthalpies of crystallization and fusion events were obtained by integrating the peaks using sigmoidal baseline.

Powder X-ray diffraction studies: A powder X-ray diffractometer (D8 Advance, Bruker AXS, Madison, WI) with CuK_α radiation and scintillation counter detector was used to examine changes in crystallinity of the samples after milling. The diffractometer was calibrated using corundum standard (SRM 674b, NIST) at d = 2.0852Å. Diffraction data were collected over 5 - 35º 2θ with step size of 0.05º and dwell time of 1s. Milled samples were packed into the sample holder without further treatment. Melt-quenched glasses were mildly ground using mortar and pestle before being packed for PXRD studies. All samples were packed into the sample holder by top filling method. PXRD data were collected using the Diffrac Plus XRD commander software (Bruker, AXS). Data analysis was performed using JADE (version 8, Materials Data Inc., Livermore, CA).

5.2.4 Quantification of amorphous content

Amorphous content can be quantified by several analytical techniques, such as calorimetry, powder X-ray diffractometry, molecular spectroscopy, and moisture sorption.[39] Although solution calorimetry or moisture sorption can potentially have superior limits of quantitation for amorphous, they are not suitable for rapid routine amorphous quantitation because they require either special sample preparation or are time intensive. We adopted the DSC method in this study for amorphous quantitation because of the large number of samples that needed to be analyzed, due to several compounds each with multiple milling time points. An advantage of DSC method is that quantification on freshly milled samples can be performed with no sample exposure to the ambient environment with minimal sample preparation requirements (samples crimped in humidity controlled glove box). The amorphous content (φ) of the milled samples was quantified using the enthalpies of crystallization (H_c) and melting (H_m) measured using DSC in non-isothermal mode (10K/min). H_m was corrected for the difference over the temperatures between crystallization and fusion (equation 1).

$$\varphi = \frac{H_m - \Delta C_p^{\ell - c} \times (T_m - T_c)}{H_c} \qquad (1)$$

In this expression, $\Delta C_p^{l\text{-}c}$ is the difference in heat capacities between the liquid and crystalline phases. The corrected H_m is the total enthalpy required to "melt" the crystal at the temperature of crystallization, which is equal to the heat of crystallization for a pure

amorphous phase. This heat capacity correction is necessary to account for the thermal dependence of enthalpy of a material.

Amorphization potential of crystals was quantified using their rate constants (k_a) of solid-state amorphization during a given milling duration (t), which was calculated using equation 2. This treatment is based on the observation that amorphization generally follows first-order kinetics of transformation.[31, 40]

$$k_a = \frac{-\ln(1-\varphi)}{t} \qquad (2)$$

5.2.5 Heat capacity measurements

Heat capacity at constant pressure (C_p) was measured using modulated differential scanning calorimetry (Q1000, TA Instruments, New Castle, DE) equipped with a refrigerated cooling system. DSC heat capacity was calibrated using crystalline sucrose, where the heat capacity constants (ratio of theoretical to actual C_p) were 0.988 for the direct signal and 1.049 for the reversing signal (acceptable C_p constant range: 0.9 - 1.1). Several factors can lead to erroneous heat capacity measurements even when the calorimeter is properly calibrated, such as sample size, thermal contact, type and flow rate of purge gas, pan crimping, moisture, and amplitude and frequency of modulation employed.[41] A low purge flow rate of nitrogen (~5 mL/min) was used to improve the accuracy of heat capacity measurements by minimizing thermal fluctuations. With helium as purging medium, the purge flow rate can be further reduced to ~1mL/min. A sinusoidal modulation of ±1K was employed every 100 seconds, with a ramp rate of

2K/min. Sample weights for heat capacity measurements were on average ~15 mg. To maximize thermal contact of the sample, powders were mildly pressed into thin compacts to fit inside the bottom of DSC pans. Extra care was taken during sample packing to ensure that samples covered only the bottom of the aluminum DSC pans, with no sample residues sticking to the sides of the pans. Hermetically sealed aluminum pans with pinholes were used. Samples were first isothermally held at 110°C for 10 min to eliminate residual moisture before commencing with the heat capacity measurements for 100% crystalline drugs.

5.2.6 Estimation of lattice strength of crystals

Lattice strength of crystal was quantified by measuring volume expansivity of crystals[42] of different materials using variable temperature-single crystal X-ray diffractometry (VT-SXRD). Expansivity, V_T, defined as the relative thermal dilation in a crystal at the ambient pressure, is mathematically expressed in equation 3.[42]

$$V_T = \left(\frac{\delta V / V}{\delta T} \right)_p \qquad (3)$$

In the literature, crystal lattice strength has often been characterized using parameters such as lattice energy calculated by computational modeling of crystal structure,[43] or hydrogen bond strength calculations using molecular spectroscopy, which are, at best, indirect evidence of the actual lattice strength of crystals.[44, 45] However, VT-SXRD is advantageous as it directly probes lattice strength (through expansivity) as function of

temperature and provides a wealth of structural information on the packing strength of crystals at a molecular level. VT-SXRD data were collected over 123-298 K temperature range using Bruker SMART diffractometer (Bruker AXS, operated at 40 kV and 50 mA) equipped with an APEX II CCD detector. A Mo-K_α radiation source was employed (0.71073 Å) for X-rays and the radiations filtered with a graphite monochromator. For collecting diffraction data, a single crystal was glued to the goniometer glass fiber tip using epoxy adhesive. Data were collected between $5^\circ \leq 2\theta \leq 75^\circ$ using ω and ϕ scans with 0.5° scan width. Beam exposure times varied between 5 to 30 s depending on the nature and quality of crystals. To eliminate variations in diffraction data due to different crystal quality, the same crystal was used for each material at all temperatures. Temperature was controlled with a temperature controller (Cryostream Controller 600, Oxford) fitted with CFT-25 refrigerated recirculator (set at 9 psig) to deliver liquid nitrogen. After the data collection at a temperature was completed, the temperature was increased at a ramp rate of 6 K/min to the next higher target temperature and held at the target temperature for 10-15 minutes before data acquisition to ensure thermal equilibrium of the molecules.

5.2.7 Configurational amorphous stability

Thermodynamic stability of amorphous phase, prepared by *in situ* melt-quenching in DSC, for each compound was assessed using the configurational entropy using heat capacity ($C_{p,conf}$) as a function of temperature. $C_{p,conf}$ is defined as the difference in the measured heat capacities between the amorphous and the crystalline phases (equation 4). Figure 5.2A shows a representative plot of the difference of heat capacities of crystalline

and amorphous solid for griseofulvin. The corresponding $C_{p,conf}$ in the vicinity of the glass transition is plotted in Figure 5.2B.

$$C_{p\ conf} = C_{p\ amorphous} - C_{p\ crystal} \qquad (4)$$

The configurational entropy of crystallization, *i.e.,* the entropy difference between the amorphous and the crystal (ΔS_{conf}) was then computed by integrating the $C_{p,conf}$ over a range of temperature of interest (Origin 8.6) and using fusion enthalpy, ΔH_{melt} of each material (equation 5).

$$\Delta S_{conf} = \Delta S_{melt} + \int_{T_m}^{298\ K} \frac{C_{p\ conf}}{T}\, dT = \frac{\Delta H_{melt}}{T_{melt}} + \int_{T_m}^{298\ K} \frac{C_{p\ conf}}{T}\, dT \qquad (5)$$

For sucrose, because of the decomposition on fusion, melt-quenching was not feasible. So, freeze dried amorphous sucrose was used to measure the configurational entropy. ΔS_{conf} was compared for different materials at room temperature (298K), which is the temperature of interest concerning amorphous stability in this work. For materials that crystallized during melt-quenching, configurational entropy was calculated by extrapolating the heat capacity of the liquidus phase prior to crystallization, and calculating the configurational parameters between extrapolated liquid and crystal (Figure 5.2C).

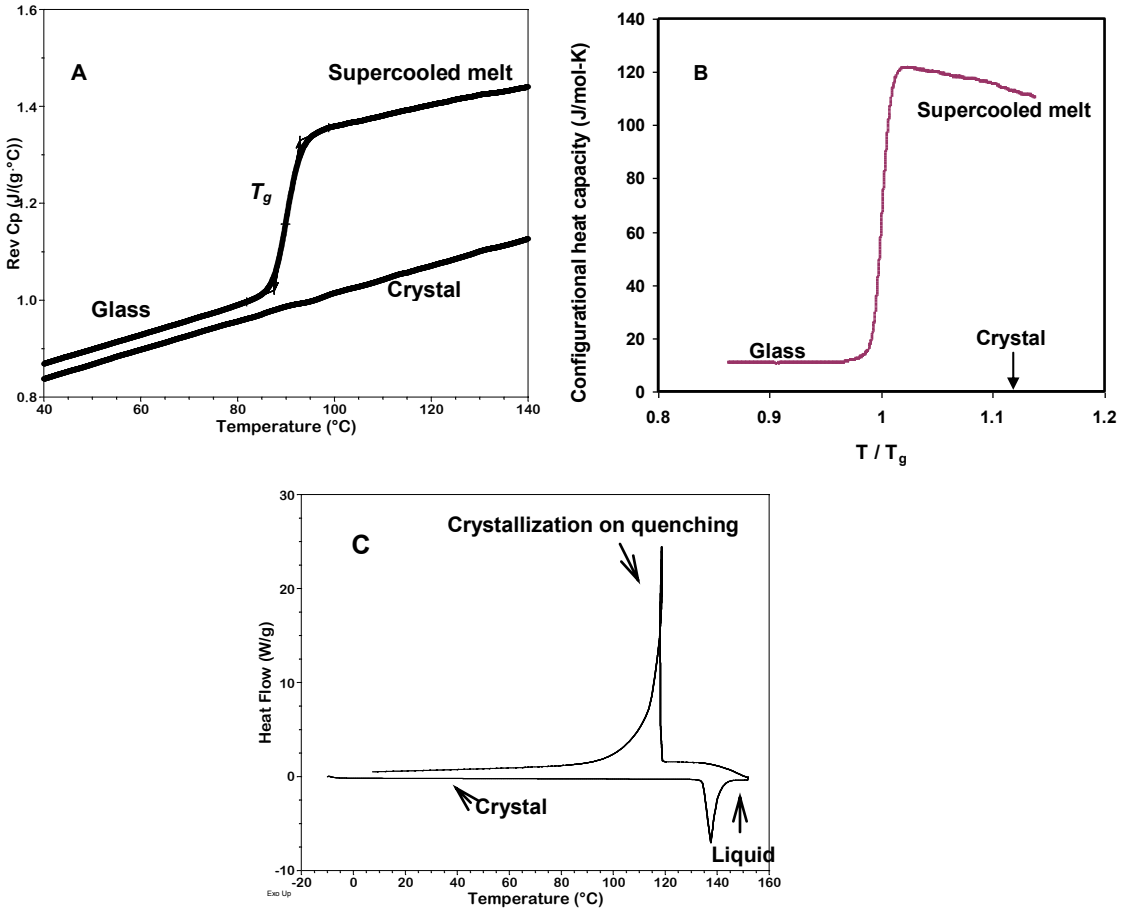

Figure 5.2. Various quenching behaviors of melts *in situ* in differential scanning calorimeter: (A) Heat capacities of crystalline and amorphous griseofulvin, (B) configurational heat capacity in the vicinity of T_g of griseofulvin; and (C) crystallization during melt-quenching of phenacetin using the 'jump' function in DS Q2000.

5.2.8 Crystallization activation energy of glass

Activation energy of non-isothermal crystallization (in DSC) of melt-quenched glass was quantified by fitting Avrami-Erofeev model[46-48] of the third order to a modified Coats-Redfern equation[49, 50] (equation 6).

$$\ln \beta . g(\alpha) = \ln \left[\frac{A R T^2}{E_a} \left\{ 1 - \left(\frac{2 R T}{E_a} \right) \right\} \right] - \frac{E_a}{R T} \qquad (6)$$

In this expression, β is the linear heating rate, $g(\alpha)$ is the crystallization model in the integral from, E_a is the activation energy, A is frequency factor of Arrhenius equation, R is the gas constant, and T is the temperature in Kelvin. Activation energy was obtained from the slope of the linear plot between $\ln \beta g(\alpha$ and $\frac{1}{T}$. Avrami-Erofeev model of the third order was found to provide the best statistical fit to the crystallization data between 25 - 75% of conversion, consistent with previous literature.[51] At very low and high extents of crystallization, the fit deviated from linearity and data from these portions were not used for calculating E_a by model-fitting.

5.2.9 Statistical modeling

Statistical analysis of data and development of regression models for amorphization prediction were performed using Arc statistical software (v1.06, Department of Statistics, University of Minnesota, 2004). Further details are provided in the Appendix I.

5.3 RESULTS AND DISCUSSIONS

5.3.1 Amorphization behaviors of crystals

The amorphization potential of the crystalline materials is summarized in Table 5.2. Some materials are resistant to amorphization under mechanical stress during cryomilling. No detectable amorphous content is observed in these cryomilled crystals, either by DSC and PXRD, up to two hours of cryomilling. Acetaminophen polymorph I

is a good example of this kind of behavior. The non-isothermal DSC profiles of cryomilled acetaminophen are shown in Figure 5.3A. No glass transition or crystallization event is observed when the cryomilled samples are heated, indicating that the samples are crystalline after milling. PXRD also shows no evidence of detectable amorphous phase or formation of a different crystalline phase in the milled samples (Figure 5.3B). Therefore, this crystal is either intrinsically resistant to amorphization by milling or its amorphous phase crystallizes extremely quickly after sample withdrawal from cryomill. The latter mechanism is confirmed by data that will be discussed in a subsequent section.

Table 5.2. Amorphization behaviors of model crystals. Data presented as mean ± one standard deviation of measurements (n = 3).

Compound	Amorphized up to 2 hrs of cryomilling		Amorphous content after 2 hr cryomilling φ (%)	Post-onset amorphization rate constant k_a (min^{-1})
	DSC	PXRD		
Acetaminophen-I (ACM-I)	No	No	0	0.00
Acetaminophen-II (ACM-II)	No	No	0	0.00
Phenacetin (PHE)	No	No	0	0.00
Aspirin (ASP)	No	No	0	0.00
Sulfacetamide (SCT)	No	No	0	0.00
Sulfadiazine (SDZ)	No	No	0	0.00
Sulfamethoxazole (SMET)	No	No	0	0.00
Sulfamerazine-I (SMZ-I)	Yes	Yes	79.58 ± 4.98	0.0103 ± 0.002
Sulfamerazine-II (SMZ-II)	No	No	0	0.00
Sulfamethazine (SMT)	Yes	Yes	73.47 ± 4.36	0.0100 ± 0.002
Hydrochlorothiazide (HCT)	Yes	Yes	73.85 ± 5.61	0.0124 ± 0.001
Sulfadoxin (SDOX)	Yes	Yes	61.74 ± 4.56	0.0081 ± 0.003
β-piroxicam (PRX)	Yes	Yes	54.54 ± 5.12	0.0073 ± 0.001
Danazol (DNZ)	Yes	Yes	61.11 ± 9.13	0.0086 ± 0.002
Sucrose (SUC)	Yes	Yes	63.24 ± 4.21	0.0080 ± 0.005
Nifedipine (NFD)	Yes	Yes	49.23 ± 3.03	0.0068 ± 0.001
Griseofulvin (GRF)	Yes	Yes	79.65 ± 4.51	0.0100 ± 0.001
γ-Indomethacin (IMC)	Yes	Yes	72.36 ± 2.54	0.0137 ± 0.003
Felodipine (FLD)	Yes	Yes	69.52 ± 2.47	0.0110 ± 0.001
Terfenadine (TFD)	Yes	Yes	98.63 ± 3.31	0.0379 ± 0.012
Dipyridamole (DPD)	Yes	Yes	88.68 ± 7.45	0.0184 ± 0.002
Ketoconazole (KNZ)	Yes	Yes	80.21 ± 4.60	0.0098 ± 0.001

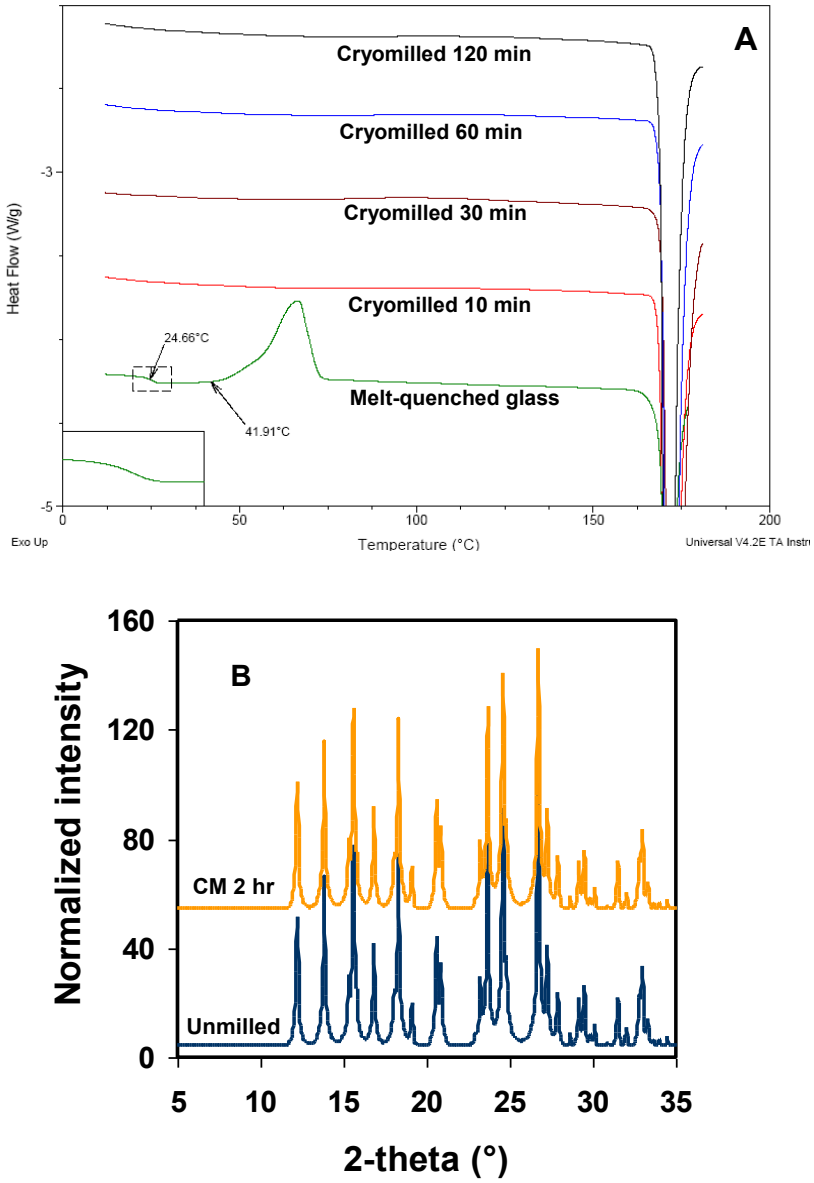

Figure 5.3. (A) DSC (standard, 10K/min) and (B) Powder XRD profiles of cryomilled (CM) acetaminophen (polymorph I). While the melt-quenched sample is clearly amorphous, showing amorphous signatures such as T_g and crystallization exotherm, the milled samples stay crystalline till 2 hours of cryomilling.

An analysis of amorphous conversion data (Table 5.2) suggests that up to 2 hours of cryomilling led to partial amorphization of the crystals in many cases. This kind of

behavior is illustrated by γ-indomethacin. The DSC profiles of milled indomethacin are shown in Figure 5.4A. Ramping up the milled samples produces T_g at ~ 44°C (from rev C_p), followed by crystallization, both events indicating the presence of amorphous domains in the milled samples. The crystallization onset is depressed compared to melt-quenched glass, due to the presence of residual γ–indomethacin nuclei in milled samples (PXRD, Figure 5.4B). The residual γ–polymorph nuclei also facilitate preferential crystallization of milled samples into the γ–polymorph, while melt-quenched glass crystallizes into a mixture of α (melting point of ~151ºC) and γ–polymorphs (melting point ~161ºC). Similar effects on crystallization by seed nuclei have been observed for all model systems that amorphized on applying mechanical stress.[23]

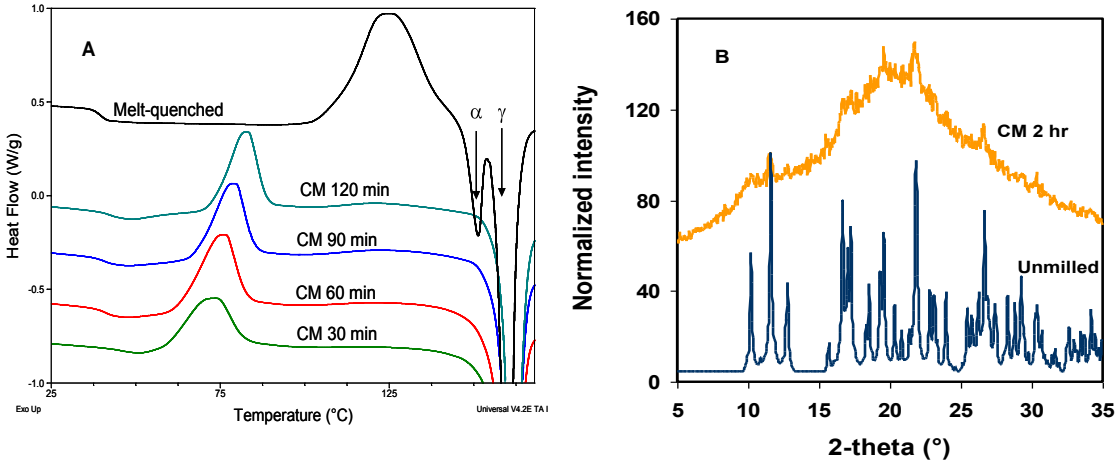

Figure 5.4. (A) DSC (standard, 10K/min) and (B) PXRD profiles of cryomilled (CM) indomethacin (polymorph γ). Cryomilling leads to amorphization in this case, even though amorphization is not complete as crystalline peaks are still visible.

The time course of solid-state amorphous transformation can be described by first order kinetics as shown by the representative plot in Figure 5.5 for felodipine. This is consistent with previous observations on non-pharmaceutical crystals,[31, 40] which agrees with the assumption that two events, amorphous generation and elimination through crystallization, are involved in the bulk amorphization by milling. Compounds differ in their onset times for amorphization. For instance, felodipine, the first evidence of amorphization is observed after 10 min of milling, which is taken as the onset time of amorphization under cryomilling conditions. The first order rate constants for amorphization beyond the onset (k_a) are summarized in Table 5.2, along with the extent amorphized in 2 hours of cryomilling, calculated using equation 1.

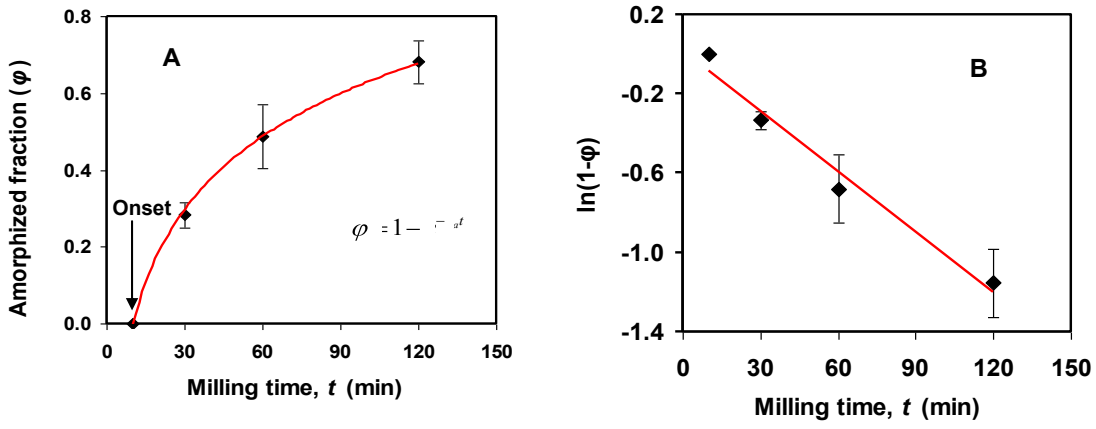

Figure 5.5. An illustration of sample amorphization kinetics for the model drug felodipine. In this crystal, amorphization is first observed after 10 min of cryomilling. Post onset, solid-state amorphization follows first-order kinetics of transformation with amorphization rate constant k_a. Data are presented as mean ± one standard deviation of DSC measurements (n = 3).

5.3.2 Identification of amorphization correlators

The wide differences in the amorphization behaviors observed for the model compounds under identical milling conditions raises the fundamental question as to what factor(s) lead to such differences. As a starting point, we screened for the influence of several fundamental molecular factors on the amorphization propensity of materials using linear regression analysis. The factors tested related to two broad categories: (a) crystal lattice strength, including volume expansivity, fusion enthalpy, melting point, and molar volume; and (b) amorphous stability, including configurational entropy, T_g, and kinetic fragility of glass. Using statistical regression modeling following the process of forward parameter selection[52] (see Appendix I), volume expansivity, configurational entropy and molecular weight were identified as particularly influential in the amorphization process. The final predictive regression model for amorphization rate constant (k_a, min^{-1}) is given by equation 7.

$$k_a = (5.3\times 10^{-1}).\Delta S_c + (2.7\times 10^{-2}).V_T + (2.8\times 10^{-3}).M_w - 0.01; \quad F = 10.9,\ p = 0.001 \quad (7)$$

In this expression, ΔS_c is configurational entropy (J/mol-K), V_T is volume expansivity ($\times 10^{-6}$ K^{-1}) and M_w is molecular weight (g/mol). The large F and $p < 0.05$ at 95% confidence level indicates a statistically significant model. The influence of volume expansivity and configurational entropy on amorphization potential of materials indicates that mechanical amorphization is influenced by both the lattice strength of the crystal and the stability of the generated amorphous phase. These effects will be discussed in detail in this chapter, while the role of molecular weight will be discussed in Chapter 6.

5.3.3 Concurrent influence of crystal lattice strength and amorphous stability

The ability of materials to form stable amorphous phase has often been analyzed in terms of their glass forming ability (GFA) and amorphous stability (AS).[53-55] GFA is normally assessed by quantifying the critical cooling rate from liquid required to avoid nucleation and initiate vitrification.[56, 57] However, for solid-state amorphization that avoids the liquid intermediate, GFA is essentially determined by the crystal lattice strength (*LS*). Stronger crystal lattice will resist amorphization, while weaker lattices will favor amorphization. Volume expansivity is used in this work as a measure of *LS*, and therefore quantifies the *GFA* of materials. A higher expansivity corresponds to weaker lattice and presumably a higher *GFA*. In general, we observe that materials with higher expansivity (>150 × 10^{-6} K^{-1}) tend to amorphize more readily under mechanical stress (Table 5.3). However, there are exceptions. Sucrose has a low expansivity owing to a dense three-dimensional hydrogen bonded molecular packing, but still amorphizes when milled beyond 30 min under cryogenic conditions. We, however, have not observed amorphous generation in sucrose at shorter milling times (<10 min). Phenacetin and aspirin also are exceptions. They have high expansivity (weak lattice) but do not show amorphous conversion after milling.

These exceptions are not unexpected. As evident based on the linear regression model, amorphization is a multi-factorial problem and no single predictor is sufficient to describe the process fully across all compounds. It is also necessary to consider the other critical factor in this transformation, *i.e.,* the amorphous elimination step that is controlled by amorphous stability. Amorphous stability has been characterized by

several parameters in the literature,[58, 59] such as thermodynamic configurational parameters,[60, 61] molecular mobility[58] and activation energy of crystallization.[62] While all these parameters have their own merits, in this work we probed the fundamental thermodynamic barrier to crystallization from glass, which is governed by the configurational flexibility of the molecules in the disordered phase, *i.e.,* their configurational entropy (Table 5.3). Molecules with higher configurational entropy have a larger number of possible configurations in the disordered phase, which has been speculated to lead to greater difficulty for the amorphous phase to crystallize.[60] However, such a correlation between configurational parameters and ease of crystallization has not yet been established for a large set of compounds. Figure 5.6 shows the correlation between configurational entropy and activation energy of crystallization. Since higher activation energy corresponds to a higher kinetic barrier to crystallization, this plot shows that higher entropy does correspond to slower crystallization, as previously speculated.

Going back to the case studies on sucrose, phenacetin, and aspirin that were exceptions in the volume expansivity rank order, their amorphization behaviors can be well explained when we consider the amorphous stability aspect. Sucrose has a large configurational entropy (Table 5.3) and high activation energy of crystallization, which indicates that any amorphous phase generated by milling is kinetically stable. Therefore, even though it resists amorphization at short milling duration, longer cryomilling duration (>30min) eventually produces detectable amorphous phase. Phenacetin and aspirin on the contrary have low configurational entropy and crystallize fast. Therefore, despite

having weak crystal lattice that can readily be disrupted, their amorphous phase crystallizes rapidly during sample withdrawal. This interaction effect between the lattice strength and amorphous stability on the amorphization process is clearly demonstrated by the amorphization behaviors of these apparent exception cases. Amorphization occurs most easily for materials having simultaneously high expansivity (weak lattice) and high configurational entropy (slow recrystallization). Terfenadine is an example of such a material that undergoes almost 100% amorphous conversion after 2 hr cryomilling.

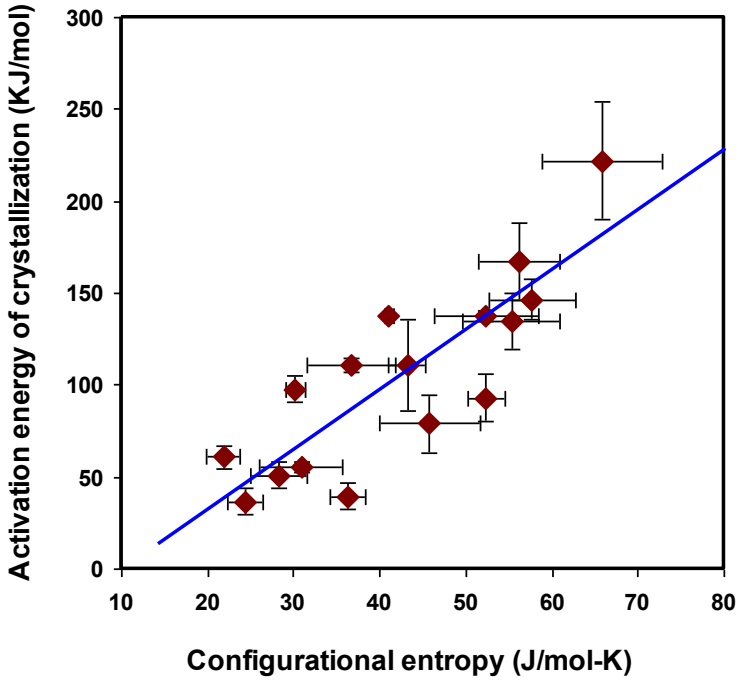

Figure 5.6. Correlation between configurational entropy and activation energy of crystallization measured by the model fitting of non-isothermal crystallization data to Avrami-Erofeev kinetic model. Molecules with higher configurational entropy, *i.e.* those with more number of configurations in the disordered phase, have lower recrystallization tendency, indicated by higher activation energy barrier to crystallization. Data are presented as mean ± one standard deviation of DSC measurements (n = 3). Correlation equation: $E_a = 0.43 \times \Delta S_{conf} - 5.6;\ R^2 = 0.75$

5.3.4 Amorphization Classification System (ACS) maps

Based on the understanding of the dual influential factors on amorphization of crystals, an Amorphization Classification System (ACS) can be constructed for solid-state amorphization by cryomilling. Figure 5.7 shows an illustration of one such quantitative map plotted using expansivity on Y axis (*i.e.,* lattice strength) and configurational entropy on X axis (*i.e.,* amorphous stability). The map is divided into four regions: I (high *LS*, low *AS*), II (low *LS*, low *AS*), III (high *LS*, high *AS*), and IV (low *LS*, high *AS*). The location of various model compounds in this study is also marked on this map (also indicated in Table 5.3). Classes I and II materials will be better for developing their crystalline solid form because of their lack of amorphization tendency, attributed to fast recrystallization. Class IV materials will likely be the well suited for amorphous preparation. Figure 5.8 shows a generic version of the map indicating various classes and decision arrows to guide solid form selection in terms of phase stability.

The delineation between different classes is based on the criterion described with Table 3. This criterion has been developed based on the experimental observations of the milling-induced amorphization behaviors of different compounds by DSC and PXRD studies. Materials with lattice expansivity $>150 \times 10^{-6}$ K^{-1} and configurational entropy >25 J $mol^{-1}K^{-1}$ always formed stable amorphous by 2 hr cryomilling. These materials are clubbed together in Class IV, which will likely be the best suited to develop stable amorphous phase.

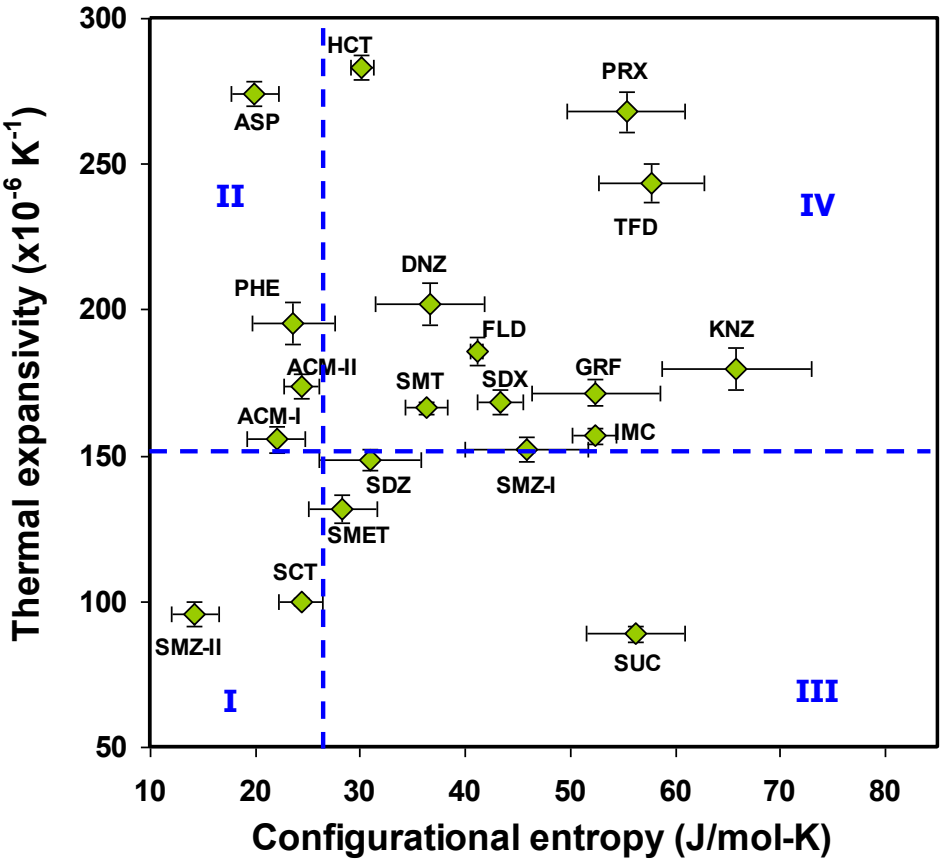

Figure 5.7. Quantitative map for Amorphization Classification System (ACS) showing the spatial distribution of various molecules in this study. Data are presented as mean ± one standard deviation of measurements (n = 3).

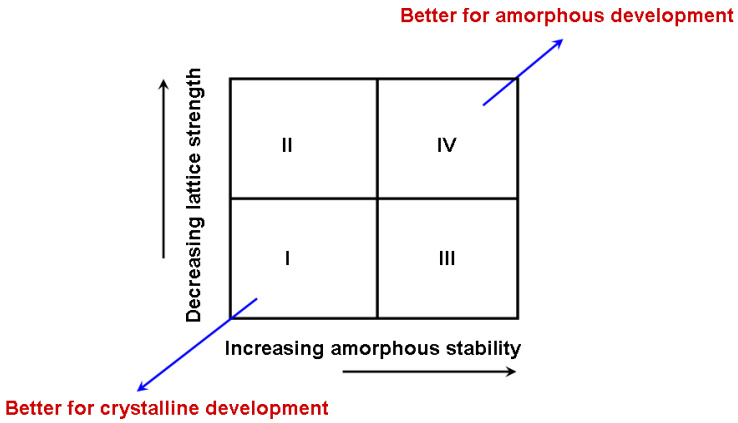

Figure 5.8. Generic map for Amorphization Classification System (ACS) plotted considering crystal lattice strength (Y axis) against amorphous stability (X axis). Predicted order for solid-state amorphization potential is IV >> III >> II > I.

Table 5.3. Volume expansivity, configurational entropy and amorphization classification of model compounds. Both expansivity and configurational entropy are calculated at 298K. Data presented as mean ± one standard deviation of measurements (n = 3).

Compound	Volume expansivity, V_T	Configurational entropy, S_c	Amorphization Class
	x10^{-6} (K^{-1}) at 25°C	(J mol^{-1} K^{-1}) at 25°C	
Acetaminophen-I (ACM-I)	150.54 ± 4.36	21.9 ± 2.7	II
Acetaminophen-II (ACM-II)	173.67 ± 4.29	24.3 ± 1.7	II
Phenacetin (PHE)	195.44 ± 7.42	23.6 ± 3.9	II
Aspirin (ASP)	274.09 ± 4.41	19.9 ± 2.3	II
Sulfacetamide (SCT)	100.13 ± 1.21	24.3 ± 2.1	I
Sulfadiazine (SDZ)	131.85 ± 4.63	28.3 ± 3.2	III
Sulfamethoxazole (SMET)	148.55 ± 3.71	30.9 ± 4.8	III
Sulfamerazine-II (SMZ-II)	95.66 ± 4.24	14.3 ± 2.2	I
Sulfamerazine-I (SMZ-I)	152.09 ± 4.18	45.8 ± 5.8	IV
Sulfamethazine (SMT)	166.40 ± 2.01	36.3 ± 2.0	IV
Hydrochlorothiazide (HCT)	283.16 ± 3.96	30.2 ± 1.1	IV
Sulfadoxin (SDOX)	168.32 ± 4.04	43.2 ± 2.2	IV
β-piroxicam (PRX)	267.89 ± 6.86	55.3 ± 5.7	IV
Danazol (DNZ)	202.07 ± 7.36	36.7 ± 5.2	IV
Sucrose (SUC)	88.91 ± 2.61	56.2 ± 4.7	III
Nifedipine (NFD)	166.99 ± 5.84	37.3 ± 3.1	IV
Griseofulvin (GRF)	171.62 ± 4.69	52.4 ± 6.1	IV
γ-indomethacin (IMC)	156.78 ± 2.88	52.3 ± 2.1	IV
Felodipine (FLD)	186.05 ± 4.76	41.0 ± 0.6	IV
Terfenadine (TFD)	243.36 ± 6.69	57.7 ± 5.1	IV
Dipyridamole (DPD)	113.36 ± 3.36	50.4 ± 2.4	III
Ketoconazole (KNZ)	179.87 ± 7.36	65.8 ± 7.1	IV
Classification criterion:	I -	V_T <150×10^{-6} K^{-1}, S_c <25 J mol^{-1} K^{-1}	
	II -	V_T >150×10^{-6} K^{-1}, S_c <25 J mol^{-1} K^{-1}	
	III -	V_T <150×10^{-6} K^{-1}, S_c >25 J mol^{-1} K^{-1}	
	IV -	V_T >150×10^{-6} K^{-1}, S_c >25 J mol^{-1} K^{-1}	

5.3.5 Differentiating Class I and II materials by milling in presence of a polymer

The lack of amorphization in classes I and II, up to 2 hours of cryomilling, may be for two possible reasons: a) either amorphous is not generated at all, or b) any generated amorphous phase is eliminated by rapid crystallization. The difference between Class I and II crystals, however, is in the strength of crystal lattice, while materials in both these classes have low amorphous stability and fast recrystallization tendency (illustrated by

their lower configurational entropy and lower activation energy of crystallization). Class II crystals have weaker lattice, as demonstrated by significantly higher volume expansivity than Class I crystals. Therefore, the two classes can be distinguished if recrystallization of generated amorphous phase in Class II is delayed. This can be probed by co-cryomilling class II crystals in presence of a crystallization inhibitors (polymer).

To test this, two representative drug candidates were selected, one from each class, (acetaminophen-I, a class II crystal) and (sulfamerazine-II, a class I crystal). A polymer (polyvinylpyrrolidone vinyl acetate, Kollidon®) film was initially prepared with supersaturated drug loading (~97.5 wt%) by film casting method from methanol. The films were initially dried at 60°C in a tray oven for 2 h, followed by vacuum drying for 1 h, and then equilibrated in a humidity controlled glove box purged with dry nitrogen. The polymer film was then mixed with acetaminophen crystals and milled. The intentional supersaturation of films with drug crystals at room temperature (verified by birefringence in polarized light microscopy) eliminates the possibility of the dissolution of acetaminophen into the polymer during cryomilling.[63] Therefore, any amorphization of acetaminophen crystal is due to the milling.

Figure 5.9 shows the powder XRD results of the drug-polymer co-cryomilling experiments. Unmilled drug-polymer film composite appears crystalline and the halo of the amorphous polymer is barely observable. On cryomilling the drug-polymer composite, we clearly observe amorphization of the drug crystals in case of acetaminophen-I only, while sulfamerazine-II sample shows no sign of amorphization

during co-cryomilling. This suggests that the observed lack of milling-induced amorphization for pure aceteminophen (class II) is due to fast recrystallization, while for sulfamerazine-II (class I) is due to the lack of amorphous generation due to strong lattice. Longer milling may help to commence the amorphization process of sulfamerazine-II (or any materials belonging to Class I). This is in fact observed for glucose, a class I material, which can indeed amorphize if milled for a long duration, which allows sufficient mechanical stress to overcome the lattice strength of the material.[22]

5.3.6 Differentiating Class III and IV materials by short duration milling

Both Class III and IV materials can potentially generate amorphous due to high amorphous stability. However, the distinction between Class III and IV is in the lattice strength of crystals, where Class III materials have high lattice strength (low expansivity). To better distinguish between Class III and IV materials, we probed their amorphization behaviors at short milling times. The guiding hypothesis here is that materials with stronger lattice will have a delayed onset of amorphization, i.e., they would require longer duration milling for the amorphization process to commence. Materials in Class III with lower expansivity (higher lattice strength) do not amorphize at short milling times (typically require at least 30 min of cryomilling to start amorphization), contrary to materials in Class IV where amorphization starts at <10 min milling. Thus, Class IV materials will be the most prone to solid-state amorphization during processing, and also have the greatest potential to develop kinetically stable amorphous phases.

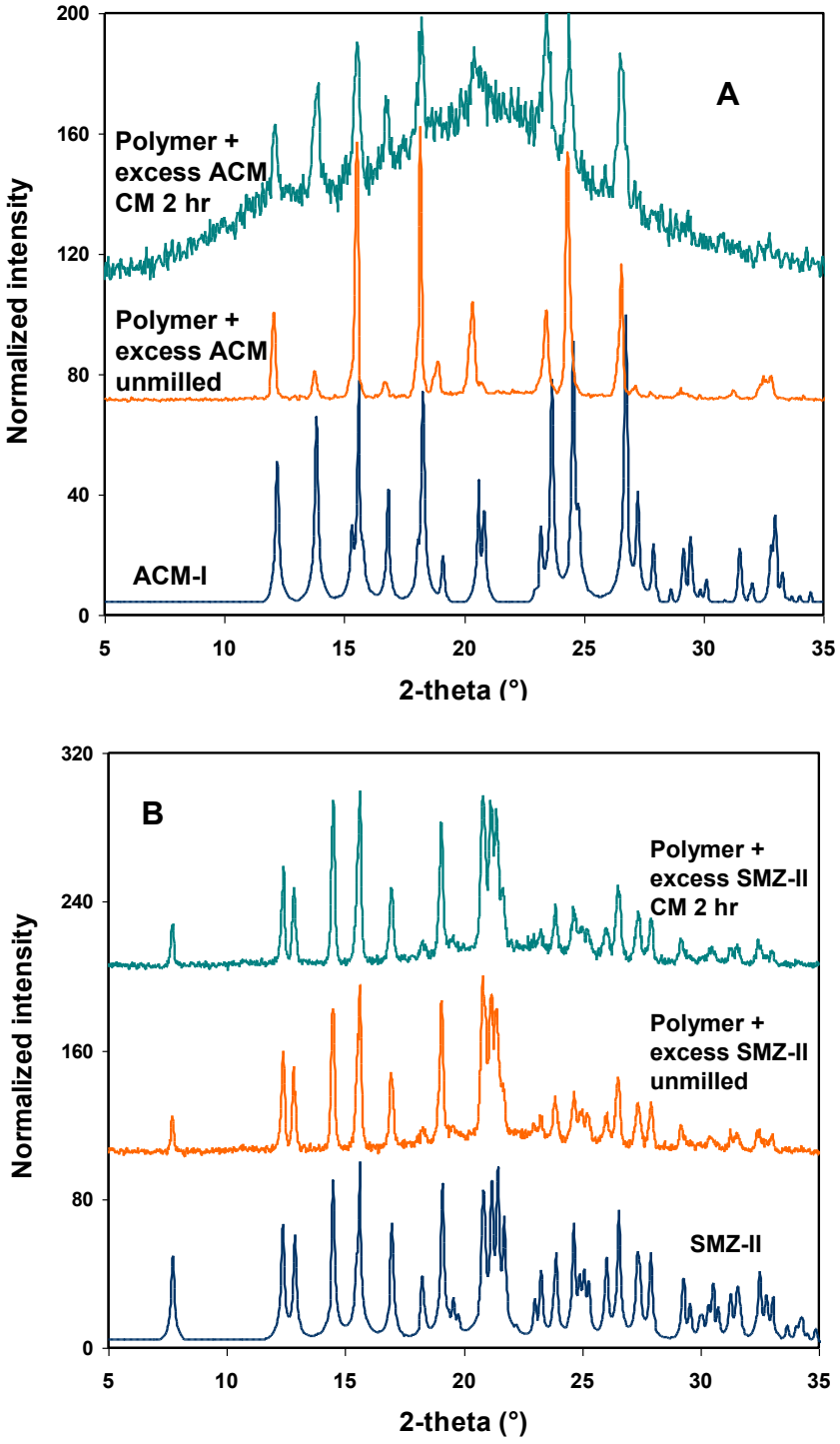

Figure 5.9. Distinction between Sulfamerazine-II (Class I) and Acetaminophen-I (Class II) illustrated by co-cryomilling in presence of crystallization inhibitor - polymer PVPVA. While Class II crystal actually amorphizes during milling, class I crystal is resistant to amorphous generation.

5.3.7 Fast DSC screen of amorphization potential

The classification system developed in this work for amorphization potential depends on lattice strength information obtained from VT-SXRD. However, VT-SXRD experiments involve significant sample preparation and experimental complexity. It is not always possible to have crystals available during early stages of drug development. In addition, SXRD facility is not readily available at all academic and industrial locations, and operating it at several temperatures can be time consuming and inefficient.

To address these practical issues, we attempted to identify a bulk powder surrogate property to volume expansivity that can more readily be quantified. The lattice strength of crystals using bulk powder has been estimated here using the "lattice enthalpy of fusion" of crystals extrapolated to the temperature of milling (H_f^{77K}) by performing a heat capacity correction between liquid and crystal (Origin 8.6) assuming linear dependence of heat capacity difference on temperature below T_g (equation 8).

$$H_f^{77\,K} = H_f - \int_{77\,K}^{T_m} \Delta C_p^{l-} \, dT \qquad (8)$$

where, T_m is the melting temperature of the crystal in Kelvin. H_f^{77K} is the energy required to covert the crystal to a disordered phase at 77 K. For crystals with very different melting points, the enthalpy of fusion at the melting temperature cannot be reliably used to measure the lattice strength because the heat capacity is temperature and material dependent. The hypothetical "fusion enthalpy" at a fixed temperature, described here, is a more appropriate parameter to compare the lattice strength of

different crystals. The temperature should be relevant to the process of interest where amorphous is generated, which is 77 K in this study.

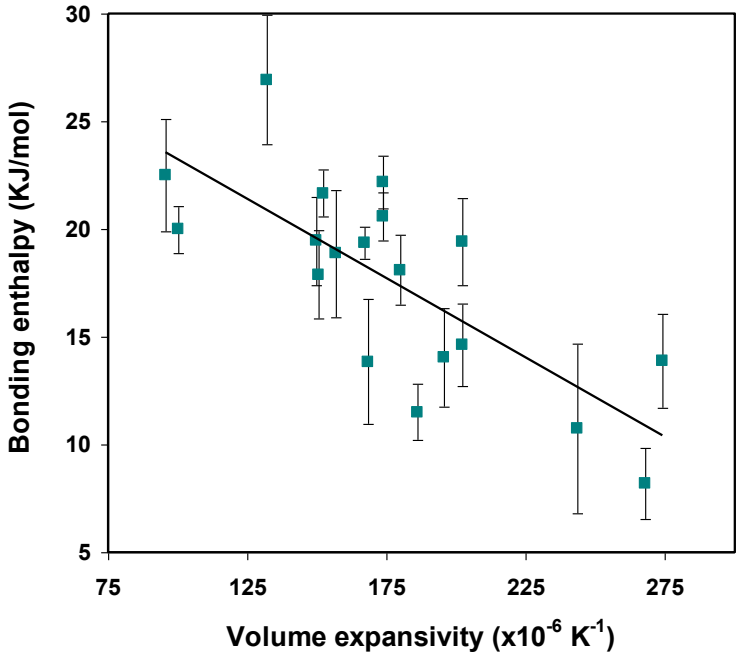

Figure 5.10. Correlation between volume expansivity of crystals measured by variable temperature single crystal X-ray diffraction and lattice enthalpy of crystalline powders at 77K measured by differential scanning calorimetry.

Figure 5.10 shows a correlation between expansivity and lattice enthalpy for a few compounds. A lower value of expansivity corresponds to higher H_f^{77K}, and hence stronger lattice. Using H_f^{77K}, the amorphization classification map can be reconstructed, which allows to assess the amorphization potential of a material based on a single instrumental technique, DSC, using a total sample weight of <20mg of powder, making this approach material-sparing. This is potentially very attractive to scientists during early stages of drug development and will aid in early solid form selection.

5.3.8 Comment on ACS classification when fluid intermediates are involved

The amorphization classification developed in this work is for solid-state amorphization, where both the lattice strength of the crystal and amorphous glass stability must be considered. However, when amorphous is generated from melt (e.g. melt-quenching), solution (e.g. freeze drying) or vapor (e.g. vapor deposition),[15] the classification is simplified, as the crystal lattice history is no longer relevant. For such cases, amorphization potential of a material will be primarily a function of the amorphous stability parameters. It must be noted that even though lattice strength is no longer an issue, the concept of glass forming ability (GFA)[54] still is valid when amorphous is produced from fluids, for instance GFA is routinely quantified using the critical cooling rate necessary to form glass by quenching melts.

5.4 CONCLUSIONS

In this study, we have designed a scheme for the fast assessment of amorphization potential of pharmaceutical crystals using structural and thermodynamic material properties. DSC and XRD have been used to create amorphization classification maps by incorporating two factors influencing solid-state amorphization: crystal lattice strength and amorphous stability. Four amorphization classes of materials have been distinguished based various combinations of lattice strength and amorphous stability. Materials in class I and II, due to fast recrystallization tendency of amorphous phase, are suitable for crystalline development. Class II materials can form amorphous if crystallization is delayed by using polymer dopants. Materials belonging to class IV are best suited for preparing stable amorphous forms. This knowledge of the amorphization

potential of materials is expected to greatly streamline the early identification of candidate materials with (a) better suitability for developing stable amorphous form (Class IV), or (b) potential problems of unexpected processing-induced amorphization (Class III, IV).

Chapter 6.

Assessing amorphization potential of crystals: Part 2. Higher molecular weight favors formation of stable amorphous phase

The objective of this chapter is to elucidate the influence of molecular weight (MW) on mechanical amorphization of small molecular organic crystals from both kinetic and thermodynamic viewpoint. Results based on 21 model compounds show that crystals of compounds with MW <260 g/mol do not form stable amorphous phase under mechanical stress. The amorphous phases of lower MW compounds have greater propensity to crystallize, as shown by their lower activation energies during non-isothermal crystallization. The influence of molecular weight on crystallization appears to be connected to the excess configurational entropy (ΔS_{conf}) in the amorphous phase. A positive correlation is observed between MW and ΔS_{conf} in this set of structurally diverse molecules. This suggests that molecular flexibility in the amorphous phase, measured by ΔS_{conf}, plays a role in the observed differences in amorphization behaviors of crystals. To gain further insight, mean structural relaxation times (τ_{calc}) have been calculated for different molecules based on the temperature dependence of ΔS_{conf} in supercooled liquid phase using Adam-Gibbs theory. Significantly shorter τ_{calc} values are obtained for materials with lower MW, indicating higher global molecular mobility and faster recrystallization. These conclusions are further supported by glass relaxation studies performed below T_g using isothermal microcalorimetry. In summary, the lack of observable amorphization of low MW crystals is a result of fast elimination of amorphous phase at ambient conditions prior to sample characterization.

6.1 INTRODUCTION

Solid-state phase transformations of pharmaceutical materials during processing can significantly affect their physicochemical stability, solubility, and dissolution kinetics, which can lead to serious consequences on drug product performance.[1, 2] An early prediction of such potential phase transformations is important for designing high quality products, maintaining product quality, facilitating regulatory approval, and ensuring batch-to-batch consistency. Solid-state amorphization, a type of phase transformation that involves direct crystal to glass transition, has been observed frequently for a large fraction of pharmaceutical crystals during milling.[3-8] Amorphous phase, which lacks the three-dimensional long range molecular order present in crystalline materials, is the higher free energy solid form with the tendency to revert to the crystalline counterparts.[9] Amorphous solids are sometimes generated intentionally to improve drug properties,[9-11] for instance, to enhance the dissolution kinetics of poorly soluble drugs,[12-15] and occasionally improve the chemical stability of materials.[16] However, when amorphous phase is unintentionally introduced during processing, detrimental effects on the physical stability (*i.e.,* recrystallization tendency), chemical stability (*i.e.,* degradation), and dissolution kinetics of the material may result. This usually leads to catastrophic consequences in development and manufacturing of solid dosage forms. If amorphous is the intended solid form, then crystallization has to be avoided. On the other hand, if amorphous phase is generated unintentionally, faster crystallization back to the stable form before the final step of manufacturing will be preferred.

The ability of preparing an amorphous phase from a crystalline solid is termed the *amorphization potential* of the material in this work. The physical stability of the amorphous form plays an important role in the amorphization potential of a crystal. Our earlier studies have shown that solid-state amorphization of crystals is affected both by the lattice strength of the starting crystalline form, and the stability of the generated amorphous phase, which encompass the amorphous phase generation and elimination steps, respectively. Materials with weaker lattice and lower amorphous crystallization tendency were able to form stable amorphous phase by milling. For any material, recrystallization from milled samples is generally easier because of facilitated heterogeneous nucleation, the larger surface area, and the presence of crystal nuclei. Therefore, an earlier crystallization onset is usually observed in mechanically activated glasses.[6, 17] This two step process of amorphization, *i.e.,* generation and elimination, is also indicated in crystal to crystal polymorphic phase transformations that involve an amorphous intermediate.[18]

Even though the phenomenon of amorphization has been extensively reported in the pharmaceutical literature, it is still not feasible to predict the amorphization of a crystal based on an assessment of its material properties. Recently, there have been attempts to correlate structural features of crystals with their amorphization propensity. For instance, the ability to amorphize has been correlated to the ease of generation of dislocations in a crystal under stress, which is then correlated to the free energy difference between amorphous and crystal.[4, 5, 19] Such an approach, however, is unrealistic, because it relies on properties not readily amenable to experimental characterization, such as the burgers

vector of an organic crystal. Other easily accessible material properties, such as T_g and molar volume, have also been used to predict the amorphization potential of crystals with some success.[5] For example, the influence of milling temperature relative to T_g on mechanical amorphization has been investigated.[3] For the same crystal, milling at temperatures above T_g reduces the amorphization potential, compared to when milled below T_g.

The focus of this work is to probe the role of molecular weight in the ability of materials to form kinetically stable amorphous phase within timescales of pharmaceutical interest. In this work, we have only considered materials belonging to Amorphization Classes II and IV (see Chapter 5). These materials have weak lattice (expansivity > 150×10^{-6} K^{-1}) and can amorphize by milling. However, the difference between Class II and IV is in amorphous stability, where class II materials are fast crystallizers (entropy < 25 J/mol-K) but class IV materials are not. Here, we have explored the relationship between molecular weight and configurational flexibility of molecules in the disordered phase, and the amorphous stability of various materials has been used to explain the observed differences in the processing-induced amorphization behaviors of their crystals.

6.2 MATERIALS AND METHODS

6.2.1 Materials

Small molecular organic materials with a wide range of molecular weights (150 - 600 g/mol) were probed in this study. Acetaminophen, griseofulvin, hydrochlorothiazide, indomethacin, piroxicam, terfenadine, sulfamerazine, sulfisoxazole, sulfadoxin,

sulfamethoxazole, aspirin, phenacetin and sulfanilamide were obtained from Sigma–Aldrich, Inc. (St. Louis, MO, USA). Felodipine, nifedipine and simvastatin were obtained from A.K. Scientific, Inc. (Union City, CA, USA). Danazol was purchased from Spectrum Pharmaceuticals, Inc. (Irvine, CA, USA). Ketoconazole was obtained from Hawkins, Inc. (Minneapolis, MN, USA).

6.2.2 Solid-state amorphization

Approximately 2g of crystalline powder for each material was cryomilled in a liquid nitrogen bath at ~77K (6750 Freezer Mill, SPEX CertiPrep, Metuchen, NJ) for up to 2 hours, with intermittent sample withdrawal at both short (10 min) and long (>30 min) milling times. Samples were milled under the impact of a magnetically-driven cylindrical stainless-steel milling bar on to two stainless-steel lids of a polycarbonate tube containing the samples. After the sample was loaded and prior to milling, the milling assembly was pre-cooled at liquid nitrogen temperature (~77K) for 2 minutes. Milling was conducted at a rate of 10 impacts per second. A 2 min cooling period was employed after each 2min of milling. Cryomilled samples were withdrawn inside a glove box purged with dry nitrogen and stored in desiccator containing anhydrous calcium sulfate (Dreirite®, W.A. Hammond Dreirite Co. Ltd., OH). Freshly milled samples were characterized typically within 5-10 minutes after sample withdrawal. Water content of milled samples was <0.5 wt% up to 100 ^{o}C by thermogravimetric analysis (TGA Q500, TA Instruments, New Castle, DE).

6.2.3 Characterization of milled samples

Thermal studies. The milled samples were studied using Differential Scanning Calorimetry (DSC Q1000 and Q2000, TA Instruments, New Castle, DE) to assess their crystallinity after milling. Universal Analysis (Version 4.1D, TA Instruments) was used for DSC data analysis. The baseline of DSC was calibrated using empty cell, followed by sapphire discs. Temperature and enthalpy calibrations were done using high purity indium (standard mode, ramp rate of 10 K/min). Heat capacity was calibrated using crystalline sucrose, where the heat capacity constants (ratio of theoretical to actual C_p) were 0.988 for the direct signal and 1.049 for the reversing signal (acceptable C_p constant range: 0.9 - 1.1). A low purge flow rate of nitrogen (~5 mL/min) was used to improve the accuracy of heat capacity measurements by minimizing thermal fluctuations. A sinusoidal modulation of ±1K was employed every 100 seconds, with a ramp rate of 2K/min. Sample weights for heat capacity measurements were on average ~15 mg. To maximize thermal contact of the sample, sample powders were mildly pressed into thin compacts to fit inside the bottom of DSC pans. Glass transition temperatures (T_g) are reported as the mid-points of the glass transition events determined from the reversing heat capacity (rev C_p) signal. Crystallization and melting temperatures are reported as the extrapolated onset temperatures of the corresponding thermal events. Enthalpies of crystallization and fusion events have been obtained by integrating the peaks using sigmoidal baseline.

The amorphous content (φ) of the milled samples was quantified using the enthalpies of crystallization (H_c) and melting (H_m) measured using DSC in non-isothermal mode

(10K/min), by performing a heat capacity correction for the temperature difference at which the melting and crystallization events occur during a non-isothermal ramp (equation 1).[20] All milled samples were handled and DSC pans crimped in glove box purged with dry nitrogen.

$$\varphi = \frac{H_c}{H_m - \Delta C_p^{l-c} \times (T_m - T_c)} \qquad (1)$$

In this expression, ΔC_p^{l-c} is the difference in heat capacities of the liquid and crystal, determined by modulated DSC at 2K/min. The corrected H_m is the total enthalpy required to "melt" the crystal at the temperature of crystallization, which is equal to the heat of crystallization for a pure amorphous phase. This heat capacity correction to account for the thermal dependence of enthalpy of materials is necessary when comparing two thermal events occurring at two widely separated temperatures (like crystallization and melting).

Powder X-ray diffraction studies: A powder X-ray diffractometer (D8 Advance, Bruker AXS, Madison, WI) with CuK_α radiation and scintillation counter detector was used to examine changes in crystallinity of the samples after milling. The diffractometer was calibrated using corundum standard (SRM 674b, NIST) at d = 2.0852Å. Diffraction data were collected over 5 - 35º 2θ with step size of 0.05º and dwell time of 1s. Milled samples were packed into the sample holder without further treatment. Melt-quenched glasses were mildly ground using mortar and pestle before being packed for PXRD studies. All samples were packed into the sample holder by top filling method. PXRD data were collected using the Diffrac Plus XRD commander software (Bruker, AXS).

Data analysis was performed using JADE (version 8, Materials Data Inc., Livermore, CA).

6.2.4 Configurational parameters

The excess thermodynamic parameters of non-equilibrium amorphous phase were quantified using the configurational heat capacity ($C_{p,conf}$), defined as the difference in the measured heat capacities between the amorphous and the crystalline phases (equation 2).

$$C_{p\ conf} = C_{p\ amorphous} - C_{p\ crystal} \qquad (2)$$

To obtain $C_{p,conf}$, crystals were melt-quenched and reheated *in situ* in DSC at 2°C/min with modulation.

The configurational entropy barrier to crystallization (ΔS_{conf}) is a measure of configurational flexibility of molecules and may be computed by integrating the configurational heat capacity as function of temperature (Origin 8.6) and using information on fusion enthalpy, ΔH_m of each material (equation 3).

$$\Delta S_{conf} = \Delta S_{melt} + \int_{T_m}^{298\ K} \frac{C_{p\ conf}}{T}\, dT = \frac{\Delta H_{melt}}{T_{melt}} + \int_{T_m}^{298\ K} \frac{C_{p\ conf}}{T}\, dT \qquad (3)$$

Configurational entropy is then correlated with molecular mobility through the Adam-Gibbs theory,[21] which will be described later. For materials that crystallized during melt-quenching, configurational entropy was calculated by extrapolating the heat capacity of the liquidus phase prior to crystallization onset.

6.2.5 Crystallization activation energy of glass

Activation energy of non-isothermal crystallization (in DSC) of melt-quenched glass was obtained by fitting crystallization data to the Avrami-Erofeev model[22-24] of the third order to a modified Coats-Redfern equation[25, 26] (equation 4).

$$\ln \beta \; g(\alpha) = \ln \left[\frac{A R T^2}{E_a} \left\{ 1 - \left(\frac{2 R T}{E_a} \right) \right\} \right] - \frac{E_a}{R T} \qquad (4)$$

In this expression, β is the linear heating rate, $g(\alpha)$ is the crystallization model in the integral from, E_a is the activation energy, A is frequency factor of Arrhenius equation, R is the gas constant, and T is the temperature in Kelvin. Activation energy was obtained from the slope of the linear plot between $\ln \beta g(\alpha$ and $\frac{1}{T}$. Nine kinetic models were tested for all compounds, such as Avrami-Erofeev model and diffusion kinetics model of different orders. Avrami-Erofeev model of the third order was found to provide the best statistical fit to the crystallization data between 25 - 75% of conversion, consistent with previous literature.[27] At very low and high extents of crystallization, the fit deviated from linearity and data from these portions were not used for calculating E_a by model-fitting.

6.2.6 Isothermal microcalorimetry

As a final step to correlate molecular weight with experimental global molecular mobility values of glasses, the structural relaxation times of a few melt-quenched glasses were measured using isothermal microcalorimetry with a Thermal Activity Monitor (TAM 2277, Thermometric, Jarfalla, Sweden). The annealing temperature in TAM was T_g – 15 for all glasses. Fixing the annealing temperature allowed us to directly compare

the rate of energy loss of different glasses as a function of molecular weight at a fixed temperature relative to T_g. Approximately 250 mg sample was sealed in glass ampoule (4 mL—Thermometric) under an atmosphere of dry nitrogen. The reference used was crystalline glycine of approximately the same weight as the sample glass. The time-dependent power decay due to structural relaxation of glass sample was fitted to the derivative form of a modified stretched exponential (MSE) function (equation 5).[28]

$$P = 277.8 \frac{\Delta H_r(\infty}{\tau_0} \left(1 + \frac{\beta t}{\tau_1}\right)\left(1 + \frac{t}{\tau_1}\right)^{\beta} \times \exp\left[-\left(\frac{t}{\tau_0}\right)\left(1 + \frac{t}{\tau_1}\right)^{\beta}\right] \quad (5)$$

In this equation, P is the power loss during annealing (in μW/g), τ is the relaxation time constant, τ is the relaxation time constant at short time limit, β is the factor indicating distribution of relaxation times, and $\Delta H_r(\infty$ is the enthalpy relaxation at time infinity, calculated using equation 6.

$$\Delta H_r(\infty\ T) = \Delta C_p(T_g - T) \quad (6)$$

where, ΔC_p is the step change in heat capacity at T_g. For TAM experiments, the initial power-time data at t<0.5 h were not used to eliminate friction effects generated by introducing sample vial into the temperature-controlled bath. The initial 30 min also allowed the samples to reach the bath temperature for each annealing experiment.

τ , τ and β were obtained through non-linear curve fitting of power-time data (Origin 8.6). These parameters were then used to compute the relaxation times (τ_G^{β}) of glasses, according to equation 7.

$$\tau_G^{\beta} = \tau \times \tau^{\beta} \quad (7)$$

The use of τ_G^{β}, instead of τ, as the structural relaxation time is because the τ value changes with annealing duration as a result of continuous change in glass structure. The scaling of relaxation time with β helps to minimize this effect.[28, 29] Post TAM experiment, DSC/PXRD was performed on the tested samples to ensure that no crystallization occurred during TAM studies.

6.3 RESULTS AND DISCUSSION

6.3.1 Influence of molecular weight on solid-state amorphization

To reach our goal of identifying key material properties that can be used to predict the amorphization behaviors of pharmaceutical crystals during processing, we have explored a large number of thermodynamic, structural and molecular factors that can potentially influence the process. A key material property that provides a promising correlation with amorphization is molecular weight. The effect of molecular weight on the amorphization potential of materials is shown in Figure 6.1. Up to 2 hrs of cryomilling, crystals of low molecular weight molecules (MW < 260 g/mol) consistently did not show detectable amorphization both by powder X-ray diffraction and DSC.

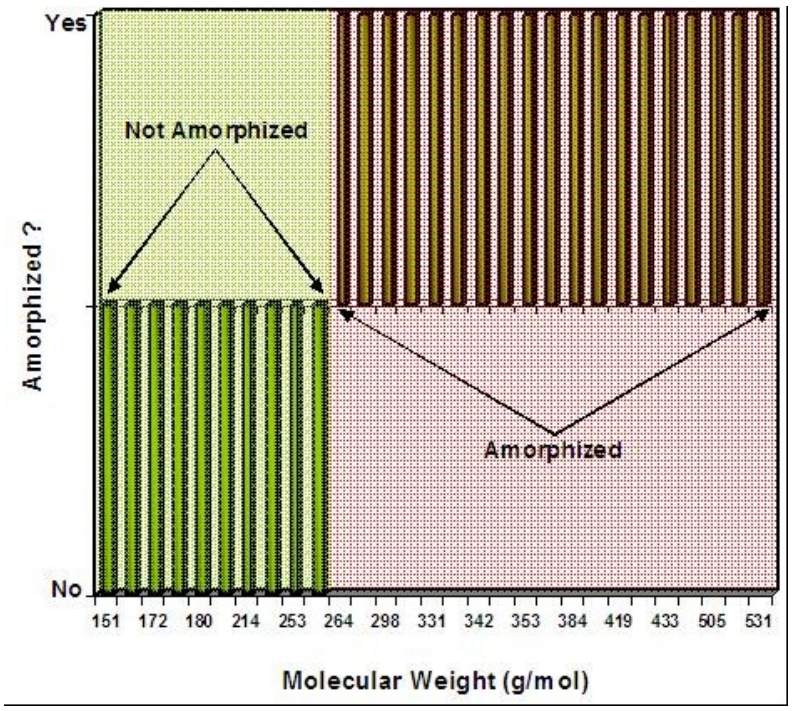

Figure 6.1. Dependence of solid-state amorphization, induced by 2 hr of cryomilling, on molecular weight of materials.

Table 6.1 summarizes the diverse amorphization behaviors of various model crystalline compounds in this study, along with some of their basic molecular parameters. There is a clear delineation in the amorphization potential of materials under mechanical stress based on their molecular weights. All materials with molecular weights higher than 260 g/mol underwent significant amorphization after 2 hrs of cryomilling, even though the extent of amorphization varied among different materials.

Table 6.1. Basic information on some relevant molecular properties of the model compounds and their solid-state amorphization behaviors. Data presented as mean ± one standard deviation of measurements (n = 3). Only compounds belonging to Amorphization Classes II and IV have been included in this work.

Compound	Molecular Weight M_w /g-mol^{-1}	Amorphized up to 2 hrs of cryomilling		Amorphous Content %	Melting point T_m /K	Melting enthalpy H_m/KJ-mol^{-1}	Glass transition T_g /K	ΔC_p at T_g J-g^{-1}K^{-1} ‡
		DSC	PXRD					
Acetaminophen-I (ACM-I)	151.2	No	No	0	439.3±0.2	26.7±1.1	296.7±0.3	0.42±0.16
Acetaminophen-II (ACM-II)	151.2	No	No	0	430.4±0.1	32.1±0.6	296.7±0.3	0.42±0.16
Phenacetin (PHE)	179.2	No	No	0	405.9±0.2	19.7±1.1	-	-
Aspirin (ASP)	180.2	No	No	0	401.8±1.2	29.7±4.2	-	-
Sulfacetamide (SCT)	214.2	No	No	0	453.1±0.1	17.1±1.7	303.5±0.5	0.42±0.03
Sulfadiazine (SDZ)	250.3	No	No	0	526.1±0.4	55.5±1.4	390.9±0.7	0.26±0.04
Sulfamethoxazole (SMET)	253.3	No	No	0	439.5±0.3	38.8±2.1	302.8±0.9	0.38±0.08
Sulfamerazine-I (SMZ-I)	264.3	Yes	Yes	79.58 ± 4.98	505.4±0.2	40.4±1.1	334.1±2.4	0.43±0.04
Sulfamethazine (SMT)	278.3	Yes	Yes	73.47 ± 4.36	470.0±1.1	60.5±4.5	348.6±0.6	0.46±0.06
Hydrochlorothiazide (HCT)	297.7	Yes	Yes	73.85 ± 5.61	534.8±0.2	34.3±1.0	391.9±1.2	0.34±0.02
Sulfadoxin (SDOX)	310.3	Yes	Yes	61.74 ± 4.56	465.8±0.1	44.2±3.8	330.7±0.2	0.47±0.01
β-piroxicam (PRX)	331.3	Yes	Yes	54.54 ± 5.12	473.9±0.1	36.0±1.8	336.0±0.2	0.41±0.01
Danazol (DNZ)	337.5	Yes	Yes	61.11 ± 9.13	494.8±1.3	39.0±1.9	345.6±0.7	0.46±0.01
Sucrose (SUC)	342.3	Yes	Yes	63.24 ± 4.21	Decomposes	-	347.2	0.54±0.02
Nifedipine (NFD)	346.3	Yes	Yes	49.23 ± 3.03	443.1±0.5	40.6±4.1	318.9±0.2	0.36±0.02
Griseofulvin (GRF)	352.8	Yes	Yes	79.65 ± 4.51	493.4±0.1	39.2±0.7	363.9±0.8	0.37±0.04
γ-Indomethacin (IMC)	357.8	Yes	Yes	72.36 ± 2.54	433.2±0.6	39.1±3.5	318.9±1.0	0.37±0.05
Felodipine (FLD)	384.3	Yes	Yes	69.52 ± 2.47	411.5±0.2	30.6±0.7	319.7±0.2	0.30±0.03
Terfenadine (TFD)	471.6	Yes	Yes	98.63 ± 3.31	419.6±0.3	55.4±2.1	332.6±0.3	0.56±0.19
Dipyridamole (DPD)	504.5	Yes	Yes	88.68 ± 7.45	434.5±0.1	31.6±0.7	311.5±0.4	0.28±0.04
Ketoconazole (KNZ)	531.4	Yes	Yes	80.21 ± 4.60	419.4±0.3	57.4±1.7	317.6±0.4	0.46±0.06

To illustrate the lack of amorphization of low MW compounds, the powder XRD profiles of unmilled and cryomilled acetaminophen (MW = 151 g/mol) are shown in Figure 6.2 . The milled material shows high intensity crystalline peaks, and is phase identical to the unmilled sample.

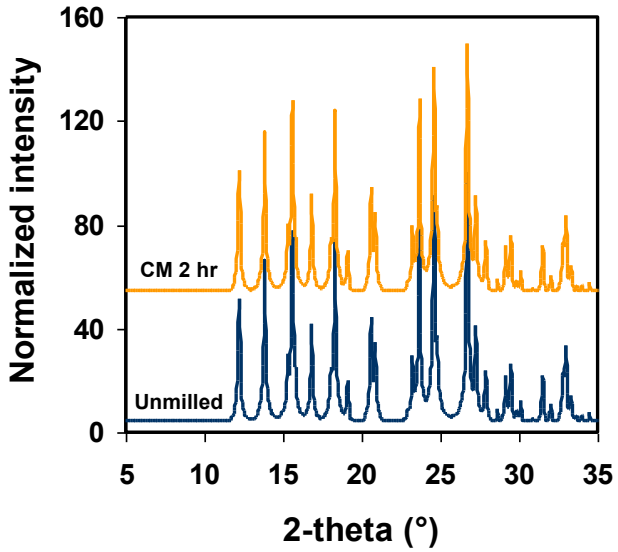

Figure 6.2. Lack of amorphous generation by cryomilling (CM) for acetaminophen (MW = 151 g/mol) is confirmed by powder X-ray diffractometry.

Using co-cryomilling with polymer to hinder crystallization, in Chapter 5, we have demonstrated that acetaminophen actually amorphizes under mechanical stress, but rapid recrystallization of the generated amorphous phase prevents its direct observation. Based on principal component analysis, Baird et al. recently showed that low molecular weight molecules tend to crystallize faster, which is linked to the possible molecular flexibility in the amorphous phase.[30] Both these results suggest that the physical stability of amorphous phase generated by milling should be carefully considered to explain the observed correlation between molecular weight and mechanical amorphization behaviors of crystals.

6.3.2 Configurational entropy

It was proposed that amorphous phase stability is related to configurational molecular flexibility in the amorphous phase.[31, 32] The excess configurational entropy, *i.e.,* the entropy difference between amorphous and crystal, was evaluated in this study as an experimental measure of molecular flexibility in the amorphous phase. Summarized in Table 6.1 are the configurational enthalpies of different crystals at their respective fusion temperatures, which can be used to calculate their corresponding configurational entropies at fusion. The configurational entropy at any other temperature below melting point can be calculated using equation 3, using fusion entropy and configurational heat capacity data. A representative plot of the dependence of configurational quantities (entropy, enthalpy and free energy) on temperature, both below and above the glass transition, is shown in Figure 6.3. These plots for any other molecule can be obtained using the same approach. As expected, the configurational entropy and enthalpy increase with increasing temperature, while the configurational free energy decreases as temperature gradually approaches melting. The difference in configurational free energy is zero at melting temperature since the crystal is in equilibrium with its liquid. The non-linear decrease in free energy is attributed to the fact that enthalpy and entropy of materials do not change at the same rates with temperature. For molecules, which could not be amorphized by melt-quenching due to fast recrystallization (indicated in Table 6.1), the configurational parameters were predicted based on the heat capacity difference between liquid (instead of amorphous) and crystal.

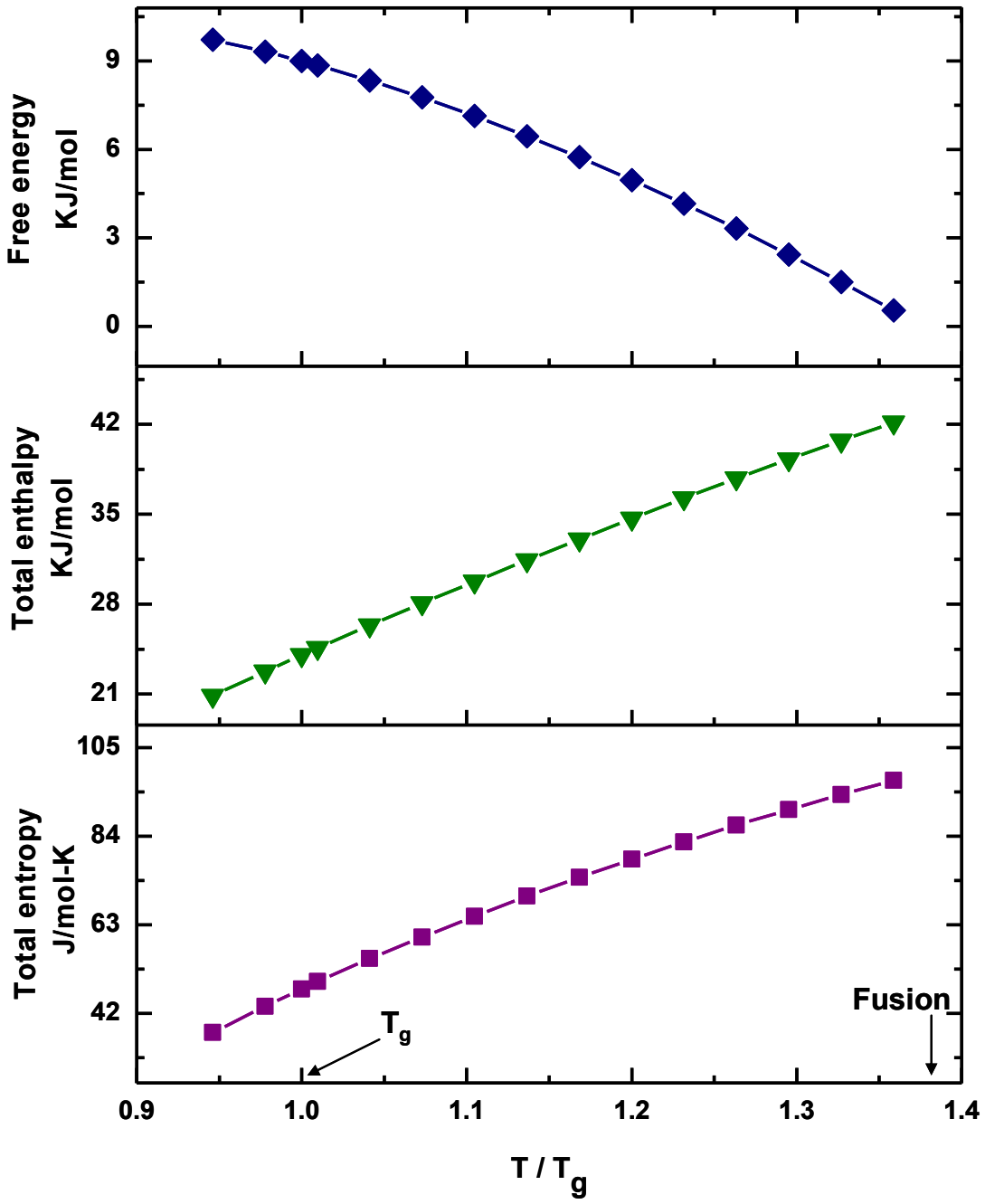

Figure 6.3. Configurational parameters (enthalpy, entropy, and free energy) as function of temperature for amorphous indomethacin, calculated based on configurational heat capacity data.

Figure 6.4 shows a positive correlation between molecular weight of several structurally diverse molecules and their configurational entropy. This indicates that with increasing molecular weight, the configurational entropy increases. Over the molecular weight range of compounds probed in this study (150 - 600 g/mol), the configurational entropy increased by approximately 3.5 folds. Some degree of scatter observed in the data is not unexpected given the structural diversity of molecules explored in this study. .

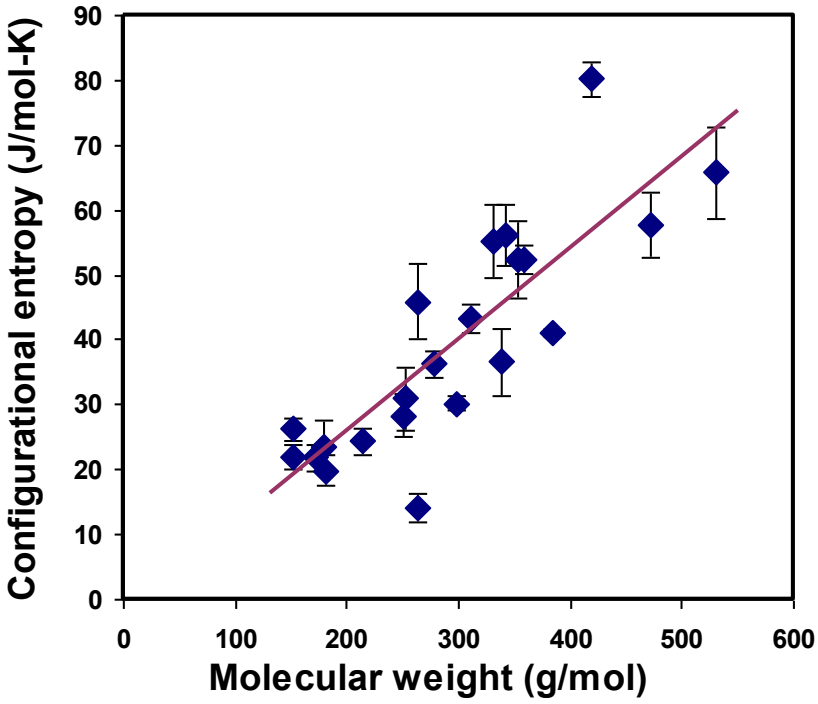

Figure 6.4. Correlation between molecular weight (M_w) and configurational entropy (ΔS_{conf}) of molecules in the disordered phase at roomn temperature. Data are presented as mean ± one standard deviation of DSC measurements (n = 3). Linear fit correlation equation: $\Delta S_{conf} = 0.18 \times M_w + 29.77$; $R^2 = 0.58$.

6.3.3 Molecular mobility from configurational entropy

The significance of configurational entropy in amorphous stability has been a topic of interest for some time.[31] However, contradicting results have been reported regarding the true effect of this parameter on crystallization. It has been argued, using compounds such as ritonavir and acetaminophen, that a higher configurational entropy indicates a higher number of possible molecular configurations in the amorphous phase, which will retard crystallization. In other words, crystallization is facilitated when molecules easily assume proper configurations, *i.e.,* have lower configurational entropy.[31] However, it was also suggested, while evaluating amorphous stability of hexitols,[33] that molecules with higher configurational entropy at fusion crystallized faster.

To address this contradiction and clarify the role of configurational entropy (hence, molecular weight) in crystallization, we correlated entropy with molecular mobility (quantified by inverse structural relaxation time, $1/\tau_{calc}$) in the amorphous phase using Adam-Gibbs equation (equation 8).[21]

$$\tau_{calc} = \tau_{\infty} \exp\left(\frac{C}{T \Delta S_{conf}}\right) \qquad (8)$$

In equation 8, τ_{∞} is the structural relaxation time constant at infinite temperature (typically taken as 10^{-14} sec corresponding to the mobility at fusion), C is a temperature independent but material dependent constant, and T is the absolute temperature. First, at $T=T_g$, the Adam-Gibbs theory is evaluated to derive the value of constant C using a

mobility value of 100 sec for T_g and ΔS_{conf} from the configurational heat capacity data. Thereafter, the constant C is used to determine the τ_{calc} values based on the thermal variation of ΔS_{conf}.

Molecular mobility in amorphous phase involves global mobility (α relaxation), *i.e.,* the mobility associated with glass transition, and secondary[34, 35] and surface[36] relaxations below T_g. The discussion here is limited to the molecular global mobility in supercooled liquids. The effect of molecular weight on calculated global mobility is investigated by comparing 4 amorphous solids with different molecular weights: acetaminophen (MW = 151 g/mol), sulfamerazine (MW = 264 g/mol), danazol (MW = 338 g/mol) and terfenadine (MW = 471 g/mol). The plot of calculated mobility values as a function of T/T_g (Figure 6.5) shows that the molecular mobility (inverse of relaxation time) sharply decreases, over several orders of magnitude at a fixed temperature above T_g, with increasing molecular weight.

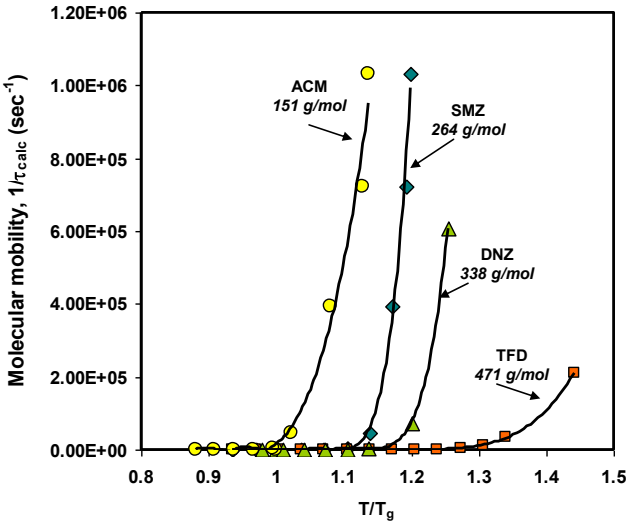

Figure 6.5. Correlation between calculated global mobility ($1/\tau_{calc}$) and molecular weight with temperature scaled to T_g. Polynomial of the fifth order was found to best fit the calculated mobility data. ACM: Acetaminophen, SMZ: Sulfamerazine, DNZ: Danazol, TFD: Terfenadine

Adam-Gibbs equation allows us to calculate mean relaxation times of molecules in the supercooled liquid phase from entropy data. According to this calculation, we observe the inverse rank order of mobility (terfenadine < danazol < sulfamerazine < acetaminophen) to their molecular weight (terfenadine > danazol > sulfamerazine > acetaminophen). These data suggest that a molecule with higher MW is likely to be less mobile, at least in the supercooled liquid temperature region. Whether the same can be said for temperature below T_g will be investigated using isothermal relaxation studies.

6.3.4 Isothermal relaxation studies

To check if the mobility rank order holds for amorphous solids below T_g, we experimentally determined global relaxation times of freshly melt-quenched glasses of these compounds at T_g - 15 using Thermal Activity Monitor (TAM). A representative TAM power decay, with the associated post TAM DSC profile for terfenadine glass, is shown in Figure 6.6. TAM studies were not performed on milled samples, because we could not obtain pure amorphous materials by milling for all compounds. We also must preclude the probability of glass crystallizing during the TAM isothermal annealing for the TAM data to be meaningful. However, milled samples tend to crystallize during annealing due to facilitated heterogeneous nucleation due to their activated surfaces and residual seed nuclei.[6, 17]

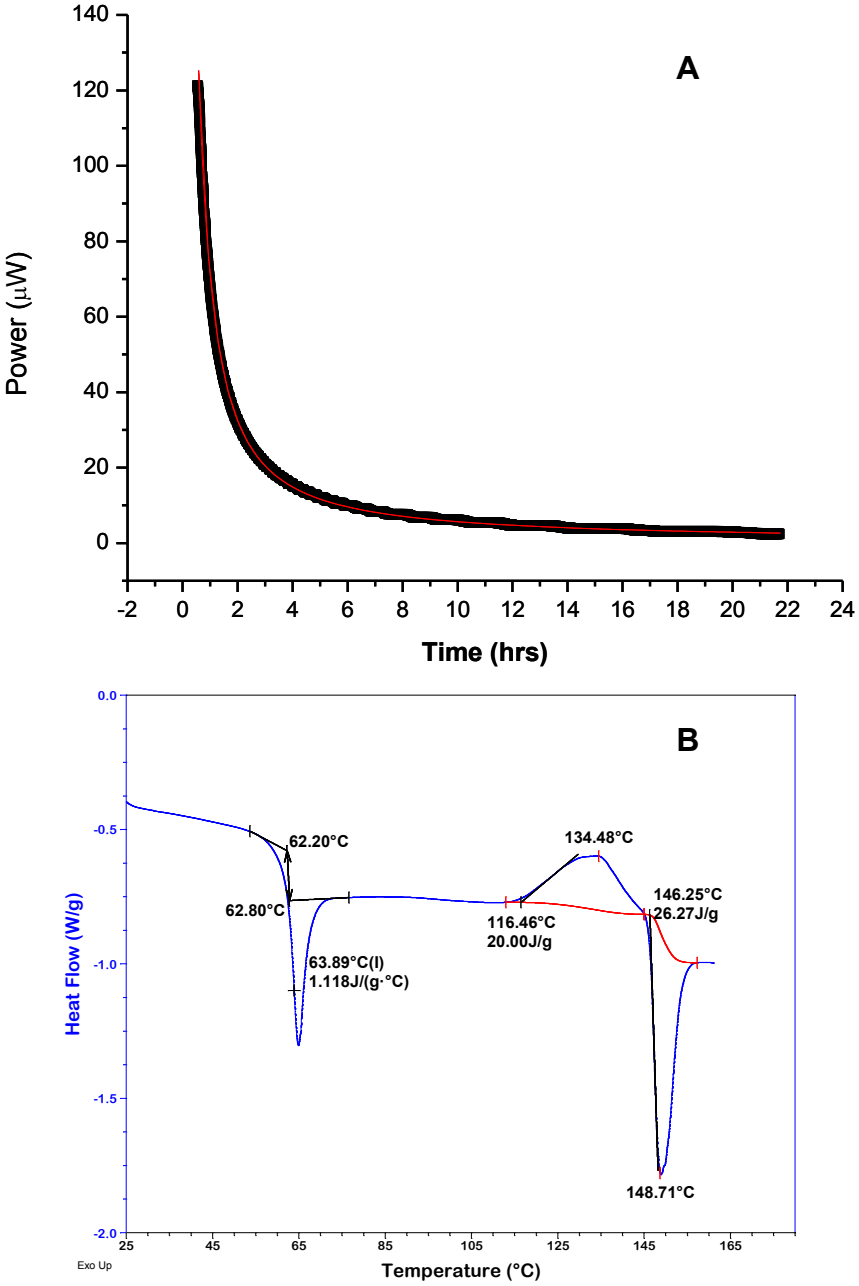

Figure 6.6. **(A)** Representative power decay plot from isothermal microcalorimetry for terfenadine melt-quenched glass at T_g - 15 (~45°C). The data were fit to the derivative of the MSE equation.[28] Fit parameters: τ = 1.52 ± 0.1 hr, τ = 0.11 ± 0.005 hr, β = 0.14 ± 0.002, Reduced χ^2 = 0.42. **(B)** Post TAM DSC (10K/min)

TAM has been widely used to study the relaxation behavior of amorphous pharmaceuticals.[29, 37, 38] The temperature regime where TAM works is ~25 - 90°C. Therefore, acetaminophen could not be tested as its T_g is 24°C. For the 3 other compounds for which calculated mobility analysis was performed, the corresponding TAM data at T_g *-15* are summarized in Table 6.2, and the rank order of mobility (inverse τ_G^{β}) is terfenadine < danazol < sulfamerazine, which is the same as that for supercooled liquids. These experimental data confirm the hypothesis that higher MW molecules are likely to form more stable amorphous phases driven by the lower molecular mobility.

Table 6.2. Isothermal relaxation studies using TAM at T_g-15. Data presented as mean ± one standard deviation of measurements (n = 3).

Glass	$\Delta H_r(\infty$	τ_G^{β}	**Reduced** χ^2
	J/g	**hr**	
Sulfamerazine	6.45	5.96 ± 0.55	0.23
Danazol	6.72	7.15 ± 0.86	0.72
Terfenadine	14.4	10.56 ± 0.61	0.41

6.3.5 Correlations with crystallization

Kinetic stability of amorphous materials was quantified using the activation energy of non-isothermal crystallization, calculated using model-dependent kinetics at multiple heating rates between 2-20 K/min. *Ex situ* melt-quenched glass was used in this study, as some of the *in* situ melt-quenched glasses never crystallize in DSC, e.g., felodipine.

Among common models, Avrami-Erofeev model of the third order was used for deriving activation energy because it gave correlation coefficients closest to unity. Activation energy by this approach was obtained only for model systems that could form a reasonably stable glass by quenching melts, which crystallize on heating. Crystallization when quenching a melt, e.g., for phenacetin, precluded several model systems from this analysis. Figure 6.7 shows the dependence of activation energy of crystallization on the molecular weight of the compounds, showing a relatively strong relationship. This relationship confirms the earlier hypothesis that higher MW molecules form more stable amorphous solids.

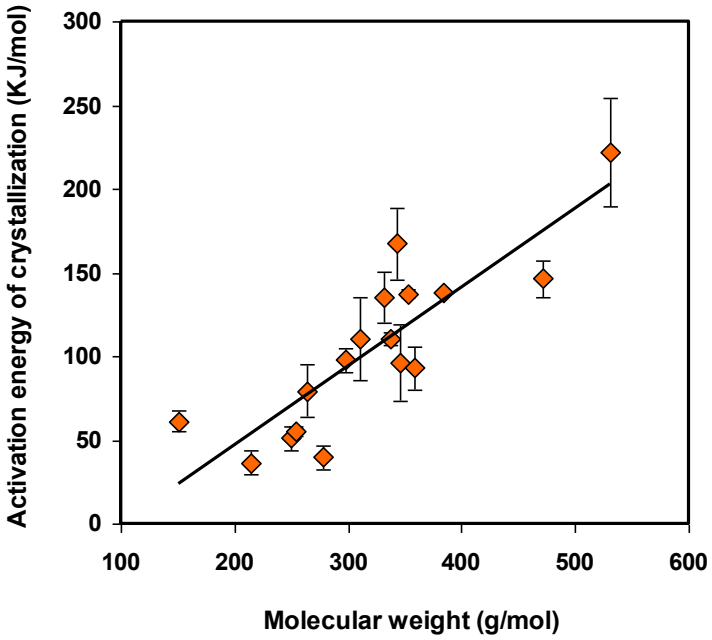

Figure 6.7. Correlation between molecular weight and activation energy of non-isothermal crystallization of glasses, calculated by model-fitting to Avrami-Erofeev[22-24] of the third order.

Molecular mobility has been recognized as a major factor that influences the crystallization of amorphous phase, thus their physical stability, [34, 35, 39, 40] along with other factors such as secondary relaxations[29, 41] and surface relaxations[36] below T_g. Studies have shown that the mean global relaxations are either completely or partially coupled with amorphous crystallization.[42-44] This work provides additional evidences to such a coupling through the demonstration of correlations among molecular weight, configurational entropy, molecular mobility in amorphous phase, and recrystallization activation energy. This insight helps us to evaluate the solid-state amorphization behaviors of molecules (Table 6.1). No low molecular weight crystals showed amorphous conversion, while higher molecular weight materials all amorphized after 2 hrs of cryomilling. Our data, therefore, suggest that fast crystallization contributes to the lack of observed amorphous by milling for crystals of low molecular weight materials. The same concept of molecular weight influence on amorphous stability can, in principle, be extended to amorphous phase generated through other routes.[30]

6.3.6 Shared glass - different excess entropy: Polymorphs

So far we have demonstrated the relationship among MW, configurational flexibility of molecules in the amorphous phase, and stability of amorphous solids using chemically diverse molecules. This insight gives rise to an opportunity to answer an outstanding question: What determines the amorphization potential of polymorphs of the same molecule? The different configurational entropies of the polymorphs mean different barriers to their crystallization from the same amorphous phase, even though the glass is

shared. We attempted to approach this question by studying the amorphization potential of polymorphs of molecules of different molecular weights.

***Low MW polymorphs*:** Amorphization potential of acetaminophen polymorphs I and II (MW ~151 g/mol) was investigated by performing 2 hours of cryomilling. Both polymorphs of acetaminophen did not show detectable amorphous conversion up to 2 hours of milling (Figure 6.8A).

High MW polymorphs: Amorphization potential of piroxicam polymorphs α and β (MW ~331 g/mol) was investigated by performing 2 hours of cryomilling. Both polymorphs of piroxicam underwent partial amorphization (Figure 6.8B).

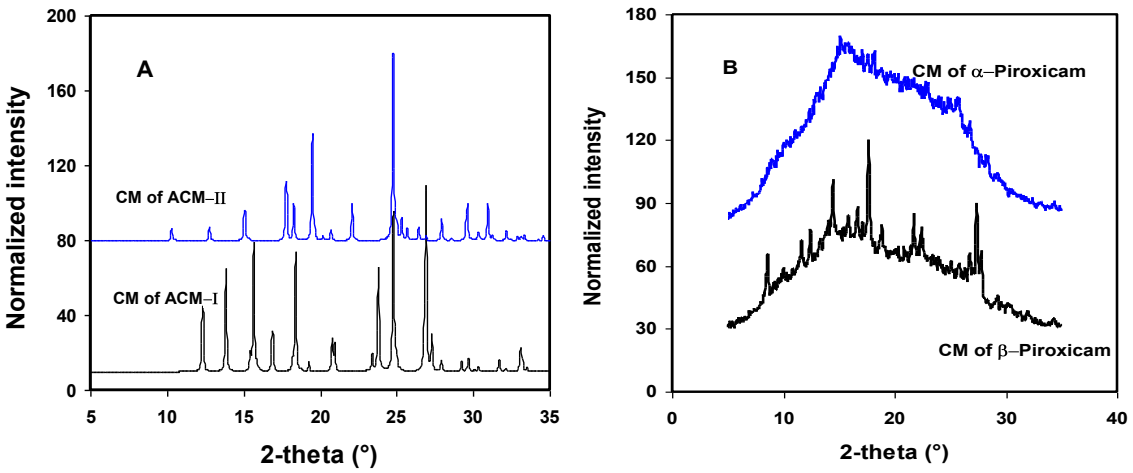

Figure 6.8. 2 hours cryomilling (CM) of **(A)** acetaminophen I and II, and **(B)** piroxicam α and β.

Intermediate MW polymorphs: Amorphization potential of sulfamerazine (SMZ) polymorphs I and II (MW ~264 g/mol) was investigated by performing 2 hours of cryomilling. Polymorph II did not amorphize but polymorph I underwent ~76% amorphization (Figures 6.9A&B), after 2 hours of milling. When heated, the amorphous SMZ recrystallized into polymorph II, which converted to polymorph I upon further heating in DSC. Summarized in Table 6.3 are lattice strength and amorphous stability parameters of polymorphs necessary to evaluate the amorphization potential.

Table 6.3. Factors relevant for glass formation of polymorphs. Data presented as mean ± one standard deviation of measurements (n = 3).

Polymorph	Volume expansivity ($x10^{-6}$ K^{-1})*	Configurational entropy (J/mol-K)	Amorphization Class
Acetaminophen I	150.54 ± 4.36	21.98 ± 2.73	II
Acetaminophen II	173.67 ± 4.29	24.37 ± 1.67	II
Sulfamerazine I	152.09 ± 4.18	45.82 ± 5.82	IV
Sulfamerazine II	95.66 ± 4.24	14.25 ± 2.21	I
α–piroxicam	Not tested	50.37 ± 2.13	Likely IV
β–piroxicam	267.89 ± 6.86	55.32 ± 5.86	IV

* Measured using variable temperature single crystal XRD. Higher expansivity correlates with weaker lattice strength.

Classification criterion:

I	-	V_T <150×10^{-6} K^{-1}, S_c <25 J mol^{-1} K^{-1}
II	-	V_T >150×10^{-6} K^{-1}, S_c <25 J mol^{-1} K^{-1}
III	-	V_T <150×10^{-6} K^{-1}, S_c >25 J mol^{-1} K^{-1}
IV	-	V_T >150×10^{-6} K^{-1}, S_c >25 J mol^{-1} K^{-1}

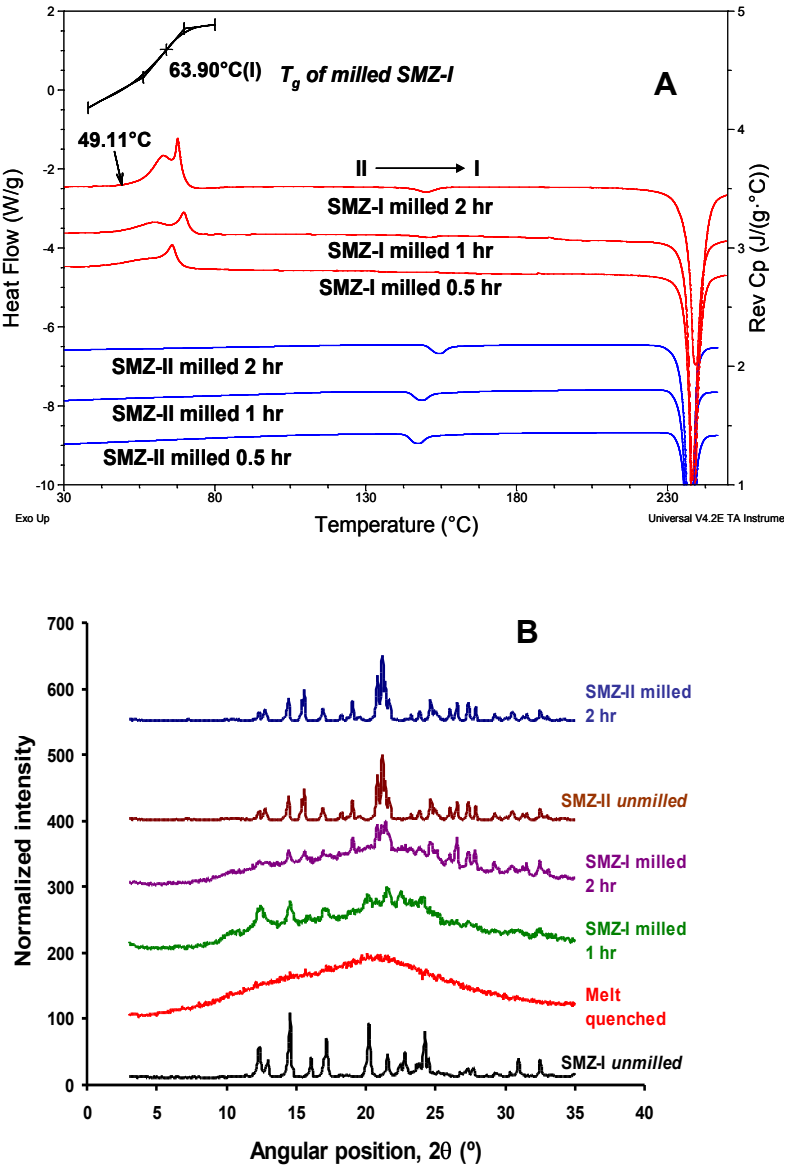

Figure 6.9. Cryomilling (CM) of sulfamerazine polymorphs I and II. **(A)** DSC and **(B)** powder XRD overlay. Form II does not show any amorphous conversion till two hours of milling.

Results from the polymorph milling studies validate the proposed role of molecular weight in stability of amorphous phase. Our earlier work has shown that both crystal lattice strength and amorphous stability influence amorphization potential of pharmaceutical crystals. A lower expansivity indicates stronger lattice, while a lower configurational entropy indicates faster amorphous crystallization tendency (Table 6.3). Polymorphs differ both in their crystal lattice strength and amorphous stability. For polymorphs of low molecular weight molecules, e.g., acetaminophen, neither polymorph can form stable glass irrespective of crystal lattice strength. This lack of observed amorphization is attributed to fast recrystallization of both polymorphs, which is indicated by lower configurational entropy values (Table 6.3). When molecular weight is high (piroxicam polymorphs), both polymorphs can amorphize due to slower recrystallization of amorphous phase generated, indicated by higher configurational entropy (Table 6.3). Therefore, amorphization behaviors do not appear sensitive to crystal packing for these two types of molecules. However, for polymorphs of molecules with intermediate MW (250 - 300 g/mol), amorphization is sensitive to crystal packing. Form II sulfamerazine polymorph has stronger lattice and belongs to Class I crystal according to the Amorphization Classification System (see chapter 5 for explanation). Form I polymorph belongs to Class IV because of its weak crystal lattice. Form II crystal lattice is sufficiently strong to resist significant amorphization by milling. Crystallization into Form II is also easier because of the lower entropic barrier to crystallization (Table 6.3). That explains why amorphous phase generated from milling Form I crystal crystallizes into Form II, despite the abundant Form I seeds in the milled material.

6.4 CONCLUSIONS

Molecular weight is a relatively reliable parameter for predicting amorphization of organic crystals, where high molecular weight is required to avoid fast elimination of the amorphous phase generated by milling. This effect of molecular weight is explained based on the configurational molecular flexibility in the amorphous phase, as measured by excess entropy, and molecular mobility. It is clear that lower molecular weight materials have faster mobility in the amorphous phase, which explains their lower activation energy to recrystallize.

Chapter 7.

Modulating amorphization of drug crystals through cocrystallization

Based on the knowledge of the concurrent influence of crystal lattice strength and amorphous stability on amorphization potential of crystals, in this chapter, our objective is to assess the utility of using cocrystals to modify the amorphization potential of drugs. The model compounds are sulfamethazine (SMT) and its 1:1 cocrystals with p-hydroxybenzoic acid (HBA) and benzamide (BZM). The stability of melt-quenched amorphous follows the order of SMT-HBA > SMT-BZM > SMT, based on both configurational entropy (ΔS_{conf}) and structural relaxation times calculated using Adam-Gibbs equation. The onset of amorphization is the earliest for the SMT-BZM cocrystal (~10 min cryomilling) and the most delayed for the SMT-HBA cocrystal (>30 min cryomilling), corresponding to the lowest and highest crystal lattice strength, respectively. However, the extent of amorphous conversion after 2hrs of milling follows a different rank order of glass stability, *i.e.,* SMT-HBA > SMT-BZM > SMT. The lowest net conversion of the SMT is explained by its faster recrystallization propensity, despite an earlier amorphization onset. This work illustrates that cocrystals may be used to either minimize unintended amorphization of crystalline drugs during processing or enable the preparation of stable amorphous drug products.

7.1 INTRODUCTION

An objective of crystal engineering is to create new functional materials having desired physicochemical and mechanical properties by modifying the molecular packing in crystalline solids.[1, 2] A useful approach in crystal engineering is cocrystallization, where two or more non-volatile components crystallize in stoichiometric ratios within the same crystalline structure.[2, 3] To be distinguished from salts, at least one of the components must be neutral, irrespective of the temperature. Cocrystals have found utility in modifying a number of pharmaceutical properties,[4] such as physical stability,[5] chemical stability,[6] solubility and bioavailability,[7] and mechanical properties.[8, 9]

The purpose of this work is to demonstrate the feasibility to modify the amorphization potential of crystalline drugs by cocrystallization. Amorphous solids, unlike crystals, lack three-dimensional long range molecular order, and possess higher free energy.[10, 11] For pharmaceutical applications, the generation of amorphous phase can either be intentional or unintentional. Intentional amorphous conversion of crystals is desired to enhance the 'apparent' solubility, dissolution kinetics, and bioavailability of poorly soluble drugs,[11] which constitute a large number of newer drug molecules.[12, 13] Sometimes, amorphous solids may also exhibit better chemical stability than their crystalline counterparts.[14] A key challenge in intentionally developing an amorphous drug product is to maintain the physical stability. On the other hand, mechanical stress involved in processing operations, such as milling, can lead to unintended amorphization.[15-18] This usually leads to problems, such as deteriorated physicochemical

stability, variable dissolution kinetics, and issues with manufacturing the drug product.[19, 20]

The amorphization potential of a crystal may be defined as "the ability to form a stable amorphous phase within pharmaceutically relevant timescales". Our previous work with solid-state amorphization (chapters 5 and 6) has revealed that the amorphization potential is dependent on both the crystal lattice strength (which dictates the ease of amorphous generation) and amorphous stability (which dictates amorphous elimination through recrystallization). In essence, the observed solid-state amorphization of a crystal is the net outcome of a balance between the amorphous generation and elimination processes. This differs from other amorphization routes where a liquid intermediate is involved, for instance melt-quenching, lyophilization or spray drying,[10] where only the stability of glass directs the outcome of the process.

The solid-state amorphization behaviors of single component crystals, both pharmaceutical[15-17, 21-24] and non-pharmaceutical,[25-27] have been widely investigated. In this work, we are interested in probing the solid-state amorphization potential of multi-component cocrystals in an effort to examine the effectiveness of cocrystallization as a strategy to alter the amorphization potential of drug crystals by influencing both the crystal lattice strength and the stability of the amorphous glass. The exploration of cocrystal glass opens up interesting new opportunities to widen the solid-state landscape of drugs.

7.2 MATERIALS AND METHODS

7.2.1 Materials

Sulfamethazine (SMT), p-Hydroxybenzoic acid (HBA), and benzamide (BZM) were purchased from Sigma–Aldrich, Inc. (St. Louis, MO, USA). Their molecular structures are shown in Figure 7.1. The cocrystals have been previously reported.[28] Some of the basic properties of the drug and cocrystals are summarized in Table 7.1. SMT is used in this study based on the earlier observation that it underwent significant amorphization on cryomilling.

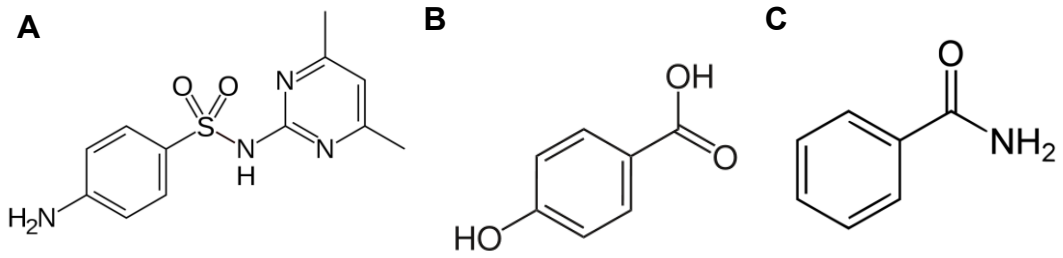

Figure 7.1. Molecular structures of sulfamethazine (A) and coformers p-hydroxybenzoic acid (B) and benzamide (C)

7.2.2 Preparation of bulk cocrystals and phase identification

SMT-HBA cocrystal: 2.78 g of SMT and 1.38 g of HBA were suspended in 60 mL of acetonitrile in a conical flask under ambient conditions (23.6°C, 48.4% RH). The suspension was stirred under stable vortex using a magnetic stirrer for 3 days. The flask, was covered with parafilm to avoid loss of solvent during the course of stirring.

SMT-BZM cocrystal: 2.78 g SMT and 1.21 g BZM were suspended in 90 mL of acetonitrile in a conical flask under ambient conditions (23.6°C, 48.4% RH). The

suspension was stirred under stable vortex using a magnetic stirrer for 5 days. The flask, was covered with parafilm to avoid loss of solvent during the course of stirring.

Table 7.1. Molecular properties of sulfamethazine (SMT), sulfamethazine-hydroxybenzoic acid cocrystal (SMT-HBA) and sulfamethazine-benzamide cocrystal (SMT-BZM). Data represented as mean ± standard deviation of measurement in DSC (n=3). A heating rate of 10K/min was used in DSC to estimate the melting point and enthalpy. Heat capacity at T_g was obtained using a heating rate of 2K/min

Material	Molecular weight (g/mol)	Melting point (K)	Melting enthalpy (J/g)	Glass transition, T_g (K)	ΔC_p at T_g (J/g-K)
SMT	278.33	471.6 ± 1.9	111.9 ± 2.1	343.0 ± 0.6	0.783 ± 0.052
SMT-HBA	416.45	492.4 ± 1.3	201.2 ± 1.2	350.3 ± 1.1	0.338 ± 0.021
SMT-BZM	399.47	458.4 ± 1.5	165.3 ± 0.9	306.6 ± 0.8	0.554 ± 0.038

Glass transition temperatures (T_g) are reported as the mid-points of the glass transition events determined from the reversing heat capacity (rev C_p) signal. Melting temperatures are reported as the extrapolated onset temperatures. Enthalpies of fusion events have been obtained by integrating the peaks using sigmoidal baseline.

The conversion of coformers to cocrystals was monitored by examining the phase purity of each suspended solid. For this purpose, an aliquot of the suspension was withdrawn, filtered, and vacuum dried at room temperature. The solid was analyzed using powder X-ray diffractometry (PXRD, Bruker AXS D5005, Madison, WI). Experimental PXRD pattern was compared against patterns calculated from single crystal structures. The reference codes for the single crystal structures solved at room temperature are EXAMUM (SMT-HBA 1:1 cocrystal) and EXAPAV (SMT:BZM 1:1

cocrystal). The bulk powder was harvested after a confirmation of complete conversion to the cocrystal and the phase purity of the final powder was again verified using PXRD.

7.2.3 Assessment of solid-state amorphization

Approximately 2g of crystalline powder for each material was cryomilled in a liquid nitrogen bath at ~77K (6750 Freezer Mill, SPEX CertiPrep, Metuchen, NJ) for up to 2 hours, with intermittent sample withdrawal at short (10 min) and long (>30 min) milling times. Samples were milled under the impact of a magnetically-driven cylindrical stainless-steel milling bar on to two stainless-steel lids of a polycarbonate tube containing the samples. Before milling started, the milling assembly along with the sample, was pre-cooled at liquid nitrogen temperature (~77K) for 2 minutes. Milling was conducted at a rate of 10 impacts per second. A 2 min cooling period was employed after each 2min of milling. Cryomilled samples were removed from the milling chamber inside a glove box purged with dry nitrogen and stored in desiccator containing anhydrous calcium sulfate (Dreirite®, W.A. Hammond Dreirite Co. Ltd., OH). Freshly milled samples were characterized typically within 5-10 minutes after sample withdrawal. Water content of milled samples was <0.5 wt% measured using thermogravimetric analysis (TGA Q500, TA Instruments, New Castle, DE).

A powder X-ray diffractometer (D8 Advance, Bruker AXS, Madison, WI) with CuK_α radiation and scintillation counter detector was used to verify phase purity of the starting materials (drug and cocrystals), melt-quenched glasses, and milled samples. The

diffractometer was calibrated using corundum standard (SRM 674b, NIST) at d = 2.0852Å. Diffraction data were collected over 5 - 35º 2θ angles, with step size of 0.05º and dwell time of 1s. Milled samples were directly packed into the sample holder. Melt-quenched glasses were mildly ground using mortar and pestle before being packed for PXRD studies. All samples were packed into the sample holder by top filling method. PXRD data were collected using the Diffrac Plus XRD commander software (Bruker, AXS). Data analysis was performed using JADE (version 8, Materials Data Inc., Livermore, CA). Crystallinity loss of the milled samples, as function of milling time, was quantified using powder X-ray diffractometry with step size of 0.02º and dwell time of 4s, using specific peaks for each of the three materials: 20.0° 2θ (SMT), 19.1° 2θ (SMT-HBA), and 20.4° 2θ (SMT-BZM).

7.2.4 Calorimetric assessment of lattice strength

The lattice strength of crystals has been estimated using the "lattice enthalpy of fusion" of crystals at the temperature of milling (H_f^{77K}) by performing a heat capacity correction between liquid and crystal extrapolated to 77 K assuming linear dependence of delta heat capacity on temperature below T_g (equation 1).

$$H_f^{77K} = H_f - \int_{77K}^{T_m} \Delta C_p^{l-x} \, dT \qquad (1)$$

where T_m is the melting temperature of the crystal in Kelvin. H_f^{77K} is the energy required to covert the crystal to a disordered phase at 77 K. For crystals with very different melting points, the enthalpy of fusion at the melting temperature cannot be

reliably used to measure the lattice strength because the heat capacity is temperature and material dependent. The hypothetical "fusion enthalpy" at a fixed temperature, described here, is a more appropriate parameter to compare the lattice strength of different crystals. The temperature should be relevant to the process of interest where amorphous is generated, which is 77 K in this study.

7.2.5 Amorphous stability

Amorphous stability is influenced both by thermodynamic and kinetic factors.[29] In this study, the thermodynamic stability was quantified by deriving the configurational entropy (ΔS_{conf}) of the amorphous phase using heat capacity data. Molecular mobility, was obtained from entropy data through Adam-Gibbs equation.[30] Kinetic stability was evaluated using activation energy of crystallization during non-isothermal heating in DSC.

Configurational parameters: The excess configurational entropy of non-equilibrium amorphous phase (*in* situ melt-quenched glass) was quantified using the configurational heat capacity ($C_{p\ conf}$), defined as the difference in the measured heat capacities between the amorphous and the crystalline phases (equation 2).

$$C_{p\ conf} = C_{p\ amorphous} - C_{p\ crystal} \qquad (2)$$

The configurational entropy barrier to crystallization (ΔS_{conf}) is a measure of configurational flexibility of molecules and may be computed by integrating the

configurational heat capacity as a function of temperature and using information on fusion enthalpy, ΔH_m, of each material (equation 3).[31, 32]

$$\Delta S_{conf} = \Delta S_{melt} + \int_{T_m}^{298\,K} \frac{C_{p\ conf}}{T}\, dT = \frac{\Delta H_{melt}}{T_{melt}} + \int_{T_m}^{298\,K} \frac{C_{p\ conf}}{T}\, dT \qquad (3)$$

Configurational entropy is then correlated with global molecular mobility above T_g through the Adam-Gibbs theory for the drug and cocrystal.[30] Adam-Gibbs theory suggests that the mean structural relaxation times of molecules in the supercooled liquid phase (τ_{calc}) may be calculated using equation 4. The global molecular mobility above T_g is measured by $1/\tau_{calc}$. Faster mobility, or shorter τ_{calc}, indicates less stable glass.[29]

$$\tau_{calc} = \tau_{\infty} \exp\left(\frac{C}{T\,\Delta S_{conf}}\right) \qquad (4)$$

In this equation, τ_∞ is the structural relaxation time constant at infinite temperature (typically taken as 10^{-14} sec corresponding to the mobility at fusion), C is a temperature independent but material dependent constant, and T is the absolute temperature. First, at $T=T_g$, the Adam-Gibbs theory is evaluated to derive the value of constant C using a structural relaxation time of 100 s. The ΔS_{conf} at T_g is calculated from the configurational heat capacity data according to equation 3. Once C is determined, the τ_{calc} values at a desired temperature can be calculated based on the corresponding ΔS_{conf}.

Configurational parameters were calculated using experimental data from differential scanning calorimetry (DSC Q1000 or Q2000, TA Instruments, New Castle, DE). The

baseline of DSC was calibrated using empty cell, followed by sapphire disc. The temperature and enthalpy calibrations were done using high purity indium (standard mode, ramp rate of 10K/min). Heat capacity was calibrated using crystalline sucrose, where the heat capacity constants (ratio of theoretical to actual C_p) were 0.988 for the direct signal and 1.049 for the reversing signal (acceptable C_p constant range: 0.9 - 1.1). Hermetically sealed aluminum pans (TA Instruments) without pinholes were used. The DSC cell was purged with nitrogen, at a purge rate of 50 mL/min. A low purge flow rate of nitrogen (~5 mL/min) was used to improve the accuracy of heat capacity measurements by minimizing thermal fluctuations. For modulated DSC, a sinusoidal modulation of ±1K was employed every 100 seconds, with a ramp rate of 2K/min.

7.3 RESULTS AND DISCUSSIONS

7.3.1 Phase nature of the starting materials

The phase purity of sulfamethazine and the two cocrystal powders was verified using powder X-ray diffractometry (Figure 7.2), by matching the bulk powder X-ray diffraction profiles with the calculated diffraction patterns obtained from single crystal structures solved at room temperature.

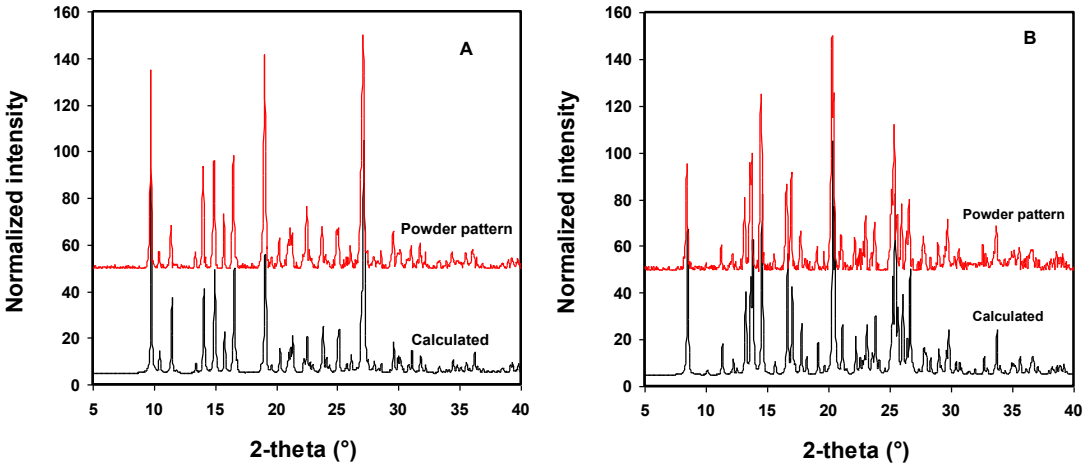

Figure 7.2. Phase purity of (A) SMT-HBA cocrystal, and (B) SMT-BZM cocrystal bulk powders tested by matching powder X-ray diffraction patterns with those calculated from single crystal structures.

7.3.2 Solid-state amorphization potential of cocrystals

Sulfamethazine and the two cocrystals were cryomilled separately for up to a total milling duration of 2 hours. Intermittent samples were withdrawn for tracking the crystallinity as a function of time. Figures 7.3 and 7.4 show the powder X-ray diffraction patterns of the sulfamethazine cocrystals, milled for various time points, along with their melt-quenched glasses. The SMT-HBA cocrystal is not amorphized up to 30 min of cryomilling but partially amorphized after longer milling as shown by the amorphous halo in the PXRD patterns and the reduced intensity diffraction peaks (Figure 7.3). In comparison, the melt-quenched cocrystal glass is fully X-ray amorphous.

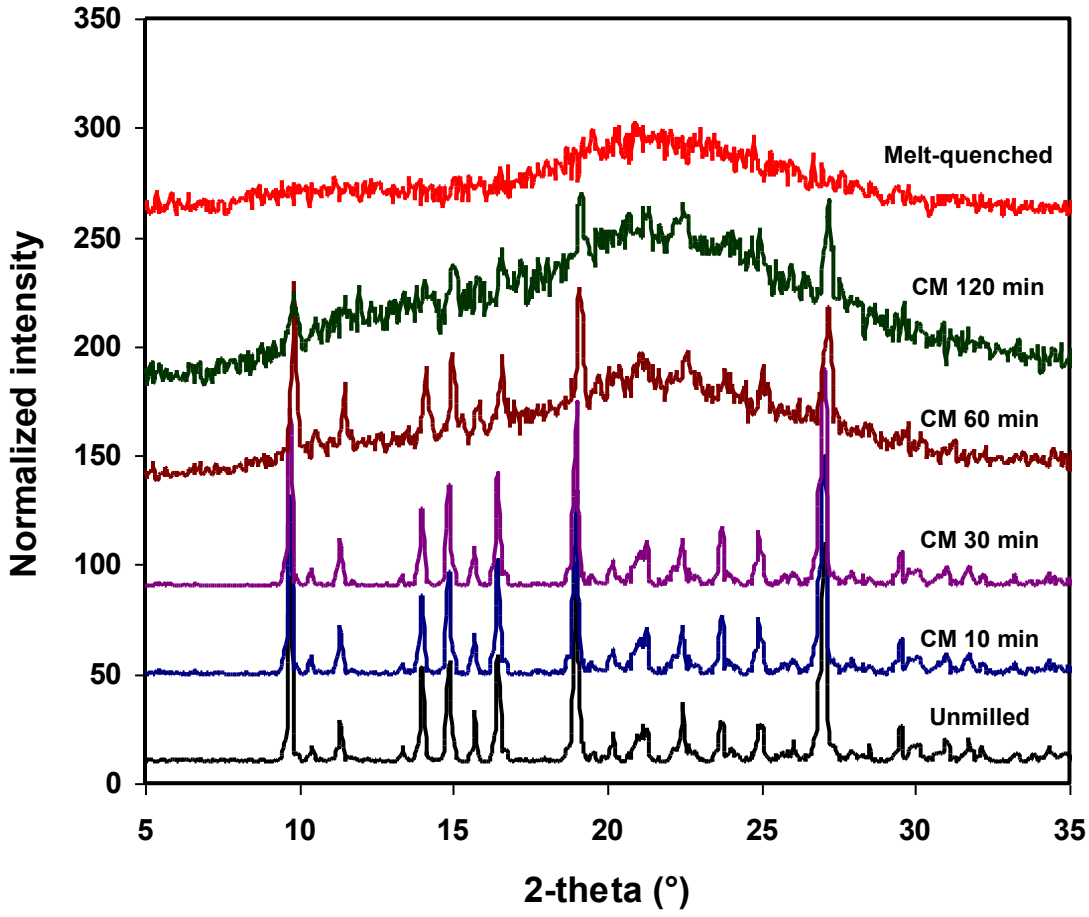

Figure 7.3. Solid-state amorphization of 1:1 cocrystal of sulfamethazine and 4-hydroxybenzoic acid (SMT-HBA): Powder X-ray diffraction overlay of unmilled, cryomilled (CM) and melt-quenched samples. The melt-quenched cocrystal is completely X-ray amorphous, while the cryomilled samples milled for greater than 30 min are partially amorphous.

In comparison, the SMT-BZM cocrystal has a much earlier amorphization onset, with amorphization clearly detected after 10 min cryomilling (Figure 7.4). Powders were only partially amorphous even after 2 hrs of milling.

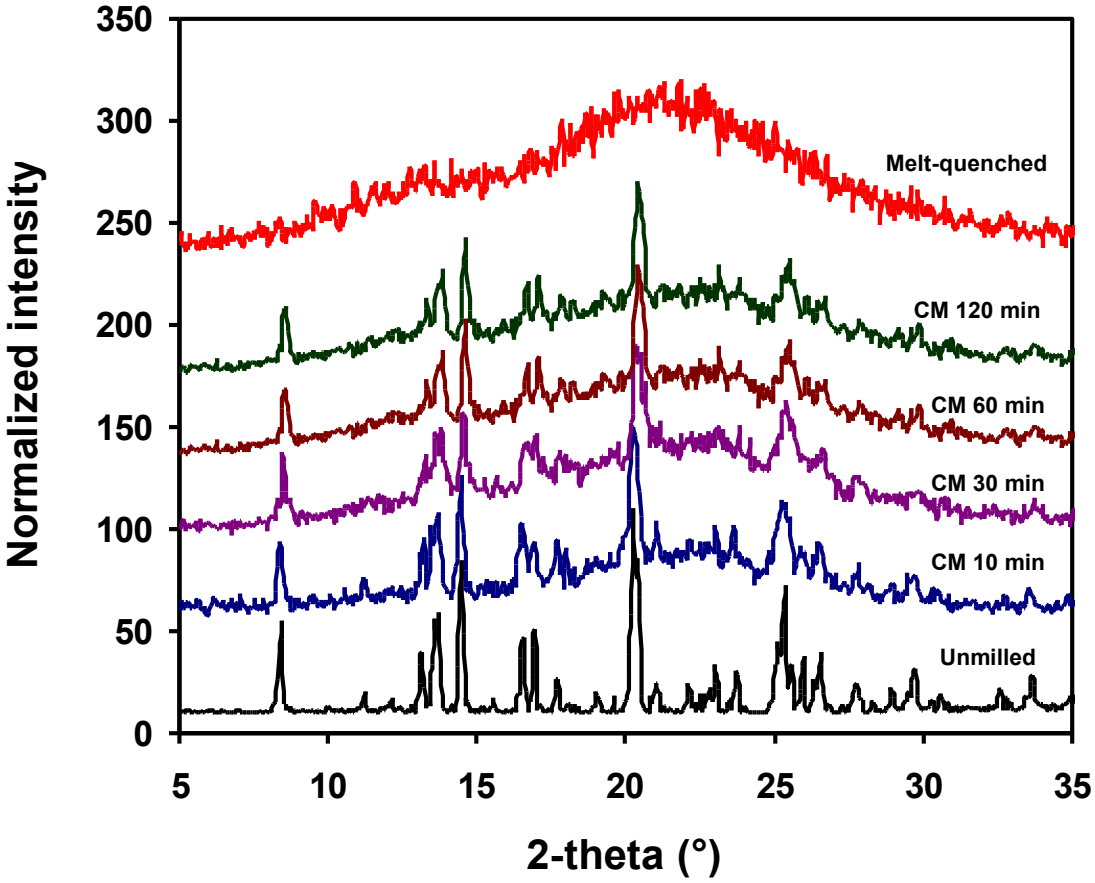

Figure 7.4. Solid-state amorphization of 1:1 cocrystal of sulfamethazine and benzamide (SMT-BZM): Powder X-ray diffraction overlay of unmilled, cryomilled (CM) and melt-quenched samples. The melt-quenched cocrystal is completely X-ray amorphous, while the samples milled for 10 min or greater are partially amorphous.

Table 7.1 summarizes the glass transition temperatures and heat capacity changes at T_g of melt-quenched glasses by modulated DSC analysis. T_g of all materials are approximately 0.71 - 0.76 times the melting point in Kelvin, consistent with most compounds.[33, 34] The milled samples have smaller ΔC_p at T_g than melt-quenched glasses, attributed to the partial amorphous nature of the milled samples, indicated by PXRD. For

example, for the 1 hour cryomilled cocrystals, the ratio of ΔC_p^{Tg} for milled and melt-quenched glass are 0.57 (SMT-HBA cocrystal) and 0.41 (SMT-BZM cocrystal).

The solid-state amorphization behavior of sulfamethazine is illustrated in Figure 7.5, along with the PXRD profile of melt-quenched glass. Similar to the two cocrystals. the milled samples are only partly amorphous.

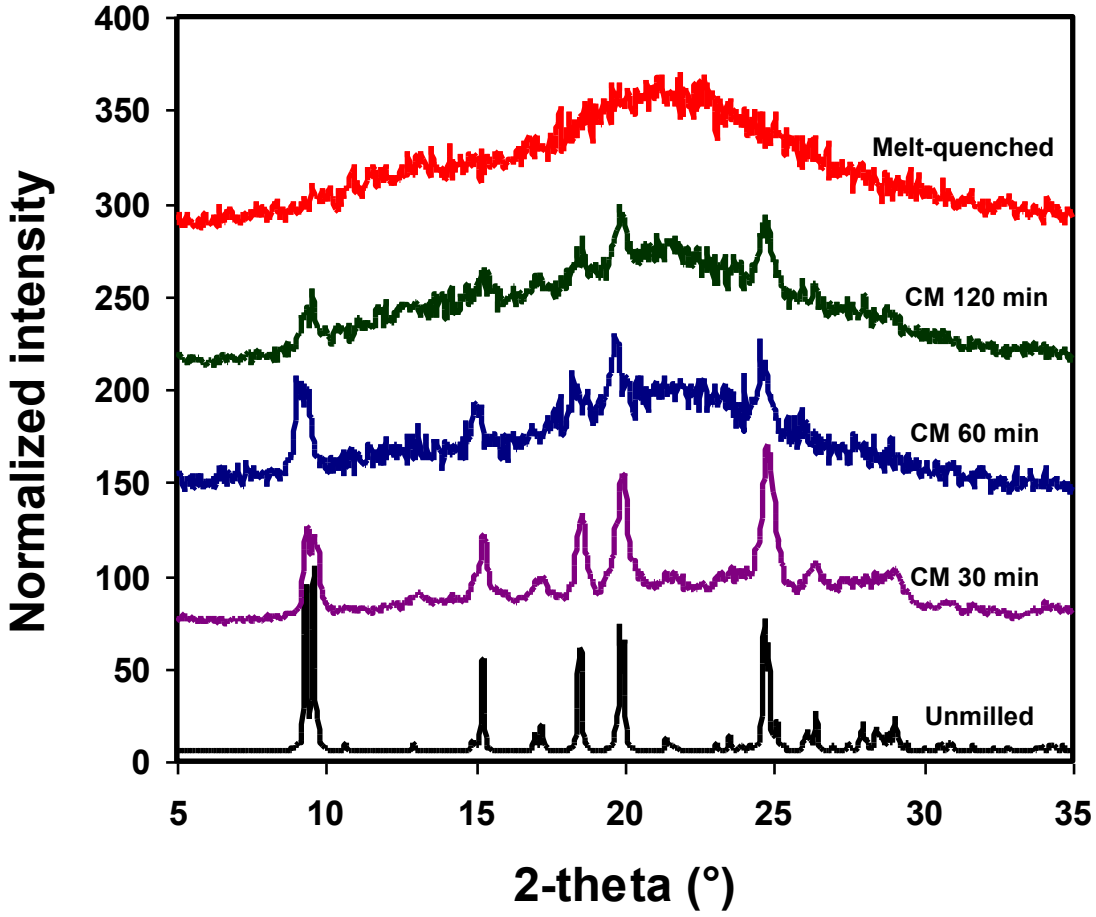

Figure 7.5. Solid-state amorphization of sulfamethazine: Powder X-ray diffraction patterns for unmilled and cryomilled (CM). Beyond 30 min of cryomilling, characteristic features of both amorphous halo and crystal peaks are visible.

Figure 7.6 shows the loss in crystallinity as a function of milling duration for SMT and the two cocrystals. At short milling times (<30 min milling), the order of the observed amorphization follows SMT-BZM cocrystal > SMT >> SMT-HBA cocrystal. However, after 2 hours of milling, the order of amorphization is changed into SMT-HBA cocrystal > SMT-BZM cocrystal > SMT.

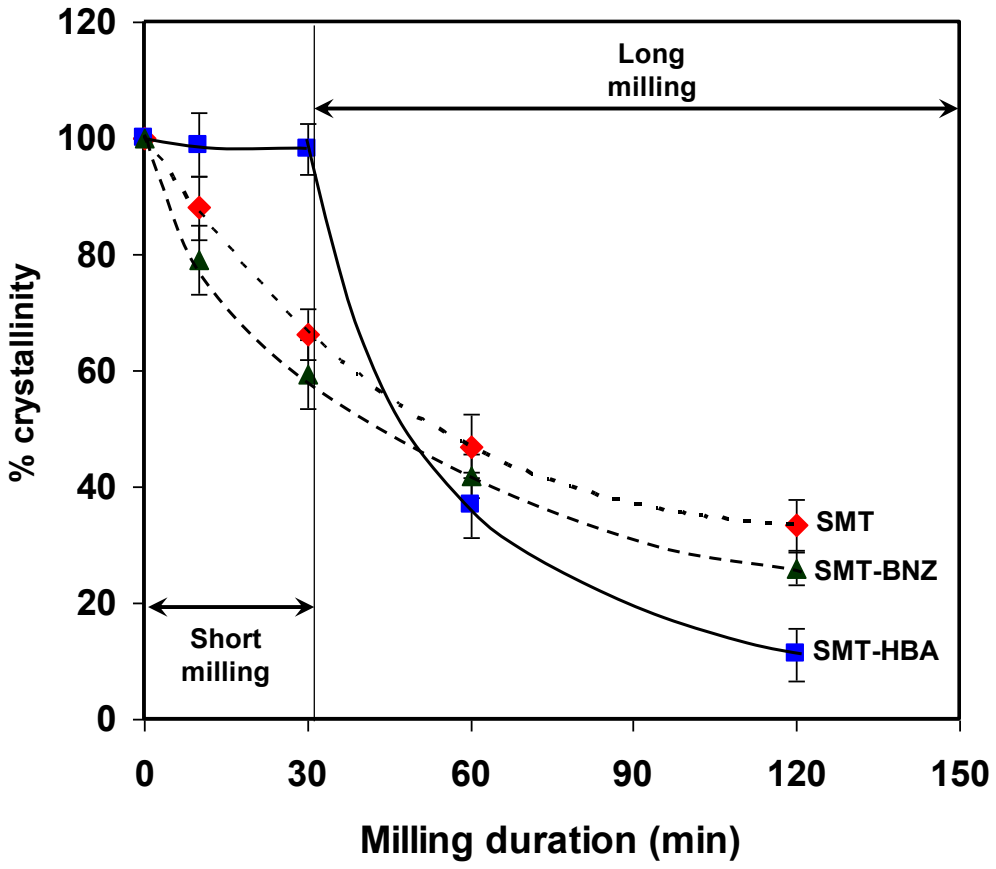

Figure 7.6. Loss of crystallinity on milling for various materials, tracked by powder X-ray diffractometry (0.02° steps, 4s dwell time).

The different amorphization behaviors indicate that the cocrystallization approach is effective in modulating the amorphization potential of drugs. However, the effect depends on the level of stress applied (milling duration in this study). As we have shown earlier, crystal amorphization is influenced by crystal lattice strength (affecting the amorphous generation) and amorphous stability (affecting amorphous elimination). Hence, a mechanistic understanding of the effect of cocrystallization on amorphization potential requires simultaneous consideration of these two aspects..

7.3.3 Crystal lattice strength

The lattice strength of the three materials may be assessed using H_f^{77K}, which are summarized in Table 7.2. A higher value of H_f^{77K} indicates a higher energy requirement to completely disrupt the crystal packing and convert the crystal into the disordered phase. The rank orders of H_f^{77K} and amorphization onset time are identical: SMT-HBA cocrystal >> SMT-BZM cocrystal > SMT. This confirms that a stronger crystal lattice is more resistant to disruption by mechanical means. The stronger lattice of SMT-HBA is also supported by FT-IR data (Table 7.2). SMT-HBA shows a shift of -86 units in the stretching frequency for the amine group (predominant hydrogen bond in both cocrystals involve N-H as donor), compared to only -8 units for the SMT-BZM cocrystal, with respect to the SMT. Since a stronger hydrogen bond will produce a larger shift to a lower wave number,[35] the IR data suggest that SMT-HBA structure involves significantly stronger hydrogen bonds, which is expected to stabilize its lattice.

Table 7.2. Lattice strength of sulfamethazine, sulfamethazine - hydroxybenzoic acid cocrystal, and sulfamethazine - benzamide cocrystal measured by quantifying fusion enthalpy extrapolated to the milling temperature. Data represented as mean ± 1 standard deviation of measurement in DSC (n=3).

Crystal	$\Delta C_p^{l\text{-}c}$ (J /mol-K)	Fusion enthalpy at 77K (KJ/mol)	IR stretching frequency $\nu(NH_2)$ assym cm^{-1} †
SMT	61.15 ± 1.01	13.65 ± 2.41	3443
SMT-HBA	82.01 ± 5.76	55.36 ± 4.13	3357 (-86)
SMT-BZM	146.77 ± 4.98	20.64 ± 2.24	3435 (-8)

† The numbers in brackets indicate frequency shifts compared to groups in SMT crystal.

The relative hydrogen bond strength among the cocrystals is further illustrated by an analysis of their molecular packing motifs (Figure 7.7). Sulfamethazine can potentially have two hydrogen bond donors, amine -NH_2 and sulfonamide –NH. The hydrogen bonding propensity and its ability to tautomerize between amidine and imidine forms render sulfamethazine a good cocrystal former.[28] In the SMT-HBA cocrystal, the coformers form a tetramer, with three moderately strong intermolecular hydrogen bonds involved. The hydroxyl moiety from HBA interacts with amine group of SMT through an O-H···N hydrogen bond (2.83Å, room temperature). Two other hydrogen bonds are formed using the imidine site in SMT with HBA: O-H···N hydrogen bond (2.79Å, room temperature) and N-H···O hydrogen bond (2.76Å, room temperature). All possible hydrogen bond donors and acceptors are utilized in this structure. In SMT-BZM

cocrystal, there is a dimer formation between the SMT imidine tautomer and benzamide via N-H···O (2.9279Å, room temperature) and N-H···N (2.7Å, room temperature) hydrogen bonds. The stronger H-bonding interaction in SMT-HBA supports the IR data and suggests it is more difficult to displace molecules from their original positions in the crystal during milling. This is in agreement with the longer onset time of milling induced amorphization. SMT also forms hydrogen bonded dimers with, but using very weak N-H···N hydrogen bonds (~3.1Å), which explains its faster amorphization onset.

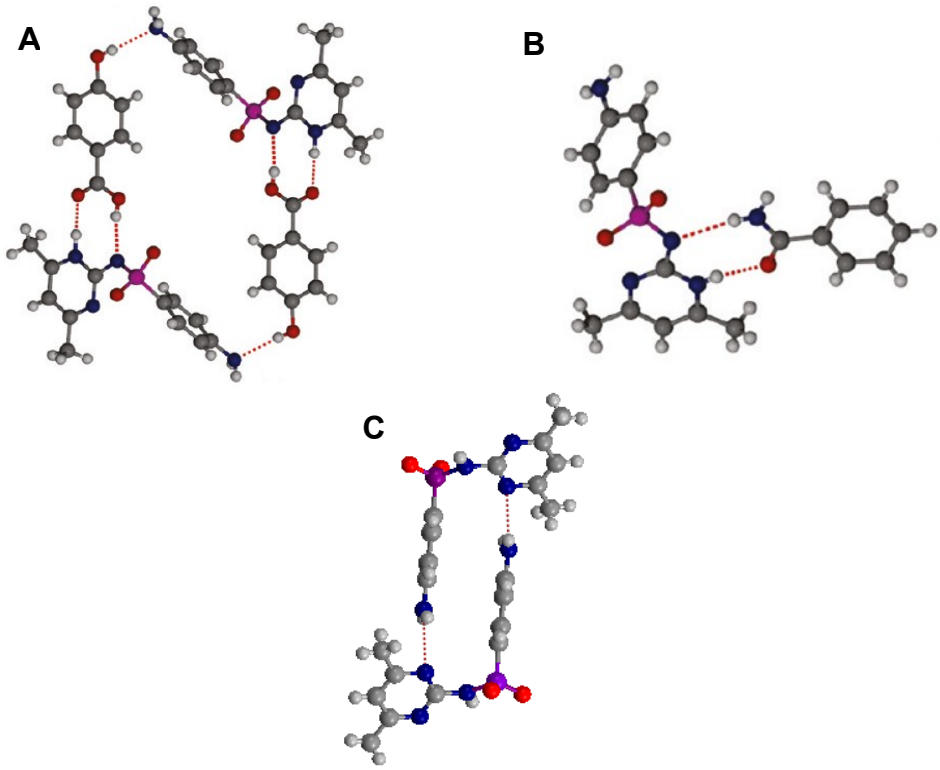

Figure 7.7. Basic supramolecular motif in crystal lattice of **(A)** sulfamethazine-hydroxybenzoic acid cocrystal tetramer, **(B)** sulfamethazine-benzamide cocrystal dimer, and **(C)** sulfamethazine dimer.

7.3.4 Amorphous stability considerations

Amorphous stability of sulfamethazine and the two cocrystal glasses was assessed using both the thermodynamic (configurational entropy) and kinetic (calculated mobility, fragility, and activation energy of crystallization) parameters. Figure 7.8 illustrates the concept of configurational difference between amorphous and crystal, using SMT-BZM as an example. The heat capacity of glass and the supercooled liquid is higher than that of the crystal, consistent with the laws of thermodynamics.

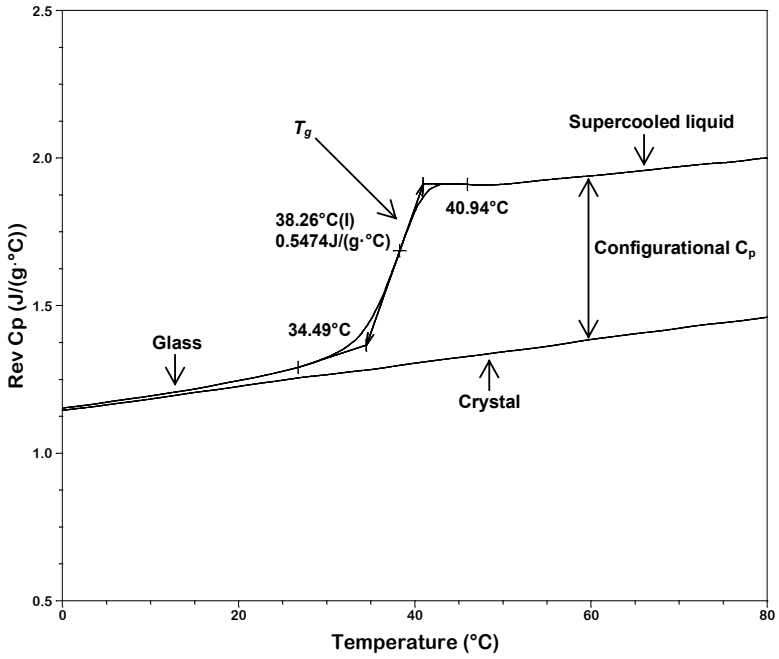

Figure 7.8. Heat capacity *versus* temperature plot for sulfamethazine-benzamide (SMT-BZM) cocrystal showing the slope changes in the heat capacities of the crystal, glass, and supercooled liquid, along with the step change in heat capacity at the glass transition. A modulated DSC was used at 2K/min heating rate with a modulation of ±1K every 100 seconds. Also shown is the configurational heat capacity difference between amorphous and crystal.

Figure 7.9 shows the configurational entropy, which is calculated based on heat capacity, of the three amorphous materials as a function of temperature. At any given temperature the rank order of configurational entropy follows: SMT-HBA > SMT-BZM > SMT. It has been shown using compounds such as ritonavir and acetaminophen that a higher configurational entropy indicates a larger number of possible molecular configurations in the amorphous phase, which is expected to retard crystallization.[31] In other words, crystallization is facilitated when molecules can easily assume proper configurations, *i.e.,* when they have lower configurational entropy. Therefore, SMT glass can be expected to be the fastest crystallizer, while the crystallization from SMT-HBA glass is expected to be the slowest.

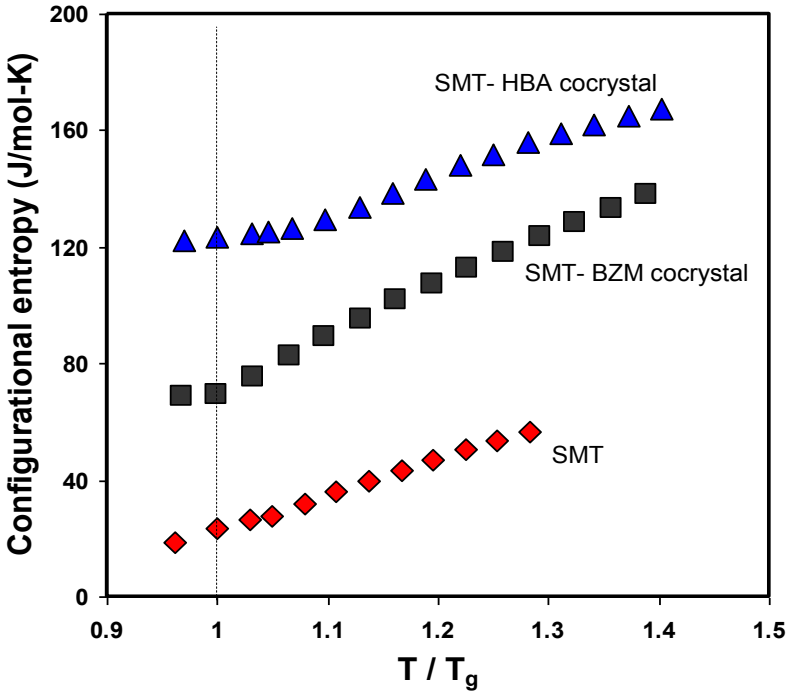

Figure 7.9. Thermal variations of configurational entropy ($S^{amorph} - S^{cryst}$) of sulfamethazine (SMT), sulfamethazine-benzamide cocrystal (SMT-BZM), and sulfamethazine-hydroxybenzoic acid cocrystal (SMT-HBA) glasses. The dotted line indicates the glass transition temperature.

The influence of configurational entropy on amorphous stability can be explained from the viewpoint of global molecular mobility. Studies have shown that the mean global mobility can be either completely or partially coupled with amorphous crystallization, with a faster mobility indicating faster crystallization.[36-38] Mean molecular mobility above T_g can be calculated using Adam-Gibbs theory,[30] which allows us to connect the configurational entropy with the structural relaxation times. The calculated structural relaxation times, on logarithmic scale, are plotted for the three materials in Figure 7.10A. This plot, known as the Angell plot,[39] indicates the deviation of the structural relaxation times from the Arrhenius relationship above T_g,[40] and may be used to classify materials into strong or fragile glass formers. A strong glass former will show a longer relaxation time (more stable glass) with less deviation from Arrhenius relationship as T_g is approached. By this measure, SMT glass is the most fragile, while SMT-HBA glass is the least. A higher ΔC_p at the glass transition for SMT also indicates higher fragility.[41]

Based on the structural relaxation times, the global molecular mobility is calculated as the inverse of relaxation time. The general term, "molecular mobility" includes global mobility (α relaxation), *i.e.,* the mobility associated with glass transition, and secondary[42, 43] and surface[44] relaxations below T_g. Global mobility has shown promising correlations with crystallization in many cases.[42, 43, 45, 46] In this work, the material with the lowest configurational entropy, SMT, has the fastest calculated global mobility

(Figure 7.10B). In fact, there are orders of magnitude differences in the mobility between the different glasses.

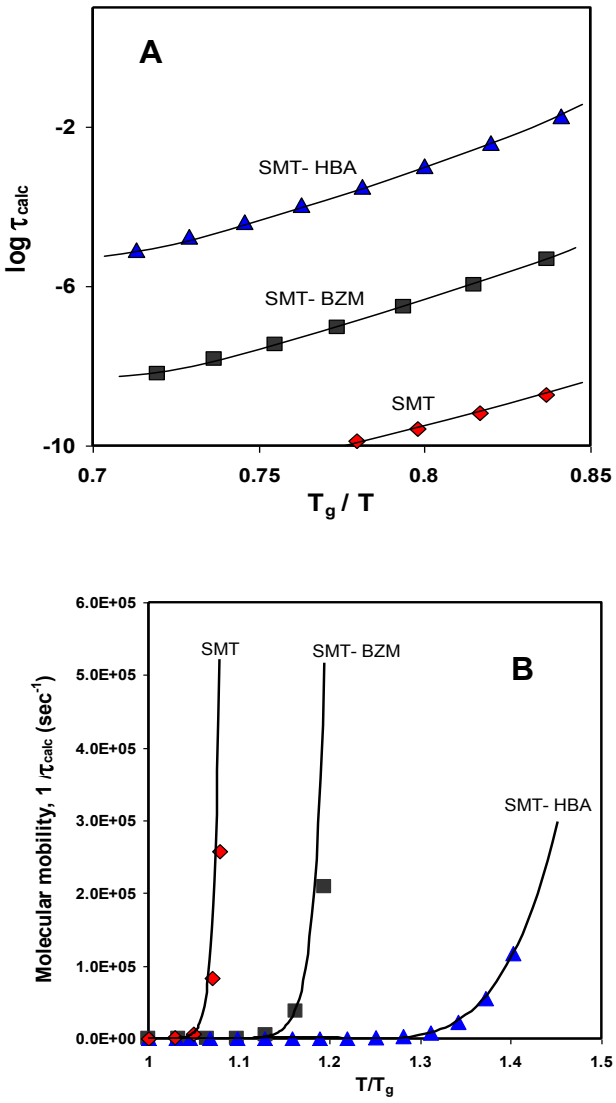

Figure 7.10. **(A)** Structural relaxation (fragility), and **(B)** global molecular mobility above the glass transition for sulfamethazine (SMT), sulfamethazine - benzamide cocrystal (SMT-BZM), and sulfamethazine - hydroxybenzoic acid cocrystal (SMZ-HBA). Mobility calculated based on Adam-Gibbs theory using configurational entropy data.

This significantly different mobility suggests the potentially different crystallization tendency of the three materials. To assess crystallization tendency, the activation energies (E_a) of non-isothermal crystallization were calculated for the three materials, using Avrami-Erofeev kinetic model of the third order.[47-49] E_a shows the following order of SMT (4.9 KJ/mol) < SMT-BZM (7.9 KJ/mol) < SMT-HBA (16.8 KJ/mol). This suggests that crystallization tendency follows the order of SMT > SMT-BZM > SMT-HBA, which is the same as that predicted based on configurational entropy or molecular mobility.

7.3.5 Explaining amorphization using lattice and amorphous stability data

The solid-state amorphization of the drug and the cocrystals has been found to depend on milling duration in our study. At short milling times, amorphization propensity follows the order of SMT-BZM > SMT >> SMT-HBA. SMT-HBA cocrystal has a much stronger lattice compared to the other two materials. This correlates well with the long amorphization onset of SMT-HBA and its low degree of amorphization at short milling times. The drug, SMT, has the weakest lattice, and is expected to amorphize the most at short milling times, contrary to the rank order observed. This apparent contradiction may be explained by the faster crystallization of amorphous SMT, which reduces the net amorphous conversion compared to that in the SMT-BZM cocrystal glass.

The amorphization behaviors after longer cryomilling can be explained in a similar manner. Here, SMT-HBA cocrystal shows the highest amorphous conversion, despite

the delayed onset. At longer milling times, the stress input is sufficient to disrupt the lattice packing in all three crystals (Figure 7.6). However, the amorphous SMT-HBA forms a kinetically more stable glass than the other two materials. Consequently, the amorphous generated for this material by milling can more easily accumulate with longer milling. This leads to its highest net amorphization after 2 hours of milling. The faster crystallization of SMT eliminates amorphous more effectively. Hence, its net amorphous conversion is lower despite its weaker crystal lattice and faster generation of amorphous phase. Thus, the seemingly complicated milling duration dependent amorphization behaviors of the three materials can be well explained by considering the interplay between crystal lattice strength and amorphous phase stability.

7.4 CONCLUSIONS

We have shown that cocrystallization is effective in modulating the amorphization potential of a drug. The relative ranking of amorphization potential of the SMT and two of its cocrystals depends on the milling duration. At short milling times (<30 min), the order of amorphization is SMT-BZM cocrystal > SMT >> SMT-HBA cocrystal. However, at long milling times (~2 hr), the amorphous conversion follows the rank order of SMT-HBA cocrystal > SMT-BZM cocrystal > SMT. The complex amorphization behaviors are explained by considering the concurrent influence of crystal lattice strength and amorphous phase stability of these materials. SMT-HBA cocrystal exhibits the longest onset time to amorphization because of its strongest crystal lattice. However, the amorphous phase of this material also has the highest configurational entropy and the

slowest molecular mobility, both favor slower recrystallization. This helps to kinetically stabilize the SMT-HBA amorphous phase that may be generated during milling. As a result, higher amorphous conversion is observed with longer milling. Systematic test of this concept using more cocrystal systems will be valuable to further elucidate the amorphization behavior of cocrystals.

Chapter 8.

Origin of two modes of non-isothermal crystallization of glasses generated by milling: Calorimetric assessment of role of amorphous surface structure in crystallization

This chapter is based on the following published research article: Chattoraj *et al.*, *Pharmaceutical Research*, 29, 1020–1032, 2012.

The purpose of this work is to mechanistically investigate the role of amorphous surface structure of milled materials in facilitating earlier crystallization onset, to explain the origin of two distinct non-isothermal crystallization modes, single-peak (unimodal) and two-peak (bimodal). Glasses of ten organic molecules were prepared by melt-quenching and cryogenic milling of crystals. Non-isothermal crystallization of glasses was monitored using differential scanning calorimetry and powder X-ray diffractometry. The non-isothermal crystallization of glass, generated by milling, is either unimodal or bimodal, while that of melt-quenched glass without being milled is always unimodal. The mode of crystallization of amorphous phase depends on the relative position of the crystallization onset (T_c) with respect to glass transition temperature (T_g), and can be explained by a surface crystallization model. Bimodal crystallization event is observed when T_c is below or near T_g, due to the fast crystallization onset at milled glass surfaces. Unimodal crystallization is observed when T_c is well above T_g. We have verified this model by intentionally inducing flip between the two crystallization modes for several compounds through manipulating glass surface area and T_c. Thus, the appearance of the two modes of non-isothermal crystallization of organic glasses is a result of the combined effects of faster surface crystallization and variation in specific surface area by milling.

8.1 INTRODUCTION

The crystallization of glasses is a topic of considerable interest to diverse research fields such as pharmaceuticals,[1, 2] food sciences,[3, 4] biochemicals [5] and inorganic material sciences.[6-8] Amorphous glasses can be generated either by evading crystallization through quenching of melts, vapor deposition, and freeze drying,[1, 2] or by mechanical activation of crystalline solids through processes such as milling,[9-12] which cause lattice disruption due to accumulation of crystal dislocations resulting from mechanical stress.[13] Irrespective of the route of amorphous generation, the amorphous phase of a solid lacks the three-dimensional long range molecular order characteristic of crystals and possesses higher free energy compared to corresponding crystalline states.[1, 14, 15] As a consequence of the higher free energy, amorphous solids are thermodynamically unstable and tend to reorder into a crystalline state.[1, 16] The physical instability of amorphous solids and their crystallization tendency are of particular importance in drug product development.[17-19]

The crystallization during heating of a glass usually emerges as a well-defined single exothermic event in DSC, *i.e.,* unimodal crystallization. However, two distinct exotherms or bimodal events have also been observed, especially during heating of amorphous phase generated through mechanical milling.[20, 21] Currently, there are different views in the literature regarding the possible physical origin of the appearance of bimodal exotherms. In one view, the bimodal exotherms were attributed to reordering of a milling-induced high energy mesophase (or a defective crystalline state), which is a phase thermodynamically distinct from the true amorphous glass.[20, 22] Others suggested

that the phenomenon may be a result of nuclei-induced glass surface crystallization followed by crystallization of bulk and amorphous particles free from crystal nuclei.[23] In addition, bimodal crystallization of melt-quenched D-mannitol [24] and nifedipine [25] glasses have been attributed to crystallization into two different polymorphs.

It appears that, despite considerable efforts in recent years, the physical basis of the bimodal phenomena remains elusive. This hinders the proper understanding of the nature of the instability of organic glasses displaying such a phenomenon and the development of effective strategies to stabilize them. In this work, we describe a model that can explain both the unimodal and bimodal crystallization behaviors of glasses, taking into consideration the relative positions of their crystallization and glass transition temperatures.

8.2 MATERIALS AND METHODS

8.2.1 Materials

A total of 10 crystalline drugs were selected as model compounds for this study (Table 8.1). Model compounds were selected on the basis of properties commonly thought to influence the amorphization tendency of crystals, such as the melting temperature and enthalpy of fusion (crystal lattice stability), and glass transition temperature (glass stability). All model compounds were used as received for amorphous preparation, and subsequent calorimetric and X-ray diffraction studies.

Table 8.1. Information on crystal forms of APIs milled, their melting points, enthalpies of fusion and glass transition temperatures (T_g). Reported T_g values are from the reversing C_p signal of modulated DSC. Other parameters have been obtained at a DSC heating rate of 10°C/min. Standard deviations are for three DSC measurements using independent samples.

Model compound	Form milled	Melting point (°C)	Enthalpy of fusion (J/g)	T_g (°C)	Supplier
Dipyridamole (DPD)	Form I	161.5±0.13	65.4±2.2	40.2±0.4	Aldrich
Ketoconazole (KNZ)	NA[a]	145.9±0.16	102.5±2.1	42.4±0.3	PHHA Assoc.
Indomethacin (IMC)	Form γ	160.2±0.69	109.1±1.2	46.2±0.3	Sigma-Aldrich
Sulfamethazine (SMT)	Form I	196.2±0.33	111.9±2.1	74.3±0.3	AK Scientific
Terfenadine (TFD)	Form I	151.0±0.25	109.8±0.6	58.6±0.3	Sigma-Aldrich
Felodipine (FLD)	Form I	140.5±0.75	74.5±1.4	46.9±0.2	Aldrich
Sulfamerazine (SMZ)	Form I	235.9±0.73	149.4±2.3	62.5±3.1	Sigma-Aldrich
Piroxicam (PRX)	Form β	200.6±0.37	118.2±3.0	63.0±0.2	Sigma
Griseofulvin (GRF)	NA[a]	219.6±0.42	111.8±1.2	91.3±0.1	Sigma-Aldrich
Hydrochlorothiazide (HCT)	Form I	267.6 ± 0.19	97.2±2.1	118.9±1.1	Sigma-Aldrich

[a] No known polymorph.

8.2.2 Preparation of amorphous phase

Amorphous glass for each model compound was prepared by cryogenic milling of crystals and quenching of melts. For cryomilling, approximately 2g of crystalline powder was milled in a polycarbonate tube submerged in liquid nitrogen bath (6750 Freezer Mill, SPEX CertiPrep, Metuchen, NJ). In this technique, a sample is milled when a magnetically-driven cylindrical stainless-steel milling bar impacts two stainless-steel lids of a polycarbonate tube within which the sample is enclosed. Before milling, the whole milling assembly was pre-cooled in liquid nitrogen (~77K) for 2 minutes. Milling was conducted at a rate of 10 impacts per second. A 2min cooling period was employed after every 2min of milling. Samples were withdrawn inside a glove box under a dry nitrogen purge at various time points during milling, and stored in a desiccator containing

anhydrous calcium sulfate (Dreirite®, W.A. Hammond Dreirite Co. Ltd., OH). Thermal and X-ray characterization on freshly milled samples were performed typically within 5-10 minutes after sample withdrawal. Amorphous glasses were also prepared by *ex situ* melt-quenching. Samples were melted in aluminum pans inside a glove box purged with dry nitrogen. Care was taken to ensure complete melting of the powders while avoiding decomposition of samples. Once the sample melted, it was quenched by placing the sample pan on a steel surface (~10ºC) inside the glove box. This melt-quenching technique was suitable for preparing amorphous phase for all compounds in this study.

8.2.3 Non-isothermal crystallization studies

Crystallization studies were done using a differential scanning calorimeter (DSC, either Q1000 or Q2000, TA Instruments, New Castle, DE) equipped with a refrigerated cooling system. The DSC cell was purged with nitrogen at a rate of 50 mL/min. The baseline of DSC was initially calibrated using an empty DSC cell, followed by placing sapphire discs, without pans, directly on the reference and sample positions. The temperature and enthalpy calibrations were done using indium. Hermetically sealed aluminum pans without pinholes were used for all studies. To enhance thermal contact with samples, pans were hermetically sealed by crimping the pan lids upside down to minimize headspace within the sealed pans. For standard DSC runs, ramp rate of 10ºC/min was used. For temperature-modulated DSC (MDSC), heat capacity was calibrated using crystalline sucrose, where the heat capacity constants were 0.988 for the direct signal and 1.049 for the reversing signal. A sinusoidal modulation of ±1ºC was employed every 100

seconds, with a ramp rate of 2ºC/min. For DSC runs, average sample weight was approximately 4 – 8 mg. Universal Analysis (Version 4.1D, TA Instruments) was used for DSC data analysis. Glass transition temperatures (T_g) were reported as the mid-points of the glass transition events determined from the reversing heat capacity (rev C_p) signal. Crystallization and melting temperatures were the extrapolated onset temperatures of the corresponding thermal events. Enthalpy of the exothermic events was obtained by integrating the peaks using a sigmoidal baseline. For bimodal events, enthalpy of each exotherm was obtained by drawing a perpendicular line from the valley between the two peaks onto the baseline.

8.2.4 Estimation of amorphous content

The amorphous content of the milled samples was quantified using equation 1.[26, 27]

$$\varphi = \frac{H_c}{H_m - \Delta C_p^{l-c} \times (T_m - T_c)} \qquad (1)$$

Where, H_c and H_m are the crystallization and melting enthalpies of the sample. For bimodal events, H_c was obtained by integrating both exotherms together because both exothermic peaks correspond to crystallization of glass as we will discuss later. ΔC_p^{l-c} is the difference in heat capacities of the super-cooled liquid and crystal, determined by MDSC for each material. The heat capacity term accounts for the temperature difference between melting and crystallization events. Standard DSC at 10ºC/min heating rate was used to measure other parameters in equations 1.

8.2.5 Powder X-Ray Diffraction (PXRD)

A powder X-ray diffractometer (D8 Advance, Bruker AXS, Madison, WI) with CuK_α radiation and scintillation counter detector was used to examine changes in crystallinity of the samples with milling. The diffractometer was calibrated using corundum standard (SRM 674b, NIST) at d = 2.0852Å. The angular range studied was 5 - 35º 2θ, with step size of 0.05º and dwell time of 1s. Milled samples were directly packed into the sample holder. Melt-quenched glasses were mildly ground using mortar and pestle before being packed for PXRD studies. All samples were packed into the sample holder by top filling method. PXRD data were collected using the Diffrac Plus XRD commander software (Bruker, AXS). Data analysis was performed using JADE (version 8, Materials Data Inc., Livermore, CA). Variable temperature XRD was conducted using D8 Advance diffractometer, fitted with temperature-controlled stage, using a heating rate of 0.167°C/s (~10°C/min).

8.2.6 Particle morphology and surface area

A thermally activated field emission gun type scanning electron microscope (FEG-SEM, JEOL 6500F, Tokyo, Japan) was used to characterize particle size and morphology of the milled samples. Before SEM analysis, a thin layer of platinum (thickness ~50 Å) was sputter-coated on the particle surfaces using an Ion Beam Sputter (IBS/TM200S, VCR Group Inc., CA, USA). The SEM sample chamber was maintained under a high vacuum (10^{-4} to 10^{-5} Pa) during the imaging process. Specific surface area of milled and unmilled

particles was estimated by BET nitrogen gas adsorption (ASAP 2000 v3.03, Micromeritics, Norcross, Georgia).

8.3 RESULTS AND DISCUSSION

For compounds in this study, the non-isothermal crystallization of cryomilled samples is either unimodal or bimodal, while that of unmilled melt-quenched glasses is always unimodal. Table 8.2 summarizes the crystallization behaviors of milled compounds at two different milling time points, using 10 ºC/min DSC heating rate.

8.3.1 Unimodal crystallization of cryomilled crystals

The crystallization behavior of γ-indomethacin glass illustrates the unimodal crystallization phenomenon (Figure 8.1). Similar to a previous observation,[16] the cryomilled samples show T_g comparable to its melt-quenched glass at 42–44°C, determined using 10°C/min DSC heating rate, followed by a single crystallization exotherm that corresponds to the crystallization of γ-indomethacin polymorph. The crystallization event of the milled samples, however, progressively shifts to a higher temperature with longer milling.

The up-shift in the crystallization temperature (T_c) may be attributed to the decreasing proportion of crystal seeds in milled samples with longer milling. The milled samples are verified by PXRD to be partially crystalline. Longer duration of milling is expected to reduce the concentration of crystal seeds in the milled samples, which can explain an elevation in T_c due to slower crystallization kinetics.

Table 8.2. Summary of various parameters of equation 1 used to calculate amorphous content (ϕ) of milled samples. Also reported are the non-isothermal crystallization modes. $\Delta C_p^{l\text{-}c}$ values are determined from MDSC. Other parameters are obtained with DSC heating rate of 10°C/min. Standard deviations are for three DSC measurements using independent samples.

Model API	$\Delta C_p^{l\text{-}c}$ (J/g-°C)	60 min CM				120 min CM			
		Cryst. enthalpy (J/g)	$T_m - T_c$ (°C)	ϕ (%)	Cryst. mode	Cryst. enthalpy (J/g)	$T_m - T_c$ (°C)	ϕ (%)	Cryst. mode
DPD	0.29±0.02	22.6±1.2	117.8±2.6	71.2±4.1	Unimodal	31.4±1.9	105.0±1.5	88.7±6.0	Unimodal
KNZ	0.51±0.03	36.6±1.4	93.4±1.8	67.3±3.1	Unimodal	46.2±1.1	87.0±2.0	80.1±2.9	Unimodal
IMC	0.47±0.07	27.9±1.6	94.6±2.2	42.9±3.1	Unimodal	42.5±2.1	85.8±1.4	61.4±3.5	Unimodal
SMT	0.32±0.02	32.2±1.0	114.1±2.4	41.9±0.7	Unimodal	56.9±2.3	108.1±2.3	73.5±5.5	Unimodal
TFD	0.66±0.03	70.2±0.9	55.8±1.3	95.9±2.8	Unimodal	79.6±1.6	44.0±3.0	98.5±1.3	Unimodal
FLD	0.34±0.03	21.3±3.2	93.5±0.9	49.8±3.8	Bimodal	30.8±0.6	89.0±1.8	70.3±1.8	Unimodal
SMZ	0.45±0.05	34.3±2.7	194.7±2.4	56.1±5.5	Bimodal	69.9±2.3	190.9±0.7	79.3±2.4	Bimodal
PRX	0.29±0.02	29.9±1.9	157.1±2.3	41.6±2.7	Bimodal	34.6±1.4	154.2±1.5	47.5±2.6	Bimodal
GRF	0.42±0.01	30.0±1.7	150.8±0.8	62.7±5.5	Bimodal	38.5±1.3	148.2±1.1	78.6±3.2	Bimodal
HCT	0.32±0.03	24.4±2.5	163.5±1.5	53.6±6.2	Bimodal	37.8±1.3	145.3±1.0	73.7±2.4	Unimodal

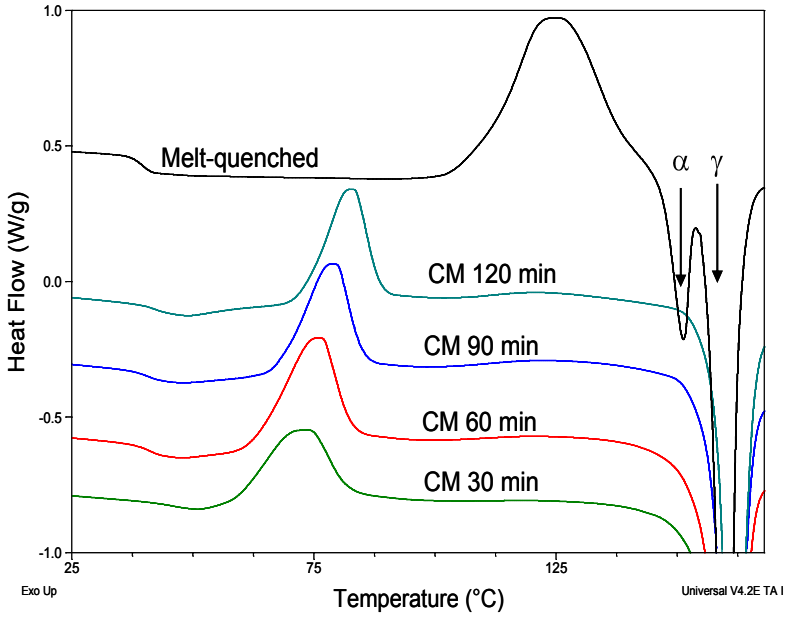

Figure 8.1. Non-isothermal crystallization of cryomilled (CM) γ–indomethacin and melt-quenched indomethacin glass under standard DSC (10ºC/min).

The crystallization temperature is the highest for melt-quenched glass, which is free from detectable crystal seeds, verified by polarized light microscopy (Nikon Eclipse E200 POL, Japan). The seeding effect also explains why the cryomilled γ–polymorph sample, containing γ–polymorph seeds, always crystallizes into pure γ–polymorph, while a mixture of α (melting point ~151ºC) and γ–polymorphs (melting point ~161ºC) crystallize from the melt-quenched glasses where no seed for either polymorph is present. This effect of seeding on crystallization has been further supported by *ex situ* controlled seeding studies described later.

8.3.2 Bimodal exotherms of cryomilled crystals

Five of the ten model compounds, after 60 min cryomilling, display bimodal exotherms when a 10°C/min DSC heating rate is used to heat the milled samples (Table 8.2). The widespread occurrence of the bimodal phenomenon highlights the necessity of mechanistically understanding its physical origin. As an illustration of this behavior, the bimodal crystallization of milled piroxicam is described here. The piroxicam samples, cryomilled for different durations, show two exothermic thermal events in the total heat flow signal of standard DSC (Figure 8.2A). However, for these milled samples showing bimodal behavior, T_g cannot be observed from the standard DSC traces. Instead, the first broad exothermic peak covers the temperature range where the glass transition event is expected (~60°C). However, we can readily identify glass transition of the milled piroxicam samples at ~55-59°C from the reversing signal of modulated DSC (Figure 8.2B), once the contribution from the non-reversing crystallization event is separated. The T_g observed for the melt-quenched piroxicam glass is ~62-63°C by modulated DSC at 2°C/min. Similarly, T_g of milled samples can also be identified from the reversing C_p signal for other compounds that display bimodal crystallization. The observation of T_g in the milled samples suggests that they do contain amorphous domains. The partially amorphous nature of the milled piroxicam samples is further verified by PXRD overlay shown in Figure 8.2C, in which both the crystalline diffraction peaks and amorphous halos are visible. There is a slight drop in T_g of the milled samples, compared to melt-quenched glass. While the exact reason for this observation is not yet clear, moisture likely does not cause the drop in T_g because all samples were handled in a dry

environment following the same procedure, and water content of freshly milled samples was <0.5%.

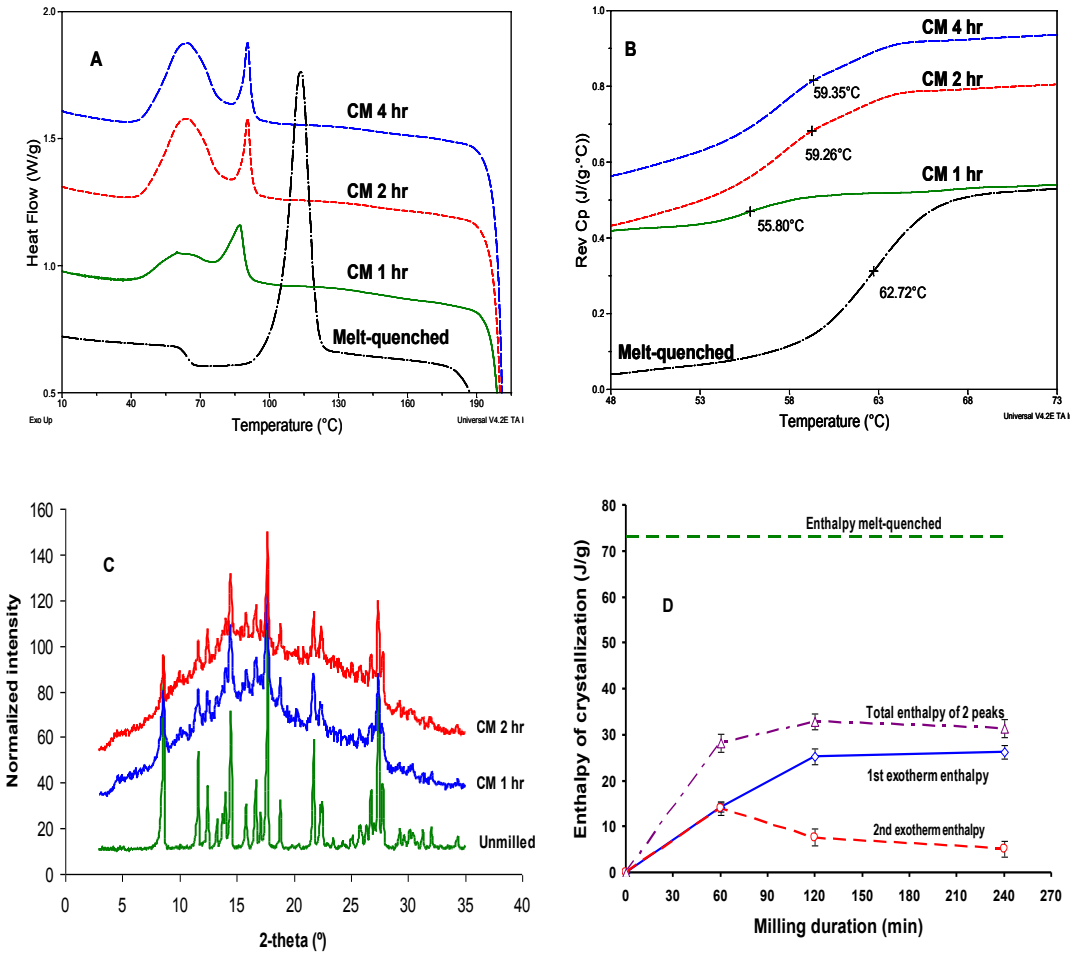

Figure 8.2. Cryomilling of crystalline piroxicam polymorph β: **(A)** Characterization of cryomilled (CM) and melt-quenched piroxicam using standard DSC (heating rate 10ºC/min), **(B)** reversing Cp signals by modulated DSC (heating rate 2ºC/min), **(C)** PXRD patterns of milled and unmilled piroxicam, **(D)** variation of crystallization enthalpies of milled piroxicam with milling duration. Error bars represent one standard deviation of DSC measurements (n = 3).

Similar to the behavior of indomethacin, the T_c of amorphous piroxicam generated through milling is significantly lower than corresponding melt-quenched glass. Similar observations of depressed T_c on milling have previously been made for compounds such as sucrose [28] and dipyridamole.[29] Some of the key factors causing depression in T_c of milled samples will be discussed in the later sections. Interestingly, the enthalpy of the first exothermic event increases with milling time up to 2 hours, while that of the second exotherm decreases (Figure 8.2D). This indicates that the physical process, responsible for the first exotherm, becomes more dominating with longer milling. Longer milling beyond 2 hours does not result in appreciable change in enthalpy ratio between the two exotherms. These changes in ratio between the two crystallization exotherms correlate well with change in particle size, which decreases with longer milling within the first two hours but is approximately constant subsequently (Figure 8.3). As will be discussed later, particle size is a key factor that leads to the observation of bimodal crystallization phenomenon in milled glasses.

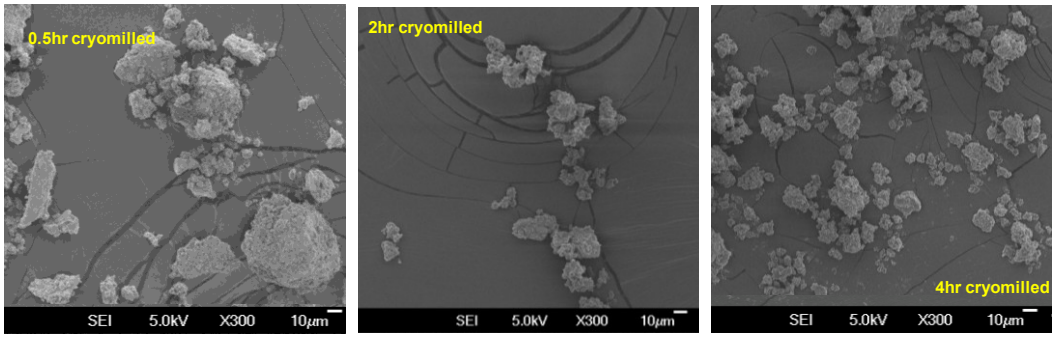

Figure 8.3. SEM data providing an estimate of particle size distribution for cryomilled piroxicam. Reduction in particle size occurs up to 2 hours of milling beyond which average size remains approximately constant. The changes in particle size correlate with change in crystallization enthalpy shown in Figure 8.2D.

8.3.3 A surface crystallization model for bimodal crystallization

In examining the crystallization behaviors of different model compounds, we find that when the crystallization onset temperature of the milled samples is very close to or below T_g, bimodal crystallization is always observed. On the other hand, when the T_c is well above the corresponding T_g of glasses, single crystallization exotherms are observed (Figure 8.4). This definite dependence of the mode of crystallization of glass on the position of T_c relative to T_g indicates that two separate crystallization mechanisms are active below and above T_g that contribute to the two types of non-isothermal crystallization behaviors in DSC.

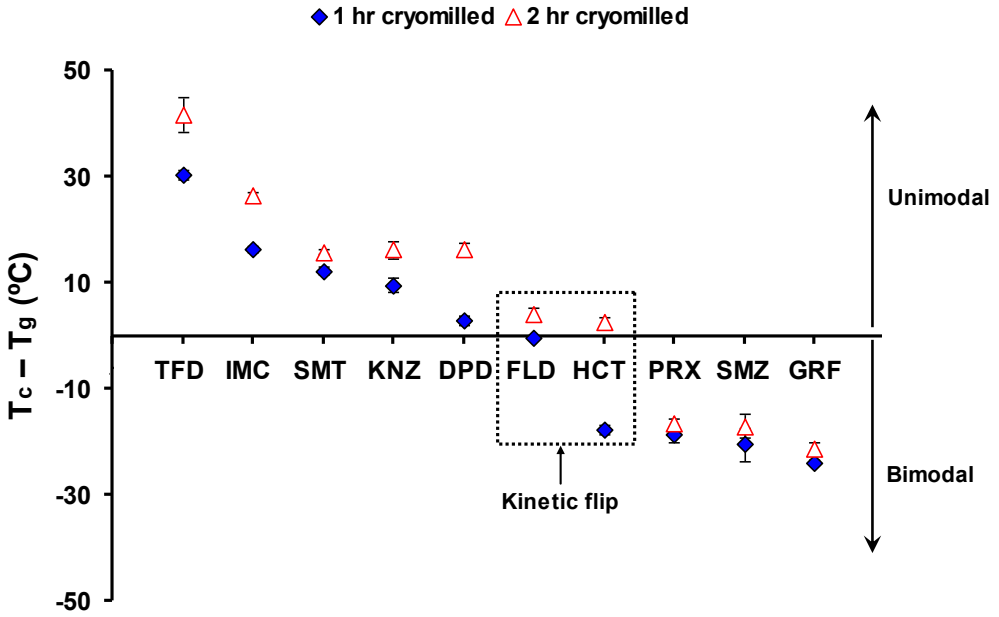

Figure 8.4. Crystallization mode, unimodal or bimodal, depends on the location of T_c relative to T_g. The dotted box shows two examples where the mode of crystallization flips depending on milling duration. Data obtained at 10ºC/min heating rate has been used for plotting this graph. Error bars represent one standard deviation of DSC measurements (n = 3).

Faster crystallization on glass surfaces, by several orders of magnitude, compared to bulk glass, has been reported for several organic glasses at temperatures below and slightly above T_g.[30-33] This faster surface crystallization phenomenon has been explained on the basis of fast surface mobility.[30, 34] An alternative explanation to this phenomenon, based on the density difference between the growing crystal and glass, [35] was recently challenged.[36] At temperatures well above T_g, surface and bulk crystallization rates of a supercooled liquid are similar due to similar molecular mobility throughout. Thus, if T_c occurs well beyond T_g, only a single crystallization exotherm is expected during DSC non-isothermal experiments. However, when the amorphous crystallization commences near or below T_g, the surface first crystallizes at a significantly faster rate, which is followed by bulk glass crystallization at higher temperatures.

The clear dependence of the mode of crystallization on T_c-T_g relationship, as shown in Figure 8.4, suggests that the faster surface crystallization below T_g may be a key factor leading to the bimodal crystallization behavior of the cryomilled materials. Assuming the surface layer thickness for the same glass is constant at a constant temperature below T_g, the fraction of the material in the surface layer will increase with decreasing particle size, as illustrated in a hypothetical model schematic (Figure 8.5A). For an unmilled melt-quenched glass, the percentage of fast crystallizing surface portion is negligible since the surface layer is very thin. Consequently, unmilled melt-quenched glasses display only single crystallization exotherm in DSC studies, corresponding to

bulk glass crystallization at a crystallization temperature well above T_g. However, with decreasing particle size on longer milling, the fraction of the glass in the surface layer is expected to increase, corresponding to the increase in surface area as milling proceeds. For example, the specific surface area of griseofulvin is enhanced by almost ~4-fold after 1 hr of milling. With increasing surface proportion, the faster surface crystallization should become more predominant and, at some point, detectable by DSC as a distinct exothermic event, followed by a second exotherm attributed to the crystallization of remaining glass. When particle size is sufficiently reduced, the second exotherm may eventually disappear as the amount of slower crystallizing bulk glass is negligible.

These expected changes in crystallization behaviors, based on the surface crystallization model, are well demonstrated with cryomilled piroxicam glass (Figure 8.5B). The crystallization of the unmilled piroxicam glass (prepared by melt-quenching) is initially unimodal, but becomes bimodal when the same glass is cryomilled for 1 minute. The first peak gains in enthalpy with longer milling, as particle size is reduced (Figure 8.5C) while the second peak diminishes. The second peak eventually disappears after 10 minutes of milling. If this model is valid, it should be possible to control the mode of crystallization of a glass by controlling the surface area and T_c, as discussed in the following sections.

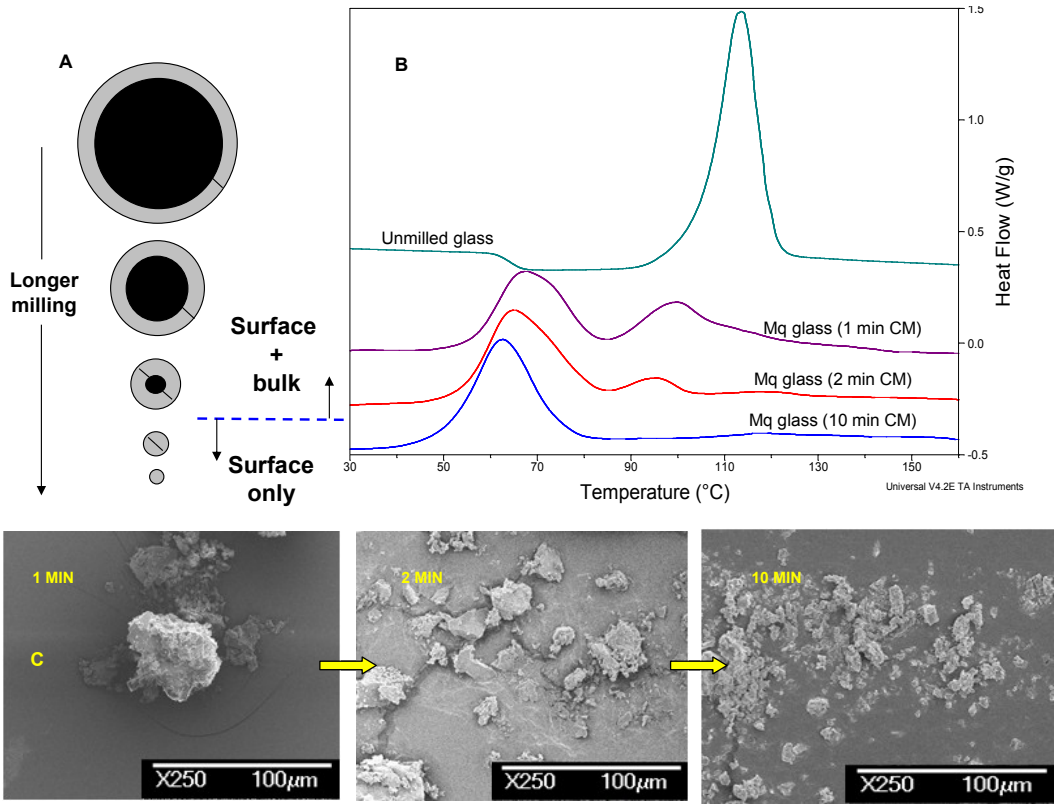

Figure 8.5. **(A)** Schematic showing the relative change in proportion of surface to bulk with longer milling **(B)** DSC curves (10°C/min heating rate) for melt-quenched (Mq) piroxicam glass which was thereafter cryomilled (CM) for different durations. The crystallization exotherm shows a time dependent evolution from unimodal (unmilled glass) to bimodal (milled <10 min) and then unimodal again (milled ≥ 10 min). **(C)** SEM images of melt-quenched piroxicam glass cryomilled for different durations.

8.3.4 Changing T_c of a glass by grinding

Reduction in particle size of glass during milling introduces more sites for heterogeneous nucleation and enhances the probability of faster surface crystallization, which should favor an earlier crystallization onset in the milled samples compared to unmilled glass. This effect of milling on T_c of glass is demonstrated for griseofulvin glass in Figure 8.6A.

The crystallization onset of glass is significantly reduced with increasing milling duration. Similar observations were previously reported on indomethacin glass.[37]

When the depressed T_c of the milled glass reaches the temperature of glass transition (visible only from reversing C_p signal), the crystallization mode switches from unimodal to bimodal, which may be explained by the activation of surface crystallization as discussed earlier. In Figure 8.6B, the variation of enthalpies of crystallization of the two peaks with milling is shown. The total enthalpy of the bimodal crystallization of milled glasses is essentially independent of the milling duration and is very close to the enthalpy of unmilled glass after correcting for the difference in crystallization onset between the unmilled and milled glasses doing a heat capacity correction.

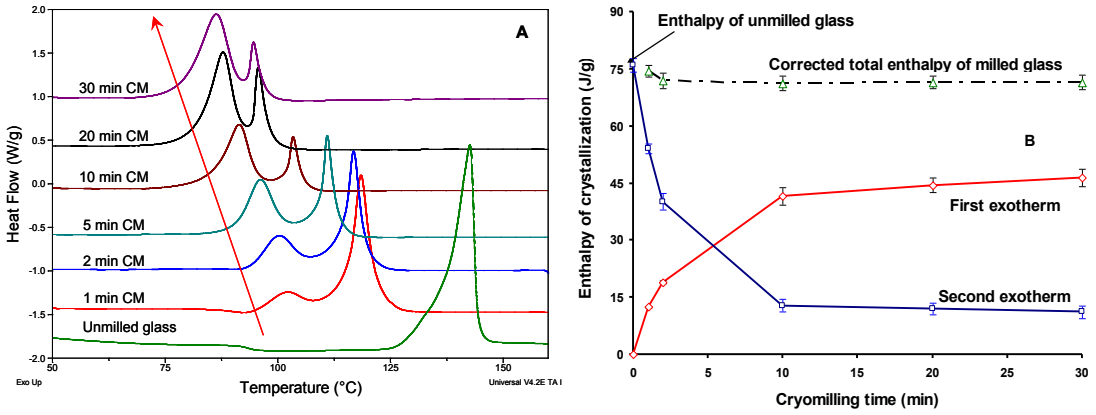

Figure 8.6. Cryomilling of melt-quenched griseofulvin glass: **(A)** Effect of milling on crystallization mode of melt-quenched griseofulvin glass tested at 10°C/min heating rate. The arrow indicates that T_c is depressed with longer milling. **(B)** Dependence of crystallization enthalpies of the two exotherms on milling duration. Also plotted is the total crystallization enthalpy for the milled samples, which match closely with the crystallization enthalpy of unmilled melt-quenched glass, after performing the heat capacity corrections according to equation 1. Error bars represent one standard deviation of DSC measurements (n = 3).

8.3.5 Effects of crystal seeds and heating rate on T_c

In addition to particle size reduction, another factor that significantly contributes to depression in T_c of milled crystals is the presence of crystal nuclei or seeds in the milled samples, which survive vitrification under mechanical stresses of milling. Figure 8.7A shows the correlation between the extent of T_c depression, ΔT_c (T_c of unmilled melt quenched glass – T_c of 1-hr cryomilled sample), and the amorphous content of milled samples for ten model compounds. Despite the scatter in the plot, there is a trend that milled materials having more seeds exhibit larger ΔT_c.

To further test the effect of seeding on T_c depression of glass, we have performed *ex situ* DSC seeding experiments by sprinkling γ–indomethacin crystal seeds on the surface of melt-quenched indomethacin glass. The non-isothermal crystallization behavior of indomethacin glass at various seed concentrations of γ–indomethacin at 2 °C/min heating rate are shown in Figure 8.7B. At this slow heating rate, T_c of seeded indomethacin glass is lower than that observed at 10°C/min, which is expected due to the well-established effect of heating rate on crystallization onset.[38] With increasing γ–indomethacin seed added, the T_c of indomethacin glasses decreases and crystallization of the γ–polymorph also becomes more predominant at the expense of α–indomethacin. This is consistent with the observations we have made in Figure 8.1, where pure γ–indomethacin crystallizes from cryomilled samples that contain large proportions of γ–indomethacin crystal seeds.

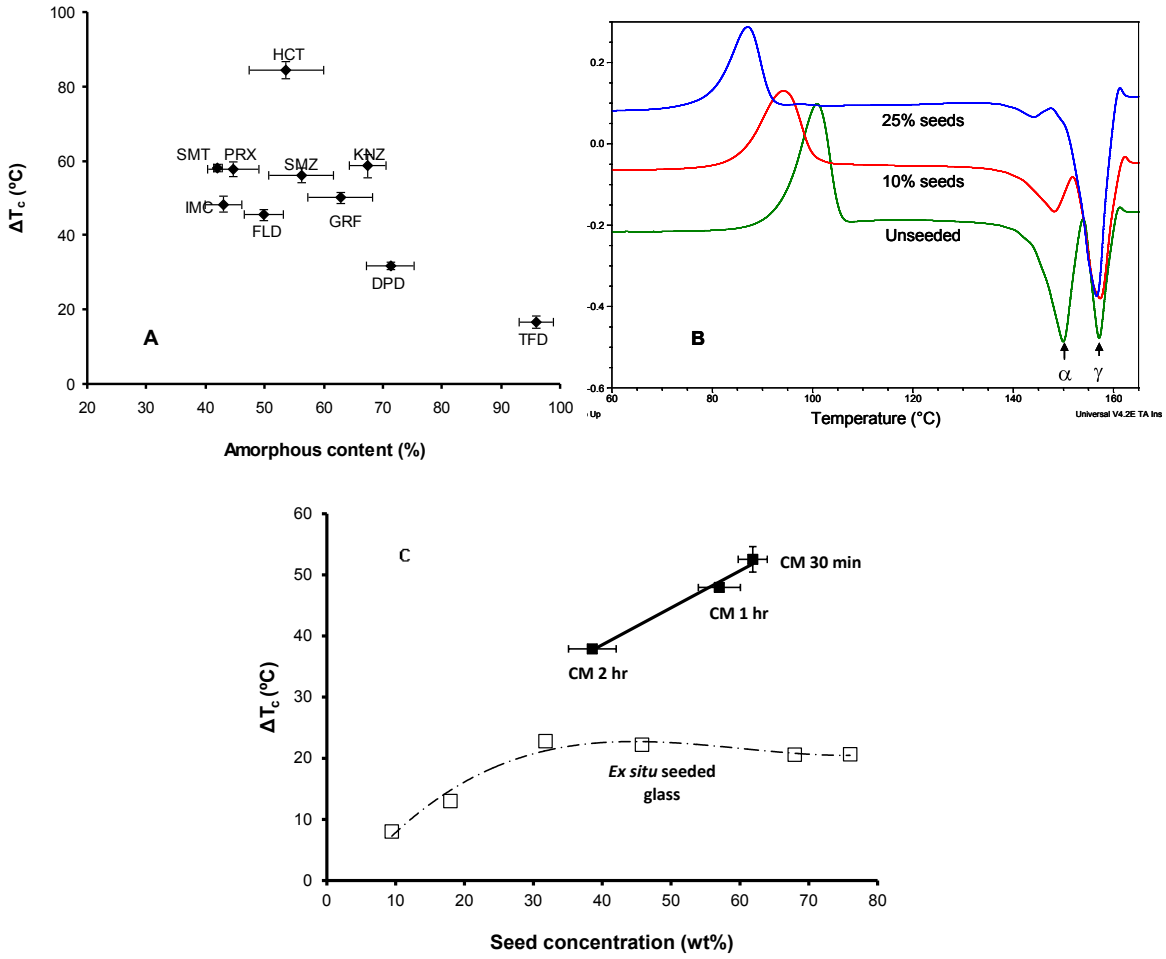

Figure 8.7. (A) Correlation between depression in T_c of milled crystals, relative to melt-quenched glass ($\Delta T_c = T_c^{melt\text{-}quenched} - T_c^{1\ hr\ milled}$) and amorphous content of milled samples (10^oC/min heating rate). **(B)** Effect of *ex situ* seeding on crystallization onset of indomethacin glass (2^oC/min heating rate). **(C)** Comparison of ΔT_c, at 10^oC/min heating rate, of indomethacin cryomilled (CM) (■, n = 3) with *ex situ* seeded melt-quenched glass (□, n=1).

The effect of T_c depression of glass by *ex situ* seeding is, however, not as drastic as observed for cryomilled materials at the same seed concentration (>45%) (Figure 8.7C). For *ex* situ seeded glasses, we do not observe further depression in T_c at seed

concentrations >30%. However, for milled samples, T_c depression continues to be observed at higher seed concentrations. This is not surprising because, for *ex* situ seeded samples, the contact between crystal seeds and glass is expected to reach a maximum once a layer of crystals completely covers the top layer of the glass surface. On the contrary, for cryomilled samples, the glass generated through milling is intimately in contact with crystal seeds at all available glass surfaces, which will promote a greater drop in T_c in milled samples.

8.3.6 Kinetic flip of crystallization modes

So far, we have shown that milling duration, seeding, and heating rate can all affect T_c of a glass. If T_c of a cryomilled sample can be kinetically controlled through these parameters to be either below or above T_g, we should observe flip between the unimodal and bimodal crystallization behaviors for the same glass if the surface crystallization model is valid.

In fact, we do observe kinetic flip between unimodal and bimodal crystallization by modifying milling duration. For example, T_c of the indomethacin crystals milled for 2 hours at 2°C/min heating rate (~43°C) is slightly lower than its T_g (~46ºC determined from rev C_p) and bimodal crystallization occurs (Figure 8.8). At the same heating rate, however, T_c of indomethacin after 4 hours of cryomilling (76ºC) is 30ºC beyond T_g and only a single crystallization peak is observed.

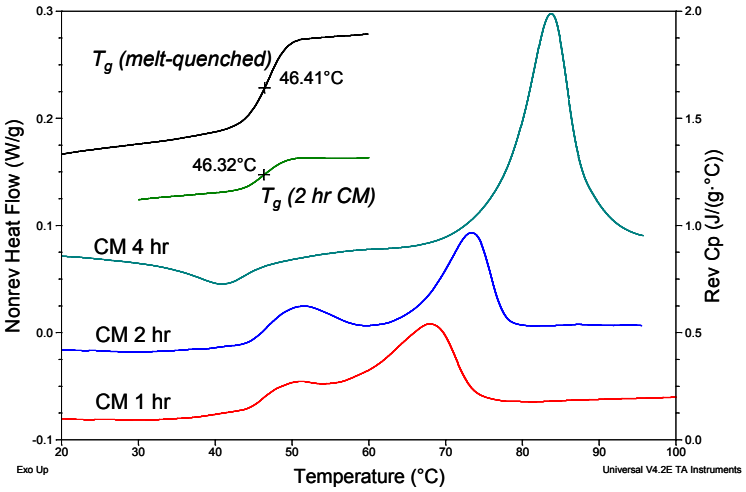

Figure 8.8. Effect of milling duration on crystallization modes of cryomilled (CM) γ-indomethacin crystals tested at 2ºC/min heating rate in DSC. Also shown are the T_gs of the milled and melt-quenched samples from the reversing C_p signal.

Similar milling-induced flipping behavior can also be observed for felodipine and hydrochlorothiazide. Provided faster surface crystallization is universal, our model predicts that any organic glass can display either crystallization behaviors depending on kinetics of crystallization. When felodipine crystals are milled for 1 hr, the T_c (46ºC) is approximately the same as T_g (~46.2ºC) and bimodal crystallization behavior is observed (Figure 8.9A). However, longer milling duration (4 hr) shifts the crystallization onset to a temperature (66ºC) much higher than its T_g. Consequently, only a single crystallization peak is observed.

At a heating rate of 10 ºC/min, the T_c of the 2 hr milled felodipine (51ºC) is ~5 ºC higher than T_g (~46 ºC). For this sample, a small leading shoulder can still be observed before the main crystallization event (Figure 8.9A), indicating faster surface

crystallization remains active at slightly above T_g. This is consistent with the observation that the faster surface crystallization process remains active up to a few degrees above T_g instead of being abruptly turned off at T_g.[30] However, when the same 2hr milled felodipine sample is heated at a slower heating rate at 2ºC/min during the MDSC experiments, the T_c (46ºC) is below its T_g (~47.2ºC determined at 2 ºC/min from reversing C_p) and we observe a clear bimodal crystallization behavior (Figure 8.9B). The heating rate-induced kinetic flip in crystallization mode for the same sample effectively excludes the possibility that the bimodal thermal behavior is simply a consequence of the presence of two size populations of particles in the cryomilled samples. Such an explanation cannot explain the unimodal crystallization behavior of some cryomilled samples anyway.

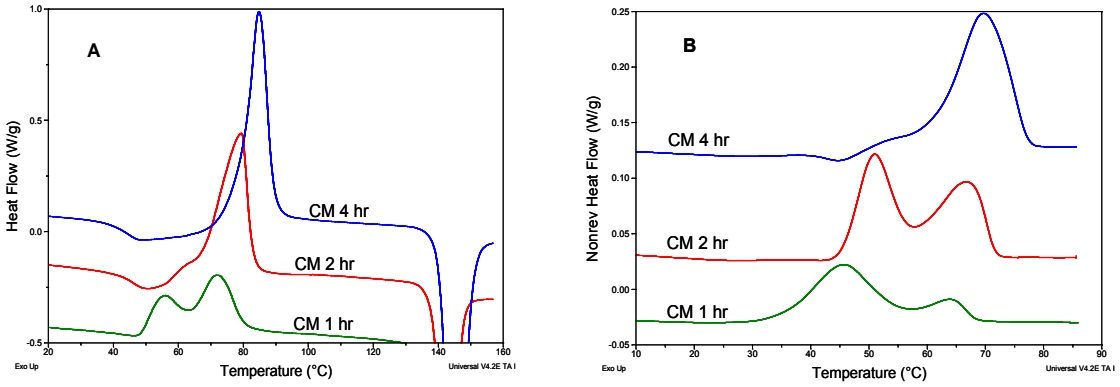

Figure 8.9. Non-isothermal crystallization of cryomilled (CM) felodipine crystals, showing flip between unimodal and bimodal crystallization under **(A)** standard DSC (10ºC/min), and **(B)** modulated DSC (non-reversing heat flow, 2ºC/min).

Similar to felodipine, heating rate-induced flipping in crystallization mode is also observed for indomethacin. Indomethacin, cryomilled for 2 hours, shows unimodal crystallization behavior (T_c of 71°C and T_g of ~44°C), when tested at a heating rate of 10°C/min in DSC. However, the same sample shows bimodal crystallization when a slower heating rate of 2°C/min is used (T_c of 42.9°C and T_g of ~46°C from reversing C_p) (Figure 8.10).

For some materials, an increase in heating rate from 2°C/min to 10°C/min does not cause a sufficient change in T_c to switch from bimodal crystallization to unimodal behavior. However, the relative sizes of the two crystallization exotherms in the bimodal event vary according to the proposed surface crystallization model. For instance, when a sample of crystalline piroxicam, cryomilled for 2 hrs, is subjected to a slower heating rate of 2°C/min during modulated DSC experiments, the ratio of the area of the first crystallization peak to that of the second peak is 26:1. However, at a faster heating rate of 10°C/min, the ratio reduces to 4.4:1 for the same sample. This is expected because more time is available for the surface to crystallize completely at a slower heating rate, which increases the first exotherm area at the expense of the second exotherm.

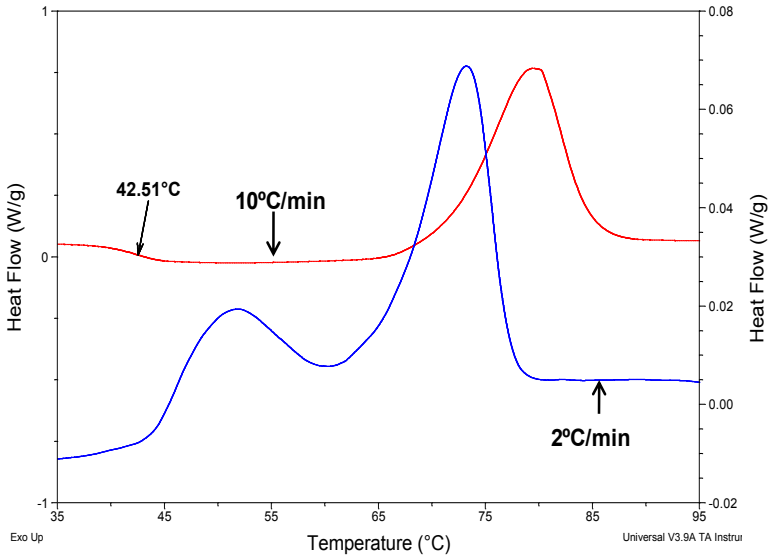

Figure 8.10. Effect of heating rate on the crystallization behaviors of crystalline indomethacin cryomilled for 2 hours. Crystallization is unimodal at 10°C/min but bimodal at 2°C/min for the same glass prepared by 2 hr milling, due to faster crystallization onset at slower heating rate.

8.3.7 Flip induced by polymer

The phenomenon of kinetic flipping between unimodal and bimodal behaviors by simply changing the heating rate or milling duration supports the surface crystallization model, which well explains the two crystallization behaviors. The validity of this model can also be further tested if we can flip the crystallization from bimodal to unimodal, by raising the T_c to above T_g of a glass using crystallization inhibitors. To test this, crystalline griseofulvin was cryomilled for 30 minutes in presence of crystallization inhibitor polyvinyl pyrrolidone vinyl acetate (PVPVA, Kollidon VA 64 Fine, BASF Corporation). Milling of griseofulvin alone for 30 minutes yields an amorphous phase

that exhibits bimodal crystallization, with T_c approximately 25°C below T_g (90°C). The presence of polymer slows down the crystallization and hence elevates T_c as expected but does not affect T_g of griseofulvin (~90°C), as seen from the reversing C_p signal in Figure 8.11. This is likely because griseofulvin does not form strong hydrogen bond interactions with PVPVA, due to lack for strong hydrogen bond donor moieties.

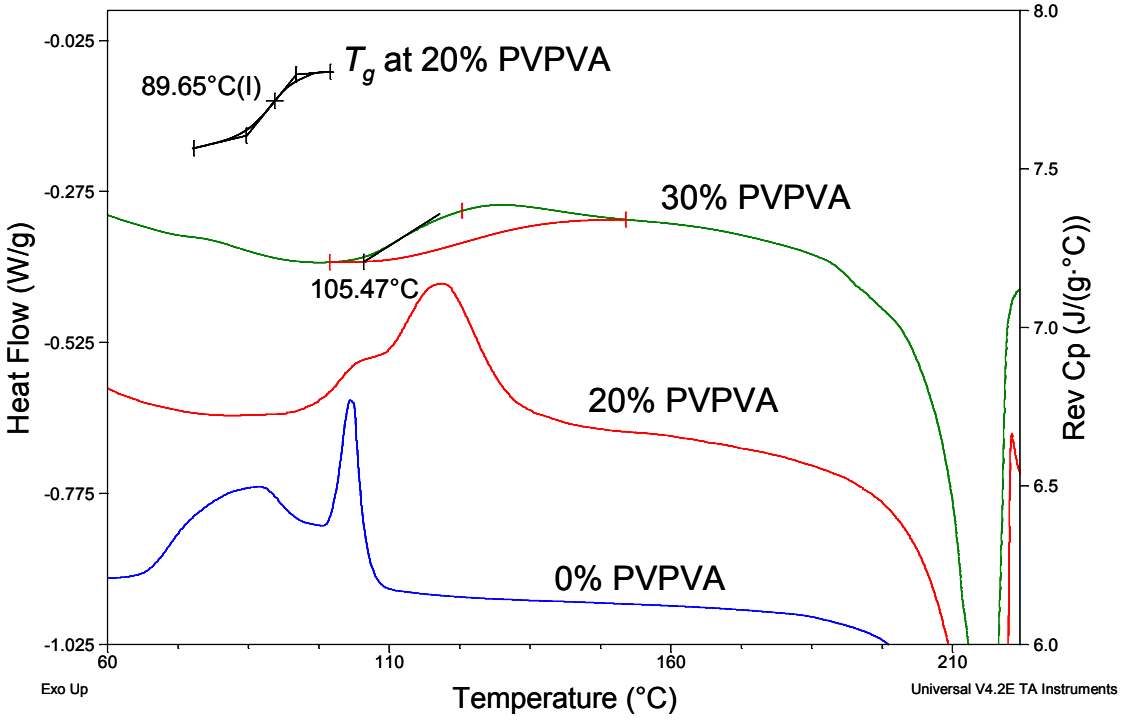

Figure 8.11. Effect of polymer on crystallization onset and mode of crystallization of 30 min cryomilled griseofulvin. Also shown is the reversing C_p signal for 20% PVPVA loading that confirms that T_g of griseofulvin (~90°C) is unchanged in presence of the polymer.

When cryomilled with 20% PVPVA, the T_c of griseofulvin almost coincides with T_g of griseofulvin and the bimodal peaks begin to merge into a single exotherm. When the

T_c (~106°C) is well beyond T_g (~90°C) at 30% PVPVA loading, only unimodal crystallization behavior is observed. This experiment further supports that the bimodal exothermic event is caused by faster glass crystallization below T_g.

8.3.8 Flip induced by surface elimination

We have shown that size reduction of glasses can induce bimodal crystallization (Figure 8.6A). An excellent further test of our model is to convert bimodal crystallization to unimodal by eliminating surface area that was originally generated by milling. Cryomilled griseofulvin glass was compressed into thin discs (4 mm diameter) at the pressures of 100 and 300 MPa. It is expected that consolidation of a powder diminishes powder porosity, hence, total surface area.[39, 40] We therefore expect reduced size of the first exotherm, which is attributed to surface crystallization, after compaction. As-milled griseofulvin glass displays clear bimodal crystallization, with the first exotherm accounting for ~70% of the total enthalpy (Figure 8.12). For the disc compressed at 100 MPa, surface proportion accounts for ~24% of overall crystallization. With 300 MPa pressure, the surface crystallization peak is eliminated (Figure 8.12), and crystallization behavior resembles that of the unmilled melt-quenched glass. The total enthalpy of crystallization (including two peaks), for milled and compacted samples, match closely with that of melt-quenched glass that has not been subjected to any mechanical stress. This experiment confirms that surface crystallization of milled samples is indeed responsible for the first exothermic event in bimodal crystallization, which can be eliminated by compaction.

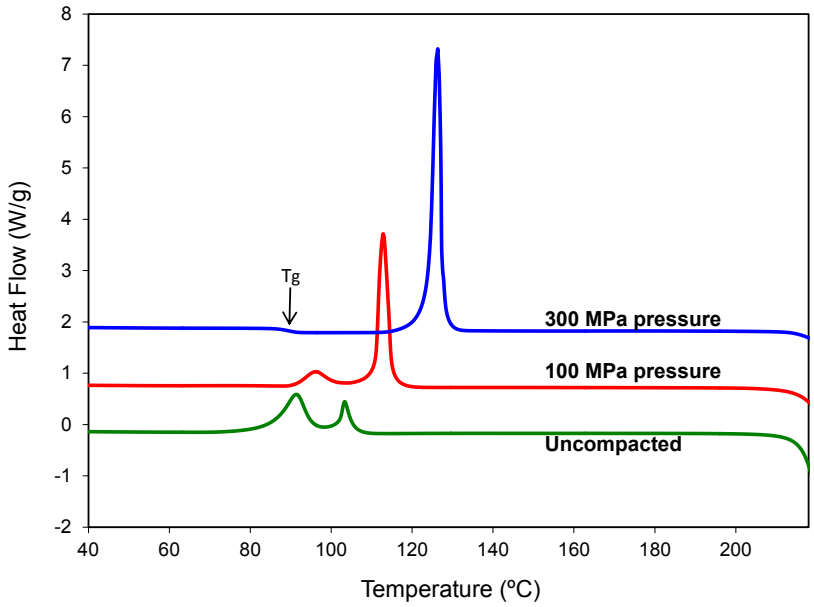

Figure 8.12. Effect of compaction on crystallization behavior of griseofulvin glass (prepared by melt-quenching followed by cryomilled for 10 min). For uncompacted cryomilled glass, crystallization is clearly bimodal, with surface proportion (*i.e.* the first exotherm) accounting for 70% of total enthalpy. After compaction at 100 MPa pressure, the surface proportion accounts for ~24% of overall crystallization. With 300 MPa pressure, the first exotherm (surface) is eliminated and the crystallization is unimodal at $T>T_g$.

8.3.9 Possibility of crystallization into different polymorphs

Crystallization into two distinct polymorphs can result in bimodal crystallization, when crystallization onset is higher than T_g for some organic glasses.[24, 25] However, the possibility of different polymorphs crystallizing can be ruled out for molecules, such as griseofulvin, which exhibit bimodal crystallization behavior despite having no known polymorphs. Figure 8.13A shows that only a single crystalline phase crystallizes during the entire process of crystallization of cryomilled griseofulvin over a temperature range covering both exotherms. In the temperature range of the bimodal events (10°C/min was

used for both VTPXRD and DSC experiments), we only observe a progressive increase in fraction of the same crystalline form of griseofulvin, estimated by integrating the area of peak maxima at 16.6° 2θ (Figure 8.13B). Both exothermic events, therefore, correspond to crystallization of the amorphous phase into the same crystal form. Moreover, all model compounds that exhibit bimodal crystallization in this work have only a single melting endotherm following crystallization during DSC experiments. Thus, the possibility of bimodal events corresponding to crystallization of different polymorphs may be excluded for these compounds.

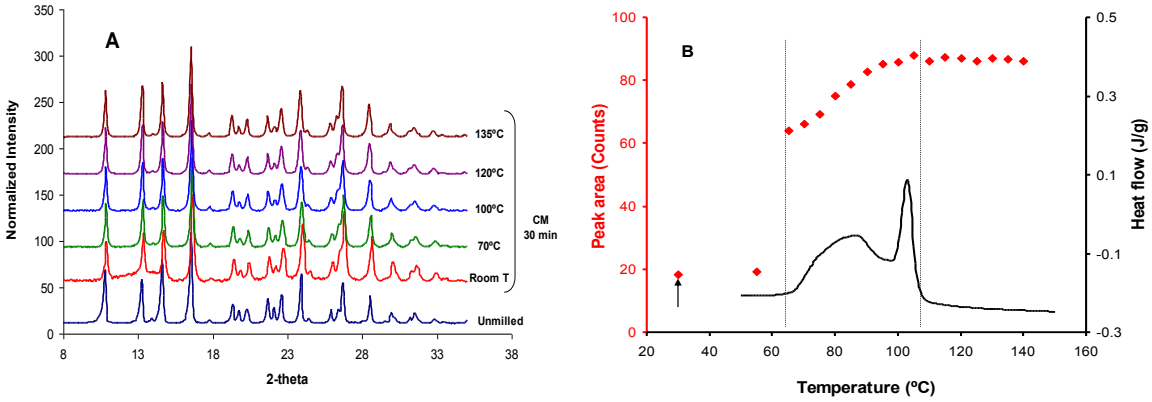

Figure 8.13. **(A)** Overlay of variable temperature XRD and **(B)** integrated area of X-ray diffraction peak at 16.6° 2θ as a function of temperature, along with the DSC trace showing the bimodal behavior, for 30 min cryomilled griseofulvin. The arrow indicates the room temperature X-ray peak area for the milled sample.

It is possible that a polymorphic transition may be exothermal (e.g. transition from polymorph III to II in acetaminophen). If so, two exotherms may be observed for a glass that undergoes unimodal crystallization. However, the two exotherms (crystallization of

the glass and polymorphic transition) are usually well separated. It is also possible that a glass may crystallize into two polymorphs at different temperatures (e.g. nifedipine). In both cases, crystallization events take place at temperatures above T_g and can be readily distinguished from the bimodal crystallization phenomenon discussed in this report.

8.4 CONCLUSIONS

In this work, we have described a surface crystallization model that can be used to explain both unimodal and bimodal crystallization of organic glasses prepared by different routes. We have shown that the modes of crystallization of all molecules in this study are determined by the relative position of crystallization onset, T_c, and glass transition temperatures, T_g. Unimodal crystallization occurs when T_c is at least several degrees higher than T_g. Bimodal crystallization takes place when T_c is lower than or close to T_g. This model clearly explains the otherwise perplexing effects of milling duration, heating rate, particle size, crystallization inhibition, and compaction on the thermal behavior of organic glasses.

Chapter 9.

Thesis Summary

The overall objective of this research work was to investigate the relationships between the structure of pharmaceutical solids, both crystalline and amorphous, with their properties relevant for processing, such as mechanical, flow, and solid-state amorphization. The key message from the various aspects of this endeavor are summarized here.

Chapter 2.

In chapter 2, the correlations between the crystal structure, crystal plasticity, and powder compaction properties were probed using the model system of theophylline anhydrate, methyl gallate, and their 1:1 cocrystal. Theophylline showed exceptionally high plasticity, indicated by very low crystal hardness measured using nanoindentation, which led to its superior powder compaction properties. The plasticity was, however, deteriorated on cocrystallizing the drug with the co-former methyl gallate. This resulted in deterioration in powder compaction properties after cocrystallization. This illustrates the importance of analyzing the effect of changing solid forms of drugs on their mechanical properties, as that will directly influence their manufacturing potential downstream. Another point of interest in this work was the observation that theophylline's compactibility was relatively insensitive to changes in particle size or morphology. This suggests that when a material's plasticity is very high, then particulate property alteration may not necessarily lead to an effect on powder compaction. Finally, we showed that the different plasticity and powder compaction properties could be well explained by the consideration of the crystal packing in different materials. The presence

of an extremely dense three-dimensional hydrogen bonded network structure lowered the plastic deformation in the methyl gallate crystal, leading to its poor compaction. In contrast, the cocrystal structure exhibited a two-dimensional hydrogen bonded layered structure, which improved its plasticity and compaction properties relative to methyl gallate by facilitating slip. Theophylline underwent the highest plastic deformation due to multiple slip layers conferred by hydrogen bonded columns.

Chapter 3.

In chapter 3, we further extended our analysis on the effect of structure on the mechanical properties of organic crystals by performing a thorough quantitative analysis of the mechanical property landscape of the model system of piroxicam-saccharin cocrystal, using single crystal nanoindentation. In addition to more widely used mechanical properties, such as hardness and modulus, we were able to experimentally measure the crystal yield strength, *i.e.* the onset of plastic deformation, by performing partial loading-unloading experiments at small strain levels (<50 nm). Using mechanical property hierarchy of crystal hardness and yield strength, we successfully explained the observed rank order of powder compaction in this system: saccharin > piroxicam > cocrystal. This work is very significant as such an in-depth analysis of crystal mechanical properties for molecular organic solids have rarely been attempted. This endeavor provided a direct quantitative correlation between the mechanical properties of single crystals, and bulk powder compaction behavior.

Chapter 4.

In chapter 4, we studied the effect of changing the surface structure of cohesive powders on their flow properties. Using a very cohesive and poorly flowing grade of microcrystalline cellulose (Avicel PH105) as substrate, we established the utility of using comilling technique to coat the substrate surfaces with nano-sized silica particles. This surface coverage with discrete silica particles, verified by SEM, helped to increase the interparticulate separation between adjacent MCC substrates, thereby minimizing cohesion. The flow properties of the optimized nanocoated batch were comparable to the gold standard material for assessing adequate flow, *i.e.,* Avicel PH102. In addition, the nanocoated batch exhibited far superior compaction properties compared to PH102. Therefore, this nanocoated composite is potentially useful for direct compression applications. This approach of using comil to dry coat the surfaces of cohesive powders is industrially very attractive, due to its efficacy, simplistic instrument set-up, and lack of appreciable stress levels that ensure no amorphization of substrates during the comil operation.

Chapter 5.

From chapter 5 onwards, the thesis focuses exclusively on milling-induced mechanical amorphization of crystals. In chapter 5, we established the concurrent influence of crystal lattice strength (LS) and amorphous phase stability (AS) on the amorphization potential of crystals. LS governed amorphous generation (crystal → amorphous), while AS governed amorphous elimination (amorphous → crystalline). An amorphization

classification map was constructed to categorize the model compounds into four classes: I (high *LS*, low *AS*), II (low *LS*, low *AS*), III (high *LS*, high *AS*), and IV (low *LS*, high *AS*). Amorphous phase of classes I and II materials were highly unstable (indicated by lower activation energy of crystallization) and underwent fast recrystallization. Materials in these two classes, therefore, had low propensity to undergo processing-induced amorphization due to rapid amorphous elimination. On the contrary, materials in class IV were more suitable for amorphization, both due to weaker lattice favoring amorphous generation, and better amorphous stability than other classes. This knowledge of different amorphization classes of crystals is expected to facilitate the drug development process by an early identification of 1) the suitability of drugs for developing stable amorphous product, or 2) potential problems of unexpected processing-induced amorphization if the crystalline phase is used for development.

Chapter 6.

In chapter 6, the role of molecular weight (MW) in solid-state amorphization was investigated, using 21 model compounds. Low MW materials (<260 g/mol) did not show amorphous conversion after milling operation, while all materials with higher MW amorphized. The effect of MW was connected to the amorphous phase stability. Lower MW compounds showed lower crystallization activation energies, indicating faster crystallization. This effect is due to the connection between MW and molecular flexibility in the amorphous phase, estimated by measuring the configurational entropy (ΔS_{conf}) of materials. Low MW materials had low ΔS_{conf}, which was connected to faster

molecular mobility using Adam-Gibbs theory. In summary, the lack of observable amorphization of low MW crystals was shown to be a result of fast elimination of amorphous phase at ambient conditions prior to sample characterization.

Chapter 7.

In chapter 7, we investigated the utility of cocrystals to modulate the amorphization potential of drugs, by manipulating both the crystal lattice strength and amorphous phase stability. Using the model system of sulfamethazine (SMT) and its 1:1 cocrystals with p-hydroxybenzoic acid (HBA) and benzamide (BZM), we showed that the amorphization of cocrystals depended on milling duration. The onset of amorphization was the earliest for the SMT-BZM cocrystal (~10 min cryomilling) and the most delayed for the SMT-HBA cocrystal (>30 min cryomilling), corresponding to the lowest and highest crystal lattice strength, respectively. However, the extent of amorphous conversion after 2hrs of milling followed a different rank order, *i.e.,* SMT-HBA > SMT-BZM > SMT. The extent of amorphization appeared to be linked with the stability of amorphous, which followed the order of SMT-HBA > SMT-BZM > SMT, based on both configurational entropy (ΔS_{conf}) and structural relaxation times calculated using Adam-Gibbs equation. The lowest net conversion of the SMT was explained by its faster recrystallization propensity, despite an earlier amorphization onset. This work illustrates that cocrystals may be used to either minimize unintended amorphization of crystalline drugs during processing or enable the preparation of stable amorphous drug products.

Chapter 8.

In chapter 8, we investigated the role of activated surface in milled amorphous glasses on their recrystallization under non-isothermal conditions. Two crystallization modes were identified: unimodal and bimodal. The mode of crystallization of amorphous phase was found to depend on the relative position of the crystallization onset (T_c) with respect to glass transition temperature (T_g), and was explained by a surface crystallization model. Bimodal crystallization event was observed when T_c was below or near T_g, due to the fast crystallization onset at milled glass surfaces due to facilitated heterogeneous nucleation. Unimodal crystallization was observed when T_c was well above T_g where there was no distinction in surface and bulk crystallization rates. We verified this model by intentionally inducing flip between the two crystallization modes for several compounds through manipulating several kinetic factors that influence crystallization, such as glass surface area, heating rate, polymer doping, and surface elimination through compaction. Thus, the appearance of the two modes of non-isothermal crystallization of organic glasses was found to be a result of the combined effects of faster surface crystallization and variation in specific surface area by milling.

Future work

Powder compaction

The research described in chapters 2 and 3 has clearly demonstrated the association between crystal structure, crystal mechanical properties (mainly, plastic deformation), and bulk powder compaction of pharmaceutical solids. In these chapters, we have demonstrated that changing the solid form of a crystalline drug can alter the powder compaction properties. However, all studies described here have been restricted to the pure, "neat" form of the drug. The next step would be to correlate the mechanical properties of the drug or its alternate solid form with the powder compaction behaviors of formulated drug products, containing both drugs and excipients. Here, the role of drug loading is expected to play a significant role. At a higher drug loading, the mechanical properties of the drug will likely be more consequential to the powder compaction properties of the formulated product. A systematic analysis of the influence of mechanical properties of the solid drug on the compaction properties of formulations, as function drug loading, will be a logical next step.

Another aspect worth further exploration is the utility of using nanoindentation to quantify the yield strength of crystals, following the process of partial loading and unloading cycles. Yield strength is a fundamental property of materials that describes the ease of plastic deformation onset. A lower yield strength indicates easier onset of plasticity, which means the material will likely compact well under pharmaceutically relevant stress levels. While such analyses for non-pharmaceutical crystals have been

frequently attempted, studies on molecular organic materials are relatively rare, despite the significance of this parameter in pharmaceutical research. Nanoindentation provides the opportunity to accurately quantify the yield strength of materials. A systematic determination of the yield strengths of common pharmaceutical solids with appropriate correlation to their bulk powder compaction properties will be useful.

Dry surface coating for powder flow enhancement

Our work described in Chapter 4 shows that by simple surface dry coating using a common laboratory tool, such as comilling, the flow properties of highly cohesive powders can be substantially enhanced. This approach is attractive because of it does not significantly impact average particle size of the powder, unlike granulation. Therefore, a significant portion of tabletability of the powders is preserved after nanocoating. This comilled composite displays both good flow and compaction properties, making the material potentially amenable to direct compression. The next step in this study would be to apply the same concept to enhance the flow of poorly flowing drugs. A large fraction of drug powders have very fine average particle sizes (<~30μm) and are, therefore, highly cohesive and poorly flowing. This leads to a substantial challenge during powder compaction, as the powder does not flow from hopper under gravity. A successful demonstration of the nanocoating approach in enhancing the flow properties of cohesive drugs, without affecting their compaction, will justify its widespread use during drug development.

Another potential aspect that requires further evaluation is the impact of dry surface coating with hydrophobic silica on drug dissolution. Even though the silica levels required for flow enhancement are low, the effect on dissolution remains to be investigated.

Mechanical amorphization of crystals

A significant portion of our amorphization studies have focused on single component crystals. We also have briefly demonstrated that some of the concepts can potentially be extended to multi-component crystals, such as cocrystals. A useful next step would be to systematically investigate the amorphization potential of more structurally diverse cocrystals and salts to validate the concurrent influence of crystal lattice strength and amorphous stability on amorphization. Another interesting aspect to further investigate is the amorphization of solvates and hydrates. There can be several possibilities when a solvate is milled. The solvent molecule can potentially stabilize the crystal lattice to increase the resistance to amorphization. In such a scenario, a delayed amorphization onset is expected, relative to the parent desolvate. However, it is also possible that the solvent molecule actually leaves the lattice under milling stress resulting in lattice collapse. However, in this case, the evolved solvent will act as a plasticizer to potentially facilitate recrystallization. The interpretation of solvate amorphization can potentially be very challenging, but can provide fresh insight into the amorphization problem.

Finally, it would be interesting to see if there is any correlation between the Amorphization Classification System developed here with the Biopharmaceutical Classification System of drugs. Based on very preliminary analysis, I have observed that drugs in Class II and IV of BCS classification (low solubility) actually fall in Class IV of ACS classification (good amorphous candidates). This might be attributed to configurational flexibility of molecules that influence both solubility and amorphization. If such a correlation between the two classification systems is confirmed, it will imply that amorphous phase preparation is inherently appropriate as a drug solubilization approach.

BIBLIOGRAPHY

Chapter 1.

1. FDA Report, *Critical path opportunities for generic drugs*; 2007.

2. FDA White Paper, *Question-based review (QbR) for generic drugs: An enhanced pharmaceutical quality assessment system*; 2005.

3. Brittain, H. G., *Polymorphism in Pharmaceutical Solids*. Marcel Dekker: New York, 1999.

4. Datta, S.; Grant, D. J. W., Crystal structures of drugs: Advances in determination, prediction and engineering. *Nature Rev.* **2004,** 3, 42-57.

5. Bernstein, J., *Polymorphism in Molecular Crystals*. Oxford University Press: New York, 2002.

6. Grant, D. J. W.; Higuchi, T., *Solubility behavior of organic compounds*. John Wiley & Sons: New York, 1990.

7. Chen, X.; Stowell, J. G.; Morris, K. R.; Byrn, S. R., Quantitative study of solid-state acid–base reactions between polymorphs of flufenamic acid and magnesium oxide using X-ray powder diffraction. *J Pharm Biomed Anal* **2010,** 51, 866–874.

8. Sun, C. C.; Grant, D. J. W., Influence of Crystal Structure on the Tableting Properties of Sulfamerazine Polymorphs. *Pharm. Res.* **2001,** 18, 274-280.

9. Temperley, H. N. V.; Blythe, G. E. K., Mills which grind to micron size without moving parts. *Nature* **1968,** 219, 1218-1222.

10. Parrott, E. L., Comminution. In *Encyclopedia of Pharmaceutical Technology*, Swarbrick, J.; Boylan, J. C., Eds. Marcel Dekker: New York, 1990; pp 101-121.

11. Kamahara, T.; Takasuga, M.; Tung, H. H.; Hanaki, K.; Fukunaka, T.; Izzo, B.; Nakada, J.; Yabuki, Y.; Kato, Y., Generation of fine pharmaceutical particles via controlled secondary nucleation under high shear environment during crystallization—Process development and scale-up. *Org Process Res Dev* **2007,** 11, 699–703.

12. Sun, C. C., Materials science tetrahedron--a useful tool for pharmaceutical research and development. *J. Pharm. Sci.* **2009,** 98, 1671-1687.

13. Yu, L., Amorphous pharmaceutical solids: preparation, characterization and stabilization. *Adv Drug Del Rev* **2001,** 48, 27-42.

14. Hilden, L. R.; Morris, K. R., Physics of amorphous solids. *J Pharm Sci* **2001,** 93, 3-12.

15. Hancock, B. C.; Carlson, G. T.; Ladipo, D. D.; Langdon, B. A.; Mullarney, M. P., Comparison of the mechanical properties of the crystalline and amorphous forms of a drug substance. *Int J Pharm* **2002,** 241, 73-85.

16. Datta, S.; Grant, D. J. W., Crystal structures of drugs: Advances in determination, Prediction and engineering. *Nature Reviews* **2004,** 3, 42-57.

17. Burger, A.; Ramberger, R., On the Polymorphism of Pharmaceuticals and Other Molecular Crystals. I Theory of Thermodynamic Rules. *Mikrochim Acta* **1979**, 259--271.

18. Burger, A.; Ramberger, R., On the Polymorphism of Pharmaceuticals and Other Molecular Crystals. II Applicability of Thermodynamic Rules. *Mikrochim Acta* **1979**, 273--316.

19. Borka, L.; Haleblian, J. K., Crystal polymorphism of pharmaceuticals. *Acta Pharm. Jugosl.* **1990,** 40, 71–94.

20. Griesser, U. J., *The importance of solvates*. Wiley-VCH: Weinheim, 2006.

21. Morris, K. R., *Structural aspects of hydrates and solvates*. Marcel Dekker: New York, 1999.

22. Schultheiss, N.; Newman, A., Pharmaceutical Cocrystals and Their Physicochemical Properties. *Cryst Growth Des* **2009,** 9, 2950–2967.

23. Debenedetti, P. G.; Stillinger, F. H., Supercooled liquids and the glass transition. *Nature* **2001,** 410, 259-267.

24. Zeng, Q.; Sheng, H.; Ding, Y.; Wang, L.; Yang, W.; Jiang, J.-Z.; Mao, W. L.; Mao, H.-K., Long-Range Topological Order in Metallic Glass. *Science* **2011,** 332, 1404-1406.

25. Hancock, B. C.; Parks, M., What is the true solubility advantage for amorphous pharmaceuticals? *Pharm Res* **2000,** 17, 397–404.

26. Murdande, S. B.; Pikal, M. J.; Shanker, R. M.; Bogner, R. H., Solubility Advantage of Amorphous Pharmaceuticals: I. A Thermodynamic Analysis. *J. Pharm. Sci.* **2010,** 99, 1254-1264.

27. Murdande, S. B.; Pikal, M. J.; Shanker, R. M.; Bogner, R. H., Solubility Advantage of Amorphous Pharmaceuticals: II. Application of Quantitative Thermodynamic Relationships for Prediction of Solubility Enhancement in Structurally Diverse Insoluble Pharmaceuticals. *Pharm Res* **2010,** 27, 2704–2714.

28. Murdande, S. B.; Pikal, M. J.; Shanker, R. M.; Bogner, R. H., Solubility Advantage of Amorphous Pharmaceuticals, Part 3: Is Maximum Solubility Advantage Experimentally Attainable and Sustainable? *J. Pharm. Sci.* **2011,** 100, 4349–4356.

29. Amidon, G. L.; Lennernaes, H.; Shah, V. P.; Crison, J. R., A theoretical basis for a biopharmaceutic drug classification: The correlation of in vitro drug product dissolution and in vivo bioavailability. *Pharm Res* **1995,** 12, 413–420.

30. Takagi, T.; Ramachandran, C.; Bermejo, M.; Yamashita, S.; Yu, L. X.; Amidon, G. L., A provisional biopharmaceutical classification of the top 200 oral drug products in the United States, Great Britain, Spain, and Japan. *Mol Pharmaceutics* **2006,** 3, 631–643.

31. Pikal, M. J.; Rigsbee, D. R., The stability of insulin in crystalline and amorphous solids: observation of greater stability for the amorphous form. *Pharm. Res.* **1997,** 14, 1379– 1387.

32. Sukenik, C. N.; Bonapace, J. A. P.; Mandel, N. S.; Bergman, R. G.; Lau, P. Y.; Wood, G., Enhancement of a chemical reaction rate by proper orientation of reacting molecules in the solid state. *J. Am. Chem. Soc.* **1975,** 97, 5290– 5291.

33. Sukenik, C. N.; Bonapace, J. A. P.; Mandel, N. S.; Lau, P. Y.; Wood, G.; Bergman, R. G., A kinetic and X-ray diffraction study of the solid-state rearrangement of methyl p-dimethylaminobenzenesulfonate. Reaction rate enhancement due to proper orientation in a crystal. *J. Am. Chem. Soc.* **1977,** 99, 851– 858.

34. Grant, D. J. W.; Higuchi, T., *Solubility behavior of organic compounds*. John Wiley & Sons: New York, 1990; Vol. 21.

35. Byrn, S. R., *Solid State Chemistry of Drugs*. Academic Press: New York, 1982.

36. National Research Council (US), *Materials science and engineering: Forging stronger links to users*; National Academy Press: Washington, D.C., 1999.

37. Newton, J. M.; Mashadi, A. B.; Podczeck, F., The mechanical properties of a homologous series of benzoic acid esters. *Eur. J. Pharm. Biopharm* **1993,** 39, 153–157.

38. Pedersen, S.; Kristensen, H. G., Compaction behavior of 4-hydroxybenzoic acid and two esters compared to their mechanical properties. *Eur. J. Pharm. Biopharm* **1995,** 41, 323–328.

39. Roberts, R. J.; Rowe, R. C.; York, P., The relationship between Young's modulus of elasticity of organic solids and their molecular structure. *Powder Technol* **1991,** 61, 139–146.

40. Roberts, R. J.; Rowe, R. C.; York, P., The relationship between the fracture properties, tensile strength and critical stress intensity factor of organic solids and their molecular structure. *Int. J. Pharm* **1995,** 125, 157–162.

41. Roberts, R. J.; Rowe, R. C.; York, P., The relationship between indentation hardness of organic solids and their molecular structure. *J. Mater. Sci* **1994,** 29, 2289–2296.

42. Roberts, R. J.; Rowe, R. C.; York, P., The solubility parameter and fractional polarity of microcrystalline cellulose as determined by mechanical measurement. *Int J Pharm* **1989,** 52, 213–219.

43. Narayan, P.; Hancock, B. C., The relationship between the particle properties, mechanical behavior, and surface roughness of some pharmaceutical excipient compacts. *Mater Sci Eng A* **2003,** 355, 24–36.

44. Amidon, G. E.; Houghton, M. E., The effect of moisture on the mechanical and powder flow properties of microcrystalline cellulose. *Pharm. Res.* **1995,** 12, 923–929.

45. Taylor, L. J.; Papadopoulos, D. G.; Dunn, P. J.; Bentham, A. C.; Dawson, N. J.; Mitchell, J. C.; Snowden, M. J., Predictive milling of pharmaceutical materials using nanoindentation of single crystals. *Org Process Res Dev* **2004,** 8, 674-679.

46. Hiestand, E. N.; Smith, D. P., Indices of tableting performance. *Powder Technol* **1984,** 38, 145–159.

47. Sun, C. C.; Grant, D. J. W., Influence of Crystal Structure on the Tableting Properties of Sulfamerazine Polymorphs. *Pharm. Res.* **2001,** 18, (3), 274 - 280.

48. Sun, C. C.; Grant, D. J. W., Improved tableting properties of p-hydroxybenzoic acid by water of crystallization: a molecular insight. *Pharm. Res.* **2004,** 21, (2), 382-386.

49. Chattoraj, S.; Shi, L.; Sun, C. C., Understanding the relationship between crystal structure, plasticity and compaction behaviour of theophylline, methyl gallate, and their 1:1 co-crystal. *CrystEngComm* **2010,** 12, 2466-2472.

50. Perumalla, S. R.; Shi, L.; Sun, C. C., Ionized form of acetaminophen with improved compaction properties. *CrystEngComm* **2012**.

51. Schultheiss, N.; Newman, A., Pharmaceutical Cocrystals and Their Physicochemical Properties. *Cryst. Growth Des.* **2009,** 9, 2950-2967.

52. Reddy, C. M.; Krishna, G. R.; Ghosh, S., Mechanical properties of molecular crystals—applications to crystal engineering. *Cryst Eng Comm* **2010,** 12, 2296-2314.

53. Sun, C. C., Decoding powder tabletability. *J. Adhesion Sci. Technol.* **2011,** 25, 483–499.

54. Weertman, J.; Weertman, J. R., *Elemental dislocation theory*. Oxford Uni. Press: Oxford, 1992.

55. Minor, A. M.; Syed Asif, S. A.; Shan, Z.; Stach, E. A.; Cyrankowski, E.; Wyrobek, T. J.; Warren, O. L., A new view of the onset of plasticity during the nanoindentation of aluminium. *Nat. Mater.* **2006,** 5, 697–702.

56. Hirth, J. P.; Lothe, J., *Theory of Dislocations* McGraw-Hill: New York, 1968.

57. Brittain, H. G., Cocrystal Systems of Pharmaceutical Interest: 2010. *Cryst. Growth Des.* **2011**.

58. Rowe, R. C.; Roberts, R. J., *Pharmaceutical powder compaction technology*. Marcel Dekker: New York, 1996; Vol. 71.

59. Shi, L.; Sun, C. C., Overcoming Poor Tabletability of Pharmaceutical Crystals by Surface Modification. *Pharm Res* **2011,** 28, 3248-3255.

60. Karki, S.; Friscic, T.; Fabian, L.; Laity, P. R.; Day, G. M.; Jones, W., Improving Mechanical Properties of Crystalline Solids by Cocrystal Formation: New Compressible Forms of Paracetamol. *Adv. Mater.* **2009,** 21, 3905.

61. Sun, C. C., Materials Science Tetrahedron—A Useful Tool for Pharmaceutical Research and Development. *J. Pharm. Sci.* **2009,** 98, (5), 1671 - 1687.

62. Bag, P. P.; Chen, M.; Sun, C. C.; Reddy, C. M., Direct correlation among crystal structure, mechanical behaviour and tabletability in a trimorphic molecular compound. *Cryst Eng Comm* **2012,** 14, 3865-3867.

63. Sun, C. C.; Hou, H., Improving Mechanical Properties of Caffeine and Methyl Gallate Crystals by Cocrystallization. *Cryst. Growth Des.* **2008,** 8, (9), 1575 - 1579.

64. Taylor, G. I., The Mechanism of Plastic Deformation of crystals Part I. Theoretical. *Proc. R. Soc. Lond. A* **1934,** 145 362-387.

65. Sun, C. C., On the mechanism of reduced tabletability of granules prepared by roller compaction. *Int. J. Pharm.* **2008,** 347, 171 - 172.

66. Bandyopadhyay, R.; Grant, D. J. W., Plasticity and Slip System of Plate-Shaped Crystals of L-Lysine Monohydrochloride Dihydrate. *Pharm. Res.* **2002,** 19, (4), 491 - 496.

67. Argon, A.; Quentin, B., *Strengthening Mechanisms in Crystal Plasticity* Oxford Scholarship Online: 2007.

68. Sun, C. C.; Kiang, Y. H., On the Identification of Slip Planes in Organic Crystals Based on Attachment Energy Calculation. *J. Pharm. Sci.* **2008,** 97, (8), 3456 - 3461.

69. Bandyopadhyay, R.; Grant, D. J. W., Plasticity and Slip System of Plate-Shaped Crystals of L-Lysine Monohydrochloride Dihydrate. *Pharm. Res.* **2002,** 19, 491-496.

70. Cao, X.; Morganti, M.; Hancock, B. C.; Masterson, V. M., Correlating Particle Hardness With Powder Compaction Performance. *J Pharm Sci* **2010,** 99, 4307-4316.

71. Karki, S.; Friscic, T.; Fabian, L.; Laity, P. R.; Day, G. M.; Jones, W., Improving Mechanical Properties of Crystalline Solids by Cocrystal Formation: New Compressible Forms of Paracetamol. *Adv Mater* **2009,** 21, 3905-3909.

72. Perumalla, S. R.; Sun, C. C., Ionized form of acetaminophen with improved compaction properties. *Cryst Eng Comm* **2012,** 14, 2389-2390.

73. Spillmann, A.; Sonnenfeld, A.; Rohr, P. R. V., Effect of surface free energy on the flowability of lactose powder treated by PECVD. *Plasma Process. Polym.* **2008,** 5, 753–758.

74. Kendall, K., Adhesion: molecules and mechanics. *Science* **1994,** 263, 1720-1725.

75. Mei, R.; Shang, H.; Klausner, J. F.; Kallman, E., A contact model for the effect of particle coating on improving the flowability of cohesive powders. *KONA* **1997,** 15, 132-141.

76. Shi, L.; Feng, Y.; Sun, C. C., Roles of granule size in over-granulation during high shear wet granulation. *J Pharm Sci* **2010,** 99, 3322-3325.

77. Hamaker, H. C., The London – van der Waals attraction between spherical particles. *Physica* **1937,** 4, 1058–1072.

78. Yang, J.; Sliva, A.; Banerjee, A.; Dave, R. N.; Pfeffer, R., Dry particle coating for improving the flowability of cohesive powders. *Powder Technol* **2005,** 158, 21-33.

79. Narh, K. A.; Agwedicham, A. T.; Jallo, L., Dry coating polymer powder particles with deagglomerated carbon nanotubes to improve their dispersion in nanocomposites. *Powder Technol* **2008,** 186, 206-212.

80. Pfeffer, R.; Dave, R. N.; Wei, D.; Ramlakhan, M., Synthesis of engineered particulates with tailored properties using dry particle coating. *Powder Technol* **2001,** 117, 40-67.

81. Zhou, Q.; Armstrong, B.; Larson, I.; Stewart, P. J.; Morton, D. A. V., Improving Powder Flow Properties of a Cohesive Lactose Monohydrate Powder by Intensive Mechanical Dry Coating. *J. Pharm. Sci.* **2010**.

82. Zhou, Q.; Denman, J. A.; Gengenbach, T.; Das, S.; Qu, L.; Zhang, H.; Larson, I.; Stewart, P. J.; Morton, D. A., Characterization of the Surface Properties of a Model Pharmaceutical Fine Powder Modified with a Pharmaceutical Lubricant to Improve Flow via a Mechanical Dry Coating Approach. *J Pharm Sci* **2011,** 99, 969-981.

83. Fan, G. J.; Guo, F. Q.; Hu, Z. Q.; Quan, M. X.; Lu, K., Amorphization of selenium induced by high-energy ball milling. *Phys Rev B* **1997,** 55, 11010-11013.

84. Zhao, Y. H.; Jin, Z. H.; Lu, K., Mechanical-milling-induced amorphization of Se: a crystallite destabilization model. *Philos. Mag. Lett.* **1999,** 79, 747-754.

85. Chamarthy, S. P.; Pinal, R., The nature of crystal disorder in milled pharmaceutical materials. *Colloids Surf. A* **2008,** 331, 68–75.

86. Lin, Z. J.; Zhuo, M. J.; Sun, Z. Q.; Veyssiere, P.; Zhou, Y. C., Amorphization by dislocation accumulation in shear bands. *Acta Mater* **2009,** 57, 2851 - 2857.

87. Crowley, K. J.; Zografi, G., Cryogenic Grinding of Indomethacin Polymorphs and Solvates: Assessment of Amorphous Phase Formation and Amorphous Phase Physical Stability. *J. Pharm. Sci.* **2002,** 91, 492-507.

88. Elamin, A. A.; Ahlneck, C.; Alderborn, G.; Nystrom, C., Increased metastable solubility of milled griseofulvin, depending on the formation of a disordered surface structure. *Int. J. Pharm.* **1994,** 111, 159-170.

89. Trasi, N. S.; Boerrigter, S. X. M.; Byrn, S. R., Investigation of the Milling-Induced Thermal Behavior of Crystalline and Amorphous Griseofulvin *Pharm. Res.* **2010,** 27, 1377-1389.

90. Willart, J. F.; Descamps, M., Solid State Amorphization of Pharmaceuticals. *Mol. Pharm.* **2008,** 5, 905–920.

91. Zhang, G. G. Z.; Law, D.; Schmitt, E. A.; Qiu, Y., Phase transformation considerations during process development and manufacture of solid oral dosage forms. *Adv Drug Del Rev* **2004,** 56, 371-390.

92. Morris, K. R.; Griesser, U. J.; Eckhardt, C. J.; Stowell, J. G., Theoretical approaches to physical transformations of active pharmaceutical ingredients during manufacturing processes. *Adv Drug Deliv Rev* **2001,** 48, 91–114.

93. Yu, L., Amorphous pharmaceutical solids: preparation, characterization and stabilization. *Adv. Drug Del. Rev.* **2001,** 48, 27-42.

94. Pouton, C. W., Formulation of poorly water soluble drugs for oral administration: Physicochemical and physiological issues and the lipid formulation classification system. *Eur. J. Pharm. Sci.* **2006,** 29, 278–287.

95. Hilden, L. R.; Morris, K. R., Physics of amorphous solids. *J. Pharm. Sci.* **2001,** 93, 3–12.

96. Huttenrauch, R.; Fricke, S.; Zeilke, P., Mechanical activation of pharmaceutical systems. *Pharm. Res.* **1985**, 302-306.

97. Johnson, W. L.; Li, M.; Krill, C. E., The crystal to glass transformation in relation to melting. *J. Non-Cryst. Solids* **1993,** 156-158, 481-492.

98. Fecht, H. J., Defect-induced melting and solid state amorphization. *Nature* **1992,** 356, 133–135.

99. Lefort, R.; De Gusseme, A.; Willart, J. F.; Danede, F.; Descamps, M., Solid state NMR and DSC methods for quantifying the amorphous content in solid dosage forms: An application to ball-milling of trehalose. *Int J Pharm* **2004,** 280, 209–219.

100. Willart, J. F.; Descamps, M., Solid State Amorphization of Pharmaceuticals. *Mol Pharm* **2008,** 5, 905–920.

101. Chattoraj, S.; Bhugra, C.; Telang, C.; Zhong, L.; Wang, Z.; Sun, C. C., Origin of Two Modes of Non-isothermal Crystallization of Glasses Produced by Milling. *Pharm Res* **2012,** 29, 1020-1032.

102. Wildfong, P. L. D.; Hancock, B. C.; Moore, M. D.; Morris, K. R., Towards an understanding of the structurally based potential for mechanically activated disordering of small molecule organic crystals. *J Pharm Sci* **2006,** 95, 2645–2656.

103. Tse, J. S., Mechanical instability of ice Ih. A mechanism for pressure-induced amorphization. *J Chem Phys* **1992,** 96, 5482-5487.

104. Fecht, H. J., Defect-induced melting and solid-state amorphization. *Nature* **1992,** 356, 133-135.

105. Tromans, D.; Meech, J. A., Enhanced dissolution of minerals: Stored energy, amorphism and mechanical activation. *Miner Eng* **2001,** 14, 1359–1377.

106. Patterson, J. E.; James, M. B.; Forster, A. H.; Lancaster, R. W.; Butler, J. M.; Rades, T., The Influence of Thermal and Mechanical Preparative Techniques on the Amorphous State of Four Poorly Soluble Compounds. *J. Pharm. Sci.* **2005,** 94, 1998-2012.

107. Lin, Y.; Cogdill, R. P.; Wildfong, P. L. D., Informatic calibration of a materials properties database for predictive assessment of mechanically activated disordering potential for small molecule organic solids. *J Pharm Sci* **2008,** 98, 2696-2708.

108. Willart, J. F.; De Gusseme, A.; Hemon, S.; Odou, G.; Danede, F.; Descamps, M., Direct crystal to glass transformation of trehalose induced by ball milling. *Solid State Commun* **2001,** 119, 501–505.

109. York, P., Crystal engineering and particle design for the powder compaction process. *Drug Dev Ind Pharm* **1992,** 18, 677–721.

110. Sun, C. C.; Hao, H., Improving Mechanical Properties of Caffeine and Methyl Gallate Crystals by Cocrystallization. *Cryst Growth Des* **2008,** 8, 1575–1579.

Chapter 2.

1. Basavoju, S.; Bostrom, D.; Velaga, S. P., Indomethacin-saccharin co crystal: design, synthesis and preliminary pharmaceutical characterization. *Pharm. Res.* **2007,** 25, 530-540.

2. Childs, S. L., Crystal engineering approach to forming co-crystals of amine hydrochlorides with organic acids. Molecular complexes of fluoxetine hydrochloride with benzoic, succinic, and fumaric acids. *J. Am. Chem. Soc.* **2004,** 126, 13335-13342.

3. Trask, A. V.; Motherwell, W. D. S.; Jones, W., Physical stability enhancement of theophylline via cocrystallization. *Int. J. Pharm.* **2006,** 320, 114 - 123.

4. Sun, C. C.; Hou, H., Improving Mechanical Properties of Caffeine and Methyl Gallate Crystals by Cocrystallization. *Cryst. Growth Des.* **2008,** 8, (9), 1575 - 1579.

5. Karki, S.; Friscic, T.; Fabian, L.; Laity, P. R.; Day, G. M.; Jones, W., Improving mechanical properties of crystalline solids by cocrystal formation: New compressible forms of paracetamol. *Adv. Mater.* **2009,** 21, 3905-3909.

6. Morrissette, S.; Almarsson, O.; Peterson, M.; Remenar, J., High-throughput crystallisation: polymorphs, salts, co-crystals and solvates of pharmaceutical solids. *Adv. Drug Deliv. Rev.* **2004,** 56, 275-300.

7. Sun, C. C., Solid-state properties and crystallization behavior of PHA-739521 polymorphs. *International Journal of Pharmaceutics* **2006,** 319, 114 - 120.

8. Vishweshwar, P.; McMahon, J. A.; Peterson, M. L.; Hickey, M. B.; Shattock, T. R.; Zaworotko, M. J., Crystal engineering of pharmaceutical co-crystals from polymorphic active pharmaceutical ingredients. *Chem. Commun.* **2005**, 4601-4603.

9. Schartman, R. R., On the thermodynamics of cocrystal formation. *Int. J. Pharm.* **2009,** 365, 77-80.

10. Perlstein, J., *Crystal Engineering: from Molecules and Crystals to Materials*. Kluwer Academic: Boston, 1999; Vol. 538, p 23-42.

11. Datta, S.; Grant, D. J. W., Crystal structures of drugs: advances in determination, prediction and engineering. *Nature Reviews Drug Discovery* **2004,** 3, 42-57.

12. Reddy, C. M.; Gundakaram, R. C.; Basavoju, S.; Kirchner, M. T.; Padmanabhan, K. A.; Desiraju, G. R., Structural basis for bending of organic crystals. *Chem. Commun.* **2005**, 3945.

13. McBride, J. M.; Segmulle, B. E.; Hollingsworth, M. D.; Mills, D. E.; Weber, B. A., Mechanical Stress and Reactivity in Organic Solids. *Science* **1986,** 234, (4778), 830 - 835.

14. Taylor, G. I., The Mechanism of Plastic Deformation of crystals Part I. Theoretical. *Proc. R. Soc. Lond. A* **1934,** 145 362-387.

15. Sun, C. C., On the mechanism of reduced tabletability of granules prepared by roller compaction. *Int. J. Pharm.* **2008,** 347, 171 - 172.

16. Weertman, J.; Weertman, J. R., *Elemental Dislocation Theory*. Oxford Uni. Press: Oxford, 1992.

17. Bandyopadhyay, R.; Grant, D. J. W., Plasticity and Slip System of Plate-Shaped Crystals of L-Lysine Monohydrochloride Dihydrate. *Pharm. Res.* **2002,** 19, (4), 491 - 496.

18. Argon, A.; Quentin, B., *Strengthening Mechanisms in Crystal Plasticity* Oxford Scholarship Online: 2007.

19. Sun, C. C.; Kiang, Y. H., On the Identification of Slip Planes in Organic Crystals Based on Attachment Energy Calculation. *J. Pharm. Sci.* **2008,** 97, (8), 3456 - 3461.

20. Fell, J. T.; Newton, J. M., Determination of tablet strength by the diametral-compression test. *J. Pharm. Sci.* **1970,** 59, 688-691.

21. Bebout, D.; Pagola, S., *Acta Cryst E* **2009,** E65, 317-318.

22. Naqvi, A. A.; Bhattacharyya, G. C., Crystal data for anhydrous theophylline. *J. Appl. Cryst.* **1991,** 14, 464-464.

23. Oliver, W. C.; Pharr, G. M., An improved technique for determining hardness and elastic modulus using load and displacement sensing indentation experiments. *J. Mater. Res.* **1992,** 7, 1564-1580.

24. Roberts, R. J.; Rowe, R. C.; York, P., *Powder Technol.* **1991,** 65, 139-146.

25. For slip system (h k l) <u v w>, the Burgers vector magnitude is b=*m*a[u v w], where a is the unit cell axis along the direction of slip vector, and *m* is a fraction depending on the type of dislocation ($m = 0.5$ for pure dislocations and $m \leq 0.5$ for partial dislocations). As a general case, we used $m = 0.1$ in our calculations. The choice of *m*

value affects size of b but not the rank order because the same *m* has been used for all three crystals. More detailed explanations may be found in reference 16.

26. Hancock, B. C.; Carlson, G. T.; Ladipo, D. D.; Langdon, B. A.; Mullarney, M. P., Comparison of the mechanical properties of the crystalline and amorphous forms of a drug substance. *Int. J. Pharm.* **2002,** 241, 73 - 85.

27. Sun, C. C., Materials Science Tetrahedron—A Useful Tool for Pharmaceutical Research and Development. *J. Pharm. Sci.* **2009,** 98, (5), 1671 - 1687.

28. Doerner, M. F.; Nix, W. D., *J. Mater. Res.* **1986,** 1, 601.

29. Dimiduk, D. M.; Woodward, C.; LeSar, R.; Uchic, M. D., Scale-free intermittent flow in crystal plasticity. *Science* **2006,** 312, 1188-1190.

30. Rowe, R. C.; Roberts, R. J., *Pharmaceutical powder compaction technology*. Marcel Dekker: New York, 1996; Vol. 71.

31. Mayo, S. L.; Olafson, B. D.; Goddard, W. A. I., DREIDING: A generic forcefield. *J. Phys. Chem.* **1990,** 94, 8897–8909.

32. Brinckmann, S.; Siegmund, T.; Huang, Y., A dislocation density based strain gradient model. *Int. J. Plasticity* **2006,** 22, 1784-1797.

33. Kuhlmann-Wilsdorf, D., Theory of dislocation based crystal plasticity. *Philos. Magaz. A* **1999,** 79, 955-1008.

34. Mott, M. F.; Nabarro, F. R. N., *Report on strength of solids*. Physical Society: London, 1948; Vol. 1.

35. Tromans, D.; Meech, J. A., Enhanced dissolution of materials: microtopography and mechanical activation. *Miner Engg* **1999,** 12, 609-625.

36. Cuitino, A. M.; Ortiz, M., *Model Simulat. Mater. Sci. Eng.* **1992,** 1, 225-263.

Chapter 3.

1. Byrn, S. R.; Pfeiffer, R. R.; Stowell, J. G., *Solid-state Chemistry of Drugs*. 1 ed.; Academic. Press: New York, 1982.

2. Hartel, R. W., *Crystallization in Foods* Aspen Publication: Maryland, 2001.

3. Roesky, H. W.; Andruh, M., The interplay of coordinative, hydrogen bonding and π–π stacking interactions in sustaining supramolecular solid-state architectures.: A study case of bis(4-pyridyl)- and bis(4-pyridyl-N-oxide) tectons. *Coord. Chem. ReV.* **2003,** 236, 91-119.

4. Ferrer, J. R.; Lahti, P. M.; George, C.; Oliete, P.; Julier, M.; Palacio, F., Role of Hydrogen Bonds in Benzimidazole-Based Organic Magnetic Materials: Crystal Scaffolding or Exchange Linkers? *Chem. Mater.* **2001,** 13, 2447–2454.

5. Desiraju, G. R., Crystal engineering: the design of organic solids. Elsevier: 1989; Vol. 54.

6. Brittain, H. G., Polymorphism in Pharmaceutical Solids, Drugs and the Pharmaceutical Sciences. Marcel Dekker: 1999; Vol. 95.

7. Stahl, P. H.; Wermuth, C. G., *Handbook of Pharmaceutical Salts: Properties, Selection and Use*. Verlag Helvetica Chimica Acta: Zurich, 2002.

8. Hilfiker, R.; Griesser, U. J., The Importance of Solvates. In *Polymorphism: in the Pharmaceutical Industry*, Hilfiker, R., Ed. Wiley-VCH: 2006.

9. Schultheiss, N.; Newman, A., Pharmaceutical Cocrystals and Their Physicochemical Properties. *Cryst. Growth Des.* **2009,** 9, 2950-2967.

10. Brittain, H. G., Cocrystal Systems of Pharmaceutical Interest: 2010. *Cryst. Growth Des.* **2011**, 12(2), 1046–1054.

11. Bhatt, P. M.; Ravindra, N. V.; Banerjee, R.; Desiraju, G. R., Saccharin as a salt former. Enhanced solubilities of saccharinates of active pharmaceutical ingredients. *Chem. Commun.* **2005**, 1073–1075.

12. Aakeroy, C. B.; Salmon, D. J., Building Co-Crystals with Molecular Sense and Supramolecular Sensibility. *CrystEngComm* **2005,** 7, 439-448.

13. Rodríguez-Hornedo, N.; Nehm, S. J.; Jayasankar, A., *Cocrystals: Design, Properties and Formation Mechanisms*. Informa Health Care: 2006; Vol. 3.

14. Ban, M.; Bombicz, P.; Madarász, J., Thermal stability and structure of a new co-crystal of theophylline formed with phthalic acid *J. Thermal Anal. Cal.* **2009,** 95, (3), 1572.

15. Jayasankar, A. Understanding the mechanisms, thermodynamics and kinetics of cocrystallization to control phase transformations. The University of Michigan, Michigan, 2008.

16. McNamara, D. P.; Childs, S. L.; Giordano, J.; Iarriccio, A.; Cassidy, J.; Shet, M. S.; Mannion, R.; E., O. D.; Park, A., Use of a Glutaric Acid Cocrystal to Improve Oral Bioavailability of a Low Solubility API. *Pharmaceutical Research* **2006,** 23, 1888.

17. Kelley, S. P.; Fabian, L.; Brock, C. P., Failures of fractional crystallization: ordered cocrystals of isomers and near isomers. *Acta Cryst.* **2011,** B67, 79–93.

18. Trask, A. V., An Overview of Pharmaceutical Cocrystals as Intellectual Property. *Mol. Pharmaceutics* **2007,** 4, 301–309.

19. Weertman, J.; Weertman, J. R., *Elemental dislocation theory*. Oxford Uni. Press: Oxford, 1992.

20. Minor, A. M.; Syed Asif, S. A.; Shan, Z.; Stach, E. A.; Cyrankowski, E.; Wyrobek, T. J.; Warren, O. L., A new view of the onset of plasticity during the nanoindentation of aluminium. *Nat. Mater.* **2006,** 5, 697–702.

21. Hirth, J. P.; Lothe, J., *Theory of Dislocations* McGraw-Hill: New York, 1968.

22. Chou, P. C.; Pagano, N. J., *Elasticity - Tensor, Dyadic and Engineering Approaches*. Dover Publications: New York, 1992.

23. Sun, C. C., Decoding powder tabletability. *J. Adhesion Sci. Technol.* **2011,** 25, 483–499.

24. Sun, C. C.; Hou, H., Improving Mechanical Properties of Caffeine and Methyl Gallate Crystals by Cocrystallization. *Cryst. Growth Des.* **2008,** 8, (9), 1575 - 1579.

25. Karki, S.; Friscic, T.; Fabian, L.; Laity, P. R.; Day, G. M.; Jones, W., Improving Mechanical Properties of Crystalline Solids by Cocrystal Formation: New Compressible Forms of Paracetamol. *Adv. Mater.* **2009,** 21, 3905.

26. Chattoraj, S.; Shi, L.; Sun, C. C., Understanding the relationship between crystal structure, plasticity and compaction behaviour of theophylline, methyl gallate, and their 1:1 co-crystal. *CrystEngComm* **2010,** 12, 2466-2472.

27. Oliver, W. C.; Pharr, G. M., An improved technique for determining hardness and elastic modulus using load and displacement sensing indentation experiments. *J. Mater. Res.* **1992,** 7, 1564-1580.

28. Ramos, K. J.; Bahr, D. F., Mechanical behavior assessment of sucrose using nanoindentation. *J. Mater. Res.* **2007,** 22, 2037-2045.

29. Joiris, E.; Martino, P. D.; Berneron, C.; Guyot-Hermann, A.-M.; Guyot, J.-C., Compression behavior of orthorhombic paracetamol. *Pharm Res* **1998,** 15, 1122–1130.

30. Chattoraj, S.; Bhugra, C.; Telang, C.; Zhong, L.; Wang, Z.; Sun, C. C., Origin of Two Modes of Non-isothermal Crystallization of Glasses Produced by Milling. *Pharm Res* **2012,** 29, 1020-1032.

31. Sun, C. C.; Kiang, Y. H., On the Identification of Slip Planes in Organic Crystals Based on Attachment Energy Calculation. *J. Pharm. Sci.* **2008,** 97, (8), 3456 - 3461.

32. Ryshkewitch, E., Compression strength of porous sintered alumina and zirconia, 9th communication to ceramography. *J Amer Ceramic Soc* **1953,** 36, 65-68.

33. Sun, C. C., Quantifying Errors in Tableting Data Analysis Using the Ryshkewitch Equation Due to Inaccurate True Density. *Journal of Pharmaceutical Sciences* **2005,** 94, (9), 2061 - 2068.

34. Gerberich, W. W.; Yu, W.; Kramer, D.; Strojny, A.; Bahr, D.; Lilleodden, E.; Nelson, J., Elastic loading and elastoplastic unloading from nanometer level indentations for modulus determinations. *J. Mater. Res.* **1998,** 13, 421-439.

35. Lethbridge, Z. A. D.; Walton, R. I.; Marmier, A. S. H.; Smith, C. W.; Evans, K. E., Elastic anisotropy and extreme Poisson's ratios in single crystals. *Acta Mater.* **2010,** 58, 6444–6451.

36. Varughese, S.; Kiran, M. S. R. N.; Solanko, K. A.; Bond, A. D.; Ramamurty, U.; Desiraju, G. R., Interaction anisotropy and shear instability of aspirin polymorphs established by nanoindentation. *Chem. Sci* **2011,** 2, 2236–2242.

37. Johnson, K. L., *Contact Mechanics*. Cambridge University Press, New York, 1985.

38. Hill, R., *Theoy of plasticity*. Oxford University Press: 1950.

39. Sun, C. C.; Grant, D. J. W., Influence of Crystal Structure on the Tableting Properties of Sulfamerazine Polymorphs. *Pharm. Res.* **2001,** 18, (3), 274 - 280.

40. Sun, C. C.; Grant, D. J. W., Improved tableting properties of p-hydroxybenzoic acid by water of crystallization: a molecular insight. *Pharm. Res.* **2004,** 21, (2), 382-386.

41. Perumalla, S. R.; Shi, L.; Sun, C. C., Ionized form of acetaminophen with improved compaction properties. *CrystEngComm* **2012**, 14, 2389-2390.

42. Reddy, C. M.; Krishna, G. R.; Ghosh, S., Mechanical properties of molecular crystals—applications to crystal engineering. *Cryst Eng Comm* **2010,** 12, 2296-2314.

43. Doerner, M. F.; Nix, W. D., A method for interpreting the data from depth-sensing indentation instrurnents *J. Mater. Res.* **1986,** 1, 601-609.

44. Gerberich, W. W.; Mook, W. M.; Chambers, M. D.; Cordill, M. J.; Perrey, C. R.; Carter, C. B.; Miller, R. E.; Curtin, W. A.; Mukherjee, R.; Girshick, S. L., An energy balance criterion for nanoindentation-induced suingle and multiple dislocation events. *J Applied Mech* **2006,** 73, 327-334.

45. Rowe, R. C.; Roberts, R. J., *Pharmaceutical powder compaction technology*. Marcel Dekker: New York, 1996; Vol. 71.

46. Shi, L.; Sun, C. C., Overcoming Poor Tabletability of Pharmaceutical Crystals by Surface Modification. *Pharm Res* **2011,** 28, 3248-3255.

47. Sun, C. C., Materials Science Tetrahedron—A Useful Tool for Pharmaceutical Research and Development. *J. Pharm. Sci.* **2009,** 98, (5), 1671 - 1687.

48. Bag, P. P.; Chen, M.; Sun, C. C.; Reddy, C. M., Direct correlation among crystal structure, mechanical behaviour and tabletability in a trimorphic molecular compound. *Cryst Eng Comm* **2012**.

49. Sun, C. C., Hou, H., Gao, P., Ma, C., Medina, C. and Alvarez, F. J., Development of a High Drug Load Tablet Formulation Based on Assessment of Powder Manufacturability Moving Towards Quality by Design. *J. Pharm. Sci.* **2009,** 98, (1), 239 - 247.

50. Mazel, V.; Busignies, V.; Diarra, H.; Tchoreloff, P., Measurements of Elastic Moduli of Pharmaceutical Compacts: A New Methodology Using Double Compaction on a Compaction Simulator. *J. Pharm. Sci.* **2012,** 101, 2200-2228.

Chapter 4.

1. Sun, C. C., Setting the bar for powder flow properties in successful high speed tableting. *Powder Technol* **2010,** 201, 106-108.

2. Crowder, T. M.; Hickey, A. J., The physics of powder flow applied to pharmaceutical solids. *Pharm Technol* **2000,** 24, 50–58.

3. Sun, C. C.; Hou, H.; Gao, P.; Ma, C.; Medina, C.; Alvarez, P., Development of a high drug load tablet formulation based on assessment of powder manufacturability—Moving towards quality by design. *J. Pharm. Sci.* **2009,** 98, 239–247.

4. Hou, H.; Sun, C. C., Quantifying effects of particulate properties on powder flow properties using a ring shear tester. *J. Pharm. Sci.* **2008,** 97, 4030-4039.

5. Prescott, J. K.; Barnum, R. A., On powder flowability. *Pharm Technol* **2000,** 24, 60–84.

6. Spillmann, A.; Sonnenfeld, A.; Rohr, P. R. V., Effect of surface free energy on the flowability of lactose powder treated by PECVD. *Plasma Process. Polym.* **2008,** 5, 753–758.

7. Geldart, D., Types of fluidization. *Powder Technol* **1973,** 7, 285-292.

8. Shi, L.; Feng, Y.; Sun, C. C., Roles of granule size in over-granulation during high shear wet granulation. *J. Pharm. Sci.* **2010,** 99, 3322-3325.

9. Sun, C. C.; Himmelspach, M., Reduced tabletability of roller compacted granules as a result of granule size enlargement. *J Pharm Sci* **2006,** 95, 200-206.

10. Sun, C. C., On the mechanism of reduced tabletability of granules prepared by roller compaction. *Int J Pharm* **2008,** 347, 171-172.

11. Shi, L.; Feng, Y.; Sun, C. C., Origin of profound changes in powder properties during wetting and nucleation stages of high shear wet granulation. *Powder Technol.* **2011,** 208(3), 663–668.

12. Yang, J.; Sliva, A.; Banerjee, A.; Dave, R. N.; Pfeffer, R., Dry particle coating for improving the flowability of cohesive powders. *Powder Technol* **2005,** 158, 21-33.

13. Narh, K. A.; Agwedicham, A. T.; Jallo, L., Dry coating polymer powder particles with deagglomerated carbon nanotubes to improve their dispersion in nanocomposites. *Powder Technol* **2008,** 186, 206-212.

14. Pfeffer, R.; Dave, R. N.; Wei, D.; Ramlakhan, M., Synthesis of engineered particulates with tailored properties using dry particle coating. *Powder Technol* **2001,** 117, 40-67.

15. Mei, R.; Shang, H.; Klausner, J. F.; Kallman, E., A contact model for the effect of particle coating on improving the flowability of cohesive powders. *KONA* **1997,** 15, 132-141.

16. Zhou, Q.; Armstrong, B.; Larson, I.; Stewart, P. J.; Morton, D. A. V., Improving Powder Flow Properties of a Cohesive Lactose Monohydrate Powder by Intensive Mechanical Dry Coating. *J. Pharm. Sci.* **2010,** 99, 969-981.

17. Zhou, Q.; Denman, J. A.; Gengenbach, T.; Das, S.; Qu, L.; Zhang, H.; Larson, I.; Stewart, P. J.; Morton, D. A., Characterization of the Surface Properties of a Model Pharmaceutical Fine Powder Modified with a Pharmaceutical Lubricant to Improve Flow via a Mechanical Dry Coating Approach. *J Pharm Sci* **2011,** 100, 3421–3430.

18. Waltersson, J. O.; Lundgren, P., The effect of mechanical comminution on drug stability. *Acta Pharm. Suec.* **1985,** 22, 291–300.

19. Kendall, K., Adhesion: molecules and mechanics. *Science* **1994,** 263, 1720-1725.

20. Hamaker, H. C., The London – van der Waals attraction between spherical particles. *Physica* **1937,** 4, 1058–1072.

21. D18.24, S., Standard shear test method for bulk solids using the Schulze ring shear tester, ASTM Standard D6773-02. *American Society for Testing and Materials* **2002**.

22. Schulze, D., Flowability and time consolidation measurements using a ring shear tester. *Powder Hand Proc* **1996,** 3, 221–226.

23. Fell, J. T.; Newton, J. M., Determination of tablet strength by the diametral-compression test. *J. Pharm. Sci.* **1970,** 59, 688–691.

24. Jenike, A. W. *Storage and flow of solids*; Univ. Utah: Salt Lake City, 1964.

25. Behera, S.; Das, S.; Hatvani, Z.; Pahl, M. H., Flowability studies of bulk materials for design of hopper using a Jenike shear cell. *Powder Hand. Proc.* **2002,** 14, 96–101.

26. Fitzpatrick, J. J.; Barringer, S. A.; Iqbal, T., Flow property measurement of food powders and sensitivity of Jenike's hopper design methodology to the measured values. *J Food Eng* **2004,** 61, 399–405.

27. Shi, L.; Sun, C. C., Transforming powder mechanical properties by core/shell structure: compressible sand. *J. Pharm. Sci.* **2010,** 99, 4458-4462.

28. Faqih, A. M.; Chaudhuri, B.; Alexander, A. W.; Davies, C.; Muzzio, F. J.; Tomassone, M. S., An experimental/computational approach for examining unconfined cohesive powder flow. *Int J Pharm* **2006,** 324, 116–127.

29. Kurfeh, D.; Hinrichsen, H.; Zimmermann, I., Statistical model of the powder flow regulation by nanomaterials. *Powder Technol* **2005,** 159, 63 – 70.

30. Sun, C. C., Materials Science Tetrahedron—A Useful Tool for Pharmaceutical Research and Development. *J. Pharm. Sci.* **2009,** 98, (5), 1671 - 1687.

Chapter 5.

1. Datta, S.; Grant, D. J. W., Crystal structures of drugs: Advances in determination, Prediction and engineering. *Nature Reviews* **2004,** 3, 42-57.

2. Brittain, H. G., *Polymorphism in Pharmaceutical Solids*. Marcel Dekker: New York, 1999.

3. Grant, D. J. W.; Higuchi, T., *Solubility behavior of organic compounds*. John Wiley & Sons: New York, 1990.

4. Burger, A.; Ramberger, R., On the Polymorphism of Pharmaceuticals and Other Molecular Crystals. I Theory of Thermodynamic Rules. *Mikrochim Acta* **1979**, 259--271.

5. Datta, S.; Grant, D. J. W., Crystal structures of drugs: Advances in determination, prediction and engineering. *Nature Rev.* **2004,** 3, 42-57.

6. Byrn, S. R., *Solid State Chemistry of Drugs*. Academic Press: New York, 1982.

7. Chattoraj, S.; Shi, L.; Sun, C. C., Understanding the relationship between crystal structure, plasticity and compaction behaviour of theophylline, methyl gallate, and their 1 : 1 co-crystal. *Cryst. Eng. Comm.* **2010,** 12, 2466–2472.

8. Sun, C. C.; Grant, D. J. W., Influence of Crystal Structure on the Tableting Properties of Sulfamerazine Polymorphs. *Pharm. Res.* **2001,** 18, 274-280.

9. Hancock, B. C.; Parks, M., What is the true solubility advantage for amorphous pharmaceuticals? *Pharm Res* **2000,** 17, 397–404.

10. Murdande, S. B.; Pikal, M. J.; Shanker, R. M.; Bogner, R. H., Solubility Advantage of Amorphous Pharmaceuticals: I. A Thermodynamic Analysis. *J. Pharm. Sci.* **2010,** 99, 1254-1264.

11. Murdande, S. B.; Pikal, M. J.; Shanker, R. M.; Bogner, R. H., Solubility Advantage of Amorphous Pharmaceuticals: II. Application of Quantitative Thermodynamic Relationships for Prediction of Solubility Enhancement in Structurally Diverse Insoluble Pharmaceuticals. *Pharm Res* **2010,** 27, 2704–2714.

12. Murdande, S. B.; Pikal, M. J.; Shanker, R. M.; Bogner, R. H., Solubility Advantage of Amorphous Pharmaceuticals, Part 3: Is Maximum Solubility Advantage Experimentally Attainable and Sustainable? *J. Pharm. Sci.* **2011,** 100, 4349–4356.

13. Amidon, G. L.; Lennernaes, H.; Shah, V. P.; Crison, J. R., A theoretical basis for a biopharmaceutic drug classification: The correlation of in vitro drug product dissolution and in vivo bioavailability. *Pharm Res* **1995,** 12, 413–420.

14. Takagi, T.; Ramachandran, C.; Bermejo, M.; Yamashita, S.; Yu, L. X.; Amidon, G. L., A provisional biopharmaceutical classification of the top 200 oral drug products in the United States, Great Britain, Spain, and Japan. *Mol Pharmaceutics* **2006,** 3, 631–643.

15. Yu, L., Amorphous pharmaceutical solids: preparation, characterization and stabilization. *Adv Drug Del Rev* **2001,** 48, 27-42.

16. Hilden, L. R.; Morris, K. R., Physics of amorphous solids. *J Pharm Sci* **2001,** 93, 3-12.

17. Debenedetti, P. G.; Stillinger, F. H., Supercooled liquids and the glass transition. *Nature* **2001,** 410, 259-267.

18. Zeng, Q.; Sheng, H.; Ding, Y.; Wang, L.; Yang, W.; Jiang, J.-Z.; Mao, W. L.; Mao, H.-K., Long-Range Topological Order in Metallic Glass. *Science* **2011,** 332, 1404-1406.

19. Pikal, M. J.; Rigsbee, D. R., The stability of insulin in crystalline and amorphous solids: observation of greater stability for the amorphous form. *Pharm. Res.* **1997,** 14, 1379– 1387.

20. Sukenik, C. N.; Bonapace, J. A. P.; Mandel, N. S.; Bergman, R. G.; Lau, P. Y.; Wood, G., Enhancement of a chemical reaction rate by proper orientation of reacting molecules in the solid state. *J. Am. Chem. Soc.* **1975,** 97, 5290– 5291.

21. Sukenik, C. N.; Bonapace, J. A. P.; Mandel, N. S.; Lau, P. Y.; Wood, G.; Bergman, R. G., A kinetic and X-ray diffraction study of the solid-state rearrangement of methyl p-dimethylaminobenzenesulfonate. Reaction rate enhancement due to proper orientation in a crystal. *J. Am. Chem. Soc.* **1977,** 99, 851– 858.

22. Willart, J. F.; Descamps, M., Solid State Amorphization of Pharmaceuticals. *Mol Pharm* **2008,** 5, 905–920.

23. Chattoraj, S.; Bhugra, C.; Telang, C.; Zhong, L.; Wang, Z.; Sun, C. C., Origin of Two Modes of Non-isothermal Crystallization of Glasses Produced by Milling. *Pharm Res* **2012,** 29, 1020-1032.

24. Wildfong, P. L. D.; Hancock, B. C.; Moore, M. D.; Morris, K. R., Towards an understanding of the structurally based potential for mechanically activated disordering of small molecule organic crystals. *J Pharm Sci* **2006,** 95, 2645–2656.

25. Morris, K. R.; Griesser, U. J.; Eckhardt, C. J.; Stowell, J. G., Theoretical approaches to physical transformations of active pharmaceutical ingredients during manufacturing processes. *Adv Drug Deliv Rev* **2001,** 48, 91–114.

26. Zhang, G. G. Z.; Law, D.; Schmitt, E. A.; Qiu, Y., Phase transformation considerations during process development and manufacture of solid oral dosage forms. *Adv Drug Del Rev* **2004,** 56, 371-390.

27. Willart, J. F.; De Gusseme, A.; Hemon, S.; Odou, G.; Danede, F.; Descamps, M., Direct crystal to glass transformation of trehalose induced by ball milling. *Solid State Commun* **2001,** 119, 501–505.

28. Huttenrauch, R.; Fricke, S.; Zeilke, P., Mechanical activation of pharmaceutical systems. *Pharm Res* **1985**, 302-306.

29. Lin, Y.; Cogdill, R. P.; Wildfong, P. L. D., Informatic calibration of a materials properties database for predictive assessment of mechanically activated disordering potential for small molecule organic solids. *J Pharm Sci* **2008,** 98, 2696-2708.

30. Crowley, K. J.; Zografi, G., Cryogenic Grinding of Indomethacin Polymorphs and Solvates: Assessment of Amorphous Phase Formation and Amorphous Phase Physical Stability. *J Pharm Sci* **2002,** 91, 492-507.

31. Delogu, F.; Cocco, G., Impact-induced disordering of intermetallic phases during mechanical processing. *Mater. Sci. Engg. A* **2003,** 343, 314-317.

32. Fan, G. J.; Guo, F. Q.; Hu, Z. Q.; Quan, M. X.; Lu, K., Amorphization of selenium induced by high-energy ball milling. *Phys Rev B* **1997,** 55, 11010-11013.

33. Suryanarayana, C., Mechanical alloying and milling. *Prog Mater Sci* **2001,** 46, 1.
34. Tse, J. S., Mechanical instability of ice Ih. A mechanism for pressure-induced amorphization. *J Chem Phys* **1992,** 96, 5482-5487.

35. Fecht, H. J., Defect-induced melting and solid-state amorphization. *Nature* **1992,** 356, 133-135.

36. Lin, Z. J.; Zhuo, M. J.; Sun, Z. Q.; Veyssiere, P.; Zhou, Y. C., Amorphization by dislocation accumulation in shear bands. *Acta Mater* **2009,** 57, 2851 - 2857.

37. Tromans, D.; Meech, J. A., Enhanced dissolution of minerals: Stored energy, amorphism and mechanical activation. *Miner Eng* **2001,** 14, 1359–1377.

38. Sun, C. C., Materials science tetrahedron--a useful tool for pharmaceutical research and development. *J. Pharm. Sci.* **2009,** 98, 1671-1687.

39. Grisedale, L. C.; Jamieson, M. J.; Belton, P. S.; Barker, S. A.; Craig, D. Q. M., Characterization and Quantification of Amorphous Material in Milled and Spray-Dried Salbutamol Sulfate: A Comparison of Thermal, Spectroscopic, and Water Vapor Sorption Approaches. *J Pharm Sci* **2011,** 100, 3114-3129.

40. Szabo, Z. G., In *Comprehensive Chemical Kinetics. The Theory of Kinetics*, Bamford, C. H.; Tipper, C. F. H., Eds. Elsevier: Oxford, 1965; p 15.

41. Hill, V. L.; Craig, D. Q. M.; Feely, L. C., The effects of experimental parameters and calibration on MTDSC data. *Int J Pharm* **1999,** 192, 21–32.

42. Taylor, R. E., *Thermal expansion of solids*. ASM International: Materials Park, Ohio, 1998; Vol. I-4.

43. Li, Z. J. G., D. J. W, Relationship between physical properties and crystal structures of chiral drugs. *Journal of Pharmaceutical Sciences* **1997,** 86, 1073-1078.

44. Tang, X. C.; Pikal, M. J.; Taylor, L. S., The Effect of Temperature on Hydrogen Bonding in Crystalline and Amorphous Phases in Dihydropyrine Calcium Channel Blockers. *Pharm Res* **2002,** 19, 484-490.

45. Tang, X. C.; Pikal, M. J.; Taylor, L. S., A Spectroscopic Investigation of Hydrogen Bond Patterns in Crystalline and Amorphous Phases in Dihydropyridine Calcium Channel Blockers. *Pharm Res* **2002,** 19, 477-483.

46. Avrami, M., Kinetics of Phase Change. I General Theory. *J. Chem. Phys.* **1939,** 7, 1103-1112.

47. Avrami, M., Kinetics of Phase Change. II TransformationTime Relations for Random Distribution of Nuclei *J. Chem. Phys.* **1940,** 8, 212-224.

48. Avrami, M., Granulation, Phase Change, and Microstructure Kinetics of Phase Change. III. *J. Chem. Phys.* **1941,** 9, 177-184.

49. Coats, A. W.; Redfern, J. P., Kinetic parameters from thermogravimetric data. *Nature* **1964,** 201, 68-69.

50. Coats, A. W.; Redfern, J. P., Kinetic parameters from thermogravimetric data II. *J. Polym. Sci. B: Polym. Lett.* **1965,** 3, 917-920.

51. Zhou, D.; Schmitt, E. A.; Zhang, G. G.; Law, D.; Vyazovkin, S.; Wight, C. A.; Grant, D. J. W., Crystallization Kinetics of Amorphous Nifedipine Studied by Model-Fitting and Model-Free Approaches. *J. Pharm. Sci.* **2003,** 92, 1779-1792.

52. Cook, R. D.; Weisberg, S., *Applied Regression Including Computing and Graphics*. Wiley: New Jersey, 1999.

53. Baird, J. R.; Eerdenbrugh, B. V.; Taylor, L. S., A Classification System to Assess the Crystallization Tendency of Organic Molecules from Undercooled Melts. *J. Pharm. Sci.* **2010,** 99, 3787-3806.

54. Avramov, I.; Zanotto, E. D.; Prado, M. O., Glass-forming ability versus stability of silicate glasses. II. Theoretical demonstration. *J Non-Crystalline Solids* **2003,** 320, 9-20.

55. Nascimento, M. L. F.; Souza, L. A.; Ferreira, E. B.; Zanotto, E. D., Can glass stability parameters infer glass forming ability? *J Non-Crystalline Solids* **2005,** 351, 3296–3308.

56. Barandiaran, J. M.; Colmenero, J., Continuous cooling approximation for the formation of a glass. *J Non-Crystalline Solids* **1981,** 46, 277-287.

57. Cabral, A. A.; Cardoso, A. A. D.; Zanotto, E. D., Glass-forming ability versus stability of silicate glasses. I. Experimental test. *J Non-Crystalline Solids* **2003,** 320, 1-8.

58. Bhugra, C.; Pikal, M. J., Role of Thermodynamic, Molecular, and Kinetic Factors in Crystallization From the Amorphous State. *J Pharm Sci* **2008,** 97, 1329-1349.

59. Bhugra, C.; Rambhatla, S.; Bakri, A.; Duddu, S. P.; Miller, D. P.; Pikal, M. J.; Lechuga-Ballesteros, D., Prediction of the Onset of Crystallization of Amorphous Sucrose below the Calorimetric Glass Transition Temperature from Correlations with Mobility. *J Pharm Sci* **2007,** 96, 1258-1269.

60. Zhou, D.; Zhang, G. G. Z.; Law, D.; Grant, D. J. W.; Schmitt, E. A., Physical Stability of Amorphous Pharmaceuticals: Importance of Configurational Thermodynamic Quantities and Molecular Mobility. *J Pharm Sci* **2002,** 91, 1863-1872.

61. Shamblin, S. L.; Tang, X. C.; Hancock, B. C.; Pikal, M. J., Characterization of the time scales of molecular motion in pharmaceutically important glasses. *J Phys Chem B* **1999,** 103, 4113–4121.

62. Zhou, D.; Schmitt, E. A.; Zhang, G. G.; Law, D.; Vyazovkin, S.; Wright, C. A.; Grant, D. J. W., Crystallization Kinetics of Amorphous Nifedipine Studied by Model-Fitting and Model-Free Approaches. *J Pharm Sci* **2003,** 92, 1779-1792.

63. Sun, Y.; Tau, J.; Zhang, G. G. Z.; Yu, L., Solubilities of crystalline drugs in polymers: An improved analytical method and comparison of solubilities of indomethacin and nifedipine in PVP, PVP/VA, and PVAc. *J Pharm Sci* **2010,** 99, 4023-4031.

Chapter 6.

1. Morris, K. R., *Structural aspects of hydrates and solvates*. Marcel Dekker: New York, 1999.

2. Zhang, G. G. Z.; Law, D.; Schmitt, E. A.; Qiu, Y., Phase transformation considerations during process development and manufacture of solid oral dosage forms. *Adv Drug Del Rev* **2004,** 56, 371-390.

3. Willart, J. F.; Descamps, M., Solid State Amorphization of Pharmaceuticals. *Mol Pharm* **2008,** 5, 905–920.

4. Wildfong, P. L. D.; Hancock, B. C.; Moore, M. D.; Morris, K. R., Towards an understanding of the structurally based potential for mechanically activated disordering of small molecule organic crystals. *J Pharm Sci* **2006,** 95, 2645–2656.

5. Lin, Y.; Cogdill, R. P.; Wildfong, P. L. D., Informatic calibration of a materials properties database for predictive assessment of mechanically activated disordering potential for small molecule organic solids. *J Pharm Sci* **2008,** 98, 2696-2708.

6. Chattoraj, S.; Bhugra, C.; Telang, C.; Zhong, L.; Wang, Z.; Sun, C. C., Origin of Two Modes of Non-isothermal Crystallization of Glasses Produced by Milling. *Pharm Res* **2012,** 29, 1020-1032.

7. Crowley, K. J.; Zografi, G., Cryogenic Grinding of Indomethacin Polymorphs and Solvates: Assessment of Amorphous Phase Formation and Amorphous Phase Physical Stability. *J Pharm Sci* **2002,** 91, 492-507.

8. Feng, T.; Pinal, R.; Carvajal, M. T., Process Induced Disorder in Crystalline Materials: Differentiating Defective Crystals from the Amorphous Form of Griseofulvin. *J Pharm Sci* **2008,** 97, 3207-3221.

9. Yu, L., Amorphous pharmaceutical solids: preparation, characterization and stabilization. *Adv Drug Del Rev* **2001,** 48, 27-42.

10. Hilden, L. R.; Morris, K. R., Physics of amorphous solids. *J Pharm Sci* **2001,** 93, 3-12.

11. Hancock, B. C.; Zografi, G., Characteristics and Significance of the Amorphous State in Pharmaceutical Systems. *J Pharm Sci* **1997,** 86, 1-12.

12. Hancock, B. C.; Parks, M., What is the true solubility advantage for amorphous pharmaceuticals? *Pharm Res* **2000,** 17, 397–404.

13. Murdande, S. B.; Pikal, M. J.; Shanker, R. M.; Bogner, R. H., Solubility Advantage of Amorphous Pharmaceuticals: I. A Thermodynamic Analysis. *J. Pharm. Sci.* **2010,** 99, 1254-1264.

14. Murdande, S. B.; Pikal, M. J.; Shanker, R. M.; Bogner, R. H., Solubility Advantage of Amorphous Pharmaceuticals: II. Application of Quantitative Thermodynamic Relationships for Prediction of Solubility Enhancement in Structurally Diverse Insoluble Pharmaceuticals. *Pharm Res* **2010,** 27, 2704–2714.

15. Murdande, S. B.; Pikal, M. J.; Shanker, R. M.; Bogner, R. H., Solubility Advantage of Amorphous Pharmaceuticals, Part 3: Is Maximum Solubility Advantage Experimentally Attainable and Sustainable? *J. Pharm. Sci.* **2011,** 100, 4349–4356.

16. Pikal, M. J.; Rigsbee, D. R., The stability of insulin in crystalline and amorphous solids: observation of greater stability for the amorphous form. *Pharm. Res.* **1997,** 14, 1379– 1387.

17. Bhugra, C.; Shmeis, R.; Pikal, M. J., Role of Mechanical Stress in Crystallization and Relaxation Behavior of Amorphous Indomethacin. *J Pharm Sci* **2007,** 97, 4446-4458.

18. Brittain, H. G., Effects of mechanical processing on phase composition. *J Pharm Sci* **2002,** 91, 1573-1580.

19. Tromans, D.; Meech, J. A., Enhanced dissolution of minerals: Stored energy, amorphism and mechanical activation. *Miner Eng* **2001,** 14, 1359–1377.

20. Grisedale, L. C.; Jamieson, M. J.; Belton, P. S.; Barker, S. A.; Craig, D. Q. M., Characterization and Quantification of Amorphous Material in Milled and Spray-Dried Salbutamol Sulfate: A Comparison of Thermal, Spectroscopic, and Water Vapor Sorption Approaches. *J Pharm Sci* **2011,** 100, 3114-3129.

21. Adam, G.; Gibbs, J. H., On the temperature dependence of cooperative relaxation properties in glass-forming liquids. *J Chem Phys* **1965,** 43, 139–146.

22. Avrami, M., Kinetics of Phase Change. I General Theory. *J. Chem. Phys.* **1939,** 7, 1103-1112.

23. Avrami, M., Kinetics of Phase Change. II TransformationTime Relations for Random Distribution of Nuclei *J. Chem. Phys.* **1940,** 8, 212-224.

24. Avrami, M., Granulation, Phase Change, and Microstructure Kinetics of Phase Change. III. *J. Chem. Phys.* **1941,** 9, 177-184.

25. Coats, A. W.; Redfern, J. P., Kinetic parameters from thermogravimetric data. *Nature* **1964,** 201, 68-69.

26. Coats, A. W.; Redfern, J. P., Kinetic parameters from thermogravimetric data II. *J. Polym. Sci. B: Polym. Lett.* **1965,** 3, 917-920.

27. Zhou, D.; Schmitt, E. A.; Zhang, G. G.; Law, D.; Vyazovkin, S.; Wight, C. A.; Grant, D. J. W., Crystallization Kinetics of Amorphous Nifedipine Studied by Model-Fitting and Model-Free Approaches. *J. Pharm. Sci.* **2003,** 92, 1779-1792.

28. Liu, J.; Rigsbee, D. R.; Stotz, C.; Pikal, M. J., Dynamics of pharmaceutical amorphous solids: the study of enthalpy relaxation by isothermal microcalorimetry. *J Pharm Sci* **2002,** 91, 1853-1862.

29. Bhugra, C.; Shmeis, R.; Krill, S. L.; Pikal, M. J., Predictions of onset of crystallization from experimental relaxation times I - Correlations of molecular mobility from temperatures above the glass transition to temperatures below the glass transition. *Pharm Res* **2006,** 23, 2277-2290.

30. Baird, J. R.; Eerdenbrugh, B. V.; Taylor, L. S., A Classification System to Assess the Crystallization Tendency of Organic Molecules from Undercooled Melts. *J. Pharm. Sci.* **2010,** 99, 3787-3806.

31. Zhou, D.; Zhang, G. G. Z.; Law, D.; Grant, D. J. W.; Schmitt, E. A., Physical Stability of Amorphous Pharmaceuticals: Importance of Configurational Thermodynamic Quantities and Molecular Mobility. *J Pharm Sci* **2002,** 91, 1863-1872.

32. Crowley, K. J.; Zografi, G., The use of thermal methods for predicting glass-former fragility. *Thermochim Acta* **2001,** 380, 79-93.

33. Siniti, M.; Carre, J.; Letoffe, J. M.; Bastide, J. P.; Claudy, P., The thermal behaviour of hexitols: Part 1. Vitrification and crystallization of iditol, mannitol, sorbitol and dulcitol. *Thermochim Acta* **1993,** 224, 97–104.

34. Bhugra, C.; Rambhatla, S.; Bakri, A.; Duddu, S. P.; Miller, D. P.; Pikal, M. J.; Lechuga-Ballesteros, D., Prediction of the Onset of Crystallization of Amorphous Sucrose below the Calorimetric Glass Transition Temperature from Correlations with Mobility. *J Pharm Sci* **2007,** 96, 1258-1269.

35. Bhugra, C.; Shmeis, R.; Krill, S. L.; Pikal, M. J., Prediction of Onset of Crystallization from Experimental Relaxation Times. II. Comparison between Predicted and Experimental Onset Times. *J Pharm Sci* **2008,** 97, 455-472.

36. Zhu, L.; Brian, C. W.; Swallen, S. F.; Straus, P. T.; Ediger, M. D.; Yu, L., Surface Self-Diffusion of an Organic Glass. *Phys Rev Lett* **2011,** 106, 256103-1 - 256103-4.

37. Liu, J.; Rigsbee, D. R.; Stotz, C.; Pikal, M. J., Dynamics of pharmaceutical amorphous solids: The study of enthalpy relaxation by isothermal microcalorimetry. *J Pharm Sci* **2002,** 91, 1853–1862.

38. Kawakam, K., Investigation of the structural relaxation process of amorphous formulation by isothermal microcalorimetry. *Netsu Sokutei* **2004,** 31, 74-79.

39. Caron, V.; Bhugra, C.; Pikal, M. J., Prediction of Onset of Crystallization in Amorphous Pharmaceutical Systems: Phenobarbital, Nifedipine/PVP, and Phenobarbital/PVP. *J Pharm Sci* **2010,** 99, 3887-3900.

40. Bhardwaj, S.; Suryanarayanan, R., Molecular mobility as an effective predictor of the physical stability of amorphous trehalose. *Mol Pharm* **2012**.

41. Bhugra, C.; Pikal, M. J., Role of Thermodynamic, Molecular, and Kinetic Factors in Crystallization From the Amorphous State. *J Pharm Sci* **2008,** 97, 1329-1349.

42. Aso, Y.; Yoshioka, S.; Kojima, S., Relationship between the crystallization rates of amorphous nifedipine, phenobarbital, and flopropione, and their molecular mobility as measured by their enthalpy relaxation and 1H NMR relaxation times. *J Pharm Sci* **2000,** 89, 408–416.

43. Aso, Y.; Yoshioka, S.; S., K., Explanation of the crystallization rate of amorphous nifedipine and phenobarbital from their molecular mobility as measured by 13C nuclear magnetic resonance relaxation time and the relaxation time obtained from the heating rate dependence of the glass transition temperature. *J Pharm Sci* **2001,** 90, 798–806.

44. Richard, V. T., Remarks concerning the formation and crystallization of vitreous media. *J Chem Phys* **1936,** 4, 449–457.

Chapter 7.

1. Desiraju, G. R., *Crystal engineering: the design of organic solids*. Elsevier: 1989; Vol. 54.

2. Aakeroy, C. B.; Salmon, D. J., Building Co-Crystals with Molecular Sense and Supramolecular Sensibility. *CrystEngComm* **2005,** 7, 439-448.

3. Jayasankar, A. Understanding the mechanisms, thermodynamics and kinetics of cocrystallization to control phase transformations. The University of Michigan, Michigan, 2008.

4. Brittain, H. G., Cocrystal Systems of Pharmaceutical Interest: 2010. *Cryst. Growth Des.* **2011**.

5. Trask, A. V.; Motherwell, W. D. S.; Jones, W., Physical stability enhancement of theophylline via cocrystallization. *Int. J. Pharm.* **2006,** 320, 114 - 123.

6. Vangala, V. R.; Chow, P. S.; Tan, R. B. H., Characterization, physicochemical and photo-stability of a co-crystal involving an antibiotic drug, nitrofurantoin, and 4-hydroxybenzoic acid. *CrystEngComm* **2011,** 13, 759-762.

7. McNamara, D. P.; Childs, S. L.; Giordano, J.; Iarriccio, A.; Cassidy, J.; Shet, M. S.; Mannion, R.; E., O. D.; Park, A., Use of a Glutaric Acid Cocrystal to Improve Oral Bioavailability of a Low Solubility API. *Pharmaceutical Research* **2006,** 23, 1888.

8. Chattoraj, S.; Shi, L.; Sun, C. C., Understanding the relationship between crystal structure, plasticity and compaction behaviour of theophylline, methyl gallate, and their 1:1 co-crystal. *CrystEngComm* **2010,** 12, 2466-2472.

9. Sun, C. C.; Hou, H., Improving Mechanical Properties of Caffeine and Methyl Gallate Crystals by Cocrystallization. *Cryst. Growth Des.* **2008,** 8, (9), 1575 - 1579.

10. Yu, L., Amorphous pharmaceutical solids: preparation, characterization and stabilization. *Adv Drug Del Rev* **2001,** 48, 27-42.

11. Hilden, L. R.; Morris, K. R., Physics of amorphous solids. *J Pharm Sci* **2001,** 93, 3-12.

12. Amidon, G. L.; Lennernaes, H.; Shah, V. P.; Crison, J. R., A theoretical basis for a biopharmaceutic drug classification: The correlation of in vitro drug product dissolution and in vivo bioavailability. *Pharm Res* **1995,** 12, 413–420.

13. Takagi, T.; Ramachandran, C.; Bermejo, M.; Yamashita, S.; Yu, L. X.; Amidon, G. L., A provisional biopharmaceutical classification of the top 200 oral drug products in the United States, Great Britain, Spain, and Japan. *Mol Pharmaceutics* **2006,** 3, 631–643.

14. Pikal, M. J.; Rigsbee, D. R., The stability of insulin in crystalline and amorphous solids: observation of greater stability for the amorphous form. *Pharm. Res.* **1997,** 14, 1379– 1387.

15. Chattoraj, S.; Bhugra, C.; Telang, C.; Zhong, L.; Wang, Z.; Sun, C. C., Origin of Two Modes of Non-isothermal Crystallization of Glasses Produced by Milling. *Pharm Res* **2012,** 29, 1020-1032.

16. Willart, J. F.; Descamps, M., Solid State Amorphization of Pharmaceuticals. *Mol Pharm* **2008,** 5, 905–920.

17. Lin, Y.; Cogdill, R. P.; Wildfong, P. L. D., Informatic calibration of a materials properties database for predictive assessment of mechanically activated disordering potential for small molecule organic solids. *J Pharm Sci* **2008,** 98, 2696-2708.

18. Feng, T.; Bates, S.; Carvajal, M. T., Toward understanding the evolution of griseofulvin crystal structure to a mesophase after cryogenic milling. *Int J Pharm* **2008,** 367, 16-19.

19. Morris, K. R.; Griesser, U. J.; Eckhardt, C. J.; Stowell, J. G., Theoretical approaches to physical transformations of active pharmaceutical ingredients during manufacturing processes. *Adv Drug Deliv Rev* **2001,** 48, 91–114.

20. Zhang, G. G. Z.; Law, D.; Schmitt, E. A.; Qiu, Y., Phase transformation considerations during process development and manufacture of solid oral dosage forms. *Adv Drug Del Rev* **2004,** 56, 371-390.

21. Willart, J. F.; De Gusseme, A.; Hemon, S.; Odou, G.; Danede, F.; Descamps, M., Direct crystal to glass transformation of trehalose induced by ball milling. *Solid State Commun* **2001,** 119, 501–505.

22. Chamarthy, S. P.; Pinal, R., The nature of crystal disorder in milled pharmaceutical materials. *Colloids Surf A* **2008,** 331, 68–75.

23. Trasi, N. S.; Boerrigter, S. X. M.; Byrn, S. R., Investigation of the Milling-Induced Thermal Behavior of Crystalline and Amorphous Griseofulvin. *Pharm Res* **2010,** 27, 1377-1389.

24. Wildfong, P. L. D.; Hancock, B. C.; Moore, M. D.; Morris, K. R., Towards an understanding of the structurally based potential for mechanically activated disordering of small molecule organic crystals. *J Pharm Sci* **2006,** 95, 2645–2656.

25. Fan, G. J.; Guo, F. Q.; Hu, Z. Q.; Quan, M. X.; Lu, K., Amorphization of selenium induced by high-energy ball milling. *Phys Rev B* **1997,** 55, 11010-11013.

26. Tromans, D.; Meech, J. A., Enhanced dissolution of minerals: Stored energy, amorphism and mechanical activation. *Miner Eng* **2001,** 14, 1359–1377.

27. Zhao, Y. H.; Jin, Z. H.; Lu, K., Mechanical-milling-induced amorphization of Se: a crystallite destabilization model. *Philos Mag Lett* **1999,** 79, 747-754.

28. Ghosh, S.; Bag, P. P.; Reddy, C. M., Co-Crystals of Sulfamethazine with Some Carboxylic Acids and Amides: Co-Former Assisted Tautomerism in an Active

Pharmaceutical Ingredient and Hydrogen Bond Competition Study. *Cryst Growth Des* **2011,** 11, 3489–3503.

29. Bhugra, C.; Pikal, M. J., Role of Thermodynamic, Molecular, and Kinetic Factors in Crystallization From the Amorphous State. *J Pharm Sci* **2008,** 97, 1329-1349.

30. Adam, G.; Gibbs, J. H., On the temperature dependence of cooperative relaxation properties in glass-forming liquids. *J Chem Phys* **1965,** 43, 139–146.

31. Zhou, D.; Zhang, G. G. Z.; Law, D.; Grant, D. J. W.; Schmitt, E. A., Physical Stability of Amorphous Pharmaceuticals: Importance of Configurational Thermodynamic Quantities and Molecular Mobility. *J Pharm Sci* **2002,** 91, 1863-1872.

32. Crowley, K. J.; Zografi, G., The use of thermal methods for predicting glass-former fragility. *Thermochim Acta* **2001,** 380, 79-93.

33. Kere, J.; Sreie, S., Thermal analysis of glassy pharmaceuticals. *Thermochim Acta* **1995,** 248, 81–95.

34. Fukuoka, E.; Makita, M.; Nakamura, Y., Glassy state of pharmaceuticals.V. Relaxation during cooling and heating of glass by differential scanning calorimetry. *Chem. Pharm. Bull.* **1991,** 39, 2087–2090.

35. Nakamoto, K.; Margoshes, M.; Rundle, R. E., Stretching frequencies as a function of distances in hydrogen bonds. *J. Amer. Chem.Soc.* **1955,** 77, 6480–6486.

36. Aso, Y.; Yoshioka, S.; Kojima, S., Relationship between the crystallization rates of amorphous nifedipine, phenobarbital, and flopropione, and their molecular mobility as measured by their enthalpy relaxation and 1H NMR relaxation times. *J Pharm Sci* **2000,** 89, 408–416.

37. Aso, Y.; Yoshioka, S.; S., K., Explanation of the crystallization rate of amorphous nifedipine and phenobarbital from their molecular mobility as measured by 13C nuclear magnetic resonance relaxation time and the relaxation time obtained from the heating rate dependence of the glass transition temperature. *J Pharm Sci* **2001,** 90, 798–806.

38. Richard, V. T., Remarks concerning the formation and crystallization of vitreous media. *J Chem Phys* **1936,** 4, 449–457.

39. Angell, C. A., Relaxation in liquids, polymers and plastic crystals -strong/ fragile patterns and problems. *J. Non-Crystalline Solids* **1991,** 13, 131–133.

40. Bruning, R.; Sutton, M., Fragility of glass-forming systems and the width of the glass transition. *J. Non-Crystalline Solids* **1996,** 205-207, 480–484.

41. Hodge, I. M., Strong and fragile liquids—A brief critique. *J Non-Crystalline Solids* **1996,** 202, 164–172.

42. Bhugra, C.; Rambhatla, S.; Bakri, A.; Duddu, S. P.; Miller, D. P.; Pikal, M. J.; Lechuga-Ballesteros, D., Prediction of the Onset of Crystallization of Amorphous Sucrose below the Calorimetric Glass Transition Temperature from Correlations with Mobility. *J Pharm Sci* **2007,** 96, 1258-1269.

43. Bhugra, C.; Shmeis, R.; Krill, S. L.; Pikal, M. J., Prediction of Onset of Crystallization from Experimental Relaxation Times. II. Comparison between Predicted and Experimental Onset Times. *J Pharm Sci* **2008,** 97, 455-472.

44. Zhu, L.; Brian, C. W.; Swallen, S. F.; Straus, P. T.; Ediger, M. D.; Yu, L., Surface Self-Diffusion of an Organic Glass. *Phys Rev Lett* **2011,** 106, 256103-1 - 256103-4.

45. Caron, V.; Bhugra, C.; Pikal, M. J., Prediction of Onset of Crystallization in Amorphous Pharmaceutical Systems: Phenobarbital, Nifedipine/PVP, and Phenobarbital/PVP. *J Pharm Sci* **2010,** 99, 3887-3900.

46. Bhardwaj, S.; Suryanarayanan, R., Molecular mobility as an effective predictor of the physical stability of amorphous trehalose. *Mol Pharm* **2012**.

47. Avrami, M., Kinetics of Phase Change. I General Theory. *J. Chem. Phys.* **1939,** 7, 1103-1112.

48. Avrami, M., Kinetics of Phase Change. II TransformationTime Relations for Random Distribution of Nuclei *J. Chem. Phys.* **1940,** 8, 212-224.

49. Avrami, M., Granulation, Phase Change, and Microstructure Kinetics of Phase Change. III. *J. Chem. Phys.* **1941,** 9, 177-184.

Chapter 8.

1. Yu, L., Amorphous pharmaceutical solids: preparation, characterization and stabilization. *Adv Drug Del Rev* **2001,** 48, 27-42.

2. Hilden, L. R.; Morris, K. R., Physics of amorphous solids. *J Pharm Sci* **2001,** 93, 3-12.

3. Levine, H.; Slade, L.; Levine, H., *Progress in food processing and storage, based on amorphous product technology*. The Royal Society of Chemistry: Cambridge, 2002.

4. Blanshard, J. M. V.; Lillford, P., *The Glassy State in Foods*. Nottingham University Press: Nottingham, 1993.

5. Crowe, J. H.; Carpenter, J. F.; Crowe, L. M., The role of vitrification in anhydrobiosis. *Ann Rev Physiol* **1998,** 60, 73–103.

6. Greer, A. L., Metallic glasses. *Science* **1995,** 267, 1947–1953.

7. Fan, G. J.; Guo, F. Q.; Hu, Z. Q.; Quan, M. X.; Lu, K., Amorphization of selenium induced by high-energy ball milling. *Phys Rev B* **1997,** 55, 11010-11013.

8. Lin, Z. J.; Zhuo, M. J.; Sun, Z. Q.; Veyssiere, P.; Zhou, Y. C., Amorphization by dislocation accumulation in shear bands. *Acta Mater* **2009,** 57, 2851 - 2857.

9. Huttenrauch, R.; Fricke, S.; Zeilke, P., Mechanical activation of pharmaceutical systems. *Pharm Res* **1985**, 302-306.

10. Willart, J. F.; Descamps, M., Solid State Amorphization of Pharmaceuticals. *Mol Pharm* **2008,** 5, 905–920.

11. Willart, J. F.; De Gusseme, A.; Hemon, S.; Odou, G.; Danede, F.; Descamps, M., Direct crystal to glass transformation of trehalose induced by ball milling. *Solid State Commun* **2001,** 119, 501–505.

12. Suryanarayana, C., Mechanical alloying and milling. *Prog Mater Sci* **2001,** 46, 1.

13. Tromans, D.; Meech, J. A., Enhanced dissolution of minerals: Stored energy, amorphism and mechanical activation. *Miner Eng* **2001,** 14, 1359–1377.

14. Liu, J.; Rigsbee, D. R.; Stotz, C.; Pikal, M. J., Dynamics of pharmaceutical amorphous solids: The study of enthalpy relaxation by isothermal microcalorimetry. *J Pharm Sci* **2002,** 91, 1853–1862.

15. Hodge, I. M., Enthalpy relaxation and recovery in amorphous materials. *J Non-Crystalline Solids* **1994,** 169, 211–266.

16. Crowley, K. J.; Zografi, G., Cryogenic Grinding of Indomethacin Polymorphs and Solvates: Assessment of Amorphous Phase Formation and Amorphous Phase Physical Stability. *J Pharm Sci* **2002,** 91, 492-507.

17. Bhugra, C.; Rambhatla, S.; Bakri, A.; Duddu, S. P.; Miller, D. P.; Pikal, M. J.; Lechuga-Ballesteros, D., Prediction of the Onset of Crystallization of Amorphous Sucrose below the Calorimetric Glass Transition Temperature from Correlations with Mobility. *J Pharm Sci* **2007,** 96, 1258-1269.

18. Bhugra, C.; Pikal, M. J., Role of Thermodynamic, Molecular, and Kinetic Factors in Crystallization From the Amorphous State. *J Pharm Sci* **2008,** 97, 1329-1349.

19. Roberts, C. J.; Debenedetti, P. G., Engineering pharmaceutical stability with amorphous solids. *AIChE J.* **2002,** 48, 1140–1144.

20. Feng, T.; Pinal, R.; Carvajal, M. T., Process Induced Disorder in Crystalline Materials: Differentiating Defective Crystals from the Amorphous Form of Griseofulvin. *J Pharm Sci* **2008,** 97, 3207-3221.

21. Feng, T.; Bates, S.; Carvajal, M. T., Toward understanding the evolution of griseofulvin crystal structure to a mesophase after cryogenic milling. *Int J Pharm* **2008,** 367, 16-19.

22. Chamarthy, S. P.; Pinal, R., The nature of crystal disorder in milled pharmaceutical materials. *Colloids Surf A* **2008,** 331, 68–75.

23. Trasi, N. S.; Boerrigter, S. X. M.; Byrn, S. R., Investigation of the Milling-Induced Thermal Behavior of Crystalline and Amorphous Griseofulvin. *Pharm Res* **2010,** 27, 1377-1389.

24. Yu, L.; Mishra, D.; Rigsbee, D. R., Determination of Glass Properties of Mannitol using Sorbitol as an Impurity. *J Pharm Sci* **1998,** 87, 774-777.

25. Zhou, D.; Schmitt, E. A.; Zhang, G. G.; Law, D.; Vyazovkin, S.; Wright, C. A.; Grant, D. J. W., Crystallization Kinetics of Amorphous Nifedipine Studied by Model-Fitting and Model-Free Approaches. *J Pharm Sci* **2003,** 92, 1779-1792.

26. Lefort, R.; De Gusseme, A.; Willart, J. F.; Danede, F.; Descamps, M., Solid state NMR and DSC methods for quantifying the amorphous content in solid dosage forms: An application to ball-milling of trehalose. *Int J Pharm* **2004,** 280, 209–219.

27. Grisedale, L. C.; Jamieson, M. J.; Belton, P. S.; Barker, S. A.; Craig, D. Q. M., Characterization and Quantification of Amorphous Material in Milled and Spray-Dried Salbutamol Sulfate: A Comparison of Thermal, Spectroscopic, and Water Vapor Sorption Approaches. *J Pharm Sci* **2011,** 100, 3114-3129.

28. Saleki-Gerhardt, A.; Ahlneck, C.; Zografi, G., Assessment of disorder in crystalline solids. *Int J Pharm* **1994,** 101, 237-247.

29. Patterson, J. E.; James, M. B.; Forster, A. H.; Lancaster, R. W.; Butler, J. M.; Rades, T., The Influence of Thermal and Mechanical Preparative Techniques on the Amorphous State of Four Poorly Soluble Compounds. *J Pharm Sci* **2005,** 94, 1998-2012.

30. Wu, T.; Yu, L., Surface Crystallization of Indomethacin Below T_g. *Pharm Res* **2006,** 23, 2350-2355.

31. Zhu, L.; Jona, J.; Nagapudi, K.; Wu, T., Fast Surface Crystallization of Amorphous Griseofulvin Below T_g. *Pharm Res* **2010,** 27, 1558-1567.

32. Zhu, L.; Wong, L.; Yu, L., Surface-Enhanced Crystallization of Amorphous Nifedipine. *Mol Pharm* **2008,** 5, 921–926.

33. Sun, Y.; Zhu, L.; Kearns, K. L.; Ediger, M. D.; Yu, L., Glasses crystallize rapidly at free surfaces by growing crystals upward. *Proc Natl Acad Sci U.S.A.* **2011,** 108, 5990–5995.

34. Zhu, L.; Brian, C. W.; Swallen, S. F.; Straus, P. T.; Ediger, M. D.; Yu, L., Surface Self-Diffusion of an Organic Glass. *Phys Rev Lett* **2011,** 106, 256103-1 - 256103-4.

35. Schmelzer, J.; Pascova, R.; Moller, J.; Gutzow, I., Surface-induced devitrification of glasses: the influence of elastic strains. *J Non-Crystalline Solids* **1993,** 162, 26-39.

36. Gunn, E. M.; Guzei, I. A.; Yu, L., Does crystal density control fast surface crystal growth in glasses? A study with polymorphs. *Cryst Growth Des* **2011,** 11, 3979-3984.

37. Bhugra, C.; Shmeis, R.; Pikal, M. J., Role of Mechanical Stress in Crystallization and Relaxation Behavior of Amorphous Indomethacin. *J Pharm Sci* **2007,** 97, 4446-4458.

38. Ozawa, T., Critical Investigation of Methods for Kinetic Analysis of Thermoanalytical Data. *J Therm Anal* **1975,** 7, 601-617.

39. Sun, C. C.; Grant, D. J. W., Compaction properties of L-lysine salts. *Pharm Res* **2001,** 18, 281-286.

40. Sun, C. C., Mechanism of moisture induced variations in true density and compaction properties of microcrystalline cellulose. *Int J Pharm* **2008,** 346, 93-101.

Appendix I

Regression model development for predicting amorphization

Statistical regression models for amorphization prediction were developed using Arc statistical software ver 1.06 (Department of Statistics, University of Minnesota, 2004). The initial linear regression model (L1) was developed with amorphization rate constant (KA) as the response variable, and 8 model terms - configurational entropy (SC), volume expansivity (VT), molecular weight (MW), molar volume (MV), fusion enthalpy (HM), glass transition temperature (TG) and kinetic fragility (FRAG). The initial model had *F* of 3.73 and *p value* of 0.04, indicating an acceptable model at 95% confidence level.

Initial Model (L1) with 8 predictors

Data set = Amorphization, Name of Fit = L1
Normal Regression
Kernel mean function = Identity
Response = KA
Terms = (SC VT MW MV HM TG FRAG)
Coefficient Estimates

Label	**Estimate**	**Std. Error**	**t-value**	**p-value**
Constant	0.00134602	0.0312723	0.043	0.9667
SC	0.0000727903	0.0000447961	1.625	0.1428
VT	0.0000204566	0.0000217847	0.939	0.3752
MW	0.0000355063	0.0000640200	0.555	0.5943
MV	-7.544806E-6	0.0000848906	-0.089	0.9314
HM	-0.0000619598	0.000126251	-0.491	0.6368
TG	0.0000384571	0.0000438011	0.878	0.4055
FRAG	-0.0375301	0.0501962	-0.748	0.4761

R Squared: 0.765506
Sigma hat: 0.0034452
Number of cases: 16
Degrees of freedom: 8

Summary Analysis of Variance Table

Source	df	SS	MS	F	p-value

Regression	7	0.000309982	0.0000442831	3.73	0.0424
Residual	8	0.0000949555	0.0000118694		

However, we further attempted to refine the model by minimizing the number of predictors to the most influential ones. For this purpose, a forward subset model selection was performed, where we first start with the intercept as the base model. Then progressively, fresh terms are added to expand the model and a submodel is selected that results in small value of Mallow's C_I statistic, which is a total mean squared error.

$$C_I = \frac{RSS}{\sigma} + 2k_I -$$

where, k_I are the number of terms in the model and n are the number of model compounds. The criterion for submodel selection is to minimize error C_I to $<k_I$

Model parameter optimization by forward selection

Data set = Amorphization, Name of Fit = L1
Normal Regression
Kernel mean function = Identity
Response = KA
Terms = (SC VT MW MV HM TG FRAG)
Forward Selection: Sequentially add terms
that minimize the value of C_I.
All fits include an intercept.

Base terms: Intercept

	df	RSS	k	C_I
Add: SC	14	0.000164422	2	1.853
Add: MW	14	0.000169702	2	2.297
Add: MV	14	0.000194052	2	4.349
Add: VT	14	0.000280893	2	11.665
Add: FRAG	14	0.000294263	2	12.792
Add: TG	14	0.000349909	2	17.480
Add: HM	14	0.00039117	2	20.956

Base terms: (SC)

	df	RSS	k	C_I
Add: MW	13	0.000131365	3	1.068
Add: VT	13	0.000135335	3	1.402
Add: TG	13	0.000139541	3	1.756
Add: MV	13	0.000143891	3	2.123
Add: HM	13	0.000162742	3	3.711
Add: FRAG	13	0.000164176	3	3.832

Base terms: (SC MW)

	df	RSS	k	C_I
Add: VT	12	0.000108887	4	1.174
Add: TG	12	0.000121368	4	2.225
Add: MV	12	0.000128813	4	2.852
Add: FRAG	12	0.000129288	4	2.893
Add: HM	12	0.000131034	4	3.040

Base terms: (SC MW VT) - selected submodel

	df	RSS	k	C_I
Add: TG	11	0.000105994	5	2.930
Add: FRAG	11	0.00010602	5	2.932
Add: HM	11	0.000108095	5	3.107
Add: MV	11	0.000108871	5	3.172

Base terms: (SC MW VT TG)

	df	RSS	k	C_I
Add: FRAG	10	0.0000984951	6	4.298
Add: HM	10	0.000102799	6	4.661
Add: MV	10	0.000105645	6	4.901

Base terms: (SC MW VT TG FRAG)

	df	RSS	k	C_I
Add: HM	9	0.0000950492	7	6.008
Add: MV	9	0.0000978142	7	6.241

Base terms: (SC MW VT TG FRAG HM)

	df	RSS	k	C_I
Add: MV	8	0.0000949555	8	8.000

Using the submodel terms, the final predictive model is created using linear regression analysis (model L2). The final model has F of 10.88 and p =0.001 (<<0.05). The model is highly significant at 95% confidence level.

Final model

Data set = Amorphization, Name of Fit = L2
Normal Regression
Kernel mean function = Identity
Response = KA
Terms = (SC VT MW)
Coefficient Estimates

Label	Estimate	Std. Error	t-value	p-value
Constant	-0.0130138	0.00363158	-3.584	0.0038
SC	0.0000533407	0.0000314765	1.695	0.1159
VT	0.0000271099	0.0000172244	1.574	0.1415
MW	0.0000284464	0.0000166620	1.707	0.1135

R Squared: 0.731102
Sigma hat: 0.00301229
Number of cases: 16
Degrees of freedom: 12

Summary Analysis of Variance Table

Source	df	SS	MS	F	p-value
Regression	3	0.00029605	0.0000986835	10.88	0.0010
Residual	12	0.000108887	9.073920E-6		

Reference for Appendix

Cook, R.D. & Weisberg, S. *Applied Regression Including Computing and Graphics*. Wiley, New Jersey, 1999.